N O T I C E

THIS DOCUMENT HAS BEEN REPRODUCED FROM MICROFICHE. ALTHOUGH IT IS RECOGNIZED THAT CERTAIN PORTIONS ARE ILLEGIBLE, IT IS BEING RELEASED IN THE INTEREST OF MAKING AVAILABLE AS MUCH INFORMATION AS POSSIBLE

NASA-CR-169318) THE DYNAMIC FLEXURAL N82-32313
ESPONSE OF PROPELLER BLADES M.S. Thesis
ennsylvania State Univ.) 226 p
A11/MF A01 CSCL 01A Unclas
G3/02 28937

The Dynamic Flexural Response of Propeller Blades

Slobodan Živadin Djordjevic

Master of Science - November 1982

Penn State University

The Pennsylvania State University

The Graduate School

Department of Aerospace Engineering

The Dynamic Flexural Response of Propeller Blades

SEP 1982
RECEIVED
NASA STI FACILITY
ACCESS DEPT.

A Thesis in

Aerospace Engineering

by

Slobodan Zivadin Djordjevic

Submitted in Partial Fulfillment

of the Requirements

for the Degree of

Master of Science

November 1982

I grant The Pennsylvania State University the nonexclusive right to use this work for the University's own purposes and to make single copies of the work available to the public on a not-for-profit basis if copies are not otherwise available.

Slobodan Zivadin Djordjevic

We approve the thesis of Slobodan Z. Djordjevic.

Date of Signature	Signatories
August 16, 1982	Barnes W. McCormick Barnes W. McCormick Professor and Head Aerospace Engineering Thesis Advisor
August 23, 1982	Joseph J. Eisenhuth Joseph J. Eisenhuth Associate Professor of Aerospace Engineering
August 25, 1982	Robert G. Melton Robert G. Melton Assistant Professor of Aerospace Engineering

ABSTRACT

This study was concerned with the dynamic flexural response of propeller blades subjected to harmonic forces, and presents both analytical and experimental results.

The determination of the torsional constants of three blade models having NACA four-digit symmetrical airfoil cross sections is presented. Values were obtained for these models analytically and experimentally. In addition, results were obtained for three other models having rectangular, elliptical, and parabolic cross sections.

Complete modal analyses were performed for five blade models. The identification of modal parameters was done for cases when the blades were modeled as either undamped or damped multi-degree-of-freedom systems. For the experimental phase of this study, the modal testing was performed using a Dual Channel FFT analyzer and an impact hammer (which produced an impulsive excitation). The natural frequency and damping of each mode in the frequency range up to two kilohertz were measured.

A small computer code was developed to calculate the dynamic response of the blade models for comparison with the experimental results. A comparison of the undamped and damped cases was made for all five blade models at the instant of maximum excitation force. The program was capable of handling models where the excitation forces were distributed arbitrarily along the length of the blade.

TABLE OF CONTENTS

	Page
ABSTRACT	iii
LIST OF TABLES	vii
LIST OF FIGURES	viii
LIST OF SYMBOLS	xii
ACKNOWLEDGEMENTS	xvii
Chapter 1: INTRODUCTION	1
1.1. General Remarks and Objectives of the Study	1
1.2. Previous Investigations on Torsional Stiffness of Models Having Airfoil Cross Sections	2
1.2.1. Reference Books, Papers, and Literature Studied	3
1.3. Reference Books, Papers, and Literature Studied on the Dynamical Response of Propeller Blades	4
Chapter 2: ANALYTICAL METHODS FOR DETERMINATION OF TORSIONAL STIFFNESS OF BEAMS HAVING AIRFOIL-LIKE CROSS SECTIONS	8
2.1. Torsional Behavior of Beams Having an Arbitrary Cross Section	8
2.2. Prandtl's Torsion Stress Function	13
2.3. Solution of the Torsional Problem of the Beam Having an Arbitrary Cross Section by Energy Methods	19
2.4. Energy-Method Solution of Torsion of the Beams Having an Airfoil Cross Section	22
2.5. Introduction to Weighted Residual Methods	26
2.6. The Galerkin Method	27
2.7. Application of the Galerkin Method to the Torsion of Beams Having an Airfoil Cross Section	29
2.8. Application of the Galerkin Method to the Torsion of Beams Whose Cross Section is Bounded by Parabolic Curves	35
Chapter 3: EXPERIMENTAL METHODS AND TECHNIQUES FOR THE DETERMINATION OF THE TORSION OF BEAMS HAVING AIRFOIL CROSS SECTIONS	38
3.1. Introduction	38
3.2. Method of Experimental Measurement	38
3.3. Experimental Technique	46

Page

Chapter 4: PREDICTED AND EXPERIMENTAL RESULTS OF TORSIONAL STIFFNESS OF BEAMS HAVING AIRFOIL CROSS SECTIONS . . 49

4.1. Introduction 49
4.2. Comparison and Discussion of Predicted and Experimental Results 49

Chapter 5: THE DYNAMIC MODELING OF CANTILEVER BEAMS AS UNDAMPED MULTI-DEGREE-OF-FREEDOM SYSTEMS 55

5.1. Free Vibration 55
5.2. Some Properties of [k] and [m] Matrices 55
5.3. Some Properties of Natural Frequencies 57
5.4. Some Properties of Eigenvectors (Modal Shapes) . . . 59
5.5. Scaling (Normalizing) of Eigenvectors 59
5.6. Orthogonality of Modal Vectors and the Expansion Theorem 62
5.7. Response of Multi-Degree-of-Freedom Systems to Initial Excitation 66
5.8. The Dynamic Response of Multi-Degree-of-Freedom Systems to a Harmonic Force 69

Chapter 6: DAMPED MULTI-DEGREE-OF-FREEDOM SYSTEMS IN STRUCTURAL DYNAMICS 79

6.1. Introduction 79
6.2. General Consideration 80
6.3. Conditions for Uncoupling of Damping Forces 82
6.3.1. Evaluation of the Damping Matrix for Any Set of Specified Modal Damping Ratios 82
6.3.2. Defining a System Damping Matrix Using Rayleigh Proportional Damping 84
6.4. The Dynamic Response of the Damped Multi-Degree-of-Freedom Systems Subjected to Harmonic Forces . . . 89

Chapter 7: MODAL ANALYSIS PERFORMED ON FIVE BLADE MODELS USING A NICOLET 660A DUAL-CHANNEL FFT ANALYZER . . . 104

7.1. Introduction 104
7.2. An Experimental Technique 104
7.3. Calibration of an Impact Hammer 109
7.4. Geometrical and Material Properties of Blade Models 113
7.5. The Modal-Testing Procedure 116
7.6. The Results Obtained by Modal Testing 122

Page

Chapter 8: NUMERICAL MODELING AND RESULTS OF THE DYNAMIC FLEXURAL RESPONSE OF UNIFORM PROPELLER BLADES 144

8.1. Introduction 144
8.2. Formulation of the Equation of Motion 144
8.3. Eigenvalues, Natural Frequencies, and Eigenvectors . . 146
8.4. Identification of Modal Parameters Including Damping 149
8.5. The Dynamic Response of Blade Models Modeled by Modal Analysis as Undamped and Damped Multi-Degree-of-Freedom Systems 154
8.6. Predicted Results for the Dynamic Response of Blades 157

Chapter 9: CONCLUSIONS 163

BIBLIOGRAPHY 167

Appendix A: Modal Parameters Identification 173

A.1. Introduction 173
A.2. Mode Identification by the Frequency Response 175
A.3. Mode Identification by the Peak Picking Method 179

Appendix B: SYSTEM EXCITATION AND EXPERIMENTAL TECHNIQUE 190

B.1. Introduction 190
B.2. System Excitation 191
B.3. Impulsive Testing 193
B.4. Impactor Selection 196
B.5. Hammer Calibration 197

Appendix C: FLOW CHART FOR THE COMPUTER PROGRAM FOR PREDICTION OF DYNAMIC FLEXURAL RESPONSES OF PROPELLER BLADES 203

LIST OF TABLES

Table		Page
2.1.	Development of torsion equation	20
4.1.	Geometrical and material properties of blade models used in experimental measurement	51
4.2.	Analytically predicted torsional stiffness of beams having different cross sections scaled as the beams of unit length	52
4.3.	Experimentally determined torsional stiffness of blade models having airfoil cross sections scaled for the beams of unit length	53
4.4.	Predicted and measured torsional stiffness for three models having NASA four-digit symmetrical section	54
7.1.	Geometrical and material properties of blade models used for modal testing	118
7.2.	Natural frequencies and modal damping ratios obtained by modal testing	141
8.1.	Predicted and measured natural frequencies for five blade models	148
8.2.	The frequencies and normalized mode shapes for a blade having an NACA 0015 airfoil cross section	151
8.3.	The modal parameters identified for the blades modeled as damped MDOF systems	153
8.4.	The coefficients of the decoupled equation of motion of the blade models	158
8.5.	The dynamic responses of the tips of the blades subjected to a harmonic force of $F = \sin\omega_f t$ at the tip, $\omega_f = 400$ [rad/sec] (continuous and lumped parameter modeling, half-cycle of the forcing function)	159
8.6.	Ratios between undamped and damped response when the forcing function reaches a peak. The blade was forced by the $F = \sin\omega_f t$ at the tip, $\omega = 400$ [rad/sec]	162

LIST OF FIGURES

Figure		Page
2.1.	The geometry of the torsion	11
2.2.	Pictorial representation of Prandtl's torsion stress function	16
2.3.	The airfoil cross section	23
2.4.	The geometry of the cross-section bounded by parabolic curves	36
3.1.	Equivalent spring of continuous weightless cantilever beam	41
3.2.	Cantilever beam model in displaced state when force P is applied at point 1: (a) cantilever beam model; (b) equivalent single-mass-spring model	42
3.3.	Cantilever beam model in displaced state when force P is applied at point 2: (a) cantilever beam model; (b) equivalent single-mass-spring model	44
3.4.	Side view of the measurement system used	47
7.1.	(a) The control table of the Nicolet 660A Dual-Channel FFT Analyzer; (b) The impact hammer kit (hammer, impact tips, and extenders).	110
7.2.	Schematic of test setup for calibration of the impact hammer	114
7.3.	Test setup for calibration of the impact hammer	115
7.4.	The blade models used for modal testing	117
7.5.	Top view of a curved beam model	119
7.6.	The nodal points of the first five modes. (The modal shapes are greatly exaggerated.)	120
7.7.	Schematic of the setup for modal testing using the Nicolet 660A Dual Channel FFT Analyzer	123
7.8.	The setup for modal testing; (a) the blade model of the test stand, (b) the components of the setup	124
7.9.	Blade model at the stand; (a) giving the impulse to the point 1 and taking the output from point 1, (b) giving the impulse to the point 4 and taking the output from point 1	126

Figure		Page
7.10	(a) The steel blade at the test stand, (b) the setup for modal testing of the steel blade	127
7.11	The magnitude and phase of the point transfer function of a model having an NACA 0021 cross section (peaks of the magnitude correspond to the model's natural frequencies)	128
7.12	The real and imaginary parts of the point transfer function of a model having an NACA 0021 airfoil cross section	129
7.13	The coherence function related to input/output used for determining the point transfer function of a model having an NACA 0015 airfoil cross section	130
7.14	The magnitude and phase of the point transfer function of a model having an NACA 0015 cross section (peaks of the magnitude correspond to the model's natural frequencies)	131
7.15	The real and imaginary parts of the point transfer function of a model having an NACA 0015 airfoil cross section	132
7.16	The coherence function related to the input/output used for determining the point transfer function of a model having an NACA 0015 airfoil cross section	133
7.17	The magnitude and phase of the point transfer function of a model having an NACA 0009 airfoil cross section (peaks of the magnitude correspond to the model's natural frequencies)	134
7.18	The real and imaginary parts of the point transfer function of a model having an NACA 0009 airfoil cross section	135
7.19	The coherence function related to the input/output used for determining the point transfer function of a model having an NACA 0009 airfoil cross section	136
7.20	The magnitude and phase of the point transfer function of an aluminum model having a rectangular cross section (peaks of the magnitude correspond to the model's natural frequencies)	137
7.21	The real and imaginary parts of the point transfer function of an aluminum model having a rectangular cross section	138

Figure		Page
7.22	The magnitude and phase of the point transfer function of a steel model having a rectangular cross section (peaks of the magnitude correspond to the model's natural frequencies)	139
7.23	The real and imaginary parts of the point transfer function of a steel model having a rectangular cross section	140
7.24	(a) A curved blade model at the test stand, (b) the test setup for measuring frequencies of a curved blade	142
7.25	(a) Natural frequencies of a curved blade swept by a vibration analyzer over a bandwidth of 0-1000 [Hz], (b) natural frequencies swept over a bandwidth of 0-100 [Hz]	143
8.1	(a) Schematic of the blade model, (b) masses lumped at each node of the model segment, (c) final arrangement of the lumped masses of the blade model	145
8.2	Pictorial representation of the first five modes of the blade model	150
A.1	(a) Magnitude of a multi-degree-of-freedom system transfer function, (b) light modal overlap, (c) heavy modal overlap	174
A.2	Magnitude of a frequency-response function for a single-degree-of-freedom system (in the r-th mode)	177
A.3	Single-degree-of-freedom system transfer function (real modes); (a) real part, (b) imaginary part	182
A.4	Single-degree-of-freedom system transfer function; (a) real part, (b) imaginary part	183
A.5	Two-degree-of-freedom system transfer functions with two distantly coupled modes; (a) real part, (b) imaginary part	188
A.6	Two-degree-of-freedom system transfer functions with two closely coupled modes; (a) real part, (b) imaginary part	189
B.1	The setup for impulsive testing	194
B.2	(a) Typical calibration setup for an impact hammer and accelerometer set, (b) typical impact hammer with a load cell	198

Figure		Page
B.3	The mathematical model of hammer calibration, where: E_a'/E_f' and E_a/E_f are acceleration signal ratios (processed by an FFT analyzer). (S_a/S_f) is a scaling factor (the ratio of accelerometer sensitivities and hammer sensitivities). The test mass and the accelerometer assembly are of a known magnitude m_c. All variables are a function of time and frequency	200
B.4	Typical results from calibration of an impact hammer and accelerometer; (a) time record, (b) frequency response, (c) amplitude linearity	202

LIST OF SYMBOLS

General

a	semi-major axis of the modal cross section
$a_1, a_2, a_3, \ldots, a_n$	undetermined coefficients of polynomial expression for $\bar{u}(x,y)$
a_0, a_p	coefficients of Fourier Series
A	cross-sectional area of the beam model
b	semi-minor axis of the beam cross section
b_p	coefficient of Fourier Series
B	linear differential operator
$(c_{cr})_r$	critical damping in the r-th mode
C_r	damping in the r-th mode
E	Young modulus
$f(x,y)$	the function prescribed over the boundary surface
$F_i(x,y)$	the i-th term in the series expansion of $\bar{u}(x,y)$
g	thickness parameter
$g(x,y)$	the function prescribed over the body domain (volume)
G	shear modulus
$h(j\omega)$	system transfer function for the single-degree-of-freedom system
$H_{yx}(j\omega)$	system transfer function
I_x	area moment of inertia around the x-axis
k_c	the calibration factor which relates to the physical and electrical units
K_ℓ	equivalent spring stiffness of the blade model
K_t	torsional stiffness of the blade model having a unit length
K_t^*	scaled torsional stiffness of the blade model having a unit length

K_T	torsional stiffness of the blade model having an arbitrary length ℓ
ℓ	the length of the blade model
L	linear differential operator
$(M_{eff})_r$	the effective mass in the r-th mode
M_t	the torque per unit length of the blade model
M_{to}	the total mass of the blade
M_T	the torque of the beam model having an arbitrary length ℓ
n	number of segments (lumped masses)
N	number of sampling points in the time domain
p	the pole and its complex conjugate of the transfer function
R	the residue of the transfer function
$R_L=R_L(a,x,y)$	interior residual
$R_B=R_B(a,x,y)$	boundary residual
s	the complex roots
S	the uniform tension of the membrane
th	thickness of the airfoil cross section
t	time interval of the response
T	kinetic energy of the discretized system
u	an exact solution to the boundary value problem
$\bar{u}$	an approximate solution to the boundary value problem
U	strain energy (general case)
U^*	complementary strain energy (general case)
U_0	strain energy per unit volume
V	strain energy for the discretized system

w	strain displacement field
W_p	work done by the force
W_{Mt}	work done by the torque
$W_1(x,y)$	weight function
$X(j\omega)$	the input signal in a frequency domain
$Y(j\omega)$	the output signal in a frequency domain

Matrices

$[\ ]$	rectangular matrix
$\{\ \}$	column matrix
$\lceil\ \rfloor$	diagonal matrix
$[\ ]^T$	transpose of matrix
$[\ ]^{-1}$	inverse of matrix
$[B(s)]$	system matrix
$[C_s]$	scaled modal damping matrix
$\{F(t)\}$	the forcing-function column vector
$\{F_{0s}\}$	vector of amplitudes of the sine forcing function distributed arbitrarily along the length of the blade
$\{F_{0c}\}$	vector of amplitudes of the cosine function distributed arbitrarily along the length of the blade
$\{F_{0r}\}$	vector of amplitudes of the resultant sine forcing function
$\{F_s(t)\}$	scaled modal force vector
$[H(s)]$	transfer matrix in s-plane
$[H(j\omega)]$	transfer matrix in a frequency domain
$[k]$	stiffness matrix
$[K]$	modal stiffness matrix
$[K_s]$	scaled modal stiffness matrix

$[I]$	identity or scaled modal mass matrix
$[m]$	mass matrix
$[M]$	modal mass matrix
$\{q(t)\}$	vector of modal coordinates
$\{\ddot{x}(t)\}$	vector of accelerations at the stations along the blade
$\{\dot{x}(t)\}$	vector of velocities at the stations along the blade
$[\omega^2 M]$	modal stiffness matrix
$[\omega^2]$	scaled modal stiffness matrix
$[\phi]$	matrix of eigenvectors
$[\Phi]$	matrix of orthonormalized eigenvectors

Greek

Γ	Prandtl's torsion stress function
$\delta\varepsilon_{ij}$	kinematically compatible strain
δW	virtual work
δW^*	complementary virtual work
$\delta\pi^*$	the variation of complementary energy
δ_{ij}	the Kronecker delta
δ_r	the phase angle between the forcing-function vector and the displacement vector
$\varepsilon_x, \varepsilon_y, \varepsilon_z$	the strain along the axis of x,y,z
ε	$\varepsilon = \varepsilon_x + \varepsilon_y + \varepsilon_z$
θ	the angle of twist of the blade model
θ_r	the total phase angle between the resultant forcing-function vector and the displacement vector
κ	the distribution of thickness of the airfoil along the length of the blade

μ	direction cosines
ν	real part of the complex root
ζ_r	modal damping in the r-th mode
π	the total energy of the model for torsion
π^*	complementary torsional strain energy
$\sigma_x, \sigma_y, \sigma_z$	normal stress components parallel to x,y,z axes
$\tau_{xy}, \tau_{xz}, \tau_{yz}$	shearing stress components in the rectangular x,y,z coordinate system
ω	frequency of vibration
∇^2	$= (\frac{\partial^2}{\partial x^2}) + (\frac{\partial^2}{\partial x^2})$
Ψ	modified Prandtl's torsion stress function
$\psi_i, i=1,2,3,\ldots,n$	the phase angles of resultant sine forcing functions

ACKNOWLEDGEMENTS

I particularly wish to express my sincere gratitude to my thesis advisor, Dr. Barnes W. McCormick, for all his assistance, guidance, and understanding on this thesis and throughout my M.S. program.

Many thanks to my colleagues, John A. Jeyaseelan, T. R. Govindan, Baltas Constantine, and Neil Adams, for their valuable comments throughout this work, and also for making graduate studies an enjoyable experience. Special thanks also to Mr. George T. Hutchings, who helped with the proofreading, for his comments and suggestions.

The assistance and patience of Mr. Leon J. Fetterolf and Mr. Rex Jacobs in the experimental phase of this thesis are greatly appreciated.

This study was performed under the National Aeronautics and Space Administration Grant NSG 3304.

Chapter 1

INTRODUCTION

1.1. General Remarks and Objectives of the Study

The purpose of this investigation was to study, both analytically and experimentally, the dynamics of cantilevered beams having airfoil-like cross sections, including damping and inertial coupling. Information from this study will be used in a more comprehensive analysis of twisted, rotating propeller blades. The vibration and fatigue of propeller blades are important from both a comfort and safety viewpoint.

In a study of the dynamics of propeller blades, one must consider several factors, including: nonuniform mass and torsional inertia distributions; nonuniform flapwise, chordwise and torsional stiffness distributions; built-in twist; noncoincidence of the elastic axis with the body axis; and inertial coupling. Thus, before considering the complete case of propeller blade dynamics, it is instructive to study the behavior of simpler blade models.

Specifically, the objectives of the present study were:

1. To develop a method to determine the torsional stiffness of blades having airfoil cross sections. First, an analytical model was developed based on existing energy methods in solid mechanics. Secondly, these methods were applied to three models having NACA four-digit symmetrical airfoil sections, and were verified by experimental results.

2. To define analytically the dynamic flexural response of blade models, modeled as either an undamped or damped multi-degree-

of-freedom system. The amplitudes of harmonic excitation force were arbitrarily distributed along the length of the blade.

3. To undertake an analytical investigation of dynamic characteristics of multi-degree-of-freedom systems in a frequency domain, and their relation to the time domain. Special attention was given to the identification of damping.

4. To determine experimentally the natural frequencies and modal damping of models discussed above with a modern FFT analyzer using an impulsive excitation.

5. To develop a small computer code to calculate either an undamped or damped response of blade models discussed above. Special attention was paid to the modeling of damping.

6. To evaluate the results obtained by the computer program. Special emphasis was placed on damping and its influence on the dynamics of frequencies close to the natural frequency.

1.2. Previous Investigations on Torsional Stiffness of Models Having Airfoil Cross Sections

Since the torsion of models having a cross section different than that of a circle is governed by Poisson's partial differential equation, the closed form solution can be obtained only for a few regular cases. For configurations not defined analytically, torsional problems can be solved only by approximate methods such as the finite element and finite difference methods.

One of the objectives of this study was to develop analytical and experimental procedures for determining torsional constants for

beams having airfoil-like cross sections. In researching this problem, the existing literature was studied.

1.2.1. Reference Books, Papers, and Literature Studied

A very elaborate treatment of energy methods in stress analysis is given by Richards in reference 62.

Dym and Shames (14) and Crandal (11) present rigorous treatments of torsional problems by variational approaches. Emphasis is placed on the development of basic concepts of energy methods for torsional problems presented and solutions for models having rectangular, quadratic, and parabolic segment cross sections.

Chou and Pagano (7), Hartog (19), and Oden and Ripperberg (55) present detailed analogies of problems related to torsion. The analogies provide physical insight into problems of this nature and suggest experimental approaches to these problems.

Most of the analytical work done in this present study was based on the above references.

Timoshenko and Goodier (86) present a very elaborate method for determining the total energy of beams in torsion having an arbitrary cross section. They then apply the Rayleigh-Ritz method to problems having various cross sections. Basically, the total energy is found in terms of stress functions. These stress functions are then expanded by a series in order to satisfy the boundary conditions. Finally, the extremum for total energy is found with respect to parameters in the series. These researchers also present this technique for the beams having an airfoil cross section.

Cook (9) gives an extensive treatment of the method of weighted residuals for a finite element approach. Since this present study does not use a finite element approach, only Cook's concepts were used.

Finlayson and Scriven (15) and Hutton and Anderson (26) present the method of weighted residuals. They give a constructive critique on several methods, with special attention given to Galerkin's method.

Duncan (13) shows that the analytical approach to the Saint-Venant torsion problem can be readily done by using Galerkin's analytical method. He presents a detailed consideration of torsion of beams having a symmetrical airfoil and a symmetrical parabolic segment as cross sections. Furthermore, he suggests that this approach can be employed for nonsymmetrical cross sections by using a doubly infinite series of the function representing the contour of the airfoil. Although presented in 1938, this method still appears useful for studying the torsion of propeller and rotor blades.

The references discussed above were used as the basis for the numerical calculation of torsional stiffness for the three models already discussed.

1.3. Reference Books, Papers, and Literature Studied On the Dynamical Response of Propeller Blades

Kenedy and Pancy (31) present one of the first expositions on determining modal characteristics from test data. They assume that damping takes a rather specialized form, and use polar plots to determine the modal characteristics.

Lewis and Wrisley (42) present one of the first multiple-shaker systems for modal testing. They use 24 independently controlled shakers to (hopefully) drive the system into a pure normal mode. They assume that the shakers are distributed with respect to the mass, and that the damping is distributed in the same manner as the mass. They also assume that the damping is equal in all modes of vibration.

Trail and Nash (87) propose a multiple-excitation technique which makes use of Kenedy and Pancy's studies to locate the natural frequencies and the sets of linearly independent forces applied to the structure. This is done in order to calculate the required forces needed to excite a pure normal mode.

Asher (1) applies essentially the same analysis as Trail and Nash (87), but suggests an improved method of locating the natural frequencies. He uses the determinant of the real part of the flexibility matrix to define the natural frequencies.

Walgrave and Ehlbeck (90) present a good review of modal analysis which gives results in the time and frequency domains.

Caughey (6), Clough and Penzien (8), and Paz (56) present the analytical modeling of modal damping which decouples the damping forces.

Klosterman (32, 33, 34, 35, and 36) gives a very detailed treatment on various subjects in analytical and experimental modal analysis. Some of his papers are more oriented to experimental analysis.

Craig (10), Meirovitch (49), Bathe (3), and Paz (56) give rigorous consideration to various subjects on structural dynamics,

including both classical and numerical approaches. They are oriented toward treatment of vibration phenomena in the time domain. Most of them were used during the consideration of the undamped and damped multi-degree-of-freedom systems in Chapters 5 and 6 of this study.

Richardson (63, 64, 65, 66, 67, and 68), Potter (58,59) and Ramsey (60) cover the treatment of vibrational systems having multiple degrees of freedom. The authors present concepts of vibration analysis in the frequency domain, and they are pioneering efforts in treating the vibration of multi-degree-of-freedom systems via system dynamics.

In order to improve accuracy with modern FFT analyzers, the following steps should be taken:

1. Calibration of the impact hammer.
2. Conditioning of the input and output signals.
3. Consideration of the noise and its influence on the measured transfer function.
4. Proper selection of the frequency range so that all frequencies are excited within the chosen range.

The Spectral Dynamics Co. (82), Harris (17,18), the Wavetek-Rockland Co. (91), the Nicolet Scientific Co. (54), and the Hewlett-Packard Co. (21) present detailed treatments of signals in order to properly conduct vibration testing.

An important point in an experimental program is the accurate measurement of the structural transfer function. Here noise effects must be considered. Keller (28,29,30), Lally (37,38), Brown (5), Mitchel and Lynch (50), and Halvorsen and Bendat (16) present various subjects of crucial interest for determining structural

transfer functions. They give a detailed treatment of noise in the time and frequency domains and its influence during transfer function measurements. Also, they discuss the calibration of an impact hammer, and input and output signals.

Finally, measured data must be interpreted properly. Lang (39,40), the Spectral Dynamics Co. (80,81), the Nicolet Scientific Co. (51, 52, 53), the Hewlett-Packard Co. (22), and Brown and Halvorsen (5) present in detail the interpretation of data obtained by an FFT analyzer.

Chapter 2

ANALYTICAL METHODS FOR DETERMINATION OF TORSIONAL STIFFNESS OF BEAMS HAVING AIRFOIL-LIKE CROSS SECTIONS

2.1. Torsional Behavior of Beams Having an Arbitrary Cross Section

In the case of the torsion of beams not circular in cross section, we lose the arguments of symmetry and, along with them, the simplicity of the elementary theory of torsion. The argument that plane cross sections remain plane during deformation, for example, is now no longer valid. Observation shows that the cross section of a non-circular section does not remain plane upon twisting, but warps out of its plane.

Other than the fact that cross sections warp, perhaps one of the most obvious characteristics of the beam's behavior is the absence of normal stresses. No external forces or bending moments are present, and no end constraints exist; therefore, the only stress components needed to provide the equilibrium of any transverse segment are shearing stress in the cross-sectional planes. Furthermore, of the three components of shearing stress, only τ_{zy} and τ_{xz} can result in a twisting moment. The component τ_{xy} is zero. Thus, we conclude that for the noncircular beam in torsion,

$$\sigma_x = \sigma_y = \sigma_z = \tau_{xy} = 0 \tag{2.1}$$

The differential equations of equilibrium in terms of stresses and body forces reduce to

$$\frac{\partial \tau_{xz}}{\partial x} + \frac{\partial \tau_{yz}}{\partial y} = 0 \tag{2.2}$$

$$\frac{\partial \tau_{yz}}{\partial z} = \frac{\partial \tau_{xz}}{\partial z} = 0. \tag{2.3}$$

Equation (2.3) shows that the shearing stresses do not vary with z and, hence, have the same distribution on each cross section. Observing eq. (2.2), we have a statically indeterminate problem, and we are forced to turn to considerations of strains and displacements for additional information. Since the material is assumed to be homogenous isotropic, and linearly elastic, we may introduce eq. (2.1) into equations for stress and strain in a homogenous isotropic Hookean body to obtain the components of strain.

$$\varepsilon_x = \varepsilon_y = \varepsilon_z = \gamma_{xy} = 0 \tag{2.4}$$

Therefore, the strain-displacement formulas reduce to

$$\frac{\partial u}{\partial x} = \frac{\partial v}{\partial y} = \frac{\partial w}{\partial z} = 0 \tag{2.5}$$

and

$$u = f(x,y),\ v = g(y,z),\ w = h(x,z)$$

where f, g, and h are continuous functions yet to be determined. From this observation, we conclude that cross sections do not distort in their own planes. In other words, the angle between any two lines on a cross section is not changed during the deformation of the beam. This makes it possible for us to define the in-plane displacements of any point on the cross section in terms of the angle of twist of α of a straight line on the section drawn from

the x-axis to the point, as shown in Fig. 2.1. Examining the geometry of Fig. 2.1, we find

$$u = -\theta zy \text{ and } v = \theta zx. \tag{2.6}$$

Referring to equations for stress-strain relations, we have

$$\frac{\partial \tau_{xz}}{\partial z} = G \frac{\partial \gamma_{xz}}{\partial z} = G \frac{\partial}{\partial z} \left(\frac{\partial w}{\partial x} + \frac{\partial u}{\partial z}\right) = 0. \tag{2.7}$$

Then eq. (2.6) becomes

$$\frac{\partial}{\partial x} \left(\frac{\partial w}{\partial z}\right) - y \frac{\partial^2(\theta z)}{\partial z^2} = 0. \tag{2.8}$$

The first term in eq. (2.8) is zero, owing to eq. (2.4). Thus, we have

$$\frac{d^2(\theta z)}{dz^2} = 0 \tag{2.9}$$

$$\frac{d(\theta z)}{dz} = \theta = \text{const.} \tag{2.10}$$

It follows that the twist relative to the section z=0 is θz, and that eq. (2.6) may be expressed in terms of θ, x, y, and z. In summary, we express the components of displacement in the form

$$\begin{aligned} u &= -\theta yz \\ v &= \theta xz \\ w &= f(x,y) \end{aligned} \tag{2.11}$$

Thus, once θ and f(y,z) are known, the complete displacement pattern can be evaluated.

ORIGINAL PAGE IS
OF POOR QUALITY

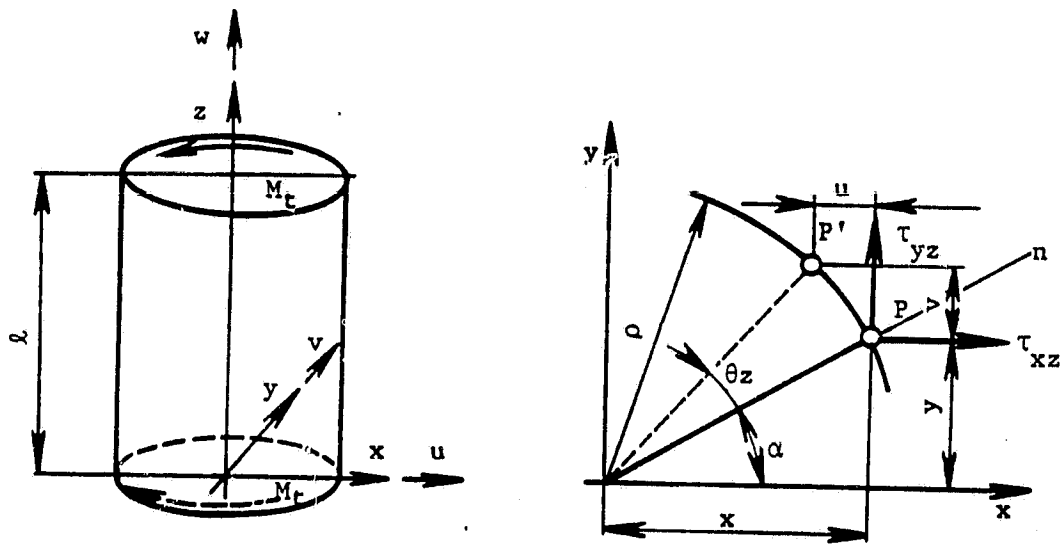

Figure 2.1. The geometry of the torsion.

Finally, from stress-strain relationships, we relate the shearing stresses and strains to the displacements by

$$\tau_{xz} = G\gamma_{xz} = G(\frac{\partial w}{\partial x} + \frac{\partial u}{\partial z}) \tag{2.12}$$

$$\tau_{yz} = G\gamma_{yz} = G(\frac{\partial w}{\partial y} + \frac{\partial y}{\partial z}). \tag{2.13}$$

Introducing eq. (2.11), we have

$$\tau_{xz} = G(\frac{\partial w}{\partial x} - \theta y) \tag{2.14}$$

$$\tau_{yz} = G(\frac{\partial w}{\partial y} + \theta x). \tag{2.15}$$

Differentiating the first of these equations with respect to y and the second with respect to z, and substituting the result into eq. (2.2), we have

$$\frac{\partial^2 w}{\partial x^2} + \frac{\partial^2 w}{\partial y^2} = 0 \tag{2.16}$$

which is the governing partial differential equation for the warping displacement. This relationship is called Laplace's equation for the warping function.

The torsion problem is now reduced to one of determining the four unknowns, τ_{xz}, τ_{yz}, w, and θ. To solve this problem, we have three relationships: eq. (2.2), which is the equilibrium condition, and the two kinematic conditions in eqs. (2.14) and (2.15), which we have written in terms of the stresses. Equation (2.16) is not independent, since it was obtained from eqs. (2.2), (2.14), and (2.15). The fourth relationship necessary to solve the problem is the simple static condition that τ_{xz} and τ_{yz} must result in a

twisting moment of magnitude M_t on each cross section.

2.2. Prandtl's Torsion Stress Function

In 1903, Ludwig Prandtl, the distinguished German mechanician, introduced a scheme whereby the torsion problem could be reduced to one of determining a single unknown. The idea is to introduce a twice-differentiable function $\Gamma(x,y)$, called the torsional stress function, which has the properties

$$\tau_{xz} = \frac{\partial \Gamma}{\partial y} \tag{2.17}$$

and

$$\tau_{yz} = -\frac{\partial \Gamma}{\partial x} . \tag{2.18}$$

When we introduce these definitions into eq. (2.2), we obtain

$$\frac{\partial^2 \Gamma}{\partial x \partial y} - \frac{\partial^2 \Gamma}{\partial y \partial x} = 0 \tag{2.19}$$

which is satisfied by any function which is continuous through its second derivatives. Thus, any such continuous function will automatically satisfy eq. (2.2) and, therefore, lead to shearing stresses which are in equilibrium. The correct solution to the torsion problem, however, must be a state of stress providing not only equilibrium but also compatible strains and displacements. Thus, out of the infinite number of functions Γ which satisfy eq. (2.2), we must choose those which also satisfy a condition of compatibility.

To arrive at this condition, we introduce eqs. (2.17) and (2.18) into eqs. (2.14) and (2.15), and differentiate first with respect to z and second with respect to y. Then we have

ORIGINAL PAGE IS
OF POOR QUALITY

$$\frac{\partial}{\partial y}\left(\frac{\partial \Gamma}{\partial y}\right) = G\,\frac{\partial}{\partial y}\left(\frac{\partial w}{\partial x} - \theta y\right) \tag{2.20}$$

$$\frac{\partial}{\partial x}\left(-\frac{\partial \Gamma}{\partial x}\right) = G\,\frac{\partial}{\partial x}\left(\frac{\partial w}{\partial y} + \theta x\right). \tag{2.21}$$

Recalling that u is also continuously differentiable, we subtract the second equation from the first and find

$$\frac{\partial^2 \Gamma}{\partial x^2} + \frac{\partial^2 \Gamma}{\partial y^2} = -2G\theta. \tag{2.22}$$

This is the equation of compatibility for the problem of torsion of beams having non-circular cross sections. Any function Γ continuous through its second derivatives which satisfies eq. (2.22) now automatically provides both equilibrium and compatibility. Any partial differential equation of this type is also called Poisson's equation.

We may visualize Γ as being a curved surface spread over the cross section of the beam. According to the definition in eqs. (2.17) and (2.18), the slope of the surface in the y direction is the stress in the x direction, and its slope is in the x direction. In fact, if n is any direction oriented α with respect to the x axis, as shown in Fig. 2.1, the stress directed normal to n is clearly

$$\tau_{yx}\cos\alpha - \tau_{xz}\sin\alpha. \tag{2.23}$$

The slope of Γ in the n-direction is, by definition,

$$\frac{d\Gamma}{dn} = \frac{\partial \Gamma}{\partial x}\frac{dx}{dn} + \frac{\partial \Gamma}{\partial y}\frac{dy}{dn} \tag{2.24}$$

ORIGINAL PAGE IS
OF POOR QUALITY

or, since $\frac{dx}{dn} = \cos\alpha$ and $\frac{dy}{dn} = \sin\alpha$,

$$\frac{d\Gamma}{dn} = -\tau_{yz}\cos\alpha + \tau_{xz}\sin\alpha \tag{2.25}$$

Hence, the slope of the Γ surface in any direction is equal to minus the shearing stress in the perpendicular direction.

Furthermore, since we proved that no shearing-stress components can act normal to the boundary of the cross-section, the slope of Γ parallel to the boundary must be zero. This is possible only if Γ is a constant along the boundary. Pictorial representation of Prandtl's torsion-stress function is given in Fig. 2.2. The slope of Γ parallel to the boundary curve s is

$$\frac{d\Gamma}{ds} = \frac{\partial\Gamma}{\partial x}\frac{dx}{ds} + \frac{\partial\Gamma}{\partial y}\frac{dy}{ds} = -\tau_{yz}(-n) + \tau_{xz}m \tag{2.26}$$

where m and n are the direction cosines of a normal to the curve. Since no surface forces are present, and the right side of this equation is zero, Γ must satisfy the boundary condition

$$\frac{d\Gamma}{ds} = 0. \tag{2.27}$$

Hence, Γ must have a constant height along the boundary. Therefore, without loss in generality, we assume that Γ is zero everywhere along the boundary of the cross-section.

Any solution to eq. (2.22) provides both equilibrium and compatibility for cross sections of any shape. To ensure that it also leads to stresses which satisfy static boundary conditions at the ends of the beam, we must also relate Γ to the twisting moment

ORIGINAL PAGE IS
OF POOR QUALITY

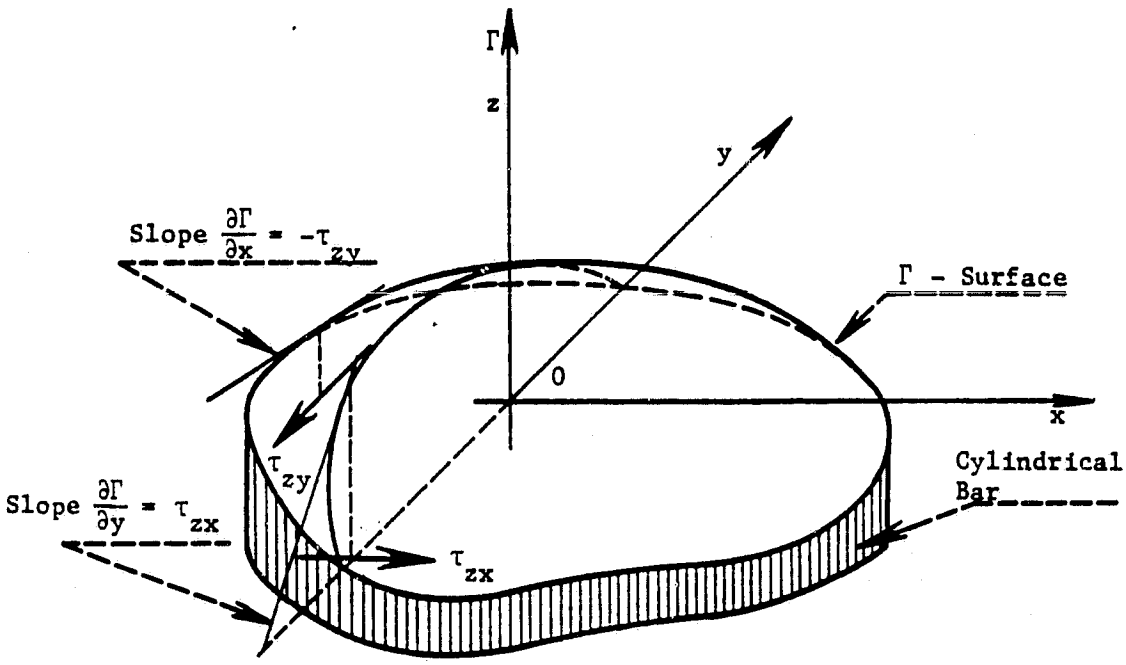

Figure 2.2. Pictorial representation of Prandtl's torsion stress function.

ORIGINAL PAGE IS
OF POOR QUALITY

developed on each section. The moment developed by the shearing stresses about the z-axis must be

$$M_z = M_t = \iint_A (-\tau_{yz} y + \tau_{xz} x)\,dxdy \tag{2.28}$$

where the integration is carried out over the entire area of the cross section. Introducing Γ, this equation becomes

$$M_t = -\iint_A \left(\frac{\partial \Gamma}{\partial y} y + \frac{\partial \Gamma}{\partial x} x\right) dxdy. \tag{2.29}$$

We can now write the integral in the form

$$-\int \left[\int_A^B \frac{d\Gamma}{dy}\, ydy\right] dx - \int \left[\int_E^D \frac{d\Gamma}{dx}\, xdx\right] dy \tag{2.30}$$

where the limits A and B stand for boundary points along a line y = constant, where C and D stand for boundary points along some line z = constant. Integrating by parts, we find

$$M_t = -\int \left[(\Gamma_B y_B - \Gamma_A y_A) - \int \Gamma dy\right] dx - \int \left[(\Gamma_D x_D - \Gamma_C x_C) - \int \Gamma dx\right] dy. \tag{2.31}$$

Now Γ_A, Γ_B, Γ_C, and Γ_D denote values of Γ at the boundary points which, according to our earlier discussion, are zero. Hence, we have

$$M_t = 2\iint_A \Gamma dxdy. \tag{2.32}$$

ORIGINAL PAGE IS
OF POOR QUALITY

This final result states that the total twisting moment on any section is equal to twice the volume under the surface Γ.

Now we can obtain the twisting moment in terms of three independent quantities: G, the modulus of rigidity, which depends upon the material; θ, the angle of twist per unit length; and the constant J, which depends upon the geometry of the cross section.

$$M_t = GJ\theta \tag{2.33}$$

J is called the torsional constant of the beam. The product GJ is called the torsional stiffness of the beam. The formula for J follows directly from eq. (2.32).

$$J = \frac{2}{G\theta} \iint_A \Gamma \, dx dy \tag{2.34}$$

Now we can introduce the modified torsion-stress function, Ψ.

$$\tau_{xz} = G\theta \frac{\partial \Psi}{\partial y} \tag{2.35}$$

$$\tau_{yz} = -G\theta \frac{\partial \Psi}{\partial x} \tag{2.36}$$

Performing the same algebraic operations we have done in derivation of Prandtl's stress function, we have

$$\frac{\partial^2 \Psi}{\partial x^2} + \frac{\partial^2 \Psi}{\partial y^2} = -2. \tag{2.37}$$

This is the modified equation of compatibility for the problem of torsion of beams having non-circular cross sections. Sometimes it is more convenient to use the above equation in practical application.

The development of the torsion equations via stress and strain approaches is summarized in Table 2.1

2.3. Solution of the Torsional Problem of the Beam Having an Arbitrary Cross Section by Energy Methods

We have seen in section 2.1 that the solution of torsional problems is reduced in each particular case to the determination of the stress function satisfying the differential equation (2.22) and boundary conditions. In deriving an approximate solution of the problem, it is useful, instead of working with the differential equation, to determine the stress function from the minimum condition of a certain integral, which can be obtained from consideration of the strain energy of the twisted bar. The stress function must satisfy the differential equation

$$\frac{\partial^2\Gamma}{\partial x^2} + \frac{\partial^2\Gamma}{\partial y^2} = -2G\theta \tag{2.38}$$

where the boundary condition is

$$\frac{\partial\Gamma}{\partial y}\frac{dy}{ds} + \frac{\partial\Gamma}{\partial x}\frac{dx}{ds} = \frac{d\Gamma}{ds} = 0. \tag{2.39}$$

For the strain energy of the twisted bar per unit length, we have

$$U = \frac{1}{2G}\iint(\tau_{xz}{}^2+\tau_{yz}{}^2)\,dxdy = \frac{1}{2G}\iint\left[(\frac{\partial\Gamma}{\partial x})^2+(\frac{\partial\Gamma}{\partial y})^2\right]dxdy \tag{2.40}$$

If we give to the stress function Γ any small variation $\delta\Gamma$, which vanishes at the boundary, the variation of the strain energy is

ORIGINAL PAGE IS
OF POOR QUALITY

Table 2.1. Development of the torsion equation.

Two strain-displacement equations	$\gamma_{xz} = \frac{\partial w}{\partial x} - \theta y$ $\gamma_{yz} = \frac{\partial w}{\partial y} + \alpha x$
Two Hooke's law equations	$\tau_{xz} = G\gamma_{xz}$ $\tau_{yz} = G\gamma_{yz}$
One equilibrium equation	$\frac{\partial \tau_{xz}}{\partial x} + \frac{\partial \tau_{yz}}{\partial y} = 0$
Five equations	τ_{xz}, τ_{yz}, γ_{xz}, γ_{yz}, w - all functions of x,y only

One compatibility equation in terms of stress $\frac{\partial \tau_{xz}}{\partial y} - \frac{\partial \tau_{yz}}{\partial x} = -2G\theta$ One equilibrium equation $\frac{\partial \tau_{xz}}{\partial x} + \frac{\partial \tau_{yz}}{\partial y} = 0$ τ_{xz}, τ_{yz}	Two stress-displacement equations $\tau_{xz} = G(\frac{\partial w}{\partial x} - \theta y)$ $\tau_{yz} = G(\frac{\partial w}{\partial y} + \theta x)$ One equilibrium equation $\frac{\partial \tau_{xz}}{\partial x} + \frac{\partial \tau_{yz}}{\partial y} = 0$ τ_{xz}, τ_{yz}, w
$\nabla^2 \Gamma = -2G\theta$ where $\frac{\partial \Gamma}{\partial x} = -\tau_{yz}$, $\frac{\partial \Gamma}{\partial y} = \tau_{xz}$ B.C. $\Gamma = 0$ on the boundary	$\nabla^2 w = 0$ B.C. $\left[\frac{\partial w}{\partial x} - y\theta\right]\mu x + \left[\frac{\partial w}{\partial y} + x\theta\right]\mu y = 0$ on the boundary Where μx, μy are the direction cosines of the outward normal of the boundary
$M_t = 2\iint \Gamma dxdy$	$M_t = G\iint \left[x^2\theta + y^2\theta + x\frac{\partial w}{\partial y} - y\frac{\partial w}{\partial x}\right] dxdy$

ORIGINAL PAGE IS
OF POOR QUALITY

$$\frac{1}{2G}\iint\left[\left(\frac{\partial\Gamma}{\partial x}\right)^2+\left(\frac{\partial\Gamma}{\partial y}\right)^2\right]dxdy$$

and the variation of the torque is

$$2\iint\delta\Gamma dxdy.$$

Substituting the above equations into eq. (2.40), we get

$$\frac{1}{2G}\,\delta\iint\left[\left(\frac{\partial\Gamma}{\partial x}\right)^2+\left(\frac{\partial^2\Gamma}{\partial y^2}\right)^2\right]dxdy = 2\theta\iint\delta\Gamma dxdy$$

$$\delta\iint\left\{\frac{1}{2}\left[\left(\frac{\partial\Gamma}{\partial x}\right)^2+\left(\frac{\partial\Gamma}{\partial y}\right)^2\right]-2G\theta\Gamma\right\}dxdy.$$

The true expression for the stress function Γ is that which makes the variation of the integral zero.

$$U = \iint\left\{\frac{1}{2}\left[\left(\frac{\partial\Gamma}{\partial x}\right)^2+\left(\frac{\partial\Gamma}{\partial y}\right)^2\right]-2G\theta\Gamma\right\}dxdy \qquad (2.41)$$

In the approximate solution of torsional problems, we replace the above problem of variational calculus by a simple problem of finding a minimum of a function. We take the stress function in the form of a series,

$$\Gamma = d_o\Gamma_o + d_1\Gamma_1 + d_2\Gamma_2 + \ldots\ d_n\Gamma_n \qquad (2.42)$$

in which Γ_o, Γ_1, Γ_2, ... , Γ_n are functions satisfying the boundary condition. These functions are vanishing at the boundary. In choosing these functions, we should be guided by the membrane

analogy and take them in a form suitable for representing the function Γ. The quantities d_o, d_1, d_2, ..., d_n are numerical factors to be determined from the minimum condition of the integral (2.41). Substituting the series (2.42) in this integral, we obtain, after integration, a function of the second degree in d_o, d_1, d_2, ..., d_n. The minimum condition of this function is

$$\frac{\partial U}{\partial d_o} = 0 \qquad \frac{\partial U}{\partial d_1} = 0 \qquad \frac{\partial U}{\partial d_2} = 0, \tag{2.43}$$

In this way, we obtain a system of linear equations from which the coefficients d_o, d_1, d_2, ..., d_n can be determined. By increasing the number of terms in the series (2.42), we increase the accuracy of our approximate solution, and by using an infinite series, we may arrive at an exact solution of the torsional problem.

2.4. Energy-Method Solution of Torsion of the Beams Having an Airfoil Cross Section

The cross section of conventional airfoils used in low-speed aerodynamic design can be approximated as follows (see Fig. 2.3). The upper curve can be determined by

$$y = d\kappa(\frac{x}{c})$$

and the lower curve can be determined by

$$y = -d_1\kappa(\frac{x}{c})$$

where

$$\kappa(\frac{x}{c}) = \kappa(th) = (th)^m[1-(th)^p]^q. \tag{2.43}$$

ORIGINAL PAGE IS
OF POOR QUALITY

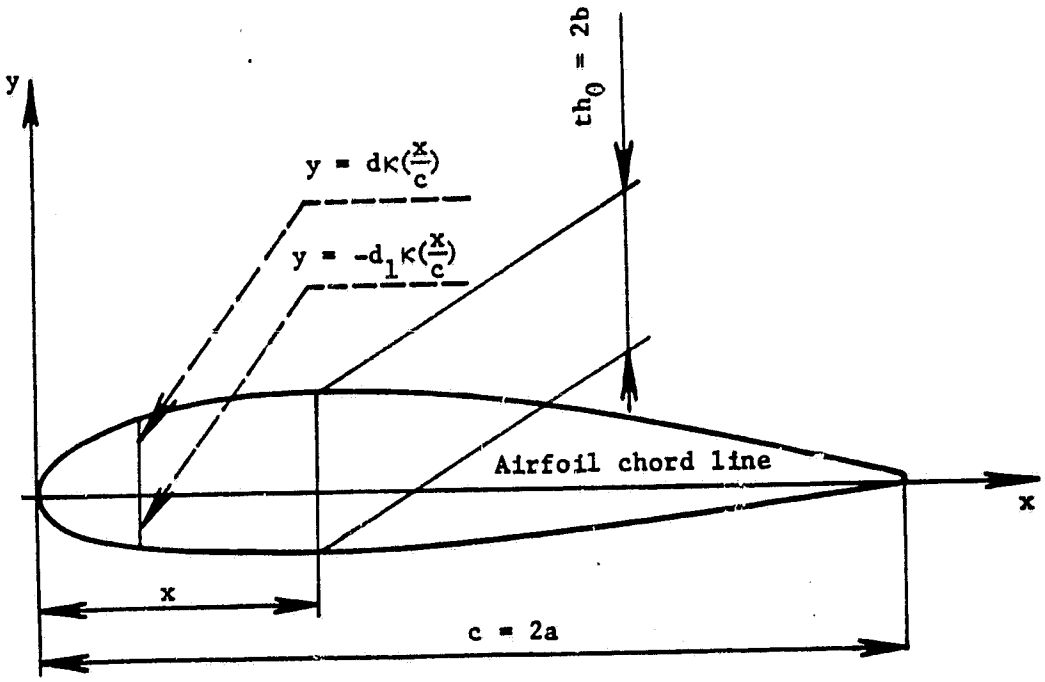

Figure 2.3. The airfoil cross section.

ORIGINAL PAGE IS
OF POOR QUALITY

The boundary conditions will be satisfied if we take for the stress function as approximate expression,

$$\Gamma = A(y-d\kappa)(y+d_1\kappa). \tag{2.44}$$

Substituting equation (2.44) into the integral (2.41) and minimizing the strain energy

$$\frac{dU}{dA} = 0. \tag{2.45}$$

We define the constant A

$$A = -\frac{G\theta}{1+\alpha(d^2+d_1{}^2+dd_1)/c^2} \tag{2.46}$$

where

$$d = \frac{\int_0^1 \kappa^3 (d\kappa/d(th))^2 d(th)}{\int_0^1 \kappa^3 dt}. \tag{2.47}$$

Using the equation already derived for the torque

$$M_t = 2\iint \Gamma\, dxdy$$

we obtain

$$M_t = -A\,\frac{c(d+d_1)^3}{3}\int_0^1 \kappa^3 d(th). \tag{2.48}$$

In the case of a symmetrical airfoil, the upper and lower curves are described by the same expression, and the following assumptions are taken:

$$m = \frac{1}{2},\ p = q = 1,\ d = d_1$$

$$y = \pm\, d\kappa(\tfrac{x}{c}) = \pm\, d\sqrt{\tfrac{x}{c}}\,[1-(\tfrac{x}{c})]. \tag{2.49}$$

ORIGINAL PAGE IS
OF POOR QUALITY

To define the constant d, we need the maximum thickness of the airfoil 2b. First, we are going to define the position of maximum thickness of the airfoil from eq. (2.49)

$$y = d\sqrt{\frac{x}{c}} - d\sqrt{\left(\frac{x}{c}\right)^3}$$

$$\frac{dy}{dx} = -\frac{d}{2c^{1/2}x^{1/2}} + d\,\frac{3}{2c^{3/2}}\,x^{1/2} \,. \qquad (2.50)$$

From the condition

$$\frac{dy}{dx} = 0$$

$$x = \frac{c}{3} = \frac{2d}{3}$$

which is the position of maximum thickness, the maximum thickness with respect to b is calculated using eq. (2.49).

$$y = \pm\, d\sqrt{\frac{x}{c}}\left[1-\left(\frac{x}{c}\right)\right]$$

$$\frac{to}{2} = b = d\sqrt{\frac{c}{3c}}\left[1-\left(\frac{c}{3c}\right)\right]$$

$$d = \frac{3\sqrt{3}}{8}b\,.$$

Now, we can define constant A as

$$A = -\frac{G\theta}{1 + \frac{11}{13}\left(\frac{d^2}{c^2}\right)}\,,$$

ORIGINAL PAGE IS
OF POOR QUALITY

and finally

$$M_t = 0.0736 \frac{Gcd^3}{1 + \frac{11}{13}(\frac{d^2}{c^2})} \theta. \tag{2.52}$$

Scaling both sides of equation (2.52) with factor $\frac{a^2+b^2}{\pi a^3 b^3}$ and introducing the substitution $c = 2a$, we have the scaled torsional stiffness per unit length:

$$K_t^* = 0.0736 \frac{G(2a)d^3}{1 + \frac{11}{13}(\frac{d^2}{4a^2})} \cdot \frac{a^2+b^2}{\pi a^3 b^3} .$$

Then, the moment-angle of twist for a beam of an arbitrary length can be found as,

$$M_t = K_t^* \frac{\pi a^3 b^3}{\ell(a^2+b^2)} \theta. \tag{2.53}$$

2.5. Introduction to Weighted Residual Methods

The solution of boundary-value problems can very often be achieved by forming a corresponding variational problem. Under such circumstances, variational calculus methods are very effective for obtaining an approximate solution. A variational principle is an integral expression (a functional) that yields the governing differential equations and nonessential boundary conditions of a problem when given the standard treatment of the calculus of variations. In areas other than mechanics of solids, it is more likely that a variational principle may not be known or may not exist.

The governing differential equation and nonessential boundary condition of the problem are

$$Bu = g \text{ in region } V$$
$$Lu = f \text{ on boundary } S. \tag{2.54}$$

The exact solution $u = u(x,y)$ is unknown. We seek an approximate solution, $\bar{u}$. It may be a polynomial that satisfies the essential boundary conditions and contains undetermined coefficients $a_1, a_2, \ldots, a_n$. Thus, $\bar{u} = \bar{u}(a,x)$. We must find the values a_i such that u and $\bar{u}$ are "close" in some sense. If $\bar{u}$ is substituted into eq. (2.54), we obtain residuals R_L and R_B because $\bar{u}$ is not exact. Residuals are functions of both x and the a_i.

$$R_L = R_L(a,x,y) = B\bar{u}(x,y) - g(x,y)$$
$$R_B = R_B(a,x,y) = L\bar{u}(x,y) - f(x,y) \tag{2.55}$$

where R_L is an interior residual and R_B is boundary residual. Residuals vanish only for the exact solution, $\bar{u}(x,y) = u(x,y)$. We presume that $\bar{u}(x,y)$ is a good approximation if the residuals are made small. This can be done by various schemes known as the collocation, least squares, least-squares collocation, Galerkin, and subdomain methods.

2.6. The Galerkin Method

This method provides approximate solutions to differential equations directly and is applicable whether the transformation into a variational problem is possible or not. Having wider scope than variational calculus methods, it is more attractive in practice since there is no need to evaluate the functional even in those situations where it existed.

Galerkin's method can be described as follows. Suppose we want to solve a linear partial-differential equation

$$L[u(x,y)] = f(x,y) \tag{2.56}$$

in a region over which $f(x,y)$ is prescribed and the boundary conditions are linear and homogeneous. L stands for a linear differential operator.

We can rewrite equation (2.56) as

$$L[u(x,y)] - f(x,y) = 0. \tag{2.57}$$

If, further, the approximate solution $\overline{u}(x,y)$ were expressible in the form of a complete series of functions

$$\overline{u}(x,y) = \sum_{i=1}^{\infty} a_i F_i(x,y) \tag{2.58}$$

satisfying the required boundary conditions, then the "exactness" of the solution could be expressed by the statement that in the region, the left-hand side of eq. (2.57) is orthogonal to every term in the series above. That is,

$$\iint_S \{L[\overline{u}(x,y)]-f(x,y)\}F_i(x,y)\,dxdy = 0, \quad i = 1,2,3,\ldots n. \tag{2.59}$$

Since we truncate the series, eq. (2.58), to a finite number of terms, n, then we are in a position to use the above ideas to impose n-conditions of orthogonality. Thus,

$$\iint_S \left\{L\left[\sum_{i=1}^{n} a_i F_i(x,y)\right]-f(x,y)\right\}F_k(x,y)\,dxdy = 0 \tag{2.60}$$

with $i = 1, 2, 3, \ldots, n$, provides a kind of averaging basis for evaluating the n unknown a_i's such that the approximate solution is

$$\bar{u}_n(x,y) = \sum_{i=1}^{n} a_i F_i(x,y). \tag{2.61}$$

We select the "weight functions" W_i and set the weighted averages of the residual to zero; for $i = 1, 2, 3, \ldots, n$. Applying this to eq. (2.55), we have

$$R_i = \int_V W_i(x,y) R_L(a,x,y) dV + \int_S W_i(x,y) R_B(a,x,y) dS = 0. \tag{2.62}$$

Weight functions W_i are, by definition, coefficients of generalized coordinates. Thus, $W_i = \frac{\partial \bar{u}}{\partial a_i}$. In structural mechanics, the residuals are proportional to forces or moments, and the W_i can be regarded as virtual displacement or rotation. Each integral in eq. (2.62) represents virtual work, which should vanish at an equilibrium configuration. Usually, in the problems of linear theory of elasticity, the Ritz coefficients are identical to the coefficients found by the Galerkin method for the same system of coordinate functions F_i.

2.7. Application of the Galerkin Method to the Torsion of Beams Having an Airfoil Cross Section

In section 2.2, we showed that the torsion problem for a beam having an arbitrary cross section can be reduced to the problem of finding a modified torsional stress function Ψ which vanishes on the boundary and which satisfies the differential equation

$$\nabla^2 \Psi + 2 = 0 \tag{2.63}$$

everywhere within the boundary. When this function has been found, the components of the shearing stress are given by

$$\tau_{xz} = G\theta \frac{\partial \Psi}{\partial y}$$

$$\tau_{xz} = -G\theta \frac{\partial \Psi}{\partial x} \tag{2.64}$$

where θ is the twist of unit length (in radians) and G is the modulus of torsional stiffness of the homogenous and isotropic material. Also, the torsional stiffness of a beam having a unit length is given by

$$K_t = 2G\iint \Psi dxdy \tag{2.65}$$

where the integral extends over the whole section. The function Ψ is proportional to the deflection of the membrane in the familiar membrane analogy of torsion.

The Galerkin method provides a means for the approximate solution of the differential equation (2.63) with the assigned boundary condition. Let $F_1, F_2, F_3, \ldots, F_n$ be a sequence of linearly independent functions of x and y which all vanish on the boundary, and put as an approximation

$$\Psi = \sum_i^n a_i F_i. \tag{2.66}$$

Let the result of substituting this expression on the left-hand side of eq. (2.63) be R_B. Then R_B is the error or residual in the differential equation corresponding to the chosen function Ψ, and it is a linear function of the coefficients a_i. In accordance with the Galerkin method, these coefficients are

determined by the condition that the n equations typified by

$$\iint R_B F_i \, dxdy = 0 \tag{2.67}$$

must be satisfied. This equation can easily be interpreted in relation to the membrane analogue. If Ψ is proportional to the displacement of the membrane in a direction perpendicular to its undisturbed position, then R_B is proportional to the external load per unit area which is left unbalanced by the tensions in the membrane, and equation (2.67) expresses the vanishing of the work done by the unbalanced loads in a virtual displacement of the membrane proportional to F_i. Thus, the coefficients a may be regarded as generalized coordinates for the membrane, and the Langrangian equations of equilibrium are then typified by eq. (2.67). Consideration of the choice of the function F_i remains. When the section is symmetrical about axis x and has a smooth boundary given by

$$y = \pm \, th \tag{2.68}$$

where th is a known function of x, the following functions, with p and q as positive integers, will be suitable:

$$F_{pq} = (th^{2p} - y^{2p})x^2. \tag{2.69}$$

These functions vanish all over the boundary. The same functions will serve if the boundary has a sharp corner or corners, except when part of the boundary is perpendicular to axis x.

It must be pointed out that an exact solution could, in general, only be reached by the employment of a doubly infinite

set of functions F_i. However, it is found that in most cases an excellent approximation is obtained by the use of only two or three functions, and as a rule it is sufficient to use only the functions which are of the second degree in y, at least for narrow sections.

The cross section of symmetrical airfoils can be approximated by the cubic oval given by

$$th^2 = g^2(2a)x(1 - \frac{x}{c})^2 \tag{2.70}$$

where c = 2a is the chord and g is the thickness parameter equal to 2b/c. This boundary very closely resembles some of the symmetrical airfoil sections in current use for conventional propeller and rotor blades. The maximum thickness occurs at one third of the chord from the nose, and its magnitude is $8ag/\sqrt{27}$. This particular case has been worked out in detail by the thickness parameter method. The expression for the stiffness obtained in this way is

$$K_t = \frac{256G(2a)^4 g^3}{3465}\left[1 - \frac{11}{13}g^2 + g^4 - \frac{379}{221}g^6\right] \tag{2.71}$$

correct to the 6th power of g within the bracket. In applying The Galerkin method, the following approximation of the modified stress function will be adopted:

$$\Psi = (t^2 - y^2)\left[c_1 + c_2(\frac{x}{c})\right] \tag{2.72}$$

Hence,

$$R_B = \nabla^2\Psi + 2 = E_o + E_1(\frac{x}{c}) + E_2(\frac{x}{c})^2 \tag{2.73}$$

ORIGINAL PAGE IS
OF POOR QUALITY

where

$$E_o = 2 - c_1(2 + 4g^2) + 2c_2g^2 \tag{2.74}$$

$$E_1 = 6c_1g^2 - c_2(2 + 12g^2) \tag{2.75}$$

and

$$E_2 = 12c_2g^2. \tag{2.76}$$

The two Galerkin equations are

$$\iint_S R_B(th^2 - y^2)dxdy = 0 \tag{2.77}$$

$$\iint R_B(th^2 - y^2)(\frac{x}{c})dxdy = 0. \tag{2.78}$$

After substitution and reduction, these become

$$c_1(13 + 11g^2) + c_2(5 + 3g^2) = 13$$

$$c_1(253 + 153g^2) + c_2(11g + 81g^2) = 255. \tag{2.79}$$

The last equations yield

$$c_1\Delta = 17 + 18g^2$$

$$c_2\Delta = 51g^2 \tag{2.80}$$

where

$$\Delta = 17 + 52g^2 + 27g^4. \tag{2.81}$$

Hence, by equation (2.71), the expression for the torsional stiffness is

ORIGINAL PAGE IS
OF POOR QUALITY

$$K_t = \frac{256G(2a)^4 g^3}{3465} \cdot \left[\frac{221 + 489g^2}{221 + 676g^2 + 351g^4}\right]. \qquad (2.82)$$

The fraction inside the bracket can be converted into an ascending power series in g, when g is small. The expansion for the term in g^6 can be expressed as

$$1 = \frac{11}{13} g^2 + g^4 - \frac{379}{221} g^6. \qquad (2.83)$$

The torsional stiffness of the cylinder of unit length is

$$K_t = \frac{256G(2a)^4 g^3}{3465} \left[1 - \frac{11}{13} g^2 + g^4 - \frac{379}{221} g^6\right]. \qquad (2.84)$$

If we scale the expression in eq. (2.84) with the factor $\frac{a^2+b^2}{\pi a^3 b^3}$, we have modified torsional stiffness in non-dimensional form

$$K_t^* = \frac{256G(2a)^4 g^3}{3465} \left[1 - \frac{11}{13} g^2 + g^4 - \frac{379}{221} g^6\right]. \qquad (2.85)$$

If the simpler approximation

$$\Psi = c_1(th^2 - y^2) \qquad (2.86)$$

were employed, then c_1 would be found from eq. (2.80) by omission of the term in c_2.

$$c_1 = \frac{13}{13 + 11g^2} \qquad (2.87)$$

In a similar manner, the torsional stiffness of the beam of unit length is derived by

$$K_t = \frac{256G(2a)^4 g^3}{3465} \left(\frac{13}{13 + 11g^2}\right). \qquad (2.88)$$

ORIGINAL PAGE IS
OF POOR QUALITY

Scaling the expression above with the factor $\frac{a^2+b^2}{\pi a^3 b^3}$, we get

$$K_t^* = \frac{256G(2a)^4 g^3}{3465} \left(\frac{13}{13 + 11g^2}\right) \frac{a^2+b^2}{\pi a^3 b^3} . \tag{2.89}$$

Finally, the relation torque-angle of twist for a beam of unit length can be established as

$$M_t = K_t \theta. \tag{2.90}$$

This expression can be generalized easily for any cylinder of length ℓ and for a given chord 2a of the cross section:

$$M_T = K_t^* \frac{\theta}{\ell} \cdot \frac{\pi a^3 b^3}{a^2+b^2} \tag{2.91}$$

2.8. Application of the Galerkin Method to the Torsion of Beams Whose Cross Section is Bounded by Parabolic Curves

A thin blade has a symmetrical section bounded by two parabolic (see Fig. 2.4) giving the thickness at disctance x from the center by

$$th = 2b[1 - (2x/2a)^2]. \tag{2.92}$$

The chosen function

$$\Gamma = A\left[y^2 - \frac{th^2}{4}\left(1 - \frac{x^2}{a^2}\right)^2\right] \tag{2.93}$$

satisfies the torsion boundary condition $\Gamma = 0$ on the boundary. Using the approach given in the previous section, the torsional stiffness per unit length is found to be

$$K_t = \frac{0.1524(a)th^3}{\left[1 + 1.333\left(\frac{th^3}{2a}\right)^3\right]}. \tag{2.94}$$

ORIGINAL PAGE IS
OF POOR QUALITY

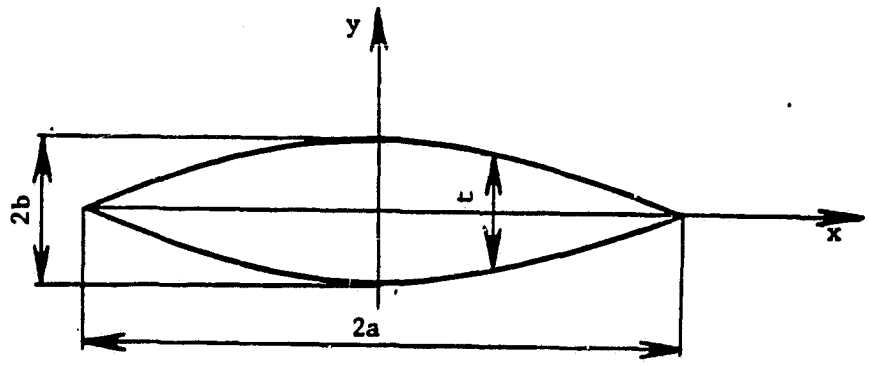

Figure 2.4. The geometry of the cross-section bounded by parabolic curves.

Scaling eq. (2.94) with the factor $\frac{a^2+b^2}{\pi a^3 b^3}$, we have the modified torsional stiffness in non-dimensional form.

$$K_t^* = \frac{0.1524(2a)th^3}{\left[1 + 1.333\left(\frac{th}{2a}\right)^2\right]} \frac{a^2+b^2}{\pi a^3 b^3} \tag{2.95}$$

Having given the geometry of the cross section and knowing the angle of twist per unit length, we can expand the expression above for a cylinder of an arbitrary length ℓ.

$$M_T = K_t^* \frac{\theta}{\ell} \cdot \frac{\pi a^3 b^3}{a^2+b^2} \tag{2.96}$$

Chapter 3

EXPERIMENTAL METHODS AND TECHNIQUES FOR THE DETERMINATION OF THE TORSION OF BEAMS HAVING AIRFOIL CROSS SECTIONS

3.1. Introduction

There are several analytical methods for the determination of the torsional stiffness of a cylinder having an airfoil cross section. Some of these methods were given in detail in the previous chapter for the types of cross sections which are reasonably good approximations of a conventional symmetric airfoil section. The contour lines of the airfoil section are usually presented as curves described with fairly complicated expressions. In trying to find the exact solution for a particular section by any method described in Chapter 2, one faces serious problems in choosing the appropriate stress functions and in matching given boundaries.

In this study the experimental method is applied to three aluminum models with three different cross sections. Since the cross sections of all three models were chosen from the family of NACA four-digit wing sections, the approximation taken in analytical methods is very close to the real cross section. The experimental method is universal and can be used for any type of beams having the airfoil cross section restricted only to the linear elasticity cases.

3.2. Method of Experimental Measurement

Since we do not know the exact position of the shear center of the models having airfoil cross sections, the relation, between

torque and angle-of-twist cannot be defined in a conventional way. During modeling of this system, the following assumptions were made:

1. For models made of isotropic materials, in the elastic region (small deformations), the applied torque, the angle of twist, the force, and the linear displacement are related linearly.

2. The continuous beam (model) with applied torque at the tip is modeled as single-spring-mass system.

3. Since the models are of small size, the weight of the model is neglected.

The model was clamped to a vertical beam of much larger mass and stiffness than that of the model. A rigid light bar with two positions for applying load was firmly attached at the tip of the model. By applying the same weight on two different moment arms successively, the model was deflected at two different angles of twist. The first observation was made in the deformed state of the model, when the weight was applied at position 1. From the theory of vibrations, we know how to model some distributed systems as single-degree-of-freedom systems, thus reducing continuously distributed parameters to equivalent single parameters lumped at one point. Using the elementary relations for work done by force and torque in linear solid mechanics, we can model a cantilever weightless beam of length ℓ and with given physical properties EI as a single-spring-mass system where:

1. E is the Young modulus of elasticity given in [lb/in^2].
2. I is the sectional moment of inertia around the axis of bending given in in^4.

A very useful relation can be established using the force-displacement relation for the linear spring $P = K_\ell \Delta$, where K_ℓ [lb/in] is the linear spring stiffness (constant). Observing Fig. 3.1, we have

$$\Delta = \frac{L^3}{3EI}$$

$$P = K_\ell \cdot \Delta = 1 = K_\ell \cdot \frac{\ell^3}{3EI}$$

$$K_\ell = \frac{3EI}{\ell^3} \tag{3.1}$$

In the equation above, K_ℓ is the equivalent spring stiffness of a continuous weightless cantilever beam of length ℓ and given EI.

The cantilever beam subjected to the force and moment in the plane of the tip cross section is modeled as the single-spring-mass system. The geometry and load conditions are given in Fig. 3.2. Force of intensity P is applied at point 1 at the distance ℓ_1 from shear center in the plane of the tip cross section. Point 2 is at the distance ℓ_2 from the shear center. The difference $\ell_2 - \ell_1$ is denoted as d_ℓ. In Figure 3.2(a) the model is shown in the displaced state, and in Figure 3.2(b) the single-spring-mass model is shown in the displaced state when force P is applied at point 1. The displacements are measured at points 1 and 2. Observing Figure 3.2, we can say that

Δ is the linear displacement of the tip of the cantilever beam subjected to the force P at the tip.

Δ_{11} is the linear displacement at point 1 due to the force P at point 1.

ORIGINAL PAGE IS
OF POOR QUALITY

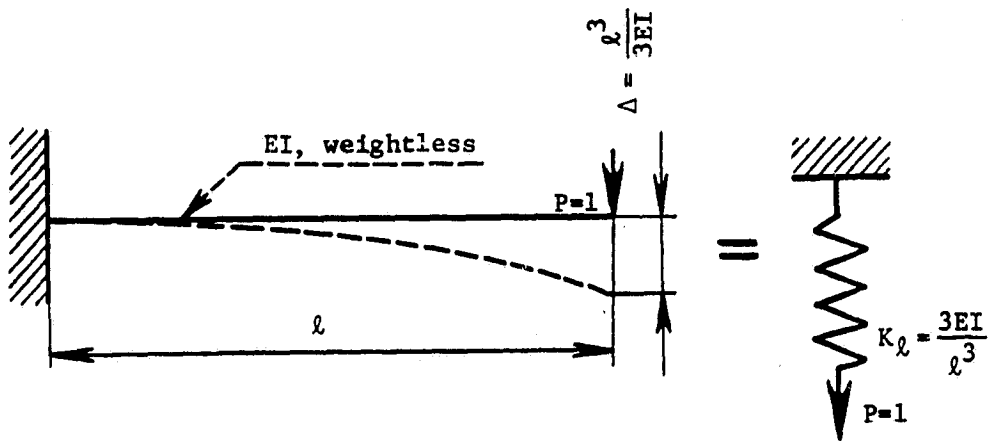

Figure 3.1. Equivalent spring of continuous weightless cantilever beam.

ORIGINAL PAGE IS
OF POOR QUALITY

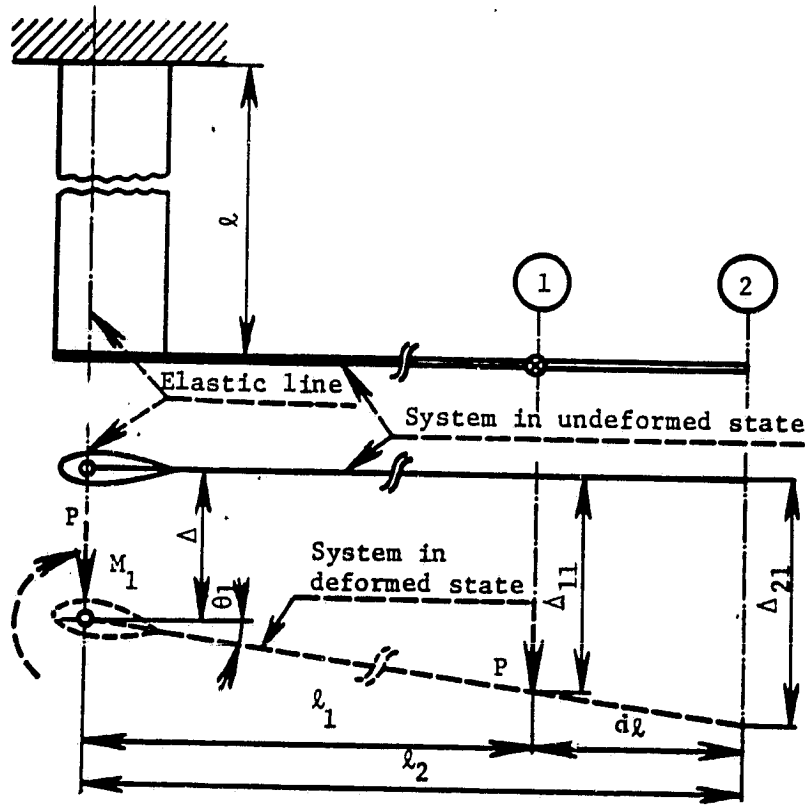

(a)

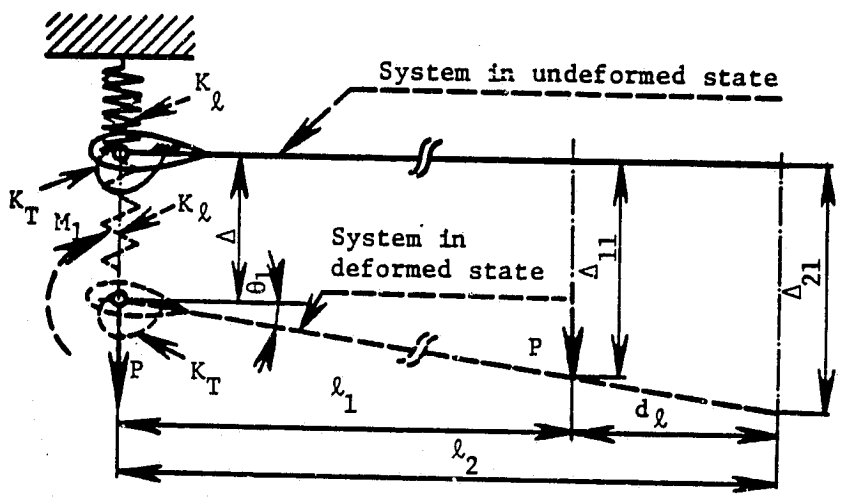

(b)

Figure 3.2. Cantilever beam model in displaced state when force P is applied at point 1: (a) cantilever beam model; (b) equivalent single-mass-spring model.

Δ_{21} is the linear displacement at point 2 due to the force P at point 1.

Using the geometry from Figure 3.2 and equations given in this chapter, we can establish the following relations;

$$\Delta = \frac{\ell^3}{3EI} \tag{3.2}$$

$$M_1 = P \cdot \ell_1 = K_T \theta_1 \tag{3.3}$$

or

$$\theta_1 = \frac{M_1}{K_T} .$$

Again, using the geometry in Figure 3.2, the following relations can be established;

$$\Delta_{11} = \Delta + \ell_1 \theta_1$$

$$\Delta_{11} = \Delta + \ell_1 \frac{M_1}{K_T} \tag{3.4}$$

$$\Delta_{21} = \Delta + \ell_2 \theta_1$$

$$\Delta_{21} = \Delta + \ell_2 \frac{M_1}{K_T} . \tag{3.5}$$

Now the cantilever beam model is observed in the second position. Force of intensity P is applied at point 2. Again, the geometry of the cantilever beam model and its single-spring-mass system analogy is given in Fig. 3.3. Using the geometry in Fig. 3.3, the following relations are established:

$$M_2 = P \cdot \ell_2 = K_T \theta_2 \tag{3.6}$$

or

$$\theta_2 = \frac{M_2}{K_T}$$

ORIGINAL PAGE IS
OF POOR QUALITY

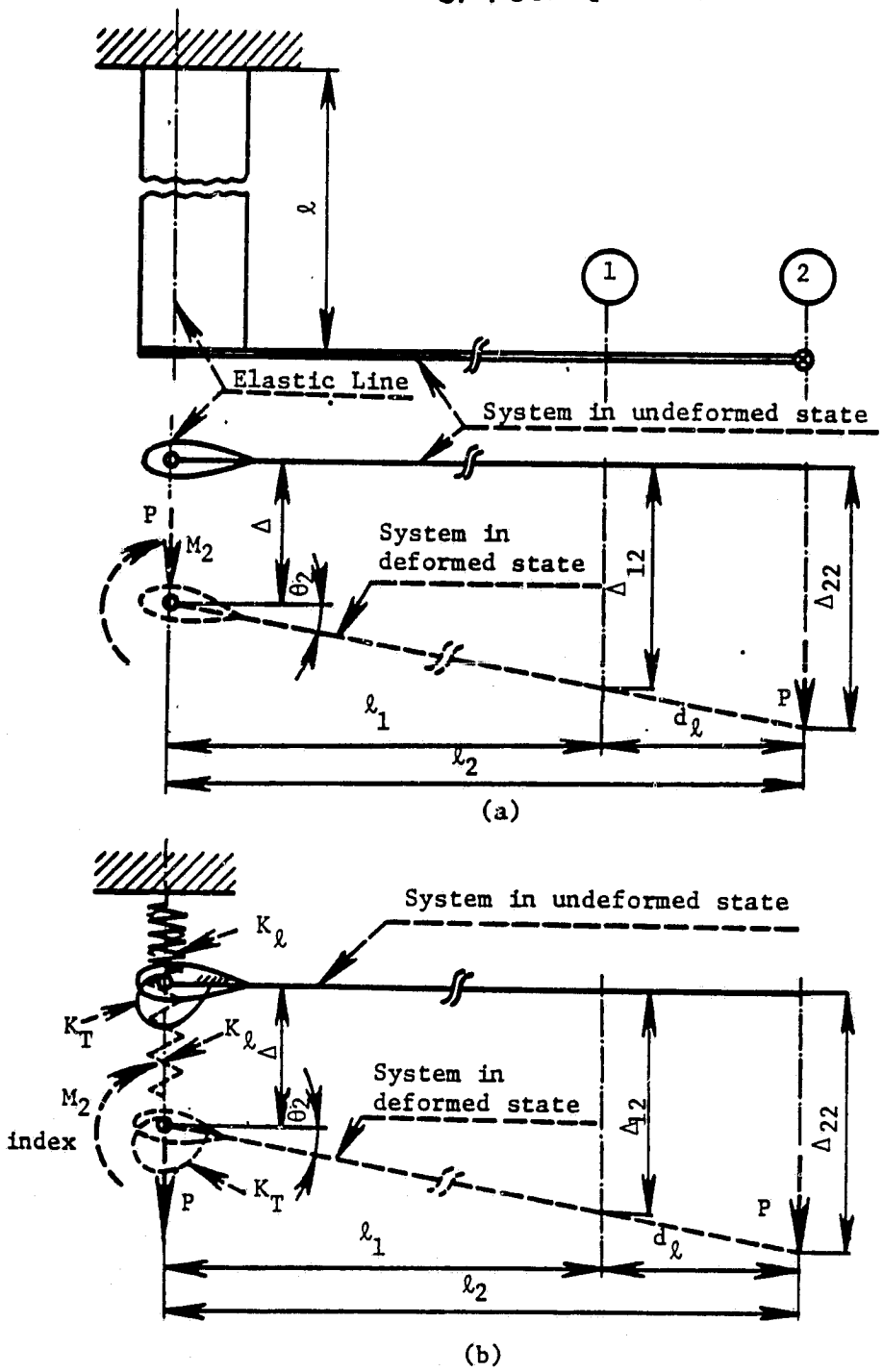

Figure 3.3. Cantilever beam model in displaced state when force P is applied at point 2: (a) cantilever beam model; (b) equivalent single-mass-spring model.

ORIGINAL PAGE IS
OF POOR QUALITY

$$\Delta_{22} = \Delta + \ell_2\theta_2$$

$$\Delta_{22} = \Delta + \ell_2 \frac{M_2}{K_T} \tag{3.7}$$

$$\Delta_{12} = \Delta + \ell_1\theta_2$$

$$\Delta_{12} = \Delta + \ell_1 \frac{M_2}{K_T} . \tag{3.8}$$

Now we can establish the following relations:

$$\Delta_{22} - \Delta_{21} = \Delta + \frac{P\ell_2^{\,2}}{K_T} - (\Delta + \frac{P\ell_1\ell_2}{K_T}) = \frac{P\ell_2}{K_T} d_\ell$$

$$\Delta_{22} - \Delta_{21} = \frac{P\ell_2}{K_T} d_\ell . \tag{3.9}$$

In a similar manner,

$$\Delta_{12} - \Delta_{11} = \Delta + \frac{P\ell_1\ell_2}{K_T} - (\Delta + \frac{P_{\ell 1}^{\,2}}{K_T})$$

$$\Delta_{12} - \Delta_{11} = \frac{P\ell_1}{K_T} d_\ell . \tag{3.10}$$

Substracting eq. (3.10) from eq. (3.9), we have

$$\Delta_{22} - \Delta_{21} - (\Delta_{12} - \Delta_{11}) = \frac{Pd_1}{K_T} (\ell_2 - \ell_1)$$

and finally

$$K_T = \frac{Pd_\ell^{\,2}}{\Delta_{22}-\Delta_{21}-\Delta_{12}+\Delta_{11}} \tag{3.11}$$

which is the torsional stiffness of the model of the length ℓ.

In order to get the torsional stiffness per unit length, we have to multiply the expression above by ℓ:

$$K_t = \frac{Pd_\ell^{\,2}\ell}{\Delta_{22}-\Delta_{21}-\Delta_{12}+\Delta_{11}} . \tag{3.12}$$

If the chord of an airfoil cross section is given as 2a, we can scale the expression above with the factor $\frac{a^2+b^2}{\pi a^3 b^3}$.

$$K_t^* = \frac{P d_\ell^{\,2} \ell}{[\Delta_{22}-\Delta_{21}-\Delta_{12}+\Delta_{11}]} \cdot \frac{a^2+b^2}{\pi a^3 b^3} \tag{3.13}$$

where

$$K_t^* = K_t \frac{a^2+b^2}{\pi a^3 b^3} . \tag{3.14}$$

We can now find the torsional stiffness for any beam of given length ℓ and chord 2a for the same family of airfoil section:

$$K_T = K_t^* \cdot \frac{\pi a^3 b^3}{\ell(a^2+b^2)} . \tag{3.15}$$

In a similar manner, the relation of the torque-angle of twist is derived;

$$M_T = K_t^* \frac{\pi a^3 b^3}{\ell(a^2+b^2)} \theta . \tag{3.16}$$

3.3. Experimental Technique

The experimental technique is based on the approach presented in the previous section. To obtain satisfactory accuracy in measurement, the system for measurement is set up as shown by Fig. 3.4.

The model is clamped to a vertical solid beam of much larger mass and stiffness. At the tip of the model, two light aluminum rods are attached. One of them has two attaching points for weight. These are shown in Fig. 3.2 as points 1 and 2, and are located at the distance d_ℓ = 10[in]. In order to avoid error in measurement, another bar is used as a reference line when

ORIGINAL PAGE IS
OF POOR QUALITY

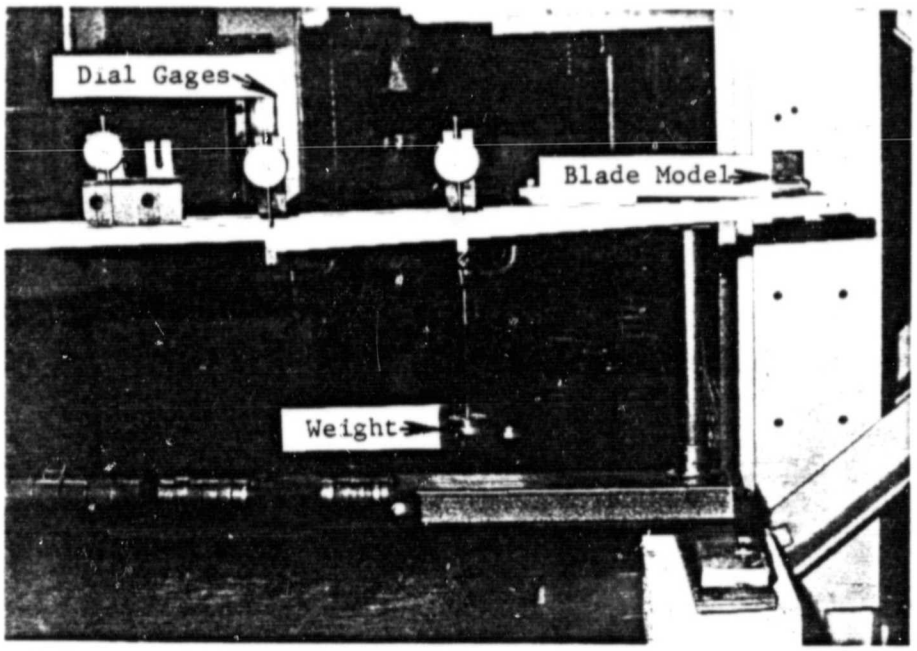

Figure 3.4. Side view of the measurement system used.

measuring the displacements at points 1 and 2. Dial gages are used for displacement measurement, with a scale of 0.001 [in] per division. Since the shear modulus of aluminum is relatively low, a small angle of twist is used on the model in order to avoid plastic deformations. Measurements are conducted in the following way:

1. The weight is hung at position 1 and the displacements are measured at position 1, Δ_{11}, and at position 2, Δ_{21}.

2. The same weight is hung at position 2 and the displacements are measured at position 2, Δ_{22}, and at position 1, Δ_{12}.

The same procedure with different weights is repeated and the displacements are measured. The same procedure is then repeated for all three models, selecting the appropriate amount of weight to be used in order to avoid plastic deformation.

Chapter 4

PREDICTED AND EXPERIMENTAL RESULTS OF TORSIONAL STIFFNESS OF BEAMS HAVING AIRFOIL CROSS SECTIONS

4.1. Introduction

In this chapter, the predicted results are given for a group of models having cross sections similar to that of the symmetrical airfoil. Experimental results are obtained for the three models having NACA four-digit symmetrical sections. The results are given in Tables 4.2, 4.3, and 4.4.

4.2. Comparison and Discussion of Predicted and Experimental Results

In Chapter 2, the formulae are derived for torsional stiffness per unit length K_t^* for beams having cross sections close to that of the symmetrical airfoil section. The models have widths and thicknesses corresponding to the dimensions of models having symmetrical airfoil sections used in the experimental part. The formulae and the results are summarized and given in Table 4.1.

In the experimental part, three models are used. They have been tested, according to the procedure given in Chapter 3, in the structural area of the Department of Aerospace Engineering of The Pennsylvania State University. The models have the following material properties:

1. The material of the models is aluminum.
2. Young's modulus of elasticity is 10.5×10^6 [lb/in^2].
3. The shear modulus is 4.0×10^6 [lb/in^2].

4. The mass density is 2.59 [lb sec^2/in^4].

The geometrical and the material properties are given in Table 4.1. With the data obtained by measurement, the torsional stiffness per unit length K_t and the scaled torsional stiffness per unit length K_t^* are calculated and given in Table 4.3.

The results predicted for models given in Table 4.2 and the results experimentally obtained for the models in Table 4.3 are summarized in Table 4.4. Observing these results, we conclude that we have fairly good agreement for scaled torsional stiffness K_t^* obtained analytically and experimentally for the same models. The results obtained experimentally are slightly below the results predicted. This is probably due to imperfect clamping of the models and the way the torque is applied to the models.

For any given model made of aluminum or any metal having a NASA four-digit symmetrical section, we can calculate the torsional stiffness if we know the length ℓ and the chord 2a;

$$K_T = K_t^* \frac{\pi a^3 b^3}{\ell(a^2+b^2)} \tag{4.1}$$

where K_t^* is predicted and measured as a function of the shear modulus. Generally, we can calculate the torque for a given angle of twist for the models above as

$$M_T = K_T \theta. \tag{4.2}$$

Since the stiffness experimentally measured is slightly below predicted, it is recommended that the first one be used in further calculation.

Table 4.1. Geometrical and material properties of blade models used in experimental measurement.

Cross section	Shape	Dimen. of cross section	Length	Material	Modulus of elasticity	Weight of the model	Mass of the model	Area moment of inertia	Cross sectional area
		a [in] b [in]	ℓ [in]	E [lb/in^2]	W [lb]	m [$\frac{lbsec^2}{in}$]	I_x [in^4]	I_x [in^4]	A [in^2]
NACA 0021	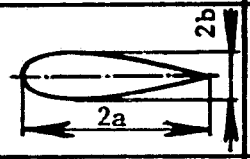	a = 1.0 b = 0.21	15.0	Aluminum	10.5×10^6	0.812	0.210×10^{-2}	0.580×10^{-2}	0.5695
NACA 0015	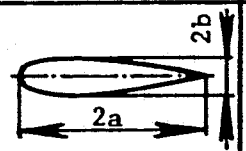	a = 1.0 b = 0.15	15.0	Aluminum	10.5×10^6	0.562	0.145×10^{-2}	0.150×10^{-2}	0.3370
NACA 0009	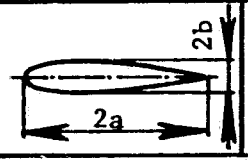	a = 1.0 b = 0.09	15.0	Aluminum	10.5×10^6	0.375	0.970×10^{-3}	0.300×10^{-3}	0.202

ORIGINAL PAGE IS
OF POOR QUALITY

Table 4.2. Analytically predicted torsional stiffness of beams having different cross sections scaled as the beams of unit length.

Mod. No.	Cross Section	Shape	Torsional stiffness per unit length	Scaled tor. stiff.	NASA 0021	NASA 0015	NASA 0009
					a = 1.0 [in] b = 0.21 [in]	a = 1.0 [in] b = 0.15 [in]	a = 1.0 [in] b = 0.09 [in]
1	Rectangular	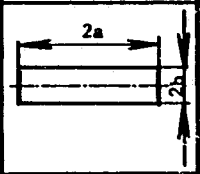	$K_1 = \frac{1}{3}\left[1 - \frac{192}{\pi^5}\frac{a}{b}\Sigma\frac{1}{n^5}\tanh\frac{n\,b}{2a}\right]$	K_1	0.12849×10^{-1}	0.69134×10^{-2}	0.25571×10^{-2}
			$K_t = 16K_1Ga^3b$	$K_t^* = K_t\frac{a^2+b^2}{\pi a^3b^3}$	0.1549Gx10	0.1600Gx10	0.1621Gx10
					0.61973×10^7	0.64003×10^7	0.64849×10^7
2	Elliptical	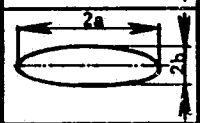	$K_t = \frac{\pi a^3b^3G}{a^2+b^2}$	$K_t^* = K_t\frac{a^2+b^2}{\pi a^3b^3}$	0.1Gx10	0.1Gx10	0.1Gx10
					0.40000×10^7	0.40000×10^7	0.40000×10^7
3	Parabolic Segment	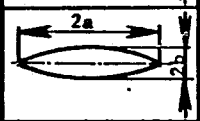	$K_t = \frac{0.1524(2a)(2b)^3G}{\left[1 + 1.333(\frac{b}{a})^2\right]}$	$K_t^* = K_t\frac{a^2+b^2}{\pi a^3b^3}$	0.7654G	0.7705G	0.7741G
					0.30616×10^7	0.30821×10^7	0.30965×10^7
4	Symmetrical airfoil	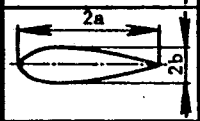	$K_t = 0.0736\frac{Gbd^3}{\left[1+\frac{11}{13}\frac{d^2}{b^2}\right]}$	$K_t^* = K_t\frac{a^2+b^2}{\pi a^3b^3}$	0.8071G	0.8140G	0.8189G
					0.32284×10^7	0.32561×10^7	0.32756×10^7
5	Symmetrical airfoil	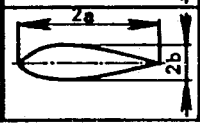	$K_t = \frac{256G(\frac{b}{a})^3(2a)^4}{3465\left[1-\frac{11}{13}(\frac{b}{a})^2+(\frac{b}{a})^4-\frac{379}{279}(\frac{b}{a})^6\right]}$	$K_t^* = K_t\frac{a^2+b^2}{\pi a^3b^3}$	0.7578G	0.7817G	0.7535G
					0.30313×10^7	0.31270×10^7	0.30141×10^7

ORIGINAL PAGE IS OF POOR QUALITY

Table 4.3. Experimentally determined torsional stiffness of blade models having airfoil cross sections scaled for the beams of unit length.

Cross Section	Shape	Dimensions	No. of meas.	Δ_{11}	Δ_{21}	Δ_{22}	Δ_{12}	P	d	K_t	K_t^*
		[in]		[in]	[in]	[in]	[in]	[lb]	[in]	[lb in]	$[\frac{lb}{in^2}]$
NACA 0021	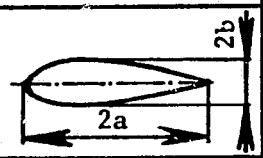	a = 1.0 b = 0.21 ℓ = 15.0	1	0.085	0.122	0.175	0.125	0.75	10.0	0.80357×10^5	0.50223×10^4
			2	0.111	0.156	0.213	0.150	1.00	10.0	0.81081×10^5	0.50675×10^4
NACA 0015	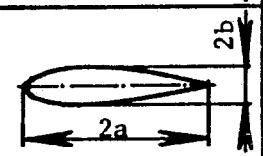	a = 1.0 b = 0.15 ℓ = 15.0	1	0.111	0.156	0.230	0.158	0.50	10.0	0.27777×10^5	0.18361×10^4
			2	0.226	0.313	0.473	0.331	1.00	10.0	0.27027×10^5	0.16891×10^4
NACA 0.009	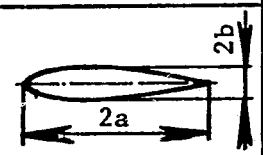	a = 1.0 b = 0.09 ℓ = 15.0	1	0.512	0.208	0.331	0.214	0.25	10.0	0.57633×10^4	0.38422×10^3
			2	0.371	0.605	0.734	0.619	0.50	10.0	0.63025×10^4	0.40390×10^3

ORIGINAL PAGE IS OF POOR QUALITY

Table 4.4 Predicted and measured torsional stiffness for three models having NASA four-digit symmetrical section.

	Model	Dimensions [in]	Predicted K_t^* (Galerkin)	Predicted K_t^* (Rayleigh-Ritz)	Measured K_t^*
No.	Units	[in]	[unitless]	[unitless]	[unitless]
1	NACA 0021	a = 1.0 b = 0.21 ℓ = 15.	0.80710G	0.7578G	0.72743G
			3.22841×10^6	3.03133×10^6	2.90973×10^6
2	NACA 0015	a = 1.0 b = 0.15 ℓ = 15.	0.81403G	0.78175G	0.70826G
			3.25614×10^6	3.12702×10^6	2.83307×10^6
3	NACA 0009	a = 1.0 b = 0.09 ℓ = 15.	0.81891G	0.75353G	0.71141G
			3.27565×10^6	3.01413×10^6	2.84567×10^6
4	Average		0.81335G	0.76437G	0.71570G
			3.25340×10^6	3.05749×10^6	2.86282×10^6

ORIGINAL PAGE IS
OF POOR QUALITY

Chapter 5

THE DYNAMIC MODELING OF CANTILEVER BEAMS AS UNDAMPED MULTI-DEGREE-OF-FREEDOM SYSTEMS

5.1 Free Vibration

The analysis of a structure in free vibration provides the most important dynamic properties of the structure, which are the natural frequencies and the corresponding modal shapes. The equations of motion are represented in a matrix form by

$$[m]\{\ddot{x}(t)\} + [k]\{x(t)\} = \{0\} \tag{5.1}$$

which represents a set of n simultaneous differential equations of the type

$$\sum_{i=1}^{n} m_{ij}\ddot{x}_j(t) + \sum_{j=1}^{n} k_{ij}x_j(t) = 0, \; i = 1,2,\ldots,n \tag{5.2}$$

where [m] and [k] are the mass and stiffness matrices. Before considering properties of frequencies and modes, it is useful to consider some of the properties of the stiffness matrices and mass matrices encountered in structural dynamics problems.

5.2. Some Properties of [k] and [m] Matrices

The strain energy and kinetic energy can be written in the form of the triple-matrix product

$$V = \frac{1}{2}\{x\}^T[k]\{x\} \tag{5.3}$$

where $\{x\}$ is the n-dimensional displacement vector and $\{x\}^T$ is its transpose matrix.

ORIGINAL PAGE IS
OF POOR QUALITY

$$\{x\} = \begin{matrix} x_1 \\ x_2 \\ \vdots \\ x_n \end{matrix} \qquad [k] = \begin{bmatrix} k_{11} & k_{12} & \cdots & k_{1n} \\ k_{21} & k_{22} & \cdots & k_{2n} \\ & \cdot & & \\ & & \cdot & \\ & & & \vdots \\ k_{n1} & k_{n2} & \cdots & k_{nn} \end{bmatrix} \tag{5.4}$$

and

$$T = \frac{1}{2}\{\dot{x}\}^T [m] \{\dot{x}\} \tag{5.5}$$

where $\{\dot{x}\}$ is the n-dimensional velocity vector.

$$\{\dot{x}\} = \begin{matrix} \dot{x}_1 \\ \dot{x}_2 \\ \vdots \\ x_n \end{matrix} \qquad [m] = \begin{bmatrix} m_{11} & m_{12} & \cdots & m_{1n} \\ m_{21} & m_{22} & \cdots & m_{2n} \\ & \cdot & & \\ & & \cdot & \\ & & & \cdot \\ m_{n1} & m_{n2} & \cdots & m_{nn} \end{bmatrix} \tag{5.6}$$

Matrices [k] and [m] for most structures are positive-definite matrices, that is, when arbitrary vectors $\{x\}$ and $\{\dot{x}\}$ are chosen and V and T are computed from eqs. (5.2) and (5.4), the resulting values of V and T are positive, except for the trivial cases $\{x\} = 0$ and $\{\dot{x}\} = 0$.

In general, the kinetic energy T is always positive-definite, so that [m] is always positive definite. The question remains as to the sign properties of the potential (strain) energy and the associated matrix [k]. Two cases of particular interest in vibrations are those in which [k] is positive-definite and [k] is only positive-semidefinite. When [k] is positive-semidefinite, V can be zero (for rigid-body modes) or greater than zero (for deformable

modes). When [k] is positive-semidefinite, det[k] = 0. Since the det[k] vanishes, [k] is called a singular matrix. When [m] is positive-definite and [k] is positive-semidefinite, the system is referred to as a semidefinite system, and the motion is called undamped free vibration. Rigid-body motion is possible because semidefinite systems are unrestrained, that is, such systems are supported in a manner in which rigid-body motion can take place.

5.3. Some Properties of Natural Frequencies

We are interested in a special form of solution of the set (5.2), namely, that in which all the coordinates have the same time dependence and the general configuration of motion does not change except for the amplitude, so that the ratio between any two coordinates $x_i(t)$ and $x_j(t)$, $i \neq j$, remains constant during the motion. This type of motion is expressed mathematically by means of a linear transformation that can be represented by the matrix of the system eigenvectors.

$$\{x(t)\} = [\phi]\{q(t)\} \tag{5.7}$$

$$\{\ddot{x}(t)\} = [\phi]\{\ddot{q}(t)\} \tag{5.8}$$

Substituting equations (5.7) and (5.8) into equation (5.1), we have

$$[m][\phi]\{\ddot{q}(t)\} + [k][\phi]\{q(t)\} = \{0\}. \tag{5.9}$$

If we assume the following type of harmonic motion for the r-th mode, the characteristic equation for the r-th mode can be derived in the following manner.

$$\{q_r(t)\} = \{A_r\}\sin(\omega_r t-\theta_r) \tag{5.10}$$

$$\{\ddot{q}_r(t)\} = -\{A_r\}\omega_r^{\,2}\sin(\omega_r t-\theta_r) \tag{5.11}$$

$$(-\omega_r^{\,2}[m] + [k])\{\phi_r\}\{A_r\}\sin(\omega_r t-\theta_r) = \{0\} \tag{5.12}$$

Since $\{A_r\}\sin(\omega_r t-\theta) \neq \{0\}$

$$(-\omega_r^{\,2}[m] + [k])\{\phi_r\} = \{0\}. \tag{5.13}$$

The equation above represents the n-th order algebraic eigenvalue problem. For a nontrivial solution, the determinant of eq. (5.13) has to vanish:

$$\det([k] - \omega^2[m]) = 0. \tag{5.14}$$

This is called the characteristic equation. When the determinant of eq. (5.14) is expanded, a polynomial equation of degree n in ω^2 is formed whose roots are the eigenvalues, or squared natural frequencies, $\omega_r^{\,2}$. These can be ordered from the lowest to the highest:

$$0 \leq \omega_1^{\,2} \leq \omega_2^{\,2} \leq \ldots\ldots \leq \omega_r^{\,2} \leq \ldots\ldots \leq \omega_n^{\,2}. \tag{5.15}$$

It is possible for several modes to have the same frequency; however, this condition is unusual in structural systems. Not so unusual is the case in which several mode frequencies are very nearly the same; so close together, in fact, that very great computational or experimental accuracy is required to distinguish among them.

5.4. Some Properties of Eigenvectors (Modal Shapes)

A mode shape is a unique deformation shape that the structural system would take on if excited solely in that mode of vibration. Mathematically, mode shapes are represented as vectors known as modal vectors. Each element of the modal vector is the deflection of one degree of freedom in the structure. Equation (5.13) can be rewritten for the r-th mode in the following way:

$$[k]\{\phi_r\} = \omega_r^2\{\phi_r\}, \quad r = 1,2,3,\ldots,n. \tag{5.16}$$

The solution vector $\{\phi_r\}$ corresponding to a particular eigenvalue is called a mode shape or characteristic eigenvector or an eigenvector, and defines a particular structural deformation pattern called a mode. Because eq. (5.16) is homogenous, there is not a unique solution, and only a ratio among the elements of a particular mode shape vector can be determined. The values of the elements themselves are arbitrary, so that if $\{\phi_r\}$ is a solution of eq. (5.16), then $\alpha_r\{\phi_r\}$ is also a solution, where α_r is an arbitrary constant. Hence, the shape of the natural modes is unique, but the amplitude is not. If one of the elements of the eigenvector is rendered unique in an absolute sense, this automatically causes an adjustment in the values of the remaining n-1 elements, and the ratio between any two elements is constant.

5.5. Scaling (Normalizing) of Eigenvectors

Since the modal vector represents a shape rather than the absolute deflection of the structure, elements of the modal vector are normally scaled in some arbitrary manner. The most common

technique is to scale the modal vector so that the largest element equals one. This allows the deflections at the remaining degrees of freedom contained in the modal vector to be expressed as a percentage of the maximum. It is a common misconception that modal vectors define actual vibratory motion of a structure. The total deformation resulting from external excitation is dependent not only on the magnitude and location of the input forces, but also on the participation of each mode in the structure's total response.

The process of scaling a natural mode so that each of its elements has a unique value is called normalization, and the resulting modal vectors are called normal modes. A very convenient normalization scheme consists of setting

$$\{\phi_r\}^T[m]\{\phi_r\} = M_r, \quad r = 1,2,3,\ldots,n \tag{5.17}$$

so that the M_r is the generalized mass or modal mass in the r-th mode. Generally the modal mass matrix is

$$[\phi]^T[m][\phi] = \lceil M \rfloor. \tag{5.18}$$

In a similar manner, the generalized stiffness or modal stiffness for the r-th mode is defined as

$$\{\phi_r\}^T[k]\{\phi_r\} = K_r, \quad r = 1,2,3,\ldots,n. \tag{5.19}$$

The modal stiffness matrix is

$$[\phi]^T[k][\phi] = \lceil \omega^2 M \rfloor . \tag{5.20}$$

The following is an especially convenient normalization for

a general system, so that the product $\{\phi_r\}^T[m]\{\phi_r\}$ has the units of unit mass. Eigenvectors obtained in a such manner are called orthonormalized eigenvectors. For a system having a consistent mass matrix (full), the normalized i-th component of the j-th modal vector is

$$\Phi_{ij} = \frac{\phi_{ij}}{\sqrt{\{\phi_j\}^T[M]\{\phi_j\}}} . \tag{5.21}$$

For a system having a diagonal mass matrix, the i-th component of the j-th modal vector is

$$\Phi_{ij} = \frac{\phi_{ij}}{\sqrt{\sum_{k=1}^{n} m_k \phi_{k_j}^2}} \tag{5.22}$$

in which $\{\phi_i\}$ and $\{\phi_j\}$ are any two modal vectors and [M] is the modal mass matrix of the system. The normal modes may be conveniently arranged in the columns of a matrix known as the modal matrix of the system, that is,

$$[\Phi] = \begin{bmatrix} \Phi_{11} & \Phi_{12} & \cdots & \Phi_{1n} \\ \Phi_{21} & \Phi_{22} & \cdots & \Phi_{2n} \\ & \cdot & & \\ & & \cdot & \\ & & \cdot & \\ \Phi_{n1} & \Phi_{n2} & \cdots & \Phi_{nn} \end{bmatrix} \tag{5.23}$$

which holds for the general case of n degrees of freedom.

5.6. Orthogonality of Modal Vectors and the Expansion Theorem

The natural modes possess a very useful property known as orthogonality. This is not an ordinary orthogonality, but an orthogonality with respect to the inertia matrix [m] (and also with respect to the stiffness matrix [k]). The following calculation is proof of the orthogonality of the modal vectors $\{\phi_r\}$. We are going to consider two distinct solutions, $\omega_r^2\{\phi_r\}$ and $\omega_s^2\{\phi_s\}$, of the eigenvalue problem presented in eq. (5.19). These solutions can be written in the form

$$[k]\{\phi_r\} = \omega_r^2[m]\{\phi_r\} \tag{5.24}$$

$$[k]\{\phi_s\} = \omega_s^2[m]\{\phi_s\}. \tag{5.25}$$

Premultiplying both sides of eq. (5.24) by $\{\phi_s\}^T$ and both sides of eq. (5.25) by $\{\phi_r\}^T$, we obtain

$$\{\phi_s\}^T[k]\{\phi_r\} = \omega_r^2\{\phi_s\}^T[m]\{\phi_r\} \tag{5.26}$$

$$\{\phi_r\}^T[k]\{\phi_s\} = \omega_s^2\{\phi_r\}^T[m]\{\phi_s\}. \tag{5.27}$$

If we transpose eq. (5.27) and assume that matrices [k] and [m] are symmetric, and subtract the result from eq. (5.26), we obtain

$$(\omega_r^2 - \omega_s^2)\{\phi_s\}^T[m]\{\phi_r\} = 0. \tag{5.28}$$

Since, in general, the natural frequencies are distinct, $\omega_r \neq \omega_s$, eq. (5.28) provides

$$\{\phi_s\}^T[m]\{\phi_r\} = 0, \; r \neq s \tag{5.29}$$

which is the statement of the orthogonality condition of the modal vectors. It is easy to see that the modal vectors are also orthogonal with respect to the stiffness matrix [k]:

$$\{\phi_s\}^T [k] \{\phi_r\} = 0, \; r \neq s. \tag{5.30}$$

We stress again that the orthogonality relations shown in eqs. (5.29) and (5.30) are valid only if [m] and [k] matrices are symmetric.

The modal vectors can be conveniently arranged in a square matrix of order n, known as the modal matrix and having the form

$$[\phi] = [\{\phi_1\}\{\phi_2\}\ldots\{\phi_n\}] \tag{5.31}$$

where $[\phi]$ is, in fact, the transformation matrix. All n solutions of the eigenvalue problem can be written in a compact matrix form:

$$[k][\phi] = [m][\phi][\omega^2]. \tag{5.32}$$

The eigenvectors $\{\phi_r\}$ $(r = 1,2,3,\ldots,n)$ form a linearly independent set, implying that an n-dimensional vector representing any possible, but otherwise arbitrary, configuration of the system can be constructed as a linear combination of eigenvectors. Physically, this implies that any motion of the system resulting from an arbitrary excitation can be regarded at a given time as a superposition of the natural modes multiplied by appropriate constants, where the constants are a measure of the degree of participation of each mode. This approach permits the transformation of a simultaneous set of differential equations of motion into an independent set, where the transformation matrix is the modal

matrix $[\phi]$. The process of deriving the system response by transforming the equations of motion into an independent set is known as modal analysis.

To prove that a set of vectors $\{\phi_r\}$ is linearly independent, we assume that the vectors are linearly dependent and arrive at a contradiction. For the set of vectors $\{\phi_r\}$ to be linearly dependent, it must satisfy an equation of the type

$$c_1\{\phi_1\} + c_2\{\phi_2\} + \ldots + c_n\{\phi_n\} = \sum_{r=1}^{n} c_r\{\phi_r\} = \{0\} \qquad (5.33)$$

where c_r $(r = 1,2,..,n)$ are non-zero constants. Premultiplying eq. (5.33) by $\{\phi_s\}^T[m]$, we obtain

$$\sum_{r=1}^{n} c_r\{\phi_s\}^T[m]\{\phi_r\} = 0. \qquad (5.34)$$

The triple-matrix product $\{\phi_s\}^T[m]\{\phi_r\}$ is equal to zero for $r \neq s$ and is less than or greater than zero for $r = s$. Repeating the operation in the equation n times, for $s = 1,2,3,\ldots,n$, we conclude that eq. (5.34) can be satisfied only in the trivial case defined by $c_1 = c_2 = \ldots = c_n = 0$. Then we have $\{\phi\}$ as a linear combination of $\{\phi_1\}$, $\{\phi_2\}$, ..., $\{\phi_n\}$, with coefficients c_1, c_2, c_3, ..., c_n:

$$\{\phi\} = c_1\{\phi_1\} + c_2\{\phi_2\} + \ldots + c_n\{\phi_n\} \neq \{0\}. \qquad (5.35)$$

Hence, any vector belonging to the space $\{\phi\}$ can be generated in the form of linear combination as shown in (5.35). Physically, this means that any possible motion of the system can be described as a linear combination of the modal vectors. The coefficients c_r are a measure of the contribution of the associated modes $\{\phi_r\}$ to the

ORIGINAL PAGE IS
OF POOR QUALITY

motion $\{\phi\}$.

$$c_r = \{\phi_r\}^T [m] \{\phi\} \tag{5.36}$$

Equations (5.35) and (5.36) are known in vibration theory as the expansion theorem. This can be applied to multi-degree-of-freedom systems:

$$\{\phi_r\}^T [m] \{\phi_s\} = 0. \tag{5.37}$$

If matrix [m] is symmetric, we can rewrite equation (5.37) as

$$m_1\phi_{1r}\phi_{1s} + m_2\phi_{2r}\phi_{2s} + \ldots + m_n\phi_{nr}\phi_{ns} = 0, \; r \neq s \tag{5.38}$$

for r = s = n

$$m_1\phi_{1n}{}^2 + m_2\phi_{2n}{}^2 + \ldots + m_n\phi_{nn}{}^2 = M_n \tag{5.39}$$

or write it in a matrix notation as

$$\{\phi_n\}^T [m] \{\phi_n\} = M_n. \tag{5.40}$$

We recognize M_n as the modal mass in the n-th mode. Generally for the system of order n the equation above becomes

$$[\phi]^T [m] [\phi] = \lceil M \rfloor = \begin{bmatrix} M_1 & & & \\ & M_2 & & \\ & & \ddots & \\ & & & M_n \end{bmatrix} \tag{5.41}$$

which is the generalized mass matrix or modal mass matrix. Using eq. (5.26) under conditions r = s = n, for the n-th mode,

$$\{\phi_n\}^T [k] \{\phi_n\} = \omega_n{}^2 \{\phi_n\}^T [m] \{\phi_n\}. \tag{5.42}$$

ORIGINAL PAGE IS
OF POOR QUALITY

In eq. (5.42), we recognize the modal stiffness in the n-th mode. Generally, for the system of order n, this equation becomes

$$[\phi]^T[k][\phi] = \lceil \omega_n^2 M_n \rfloor = \begin{bmatrix} \omega_1^2 M_1 & & & \\ & \omega_2^2 M_2 & & \\ & & \ddots & \\ & & & \omega_n^2 M_n \end{bmatrix}. \tag{5.43}$$

If the eigenvectors are scaled in the following way

$$[\Phi]^T[m][\Phi] = [I]$$

where [I] is the identity matrix, then the scaled model-stiffness matrix has the following form:

$$[\Phi]^T[k][\Phi] = \lceil \omega^2 \rfloor = \begin{bmatrix} \omega_1^2 & & & \\ & \omega_2^2 & & \\ & & \ddots & \\ & & & \omega_n^2 \end{bmatrix}. \tag{5.44}$$

5.7. Response of Multi-Degree-of-Freedom Systems to Initial Excitation

The equations of motion are represented in a matrix form by

$$[m]\{\ddot{x}(t)\} + [k]\{x(t)\} = \{0\}. \tag{5.45}$$

Equation (5.45) represents a set of simultaneous ODE's with constant coefficients. Using linear system theory, a general closed-form solution of eq. (5.45) can be shown to exist. A convenient way of deriving the solution is modal analysis, which requires the solution of a so-called eigenvalue problem for the system.

In eq. (5.45) $\{x(t)\}$ is the displacement vector or the generalized coordinate vector $x_r(t)$ $(r = 1,2,3,\ldots,n)$. We introduce the following transformation matrices:

$$\{x(t)\} = [\Phi]\{q(t)\} \tag{5.46}$$

$$\{\ddot{x}(t)\} = [\Phi]\{\ddot{q}(t)\}. \tag{5.47}$$

Substituting these two equations into eq. (5.45), we have

$$[m][\Phi]\{\ddot{q}(t)\} + [k][\Phi]\{q(t)\} = \{0\}.$$

Premultiplying the above expression by $[\Phi]^T$, we have

$$[\Phi]^T[m][\Phi]\{\ddot{q}(t)\} + [\Phi]^T[k][\Phi]\{q(t)\} = \{0\}. \tag{5.48}$$

Using the relations in eqs. (5.43a) and (5.44) derived earlier, eq. (5.48) can be rewritten as follows:

$$[I]\{\ddot{q}(t)\} + \lceil\omega^2\rfloor\{q(t)\} = \{0\} \tag{5.49}$$

or

$$\begin{Bmatrix} \ddot{q}_1(t) \\ \ddot{q}_2(t) \\ \vdots \\ \ddot{q}_n(t) \end{Bmatrix} + \begin{bmatrix} \omega_1^2 & & & \\ & \omega_2^2 & & \\ & & \ddots & \\ & & & \omega_n^2 \end{bmatrix} \begin{Bmatrix} q_1(t) \\ q_2(t) \\ \vdots \\ q_n(t) \end{Bmatrix} = \begin{Bmatrix} 0 \\ 0 \\ \vdots \\ 0 \end{Bmatrix} \tag{5.50}$$

For the r-th mode, eq. (5.50) yields

$$\ddot{q}_r(t) + \omega_r^2 q_r(t) = 0 \tag{5.51}$$

where variables $q_r(t)$ are identified as the normal coordinates

of the system. Using eq. (5.46), we can write the expansion expression for $\{x(t)\}$ as follows:

$$\{x(t)\} = \{\Phi_1\}q_1(t) + \{\Phi_2\}q_2(t) + \ldots + \{\Phi_n\}q_n(t) \qquad (5.52)$$

or

$$\{x(t)\} = \sum_{r=1}^{n} \{\Phi_r\}q_r(t) = [\Phi]\{q(t)\}. \qquad (5.53)$$

By an analogy with the free vibration solution of an undamped single-degree-of-freedom system, the solution of eq. (5.49) is

$$q_r(t) = C_r\cos(\omega_r t - \theta_r), \; r = 1,2,\ldots,n \qquad (5.54)$$

where C_r and θ_r $(r = 1,2,3,\ldots,n)$ are constants of integration representing the amplitudes and phase angles of the normal coordinates. Inserting eq. (5.54) into eq. (5.46), we have

$$\{x(t)\} = [\Phi]\{q(t)\} = \sum_{r=1}^{n} \{\Phi_r\}q_r(t) = \sum_{r=1}^{n} C_r\{\Phi_r\}\cos(\omega_r t - \theta_r) \quad (5.55)$$

so that the free vibration of a multi-degree-of-freedom system consists of a superposition of n harmonic motions with frequencies equal to the system's natural frequencies, and with amplitudes and phase angles depending on the initial conditions.

Letting $\{x(0)\} = \{x_0\}$ and $\{\dot{x}(0)\} = \{\dot{x}_0\}$ be the initial displacement and initial velocity vectors, respectively, eq. (5.55) leads to

$$\{x_0\} = \sum_{r=1}^{n} C_r\{\Phi_r\}\cos\theta_r \qquad (5.56)$$

$$\{\dot{x}_0\} = \sum_{r=1}^{n} C_r\omega_r\{\Phi_r\}\sin\theta_r . \qquad (5.57)$$

Premultiplying eq. (5.56) and (5.57) by $\{\Phi_s\}^T[m]$,

$$\{\Phi_r\}^T[m]\{x_0\} = C_r\cos\theta_r \tag{5.58}$$

$$\frac{1}{\omega_r}\{\Phi_r\}^T[m]\{\dot{x}_0\} = C_r\sin\theta_r. \tag{5.59}$$

Introducing these two equations into eq. (5.55), we obtain the general expression

$$\{x(t)\} = \sum_{r=1}^{n} [\{\Phi_r\}^T[m]\{x_0\}\cos\omega_r t$$

$$+ \{\Phi_r\}^T[m]\{\dot{q}_0\}\frac{1}{\omega_r}\sin\omega_r t]\{\Phi_r\} \tag{5.60}$$

which represents the response of the system to the initial displacement vector $\{x_0\}$ and the initial velocity vector $\{\dot{x}_0\}$. Now we assume that the initial displacement vector $\{x_0\}$ resembles a given normal mode, say $\{\Phi_s\}$, whereas the initial velocity vector is zero. Introducing $\{x_0\} = x_0\{\Phi_s\}$ and $\{\dot{x}_0\} = \{0\}$, the response is

$$\{x(t)\} = \sum_{r=1}^{n} [q_0\{\Phi_r\}^T[m]\{x_0\}\cos\omega_r t]\{\Phi_r\}. \tag{5.61}$$

5.8. The Dynamic Response of Multi-Degree-of-Freedom Systems to a Harmonic Force

The general response of a discrete system, i.e., the response to both initial and external excitations, is governed by a set of simultaneous (coupled) equations, but can be rendered independent (uncoupled) by means of linear transformation that can be represented by the matrix of the system eigenvectors. Because these eigenvectors are commonly referred to as modal vectors, the

transformation matrix is called the modal matrix and the decoupling procedure itself is known as modal analysis. The independent ordinary differential equations resemble those of low-order systems and can be solved with relative ease. The important feature of these low-order systems is that they are described in terms of a single dependent variable.

For a linear system, solutions to excitations can be obtained separately and then added up linearly to obtain the combined response. This is the essence of the so-called principle of superposition, a very powerful principle that applies to linear systems alone. In vibration, we encounter the various types of periodic excitations, which are not necessarily harmonic. Any periodic function, however, can be represented by a convergent series of harmonic functions whose frequencies are integral multiples of a certain fundamental frequency, ω_0, provided that it satisfies certain conditions. The integral multiples of the fundamental frequency are called harmonics, with the fundamental frequency being the first harmonic. Such a series of harmonic functions is known as the Fourier Series, and can be written in the form

$$F(t) = \frac{1}{2} a_0 + \sum_{p=1}^{\infty} (a_p \cos p\omega_0 t + b_p \sin p\omega_0 t) \tag{5.62}$$

where $\omega_0 = \frac{2\pi}{T}$, p are integers, p = 1,2,3,...,n, and T is the period. The coefficients a_p and b_p are given by the formulae

$$a_p = \frac{2}{T} \int_{-T/2}^{T/2} F(t) \cos p\omega_0 t dt, \quad p = 0,1,2,3,\ldots,n \tag{5.63}$$

ORIGINAL PAGE IS
OF POOR QUALITY

$$b_p = \frac{2}{T}\int_{-T/2}^{T/2} F(t)\sin p\omega_0 t dt, \quad p = 0,1,2,3,\ldots,n \tag{5.64}$$

and they represent a measure of the participation of the harmonic components $\cos p\omega_0 t$ and $\sin p\omega_0 t$, respectively, in function F(t). The term $\frac{1}{2}a_0$ represents the average value of F(t). We consider the equation of motion of an undamped n degree-of-freedom system subjected to a harmonic force, expressed in terms of Fourier components of the fundamental frequency only. The same procedure could be repeated for higher harmonics.

The amplitudes of harmonic forces are distributed arbitrarily on all mass elements of the system. The exciting force can be written as follows:

$$F(t) = \frac{F_0}{2} + F_{0s}\sin\omega_f t + F_{0c}\cos\omega_f t \tag{5.65}$$

or

$$F(t) = \frac{F_0}{2} + F_{0r}e^{j(\omega_f t+\psi)} \tag{5.66}$$

where

$$F_{0r} = \sqrt{F_{0s}^{\ 2} + F_{0c}^{\ 2}}$$

$$\psi = \arctan\left(\frac{F_{0s}}{F_{0c}}\right) \tag{5.67}$$

and where ω_f is the forcing frequency of the system and ψ is the phase angle. The equations of motion for an n degree-of-freedom system can be written in matrix form as follows:

$$[m]\{\ddot{x}(t)\} + [k]\{x(t)\} = \{F(t)\} = \frac{1}{2}\{F_0\} + \{F_{0r}\}e^{j(\omega_f t+\psi)} . \tag{5.68}$$

The linear transformation matrices can be expressed as

$$\{x(t)\} = [\Phi]\{q(t)\} \tag{5.69}$$

$$\{\ddot{x}(t)\} = [\Phi]\{\ddot{q}(t)\} \tag{5.70}$$

where the transformation matrix $[\Phi]$ was introduced earlier as the scaled modal matrix. Also, in a previous section we showed the orthogonality conditions for two modes, ω_s and ω_r, $\omega_s \neq \omega_r$

$$\{\Phi_s\}^T[m]\{\Phi_r\} = 0 \quad r \neq s \tag{5.71}$$

$$\{\Phi_s\}^T[k]\{\Phi_r\} = 0 \quad r \neq s. \tag{5.72}$$

Substituting eqs. (5.71) and (5.72) into eq. (5.68), we have

$$[m][\Phi]\{\ddot{q}(t)\} + [k][\Phi]\{q(t)\} = \{F(t)\} = \frac{1}{2}\{F_0\} + \{F_{0r}\}\, e^{j(\omega_f t+\psi)}. \tag{5.73}$$

Premultiplying (5.73) by $[\Phi]^T$, we have

$$[\Phi]^T[m][\Phi]\{\ddot{q}(t)\} + [\Phi]^T[k][\Phi]\{q\} = \frac{1}{2}[\Phi]^T\{F_0\} + [\Phi]^T\{F_{0r}\}e^{j(\omega_f t+\psi)}. \tag{5.74}$$

Using relations derived in a previous section, eq. (5.47) reduces to

$$[I]\{\ddot{q}(t)\} + \lceil\omega^2\rfloor\{q(t)\} = \frac{1}{2}[\Phi]^T\{F_0\} + [\Phi]^T\{F_{0r}\}e^{j(\omega_f t+\psi)}. \tag{5.75}$$

This is a so-called modal equation, which decouples the initial system of equations into n independent equations. The terms on the right side are called the components of modal force. They give the extent to which the components of exciting forces participate in every mode.

The equation of motion in the r-th mode due to the exciting forces lumped at all masses, having arbitrarily distributed amplitudes, evolves from eq. (5.75) as

$$\ddot{q}_r(t) + \omega_r^2 q_r = \frac{1}{2}\{\Phi_r\}^T\{F_0\} + \{\Phi\}^T\{F_{0r}\}e^{j(\omega_f t+\psi)} . \qquad (5.76)$$

The solution of eq. (5.76) can be written as

$$q_r(t) = (q_r(t))_{hom} + (q_r(t))_{part} \qquad (5.77)$$

and the homogenous solution can be expressed as

$$(q_r)_{hom} = E_r \cos\omega_r t + F_r \sin\omega_r t.$$

The particular solution can be found separately for each component of the forcing function in eq. (5.76):

$$(q_r(t))_{part} = (q_r)_{part\ 1} + (q_r)_{part\ 2} . \qquad (5.78)$$

We assume the following types of solutions:

$$(q_r)_{part\ 1} = C . \qquad (5.79)$$

Substituting eq. (5.79) into eq. (5.76), and omitting the second term on the right-hand side of eq. (5.76), we have

$$(q_r)_{part\ 1} = \frac{1}{2\omega_r^2}\{\Phi_r\}^T\{F_0\} \qquad (5.80)$$

$$(q_r)_{part\ 2} = Q_r e^{j(\omega_f t+\psi)} \qquad (5.81)$$

$$(q_r)_{part\ 2} = -Q_r \omega_f^2 e^{j(\omega_f t+\psi)} \qquad (5.82)$$

Substituting eqs. (5.81) and (5.82) into eq. (5.76), and omitting the first term on the right-hand side of the latter equation, we have

$$(q_r)_{\text{part 2}} = \frac{\{\Phi_r\}\{F_{0r}\}}{\omega_r^2 - \omega_f^2} e^{j(\omega_f t+\psi)} . \tag{5.83}$$

The general solution for the r-th mode can be written as

$$q_{r(t)} = E_r \cos\omega_r t + F_r \sin\omega_r t + \frac{1}{2\omega_r^2}\{\Phi_r\}^T \{F_0\} + \frac{\{\Phi_r\}^T\{F_{0r}\}}{\omega_r^2 - \omega_f^2} e^{j(\omega_f t+\psi)} . \tag{5.84}$$

For convenience in further calculations, eq. (5.84) can be rewritten as

$$q_r(t) = E_r \cos\omega_r t + F_r \sin\omega_r t + \frac{1}{2\omega_r^2} \{\Phi_r\}^T\{F_0\} + \frac{\{\Phi_r\}^T\{F_{0s}\}}{\omega_r^2 - \omega_f^2} \sin\omega_f t + \frac{\{\Phi_r\}^T\{F_{0c}\}}{\omega_r^2 - \omega_f^2} \cos\omega_f t . \tag{5.85}$$

To define the constants E_r and F_r, we apply the initial conditions given. The displacement and velocity vectors at $t = 0$ are given as $\{x(0)\}$ and $\{\dot{x}(0)\}$. To impose the initial conditions from the original system to a new, transformed system, we use eqs. (5.69) and (5.70) at $t = 0$:

$$\{x(0)\} = [\Phi]\{q(0)\} \tag{5.86}$$

$$\{\dot{x}(0)\} = [\Phi]\{\dot{q}(0)\}. \tag{5.87}$$

From eqs. (5.86) and (5.87),

ORIGINAL PAGE IS
OF POOR QUALITY

$$\{q(0)\} = [\Phi]^{-1}\{x(0)\} \tag{5.88}$$

$$\{\dot{q}(0)\} = [\Phi]^{-1}\{\dot{x}(0)\}. \tag{5.89}$$

In order to avoid the inversion of matrix $[\Phi]$, we are using the following relation:

$$[\Phi]^T[m][\Phi] = [I].$$

Post multiplying the relation above by $[\Phi]^{-1}$, we have

$$[\Phi]^{-1} = [\Phi]^T[m]. \tag{5.90}$$

Substituting eq. (5.90) into eqs. (5.88) and (5.89), we have

$$\{q(0)\} = [\Phi]^T[m]\{x(0)\} \tag{5.91}$$

$$\{\dot{q}(0)\} = [\Phi]^T[m]\{\dot{x}(0)\}. \tag{5.92}$$

With time equal to zero, eq. (5.85) reduces to

$$\{q_r(0)\} = \{E_r\} + \frac{1}{2\omega_r^2}[\Phi]^T\{F_0\} + \frac{[\Phi]^T\{F_{0c}\}}{\omega_r^2 - \omega_f^2}. \tag{5.93}$$

Substituting eq. (5.91) into eq. (5.93), we can calculate the vector of constants $\{E_r\}$:

$$\{E_r\} = [\Phi]^T[m]\{x_r(0)\} - \frac{1}{2\omega^2}[\Phi]^T\{F_0\} - \frac{[\Phi]^T\{F_{0c}\}}{\omega_r^2 - \omega_f^2}. \tag{5.94}$$

Finding the first derivative of eq. (5.85),

$$\{\dot{q}_r(t)\} = -\{E_r\}\omega_r\sin\omega_r t + \{F_r\}\omega_r\cos\omega_r t + \frac{\omega_f[\Phi]^T\{F_{0c}\}}{\omega^2 - \omega_f^2}\cos\omega_f t$$

$$- \frac{\omega_f[\Phi]^T\{F_{0s}\}}{\omega^2 - \omega_f^2}\sin\omega_f t. \tag{5.95}$$

ORIGINAL PAGE IS
OF POOR QUALITY

With time equal to zero, eq. (5.95) becomes

$$\{\dot{q}(0)\} = \{F_r\}\omega_r + \frac{\omega_f [\Phi]^T \{F_{0s}\}}{\omega^2 - \omega_f^2} . \tag{5.96}$$

Substituting eq. (5.92) into eq. (5.96), we can calculate the vector of constants $\{F_r\}$:

$$\{F_r\} = \frac{1}{\omega_r} [\Phi]^T [m] \{\dot{x}(0)\} - \frac{\omega_f [\Phi]^T \{F_{0s}\}}{\omega_r^2 (\omega_r^2 - \omega_f^2)} . \tag{5.97}$$

Now Eq. (5.85) can be written in a final form as

$$\begin{aligned} \{q(t)\} = {} & [\Phi]^T [m] [\{x(0)\}\cos\omega_r t + \frac{1}{\omega_r} \{\dot{x}(0)\}\sin\omega_r t] \\ & - \frac{1}{2\omega_r^2} [\Phi]^T \{F_0\}\cos\omega_r t + \frac{[\Phi]^T \{F_{0c}\}}{\omega_r^2 - \omega_f^2} (\cos\omega_f t - \sin\omega_r t) \\ & + \frac{[\Phi]^T \{F_{0s}\}}{\omega_r^2 - \omega_f^2} (\cos\omega_f t - \frac{\omega_f}{\omega_r} \sin\omega_r t) , \quad r = 1,2,3,..,n. \end{aligned} \tag{5.98}$$

The solution to all n equations in eq. (5.98) must be calculated; then the finite displacements of masses can be obtained by superposition of the response in each mode:

$$\{x(t)\} = [\Phi]\{q(t)\}. \tag{5.99}$$

Therefore, in summary, the response analysis by mode superposition requires, first, the solution of eigenvalues and eigenvectors of the problem in eq. (5.32), then the solution of the decoupled equilibrium equations in eq. (5.98), and finally, the superposition of the response of each eigenvector as expressed in eq. (5.99).

The essense of a mode superposition solution of a dynamic response is that frequently only a small fraction of the total number of decoupled equations need be considered in order to obtain a good approximate solution to the actual response of the system. Considering the problem of selecting the number of modes to be included in the modal superposition analysis, it should always be kept in mind that an approximate solution to the dynamic equilibrium equations is sought. Therefore, if not enough modes are considered, the governing equations of motion are not solved accurately enough. This means that equilibrium, including the inertia forces, is not satisfied for the approximate response calculated.

This question arises especially when a lumped mass model is used to approximate a system having a uniformly distributed mass. There is no unique criterion to determine the number of modes to be taken. Usually in shock and steady-state problems driven on high frequencies, "effective modal mass" is used as parameter. A modal effective mass can be identified in matrix form for the n-th mode as:

$$(M_{eff})_n = \frac{\{1\}^T [m] \{\Phi_n\} \{\Phi_n\}^T [m] \{1\}}{M_n} \tag{5.100}$$

or in summary form as

$$(M_{eff})_n = \frac{\left[\sum_{i=1} m_i \Phi_{in}\right]^2}{\sum_{i=1}^{n} m_i \Phi_{in}^2}$$

where m_i is the mass of the i-th point, $\{1\}^T$ is a row matrix of ones, and M_n is the modal mass in the n-th mode defined by

$$M_n = \sum_{i=1}^{n} m_i \Phi_{in}^2 . \tag{5.102}$$

Usually a good indication that enough mass has been considered by modal analysis is that the effective modal mass is very close to the actual mass of structure, that is, more than 95% of the total mass.

Chapter 6

DAMPED MULTI-DEGREE-OF-FREEDOM SYSTEMS IN STRUCTURAL DYNAMICS

6.1. Introduction

All real systems dissipate energy through one of various types of damping mechanisms, such as structural viscous or Coulomb damping. The most common method of taking into account the dissipation of energy in structural dynamics is to assume in the mathematical model the presence of damping forces which have magnitudes proportional to the relative velocity and directions opposite to the motion. This type of damping is known as viscous damping, because it is a kind of damping that will occur when there is motion in an ideal viscous fluid. The inclusion of this type of damping in the equations does not alter the linearity of the differential equations of motion. Since the amount of damping commonly presented in structural systems is relatively small, its effect is neglected in the calculation of natural frequencies and mode shapes. However, to uncouple the damped differential equation of motion, it is necessary to impose some restrictions on the values of the damping coefficients in the system. These restrictions are of no consequence due to the fact that in practice it is easier to determine or estimate modal damping ratios rather than absolute damping coefficients. In addition, when solving the equations of motion by the modal superposition method, only damping ratios are required. When the solution is sought by other methods, the absolute values of damping coefficients may be

calculated from modal damping ratios by any of the various methods.

6.2. General Consideration

The equation of motion of a linear multi-degree-of-freedom damped system is

$$[m]\{\ddot{x}(t)\} + [c]\{\dot{x}(t)\} + [k]\{x(t)\} = \frac{1}{2}\{F_0\} + \{F_{0r}\}e^{j(\omega_f t+\psi)} . \quad (6.1)$$

In general, the coefficient matrices in the above equation, [m], [c], and [k], may have nonzero coupling terms (e.g., $c_{ij} = c_{ji} \neq 0$), so that to solve eq. (6.1) in its present form would require simultaneous solution of n equations in n unknowns. The purpose in this section is to outline the mode-superposition method by which such a set of coupled equations can be transformed into a set of uncoupled equations through use of the normal modes of the system. Equation (6.1) is the original set of coupled equations of motion for an n-degree-of-freedom system, where x(t) may be physical or generalized coordinates. The response of the system to the excitation force $\frac{1}{2}\{F_0\} + \{F_{0r}\}e^{j(\omega_f t+\psi)}$ and to the initial conditions $\{x(0)\}$ and $\{\dot{x}(0)\}$ is sought.

The first step in a mode-superposition solution is to obtain the natural frequencies and modal shapes of the system. In Chapter 5 we gave a very detailed treatment of these quantities. Since the structural systems can be considered as lightly damped systems, the most important dynamic properties, the natural frequencies and the corresponding modal shapes, are not practically affected by the presence of damping. We assume that if there are any repeated frequencies, the associated modes have been orthogonalized, so that

C-2

the orthogonality equations

$$\{\Phi_r\}^T[m]\{\Phi_r\} = \{\Phi_r\}[k]\{\Phi_r\} = \{0\} \tag{6.2}$$

are satisfied for all $r \neq s$. The modes are then collected to form the scaled modal matrix $[\Phi]$ already introduced in section 5.4.4, that is,

$$[\Phi] = [\{\Phi_1\}\{\Phi_2\}\ldots\{\Phi_r\}\ldots\{\Phi_n\}]. \tag{6.3}$$

The key step in the mode-superposition procedure is to introduce the coordinate transformation, exactly the same procedure used for an undamped multi-degree-of-freedom system in Chapter 5:

$$\{x(t)\} = [\Phi]\{q(t)\} = \sum_{r=1}^{n} \{\Phi_r\}q_r(t). \tag{6.4}$$

The coordinates $q_r(t)$ are usually referred to as normal or principal coordinates. Equation (6.4) is substituted into eq. (6.1) and the resulting equation is multiplied by $[\Phi]^T$ to give the equation of motion in principal coordinates, namely,

$$[\Phi]^T[m][\Phi]\{\ddot{q}(t)\} + [\Phi]^T[c][\Phi]\{\dot{q}(t)\} + [\Phi]^T[k][\Phi]\{q(t)\}$$
$$= [\Phi]^T\left[\frac{1}{2}\{F_0\} + \{F_{0r}\}e^{j(\omega_f t+\psi)}\right]. \tag{6.5}$$

Using relations in eqs. (5.43a) and (5.44), eq. (6.5) is reduced to

$$[I]\{\ddot{q}(t)\} + [C_s]\{\dot{q}(t) + [K_s]\{q(t)\} = \{F_s(t)\} \tag{6.6}$$

where

$$[I] = [\Phi]^T[m][\Phi] = \text{scaled modal mass matrix},$$
$$[C_s] = [\Phi]^T[c][\Phi] = \text{scaled modal damping matrix}, \tag{6.7}$$

$$[K_s] = [\Phi]^T [k] [\Phi] = \text{scaled modal stiffness matrix,}$$

$$\{F_s(t)\} = [\Phi]^T \left[\frac{1}{2}\{F_0\} + \{F_{0r}\} e^{j(\omega_f t+\psi)}\right] = \text{scaled modal force vector.}$$

Due to the orthogonality conditions of eq. (6.2), [m] and [k] are diagonal matrices, so the equations of motion in modal coordinates (eq. (6.6)) are coupled only through a nonzero off-diagonal in the scaled modal damping matrix $[C_s]$. In the derivation of the modal-coordinate equations of motion, it has been assumed that the normal-coordinate transformation serves to uncouple the damping forces in the same way that it uncouples the inertia and elastic forces. In the following sections, we are going to consider the conditions under which this uncoupling occurs.

6.3. Conditions for Uncoupling of Damping Forces

Considering the analysis of systems in which damping effects cannot be neglected, we still would like to deal with decoupled equilibrium equations (eq. (6.6)) merely to be able to use essentially the same computational procedure, whether damping effects are included or neglected. In general, the damping matrix [c] cannot be constructed from element damping matrices, such as the mass and stiffness matrices, and its purpose is to approximate the overall energy dissipation during the system response.

6.3.1. Evaluation of the Damping Matrix for Any Set of Specified Modal Damping Ratios

In principle, the procedure can be explained by considering the complete diagonal matrix of the damping coefficients, which may be obtained by premultiplying and postmultiplying the damping

ORIGINAL PAGE IS
OF POOR QUALITY

matrix by the scaled modal matrix

$$[C_s] = [\Phi]^T [c] [\Phi] = \begin{bmatrix} 2\zeta_1\omega_1 & 0 & . & . & . & . & 0 \\ 0 & 2\zeta_2\omega_2 & . & . & . & . & 0 \\ & & & . & & & \\ & & & & . & & \\ & & & & & . & \\ 0 & 0 & . & . & . & & 2\zeta_n\omega_n \end{bmatrix}. \tag{6.8}$$

It is evident that the damping matrix [c] may be evaluated by postmultiplying eq. (6.8) by the inverse of the scaled modal matrix and its inverse, such that

$$[c] = [\Phi]^{-T} [C_s] [\Phi]^{-1}. \tag{6.9}$$

Therefore, for any specified set of modal damping ratios $\{\zeta\}$, matrix $[C_s]$ can be evaluated from eq. (6.8), and the full damping matrix [c] from eq. (6.9). However, in practice, the inversion of the modal matrix is a large computational effort. In Chapter 5, we proved that

$$[\Phi]^{-1} = [\Phi]^T [m]. \tag{6.10}$$

Substituting eq. (6.10) into eq. (6.9), we obtain

$$[c] = [m] [\Phi] [C_s] [\Phi]^T [m]. \tag{6.11}$$

Since, in the r-th mode, $C_{sr} = 2\zeta_r\omega_r$, substituting this expression into eq. (6.11), we have

$$[c] = [m] \left[\sum_{r=1}^{n} q\zeta_r\omega_r \{\Phi_r\}\{\Phi_r\}^T \right] [m]. \tag{6.12}$$

The damping matrix [c] obtained in eq. (6.12) will satisfy the orthogonality property; therefore, the damping term in the differential

equation (eq. (6.1)) will be uncoupled with the same transformation (eq. (6.4)), which serves to uncouple the inertial and elastic forces.

It is of interest to note in eq. (6.12) that the contribution to the damping matrix of each mode is proportional to the modal damping ratio; any undamped mode will contribute nothing to the damping matrix. As mentioned previously, the modal damping ratios are the most effective measures of the damping in the system when the modal analysis is carried out.

6.3.2. Defining a System Damping Matrix Using Rayleigh Proportional Damping

The mode superposition analysis is particularly effective if it can be assumed that the damping is proportional in the following manner:

$$\{\Phi_i\}^T [c] \{\Phi_j\} = [2\omega_i \zeta_i] \delta_{ij} \tag{6.13}$$

where ζ_i is a modal damping ratio and δ_{ij} is the Kronecker delta ($\delta_{ij} = 1$ for $i = j$, $\delta_{ij} = 0$ for $i \neq j$). Using eq. (6.13), it is assumed that the eigenvectors $\{\Phi_i\}$, $i = 1,2,3,\ldots, n$, are also $[c]$-orthogonal.

In considering the implications of using eq. (6.13) to take account of damping effects, the following observations can be made. Firstly, the assumption in eq. (6.13) means that the total damping in the structure is the sum of individual damping in each mode. In fact, the ability to measure values for the damping ratios ζ_i, and thus approximate in many cases and in a realistic manner

the damping behavior of the complete structural system, is an important consideration. A second observation relating to the mode superposition analysis is that for the numerical solution of eq. (6.6) using the decoupled equations, we do not calculate the damping matrix [c], but only the stiffness and mass matrices, [k] and [m].

As discussed, damping effects can readily be taken into account in mode superposition analysis provided that eq. (6.13) is satisfied. Rayleigh damping can be assumed to be of the form

$$[c] = a_0[m] + a_1[k] \tag{6.14}$$

where a_0 and a_1 are constants to be determined from two given damping ratios that correspond to the two unequal frequencies of vibration. Applying the orthogonality condition to eq. (6.14), that is, premultiplying both sides of this equation by the transpose of the r-th mode $\{\Phi_r\}^T$ and postmultiplying by the modal matrix $[\Phi]$, we obtain

$$\{\Phi_r\}^T[c][\Phi] = a_0\{\Phi_r\}^T[m][\Phi] + a_1\{\Phi_r\}^T[k][\Phi]. \tag{6.15}$$

The orthogonality conditions (eq. (5.30)) reduce eq. (6.15) to

$$\{\Phi_r\}^T[c][\Phi] = a_0\{\Phi_r\}^T[c]\{\Phi_r\} + a_1\{\Phi_r\}^T[k]\{\Phi_r\}. \tag{6.16}$$

Using eqs. (5.43a) and (5.44), eq. (6.16) is reduced to

$$\{\Phi_r\}^T[c][\Phi] = a_0 + a_1\omega_r^2 \tag{6.17}$$

which shows that when the damping matrix is of the form of eq. (6.14), the damping forces are also uncoupled with the transformation (eq. (6.15)). However, it can also be shown that there are other matrices formed from the mass and stiffness matrices which also

satisfy the orthogonality condition.

In general, a damping matrix that satisfies the relation presented in eq. (6.13) is obtained using the Coughey series:

$$[c] = [m] \sum_{x=0}^{p-1} a_\lambda \{[m]^{-1}[k]\}^\lambda \tag{6.18}$$

where the coefficients a_λ, $\lambda = 1,2,3,\ldots,p$, are calculated from the p simultaneous equations:

$$\zeta_i = \frac{1}{2}\left[\frac{a_0}{\omega_i} + a_1\omega_i + a_2\omega_i^{\,3} + \ldots + a_{p-1}\omega_i^{\,2p-3}\right] \quad i = 1,2,3,\ldots,p. \tag{6.19}$$

We note that with $p = 2$, eq. (6.18) is reduced to Rayleigh damping as presented in eq. (6.14). An important observation is that if $p > 2$, the damping matrix [c] in eq. (6.18) is, in general, a full matrix. Since the cost of analysis is increased by a very significant amount if the damping matrix is not banded, in most practical analysis, Rayleigh damping is assumed. In practice, reasonable Rayleigh coefficients in the analysis of a specific structure may often be selected using available information on the damping from a conducted vibration test or on the damping characteristics of a typical similar structure, i.e., approximately the same a_0 and a_1 values are used in the analysis of similar structures.

By taking two terms corresponding to $k = 0$ and $k = 1$ in eq. (6.18), it is possible to compute the damping coefficients necessary to provide uncoupling of a system having any desired damping ratios in any specified number of modes. For any mode r, the modal

ORIGINAL PAGE IS
OF POOR QUALITY

damping is given as

$$C_r = \{\Phi_r\}[c]\{\Phi_r\} = 2\zeta_r\omega_r. \tag{6.20}$$

If [c] as given by eq. (6.18) is substituted in the expression for C_r, we obtain

$$C_r = \{\Phi_r\}^T[m]\sum_{\lambda=0} a_\lambda\{[m]^{-1}[k]\}^\lambda\{\Phi_r\}. \tag{6.21}$$

Now, using relation $[k]\{\Phi_r\} = \omega_r^2[m]\{\Phi_r\}$ and performing several algebraic operations, we can show that the damping coefficient associated with any mode r may be written as

$$C_r = \sum_\lambda a_\lambda\omega_r^{2\lambda} = 2\zeta_r\omega_r \tag{6.22}$$

from which

$$\zeta_r = \frac{1}{2\omega_r}\sum_\lambda a_\lambda\omega_r^2. \tag{6.23}$$

Equation (6.23) may be used to determine the constant a_λ for any desired values of modal damping ratios corresponding to any specified number of modes. For example, to evaluate these constants specifying the η modal damping ratios, $\zeta_1, \zeta_2, \zeta_3, \ldots, \eta$ we may choose $\lambda = 0, 1,2,3,\ldots,\eta$. Equation (6.23) gives the following system of equations

$$\begin{Bmatrix} \zeta_1 \\ \zeta_2 \\ \zeta_3 \\ \vdots \\ \zeta_\eta \end{Bmatrix} = \frac{1}{2}\begin{bmatrix} \frac{1}{\omega_1} & \omega_1 & \omega_1^3 & \omega_1^5 & \omega_1^7 & \cdots & \omega_1^{\eta+2} \\ \frac{1}{\omega_2} & \omega_2 & \omega_2^3 & \omega_2^5 & \omega_2^7 & & \\ \frac{1}{\omega_3} & \omega_3 & \omega_3^3 & \omega_3^5 & \omega_3^7 & \ddots & \\ \vdots & & & & & & \\ \frac{1}{\omega_\eta} & \cdot & \cdot & \cdot & \cdot & \cdot & \omega_\eta^{\eta+2} \end{bmatrix} \begin{Bmatrix} a_1 \\ a_2 \\ a_3 \\ \vdots \\ a_\eta \end{Bmatrix} \tag{6.24}$$

or, written symbolically,

$$\{\zeta\} = \frac{1}{2}\,[Q_\lambda]\{a\} \qquad (6.25)$$

where $[Q_\lambda]$ is a square matrix having different powers of the natural frequencies. The constants $\{a\}$ could be obtained as

$$\{a\} = 2[Q_\lambda]^{-1}\{\zeta\}. \qquad (6.26)$$

Finally, the damping matrix is obtained by the substitution of eq. (6.26) into eq. (6.18).

It is interesting to observe from eq. (6.23) that in the special case when the damping matrix is proportional to the mass $[c] = a_0[M]$, $(i = 0)$, the damping ratios are inversely proportional to the natural frequencies; thus, the higher modes of the structures will be given very little damping. Analogously, when the damping is proportional to the stiffness matrix ($[c] = a_1[k]$), the damping ratios are directly proportional to the corresponding natural frequencies, as can be seen in eq. (6.23) when $i = 1$. In this case, the higher modes of the structure will be very heavily damped.

Rayleigh coefficients are to a large extent determined by the energy dissipation characteristics of the structural materials. In the above discussion, we assumed that the damping characteristics of the structure can be represented appropriately using proportional damping, either in a mode superposition analysis or in a direct integration procedure. In many analyses, the assumption of proportional damping (i.e., that eq. (6.13) is satisfied) is adequate. In analysis of a structure with widely varying material characteristics, nonproportional damping may need to be used.

We should mention at this point the circumstances under which it will be desirable to evaluate the elements of the damping matrix, as in eqs. (6.21) or (6.18). It has been stated that absolute structural damping is a rather difficult quantity to determine or even to estimate. However, modal damping ratios may be roughly estimated on the basis of past experience. This past experience indicates that values for the modal damping ratios in structures are generally in the range of 2% to 10%, probably not exceeding 20%. In other words, on this basis, and giving some consideration to the type of structure and materials utilized, we can assign numerical values to the modal damping ratios. The modal damping ratios are then used to determine the damping matrix, which is needed explicitly when dynamic response is obtained by some analytical procedure other than modal analysis, i.e., step-by-step integration of a non-linear system.

6.4. The Dynamic Response of the Damped Multi-Degree-of-Freedom Systems Subjected to Harmonic Forces

In Chapter 5 we gave a very detailed treatment of the dynamic response of an undamped multi-degree-of-freedom system subjected to harmonic forces. In this section we are going to consider the damped MDOF system. The general response of a discrete system, i.e., the response to both initial and external excitations, is governed by a set of simultaneous coupled equations. This set can be uncoupled by means of linear transformation that can be represented by the matrix of the system eigenvectors. The decoupling procedure itself is known as modal analysis, since the eigenvector matrix is referred to

as a modal matrix. We assume the proportional damping of the system; in this case, the classical modal matrix does uncouple the equations of motion. We will consider in detail the circumstances under which the decoupling of damping forces is possible.

Again, the system is going to be subjected to a periodic forcing function, which may be expanded into a Fourier Series whose terms are sine and cosine functions of successive multiples of the fundamental frequency, as shown in eq. (5.62). The coefficients of a series are given by eqs. (5.63) and (5.64). The response of the system is then obtained as the superposition of the response for each term of the Fourier expansion of the exciting function. This function is given by eq. (5.65). The equations of motion of an n-degree-of-freedom system can be written in a matrix form as:

$$[m]\{\ddot{x}(t)\} + [c]\{\dot{x}(t)\} + [k]\{\ (t)\} = \{F(t)\} = \frac{1}{2}\{F_0\} + \{F_{0r}\}e^{j(\omega_f t+\psi)} . \tag{6.27}$$

Quantities $\{F_{0r}\}$ and ψ are defined by eqs. (5.66a) and (5.67). Introducing the linear transformation matrices using the scaled modal matrix $[\Phi]$, we have

$$\begin{aligned} \{x(t)\} &= [\Phi]\{q(t)\} \\ \{\dot{x}(t)\} &= [\Phi]\{\dot{q}(t)\} \\ \{\ddot{x}(t)\} &= [\Phi]\{\ddot{q}(t)\}. \end{aligned} \tag{6.28}$$

In a previous section, we showed the orthogonality conditions for two modes, ω_s and ω_r, $\omega_s \neq \omega_r$, can be written as follows:

ORIGINAL PAGE IS
OF POOR QUALITY

$$\{\Phi_s\}^T[m]\{\Phi_r\} = 0 \quad r \neq s \tag{6.29}$$

$$\{\Phi_s\}^T[c]\{\Phi_r\} = 0 \quad r \neq s$$

$$\{\Phi_s\}^T[k]\{\Phi_r\} = 0 \quad r \neq s. \tag{6.30}$$

Substituting equations (6.29) and (6.30) into eq. (6.27), we have

$$[m][\Phi]\{\ddot{q}(t)\} + [c][\Phi]\{\dot{q}(t)\} + [k][\Phi]\{q(t)\} =$$
$$= \{F(t)\} = \frac{1}{2}\{F_0\} + \{F_{0r}\}e^{j(\omega_f t+\psi)}. \tag{6.31}$$

Premultiplying eq. (6.31) by $[\Phi]^T$, we have

$$[\Phi]^T[m][\Phi]\{\ddot{q}(t)\} + [\Phi]^T[c][\Phi]\{\dot{q}(t)\} + [\Phi]^T[k][\Phi]\{q(t)\} =$$
$$= \frac{1}{2}[\Phi]^T\{F_0\} + [\Phi]^T\{F_{0r}\}e^{(j\omega_f t+\psi)}. \tag{6.32}$$

Using the orthogonality relations derived in a previous section, eqs. (6.32) are reduced to

$$[I]\{\ddot{q}(t)\} + [2\zeta\omega]\{\dot{q}(t)\} + [\omega^2]\{q(t)\} =$$
$$= \frac{1}{2}[\Phi]^T\{F_0\} + [\Phi]^T\{F_{0r}\}e^{j(\omega_f t+\psi)}. \tag{6.33}$$

The n equations above are decoupled into n independent equations. The terms on the right-hand side represent the so-called scaled modal force. The equation of motion in the r-th mode, due to the exciting forces lumped at all masses having arbitrarily distributed amplitudes, evolves from eq. (6.33) as

$$\ddot{q}_r(t) + 2\zeta_r\omega_r\dot{q}_t(t) + \omega_r^2 q_r(t) =$$
$$= \frac{1}{2}\{\Phi_r\}^T\{F_0\} + \{\Phi_r\}^T\{F_{0r}\}e^{j(\omega_f t+\psi_r)}. \tag{6.34}$$

ORIGINAL PAGE IS
OF POOR QUALITY

The general solution of equation (6.34) can be written as

$$q_r(t) = (q_r(t))_h + (q_r(t))_p. \tag{6.35}$$

The homogenous solution is

$$(q_r(t))_h = e^{-\zeta\omega_r t}[C_r\cos\omega_{dr}t + D_r\sin\omega_{dr}t]. \tag{6.36}$$

The particular solution is composed of two components:

$$(q_r(t))_p = (q_r(t))_{p1} + (q_r(t))_{p2}. \tag{6.37}$$

We assume the following type of solution:

$$(q_r(t))_{p1} = C. \tag{6.38}$$

Substituting eq. (6.38) into eq. (6.34) and omitting the second term on the right-hand side of the latter equation, we have

$$(q_r(t))_{p1} = \frac{1.0}{2\omega_r^2}\{\Phi_r\}^T\{F_0\}, \tag{6.39}$$

$$(q_r(t))_{p2} = Q_r e^{j(\omega_f t+\psi_r)}, \tag{6.40}$$

$$(q_r(t))_{p2} = j\omega_f Q e^{j(\omega_f t+\psi_r)}, \tag{6.41}$$

$$(q_r(t))_{p2} = -\omega_f^2 Q e^{j(\omega_f t+\psi_r)}. \tag{6.42}$$

Substituting eqs. (6.40), (6.41), and (6.42) into eq. (6.43) and omitting the first term on the right-hand side of the latter equation we have,

$$\{q_r(t)\}_{p2} = \frac{\{\Phi_r\}^T\{F_{0r}\}}{\omega_r^2-\omega_f+j2\zeta_r\zeta_f\omega_r} e^{j(\omega_f t+\psi_r)} . \tag{6.43}$$

Rewriting the complex number in equation (6.43) in terms of the magnitude and phase angle, eq. (6.43) becomes

$$\{q_r(t)\}_{p2} = \frac{\{\Phi_r\}^T\{F_{0r}\}e^{j(\omega_f t+\psi_r)}}{\sqrt{(\omega_r^2-\omega_f^2)+(2\zeta_r\omega_f\omega_r)^2}e^{j\delta_r}} ,$$

or,

$$\{q_r(t)\}_{p2} = \frac{\{\Phi_r\}^T\{F_{0r}\}e^{j(\omega_f t+\psi_r-\delta_r)}}{\sqrt{(\omega_r^2-\omega_f^2)^2+(2\zeta_r\omega_f\omega_r)^2}}, \tag{6.44}$$

where

$$\delta_r = \arctan\left[\frac{2\zeta_r\omega_f\omega_r}{\omega_r^2-\omega_f^2}\right]. \tag{6.45}$$

Let $\psi_r-\delta_r = \theta_r$. Then eq. (6.44) is reduced to

$$(q_r(t))_{p2} = \frac{\{\Phi_r\}^T\{F_{0r}\}e^{j(\omega_f t+\psi_r)}}{\sqrt{(\omega_r^2-\omega_f^2)^2+(2\zeta_r\omega_f\omega_r)^2}}.$$

The general solution for the r-th mode can be written as

$$q_r(t) = e^{-\zeta_r\omega_r t}[C_r\cos\omega_{dr}t + D_r\sin\omega_{dr}t] + \frac{1}{2\omega_r^2}\{\Phi_r\}^T\{F_0\} + \\ + \frac{\{\Phi_r\}^T\{F_{0r}\}e^{j(\omega_f t+\theta_r)}}{\sqrt{\omega_r^2-\omega_f^2)+(2\zeta_r\omega_f\omega_r)^2}} . \tag{6.46}$$

The equation above can be rewritten for a very general case as

$$\{q_r(t)\} = \sum_{r=1}^{n} e^{-\zeta_r \omega_r t}[C_r \cos\omega_{dr} t + D_r \sin\omega_{dr} t] + \sum_{r=1}^{n} \frac{1}{2\omega_r^2}\{\Phi_r\}^T\{F_0\} +$$

$$+ \sum_{r=1}^{n} \frac{\{\Phi_r\}^T\{F_{0r}\}e^{j(\omega_f t+\theta_r)}}{\sqrt{(\omega_r^2-\omega_f^2)^2+(2\zeta_r\omega_f\omega_r)^2}}, \qquad (6.47)$$

or as

$$q_r(t) = e^{-\zeta_r \omega_r t}[C_r \cos\omega_{dr} t + D_r \sin\omega_{dr} t] + \frac{1}{2\omega_r^2}\{\Phi_r\}^T\{F_0\} +$$

$$+ \frac{\{\Phi_r\}^T\{F_{0r}\}e^{j(\omega_f t+\theta_r)}}{\sqrt{(\omega_r^2-\omega_f^2)^2+(2\zeta_r\omega_f\omega_r)^2}}, \quad r = 1,2,3,\ldots,n. \qquad (6.48)$$

For convenience in further calculations, the equation above can be rewritten as

$$\{q_r(t)\} = e^{-\zeta_r \omega_r t}[C_r \cos\omega_{dr} t + D_r \sin\omega_{dr} t] + \frac{1}{2\omega_r^2}[\Phi]^T\{F_0\} +$$

$$+ \frac{[\Phi]^T\{F_{0s}\}\sin(\omega_f t+\theta_r)}{\sqrt{(\omega_r^2-\omega_f^2)^2+(2\zeta_r\omega_r\omega_f)^2}} + \frac{[\Phi]^T\{F_{0c}\}\cos(\omega_f t+\theta_r)}{\sqrt{(\omega_r^2-\omega_f^2)^2+(2\zeta_r\omega_r\omega_f)^2}},$$

$$r = 1,2,3,\ldots,n. \qquad (6.49)$$

where:

$$\{F_{0r}\} = \sqrt{\{F_{0s}{}^2\} + \{F_{0c}\}} \tag{6.50}$$

$$\psi_r = \arctan\left[\frac{F_{0s}}{F_{0c}}\right]_r, \quad r = 1,2,\ldots,n, \tag{6.51}$$

$$\delta_r = \arctan\left[\frac{2\zeta_r\omega_r\omega_f}{\omega_r{}^2-\omega_f{}^2}\right], \quad r = 1,2,\ldots,n, \tag{6.52}$$

and

$$\theta_r = \psi_r - \delta_r, \quad r = 1,2,3,\ldots,n. \tag{6.53}$$

To define the vectors of constants $\{C\}$ and $\{D\}$, we apply the initial conditions given as the vectors of initial displacements and initial velocities $\{x(0)\}$ and $\{\dot{x}(0)\}$. To apply the initial conditions from the original system to a new, transformed system, we use eqs. (5.69) and (5.70) at $t = 0$.

$$\{x(0)\} = [\Phi]\{q(0)\} \tag{6.54}$$

$$\{\dot{x}(0)\} = [\Phi]\{\dot{q}(0)\}. \tag{6.55}$$

From equations (6.54) and (6.55), we have

$$\{q(0)\} = [\Phi]^{-1}\{x(0)\} \tag{6.56}$$

$$\{\dot{q}(0)\} = [\Phi]^{-1}\{\dot{x}(0)\}. \tag{6.57}$$

In order to avoid the inversion of matrix $[\Phi]$, we are using the orthogonality relation derived in Chapter 5

$$[\Phi]^T[m][\Phi] = [I] \tag{6.58}$$

ORIGINAL PAGE IS
OF POOR QUALITY

where [I] is the identity matrix. Postmultiplying equation above by $[\Phi]^{-1}$, we have

$$[\Phi]^{-1} = [\Phi]^T[m]. \tag{6.59}$$

Substituting eq. (6.59) into eqs. (6.56) and (6.57), we have

$$\{q(0)\} = [\Phi]^T[m]\{x(0)\} \tag{6.60}$$

$$\{\dot{q}(0)\} = [\Phi]^T[m]\{\dot{x}(0)\}. \tag{6.61}$$

At the time t = 0, eq. (6.49) reduces to

$$q_r(0) = C_r + \frac{1}{2\omega_r^2}\{\Phi_r\}^T\{F_0\}\frac{\{\Phi_r\}^T\{F_{0s}\}\sin\theta_r}{\sqrt{(\omega_r^2-\omega_f^2)^2+(2\zeta_r\omega_r\omega_f)^2}} +$$

$$+\frac{\{\Phi_r\}^T\{F_{0c}\}\cos\theta_r}{\sqrt{(\omega_r^2-\omega_f^2)^2+(2\zeta_r\omega_r\omega_f)^2}}, \quad r = 1,2,3,\ldots,n. \tag{6.62}$$

Substituting eq. (6.60) into eq. (6.62), we calculate the vector of constants {C}

$$C_r = \{\Phi_r\}^T[m]x_r(0) - \frac{1}{2\omega_r^2}\{\Phi_r\}^T\{F_0\} - \frac{\{\Phi_r\}^T\{F_{0s}\}\sin\theta_r}{\sqrt{(\omega_r^2-\omega_f^2)^2+(2\zeta_r\omega_r\omega_f)^2}} -$$

$$-\frac{\{\Phi_r\}^T\{F_{0c}\}\cos\theta_r}{\sqrt{(\omega_r^2-\omega_f^2)^2+(2\zeta_r\omega_r\omega_f)^2}}, \quad r = 1,2,3,\ldots,n. \tag{6.63}$$

Finding the first derivative of eq. (6.49), we have

ORIGINAL PAGE IS
OF POOR QUALITY

$$\{\dot{q}_r(t)\} = -\zeta_r\omega_r e^{-\zeta_r\omega_r t}[C_r\cos\omega_{dr}t + D_r\sin\omega_{dr}t] +$$

$$+ e^{-\zeta_r\omega_r t}[-C_r\omega_{dr}\sin\omega_{dr}t + D_r\omega_{dr}\cos\omega_{dr}t] +$$

$$+ \frac{\omega_f\{\Phi_r\}^T\{F_{0s}\}\cos(\omega_f t+\theta_r)}{\sqrt{(\omega_r^2-\omega_f^2)^2+(2\zeta_r\omega_r\omega_f)^2}} - \frac{\omega_f\{\Phi_r\}^T\{F_{0c}\}\sin(\omega_f t+\theta_r)}{\sqrt{(\omega_r^2-\omega_f^2)^2+(2\zeta_r\omega_r\omega_f)^2}},$$

$$r = 1,2,3,\ldots,n. \tag{6.64}$$

At time $t = 0$, eq. (6.64) becomes

$$\{\dot{q}_r(0)\} = -\zeta_r\omega_r C_r + D_r\omega_{dr} + \frac{\omega_f\{\Phi_r\}^T\{F_{0s}\}\cos\theta_r}{\sqrt{(\omega_r^2-\omega_f^2)^2+(2\zeta_r\omega_r\omega_f)^2}} -$$

$$- \frac{\omega_f\{\Phi_r\}^T\{F_{0c}\}\sin\theta_r}{\sqrt{(\omega_r^2-\omega_f^2)^2+(2\zeta_r\omega_r\omega_f)^2}}, \quad r = 1,2,3,\ldots,n. \tag{6.65}$$

Substituting eq. (6.62) into eq. (6.65), we calculate the vector of constants D_r, and in a similar manner, we calculate the vector of constants C_r:

$$D_r = \frac{1}{\omega_{dr}}\left[\{\Phi_r\}^T[m]\dot{x}_r(0) - \zeta_r\omega_r C_r - \frac{\omega_t\{\Phi_r\}^T\{F_{0s}\}\cos\theta_r}{\sqrt{(\omega_r^2-\omega_f^2)^2+(2\zeta_r\omega_r\omega_f)^2}} + \right.$$

$$\left. + \frac{\omega_f\{\Phi_r\}^T\{F_{0c}\}\sin\theta_r}{\sqrt{(\omega_r^2-\omega_f^2)^2+(2\zeta_r\omega_r\omega_f)^2}}\right], \quad r = 1,2,3,\ldots,n. \tag{6.66}$$

The vector C_r is defined by eq. (6.63). Now we can find the complete solution vector of the transformed system $\{q(t)\}$. Finally, the displacements of masses are obtained by superposition of the response in each mode

$$\{x(t)\} = [\Phi]\{q(t)\}. \tag{6.67}$$

Very often, only the steady state response of eq. (6.49) is of interest to us. For this case, $x_r(0) = 0$, and $\dot{x}_r(0) = 0$, $r = 1,2,3,\ldots,$ n, and eq. (6.49) is reduced to only the particular solution,

$$q_r(t) = \frac{1}{2\omega_r^2}\{\Phi_r\}^T\{F_0\} + \frac{\{\Phi_r\}^T\{F_{0s}\}\sin(\omega_f t+\theta_r)}{\sqrt{(\omega_r^2-\omega_f^2)^2+(2\zeta_r\omega_r\omega_f^2)^2}} +$$

$$+ \frac{\{\Phi_r\}^T\{F_{0c}\}\cos(\omega_f t+\theta_r)}{\sqrt{(\omega_r^2-\omega_f^2)^2+(2\zeta_r\omega_r\omega_f)^2}}, \quad r = 1,2,3,\ldots,n. \tag{6.68}$$

The vector of phase angles between the harmonic forcing-function vectors and the displacement vectors, δ_r, $r = 1,2,3,\ldots,n$, is given by eq. (5.62). The modal amplitudes of sine and cosine forcing functions are given as

$$(Q_s)_r = \frac{\{\Phi_r\}^T\{F_{0s}\}\sin(\omega_f t+\theta_r)}{\sqrt{(\omega_r^2-\omega_f^2)^2+(2\zeta_r\omega_r\omega_f)^2}}, \quad r = 1,2,3,\ldots,n, \tag{6.69}$$

and

ORIGINAL PAGE IS
OF POOR QUALITY

$$(Q_c)_r = \frac{\{\Phi_r\}T\{F_{0s}\}\cos(\omega_f t+\theta_r)}{\sqrt{(\omega_r^2-\omega_f^2)^2+(2\zeta_r\omega_r\omega_f)^2}}, \quad r = 1,2,3,\ldots,n. \qquad (6.70)$$

The dynamic amplification factor in a mode is defined by the analogy for single-degree-of-freedom system, given in Appendix A. The vector of the dynamic magnification factors in modes is defined as the ratios of the steady-state modal amplitude Q_r to the vector of the static modal deflections $(Q_r)_{st}$:

$$D_{qr} = \frac{Q_r}{(Q_r)_{st}}, \quad r = 1,2,3,\ldots n. \qquad (6.71)$$

The quantity above is usually given for a particular component of a harmonic forcing function. The response due to a sine forcing function in eq. (6.68) can be written in terms of modal amplitude:

$$q_r(t) = Q_r\sin(\omega_f t + \theta_r), \quad r = 1,2,3,\ldots,n,$$

where Q_r is the vector of modal amplitudes of the sine function, written as,

$$\theta_r = \frac{\{\Phi_r\}^T\{F_{0s}\}\sin\theta_r}{\sqrt{(\omega_r^2-\omega_f^2)^2+(2\zeta_r\omega_r\omega_f)^2}}, \quad r = 1,2,3,\ldots,n \qquad (6.72)$$

Observing eq. (6.34), the static displacement at the r-th mode is

$$(q_r)_{st} = \frac{1}{\omega_r}\left[\frac{1}{2}\{\Phi_r\}^T\{F_0\} + \{\Phi_r\}^T\{F_{0s}\}\sin\psi_r + \{\Phi_r\}^T\{F_{0c}\}\cos\psi_r\right]. \qquad (6.73)$$

ORIGINAL PAGE IS
OF POOR QUALITY

We can expand equation (6.73) for a very general case:

$$(q_r)_{st} = \frac{1}{\omega_r^2}\left[\frac{1}{2}[\Phi_r]^T\{F_0\} + \{\Phi_r\}^T\{F_{0s}\}\sin\psi_r + \{\Phi_r\}^T\{F_{0c}\}\cos\psi_r\right],$$

$$r = 1,2,3,\ldots,n. \tag{6.74}$$

The maximum dynamic steady-state displacement from eq. (6.68) is

$$Q_r = \frac{1}{2\omega_r^2}\{Q_r\}^T\{F_0\} + \frac{\{\Phi_r\}^T\{F_{0c}\}}{\sqrt{(\omega_r^2-\omega_f^2)^2+(2\zeta_r\omega_r\omega_f)^2}},$$

$$r = 1,2,3,\ldots,n. \tag{6.75}$$

The dynamic magnification factor in a mode is

$$D_r = \frac{(q_r)_{st}}{Q_r},\ r = 1,2,3,\ldots,n. \tag{6.76}$$

As a very important characteristic of the system, the damping in a mode can be defined by one of several methods given in Appendix A for a damped single-degree-of-freedom system. Amount of damping in a mode is usually determined by measurement for a particular structure or by analogy with the damping of a similar structure. To define the damping in a mode, eq. (6.34) can be set for a free vibration:

$$\ddot{q}_r(t) = 2\zeta_r\omega_r\dot{q}_r(t) + \omega_r^2 q = 0,\ r = 1,2,3,\ldots,n. \tag{6.77}$$

Letting $q_r(t) = A_r e^{pt}$, eq. (6.77) becomes

$$[p^2 + 2\zeta_r\omega_r p + \omega_r^2]A_r e^{pt} = 0.$$

ORIGINAL PAGE IS
OF POOR QUALITY

Solving the equation above, we have

$$p_{1,2} = -\zeta_r\omega_r \pm \frac{1}{2}\sqrt{4\zeta_r^{\,2}\omega_r^{\,2} - 4\omega_r^{\,2}}\ , \quad r = 1,2,3,\ldots,n. \tag{6.78}$$

We concluded in Appendix A, that transition between the imaginary and real roots of the characteristic equation (eq. (6.78)) occurs when

$$4\zeta_r^{\,2}\omega_r^{\,2} = 4\omega_r^{\,2}, \tag{6.79}$$

or

$$\zeta_r = 1.0,$$

where ζ_r is the ratio of the actual damping in the r-th mode to the critical damping in the r-th mode

$$\zeta_r = \frac{C_r}{(C_{cr})_r}\ . \tag{6.80}$$

From eq. (6.79), the critical damping in the r-th mode is

$$(C_{cr})_r = 2\omega_r. \tag{6.81}$$

The actual damping in the r-th mode is

$$C_r = 2\zeta_r\omega_r, \tag{6.82}$$

or, for a very general case,

$$(C_{cr})_r = 2\omega_r,\ r = 1,2,3,\ldots,n, \tag{6.83}$$

and

$$C_r = 2\zeta_r\omega_r,\ r = 1,2,3,\ldots,n. \tag{6.84}$$

Again, by the analogy given in Appendix A, the vibration in a mode is conventionally classified with respect to the degree of damping as

1. Critically damped when $\zeta_r = 1.0$,
2. Overdamped when $\zeta_r > 1.0$,
3. Underdamped when $\zeta_r < 1.0$.

In previous derivations we assumed that we had an underdamped case or oscillatory motion, which is the only case of interest in engineering application.

Once more, the same question arises regarding how many modes we must take in order to have the solution accurate enough for an engineering analysis. Since, for the dynamic cases, inertial forces of the system are very important, we usually want to know how well we model our system dynamically. Since we usually discretize the system in modal analysis, a very good indication of amount of mass taken into consideration is "the effective modal mass." For the r-th mode, this quantity is defined as

$$(M_{eff})_r = \frac{\{1\}^T m \{\Phi_r\}\{\Phi_r\}^T [m] \{1\}}{M_r}, \quad r = 1,2,3,\ldots,n, \qquad (6.85)$$

or, in a summation form,

$$(M_{eff})_r = \frac{\left[\sum_{i=1}^{n} m_i \Phi_{ir}\right]^2}{\sum_{i=1}^{n} m_i \Phi_{ir}^2}, \quad r = 1,2,3,\ldots,n. \qquad (6.86)$$

Where m_i is the mass at the i-th point, $\{1\}^T$ is a row matrix of ones, and M_r is the modal mass in the r-th mode defined by

$$M_r = \sum_{i=1}^{n} m_i \Phi_{ir}^{\ 2}, \quad r = 1,2,3,\ldots,n. \tag{6.87}$$

A good indication that the inertia forces have been accurately measured in modal analysis is usually that the effective mass is at least 95% of the actual mass of the system. Since the modal parameters for higher modes cannot be calculated correctly, inclusion of higher modes usually does little to increase the accuracy of the calculation. For structural systems with homogenous material characteristics, the first several modes are most often enough to calculate the dynamic response of the system.

Chapter 7

MODAL ANALYSIS PERFORMED ON FIVE BLADE MODELS USING A NICOLET 660A DUAL-CHANNEL FFT ANALYZER

7.1. Introduction

In the previous chapter, we discussed the concepts which have to be considered during modal testing using FFT analyzers. In this chapter, we are going to give a brief description of how to conduct the modal testing properly using a Nicolet 660A Dual-Channel FFT Analyzer when impulsive excitation is chosen. Selection and calibration of the impact hammer will also be discussed, and the results of testing performed on five models will be presented.

7.2. An Experimental Technique

Impulsive testing utilizes short-duration transient force inputs (with corresponding broadband spectra) to excite all frequencies in the structure simultaneously for a chosen frequency range. Modern measurement instrumentation (such as the Nicolet 660A) is fully capable of performing the modal analysis when the impulsive excitation is used.

Impulsive testing is normally conducted using some form of an instrumented hammer. A force transducer is mounted on the head of the hammer, and measures the force input to the structure. An accelerometer is used to measure the response of the structure. By far the most popular technique for impulsive excitation is to mount an accelerometer at a fixed location and excite the structure at a multiplicity of locations, using a hammer with a force transducer on its

face to impulse the system at many locations. The data are analyzed with a dual-channel FFT analyzer, using the impulse force as a transient capture trigger condition. These two transient time histories are Fourier-transformed to yield the input and output spectra. The resultant ratio of the output and input spectra is the desired frequency-response function.

Usually, the results of several transient excitations are ensemble-averaged. Then the signals are Fourier-transformed and the transfer function is displayed on the screen of the analyzer. The impulse hammer (excitation system) with sensitivity S_a(mV/lb) is attached to channel A of the FFT analyzer. The accelerometer (response transducer), with a sensitivity of S_b(mV/g), is attached to channel B of the analyzer. Based upon a preliminary examination of the structure, the input attenuator of channel A is set to a full-scale value of F_a, and the input attenuator of channel B is set to a level of F_b. The levels of F_a and F_b can only be obtained by trial measurements on the structure.

The structure to be examined is marked at M spacial locations. The response transducer (accelerometer) is fastened to the structure at one location. This transducer should be located in a local "hot spot" so that it will be capable of responding to all modes. Starting from the response-transducer location, the structure is impacted a number of times at each spatial location. Each spatial location is impacted until the coherence function (a function which indicates the validity of the transfer function) approaches unity across the selected frequency-analysis range. The first impact will always produce a coherence function equal to unity. It is essential that each

location is impacted more than once, so that the coherence function may be used as a valid indicator of the quality of acquired data. The first impact point is of particular importance.

A complete description of a mode contains four pieces of information. At the n-th mode:

1. Natural frequency of the n-th mode (f_n),
2. Amplification factor of the n-th mode (Q_n),
3. "Weight" of the n-th mode; an indication of how much structural mass is in motion in the n-th mode (W_n),
4. Motion of the m-th location in the n-th mode ($\phi_{m,n}$).

Within a given frequency range, N resonances may exist. Hence, n ranges from 1 to N. If M locations within the structure are measured, then m ranges from 1 to M. Each of the N mode shapes may be normalized so that the maximum displacement (for example, at the p-th location) is equal to one unit. The choice of mode shape normalization affects the modal weight W_n. The modal weight is defined by the summation

$$W_n = \sum_{m=1}^{M} W_m (\phi_{m,n})^2 \qquad (7.1)$$

where W_m is the physical weight at the m-th location.

At the first impact point, both input and response readings are made at the same spacial location. The input/output relationships associated with this spacial location are used as a guide to interpret all subsequent measurements. The resonant frequencies of a structure are independent of the spacial location from which they are measured. The resonant frequencies of N modes are detected

by identifying the N peaks in the imaginary part of the displayed transfer function. The quality factor Q's of the N modes are measured using information from the displayed real part of transfer function, and are defined as

$$Q_n = \frac{1}{2\zeta_n} = \frac{(f_a/f_b)_n^2 + 1}{(f_a/f_b)_n^2 - 1} \tag{7.2}$$

where

f_a = frequency above resonance, where the real part of the transfer function reaches a peak,

and

f_b = frequency below resonance, where the real part of the transfer function reaches a peak of opposite sign.

We showed in section 7.4.3 that the quality factor in a mode is directly related to the amount of damping in a mode. The first measured transfer function identifies the parameter f_n and Q_n over the range of $1 \leq n \leq N$.

Mode shapes can be estimated directly from frequency-response functions. The mode shape is estimated by measuring quadrature (imaginary) response values from all of the measured transfer functions at each resonant frequency. At each of these frequencies, the quadrature components of the response functions are distributed in proportion to the displacement at each of the measured locations throughout the structure. That is, they are distributed in an approximation of the mode shape associated with that resonance.

The imaginary values from the driving-point transfer function at each of the N resonances should be measured and retained to normalize

subsequent data. The N quadrature points, $IMAG_{bb}(f_n)$, must be retained. The driving-point location, a, is subsequently moved through the sequence of predefined spatial locations. At each of the M locations, the imaginary part of the transfer function is measured at the N preselected resonant frequencies. The quadrature values, $IMAG_{a,b}(f_a)$, are measured and retained for all values between 1 and M and all values of n between 1 and N.

If all measurements can be acquired without changing the input attenuators of channel A or channel B, then a single scale factor is sufficient to relate physical and electrical units. The constant, k_c, may be retained where

$$k_c = -S_b F_a / S_a F_b. \tag{7.3}$$

The coefficient, k_c, relates the voltage gain measured by the analyzer to physical measurements in the structure. If the imaginary part of the transfer function, $IMAG_{ab}(f_n)$, is read at the n-th resonant frequency, it is related to the physical parameters of the system by the equation

$$IMAG_{a,b}(f_n) = \frac{k_c Q_n \phi_{a,n} \phi_{b,n}}{W_n}. \tag{7.4}$$

At any frequency, f_n, the stored quadrature components, $IMAG_{a,b}(f_n)$, will have a local minimum occurring at some special location a = p. The components $IMAG_{p,b}(f_n)$ are of particular importance. These are used to compute the "weight" of each mode and to normalize the retained quadrature components from each mode to arrive at the spatial vectors $\phi_{a,n}$:

$$W_n = \frac{k_c Q_n IMAG_{bb}(f_n)}{IMAG^2_{p,b}(f_n)} \tag{7.5}$$

$$\phi_{a,n} = \frac{IMAG_{a,b}(f_n)}{IMAG_{p,b}(f_n)} . \tag{7.6}$$

These shape functions are approximations, because the measured shape (in response to a single-point excitation) is actually a linear summation of all of the mode shapes of the system. If the resonances are broadly spaced in frequency and high "Q" in nature (Q = 5 or greater), then the interaction between the modes is minimal and the distortion of any given mode shape by contribution from other modes is not significant.

7.3. Calibration of an Impact Hammer

An impact hammer of 12.5 [lb] equipped with a light Teflon tip and the Kistler Instrument Quartz Force Transducer Model 901A-903 were selected, and the force transducer output was fed directly to channel A of a Nicolet 660A Dual-Channel FFT analyzer. In Fig. 7.1, the FFT analyzer and impact hammer kit (impact tips and weight extenders) are shown. Preliminary testing on models showed that an impact hammer with a light Teflon tip and without weight extenders was enough to excite all frequencies in a frequency range of 0-2 KHz for all five models. A freely supported mass of 10.437 [lb] (steel cylinder) was impacted. An Endevco Piezoelectronic Accelerometer, Model 2233, was mounted at the center of one face of a steel cylinder of an impact hammer and the Teflon tip at the center of the opposite side was used as an impact surface. (The mass was impacted through the center of gravity.) A piezoelectric accelerometer is a self-

ORIGINAL PAGE IS
OF POOR QUALITY

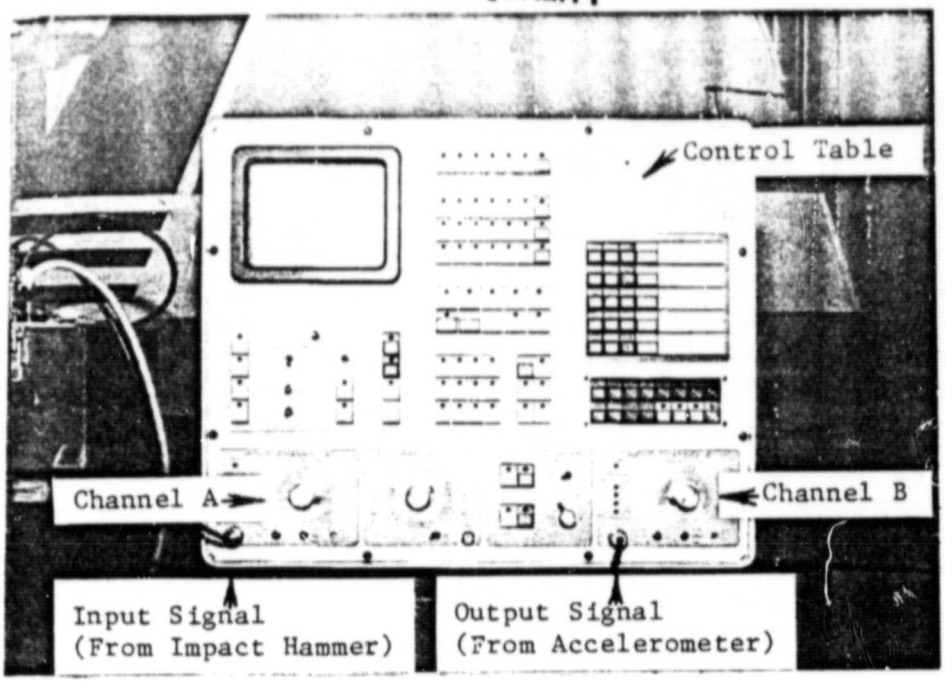

(a)

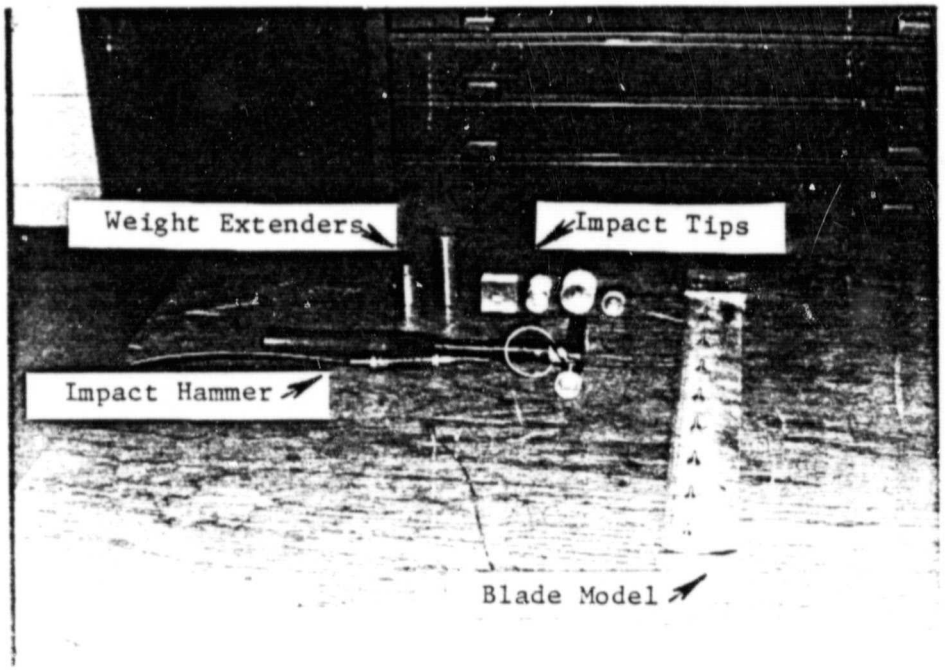

(b)

Figure 7.1 (a) The control table of the Nicolet 660A Dual-Channel FFT Analyzer; (b) The impact hammer kit (hammer, impact tips, and extenders).

generating transducer which generates an electrical output signal that is proportional to its acceleration. An Endevco Input Amplifier, Model 2614B, with an amplification of 10 was used to amplify the signal generated by the accelerometer. This signal was fed to channel B of the FFT analyzer. The whole calibration was performed in a frequency domain of 0-2 KHz.

An ensemble average of a number of impacts was done, and the calibration factor was calculated in the following manner:

The unitless constant k was calculated as:

$$k_c = \frac{F(\omega)}{A(\omega)}$$

$$k_c = \frac{6950.65}{486.73} = 14.296 \qquad (7.6)$$

$$k_c = 14.296$$

where

$F(\omega)$ is the average value of the Fourier-transformed force signal in a frequency range of 0-2 KHz,

$A(\omega)$ is the average value of the Fourier-transformed acceleration signal in a frequency range of 0-2 KHz.

The mass of an impacted cylinder was calculated as:

$$m_c = \frac{G}{q} = 0.0270 \ [\text{lbsec}^2/\text{in}]. \qquad (7.7)$$

The sensitivity of the accelerometer was

$$E_a = 37.5 \ [\text{mV/g}]. \qquad (7.8)$$

The total sensitivity of an accelerometer in engineering units was found by

$$S_a = \frac{E_a \sqrt{2}/2}{\text{Ampl. Factor}} \; [\text{V/in/sec}^2]. \tag{7.9}$$

The expression above was multiplied by $\frac{\sqrt{2}}{2}$, since the signals were displayed on the screen of FFT by their RMS values.

$$S_a = \frac{37.5\text{x}10^{-3} \text{x} \sqrt{2}/2}{10}$$

$$S_a = 0.686\text{x}10^{-5} \left[\frac{\text{V}}{\text{in/sec}^2}\right] \tag{7.10}$$

This was the total sensitivity of the accelerometer and in-line amplifier with a voltage gain of 10.

The sensitivity of the force transducer was not known. The force transducer system was calculated using eq. (b) derived in Appendix B. The two total sensitivities are related as follows:

$$\frac{F(\omega)}{A(\omega)} = k_c = \frac{m_c S_f}{S_a} \tag{7.11}$$

where

m_c is the mass of an impacted cylinder

and

S_f is the total sensitivity of the force-transducer impact-hammer system.

Thus, from eq. (7.11), we obtain

$$S_f = \frac{k_c S_a g}{G} \; [\text{mV/lb}] \tag{7.12}$$

$$S_f = \frac{14.296 \text{ x } 37.5 \text{ x } 10^{-3} \text{ x } \sqrt{2}/2}{10.437\text{x}10} .$$

Again, eq. (7.12) is multiplied by $\frac{\sqrt{2}}{2}$ to get the values on the screen

in engineering units (zero to peak).

$$S_f = 0.363 \times 10^{-2} \text{ [V/lb]} \tag{7.13}$$

This technique has the added advantage of being able to calibrate an accelerometer and impact hammer as a matched set. If the accelerometer used to measure the response of the suspended mass is the same accelerometer that is used during the modal test, then any error in the accelerometer measurement for the suspended mass will automatically be introduced into the impact hammer calibration. This error will then be eliminated when the ratio of acceleration to force is calculated, since it will be in both the numerator and denominator. Therefore, the accuracy of the calibration of the matched set of transducers depends on the accuracy to which the calibration mass is known. A very good low-frequency calibration can be obtained using this technique. The high-frequency limit is determined by the frequency response of the accelerometer and the mass. Figures 7.2 and 7.3 show the setup for the impact hammer calibration.

7.4. Geometrical and Material Properties of Blade Models

The modal testing was performed on five blade models. Three aluminum blade models had NACA four-digit symmetrical airfoils as their cross-sectional areas. The other two blade models were of aluminum and steel, and had identical rectangular cross-sectional areas and comparable lengths. The problem was to relate the damping of the geometrically identical models made of different materials, and to observe the damping of the models made of the same material

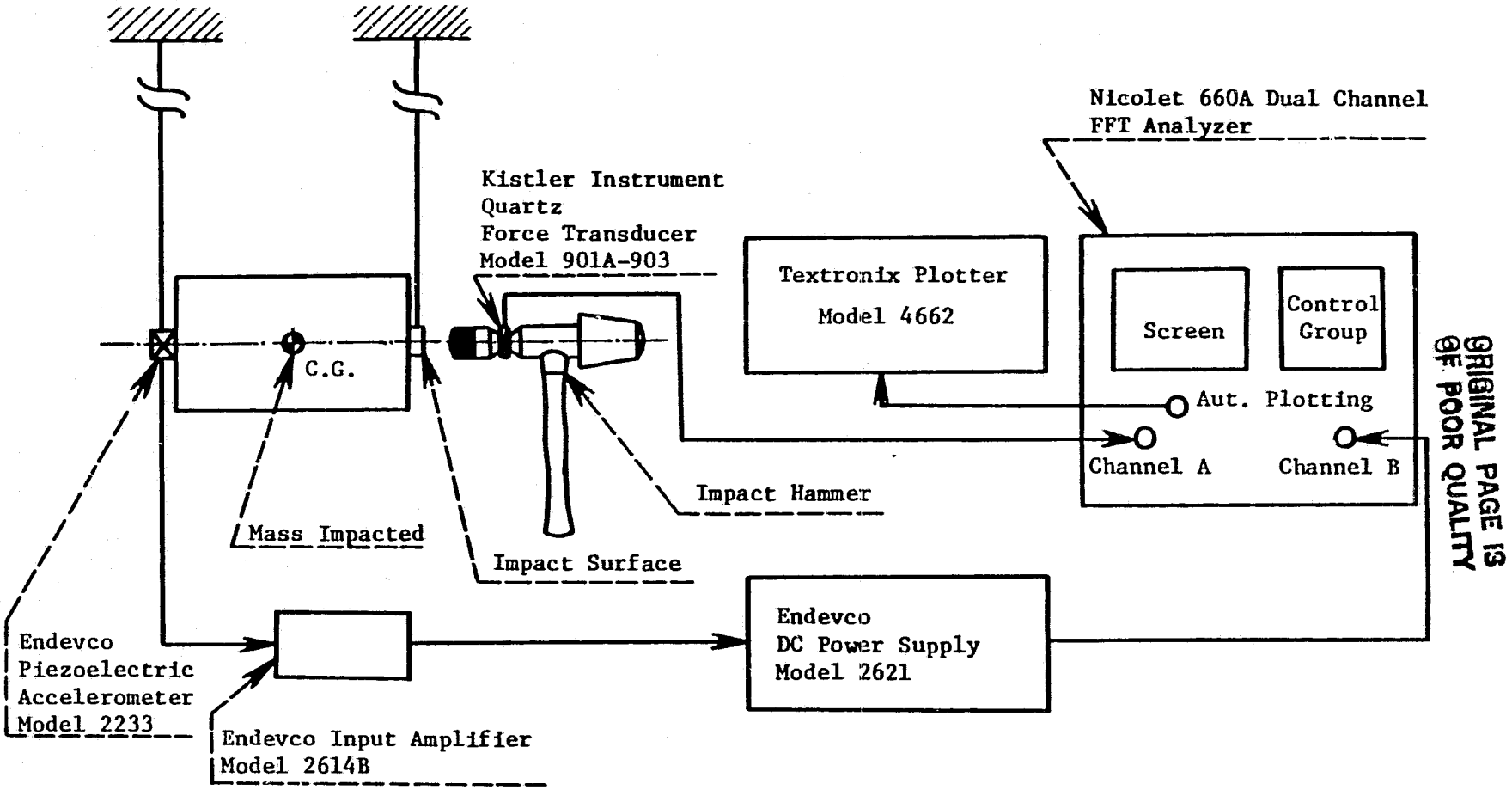

ORIGINAL PAGE IS
OF POOR QUALITY

Figure 7.2. Schematic of test setup for calibration of the impact hammer.

ORIGINAL PAGE IS
OF POOR QUALITY

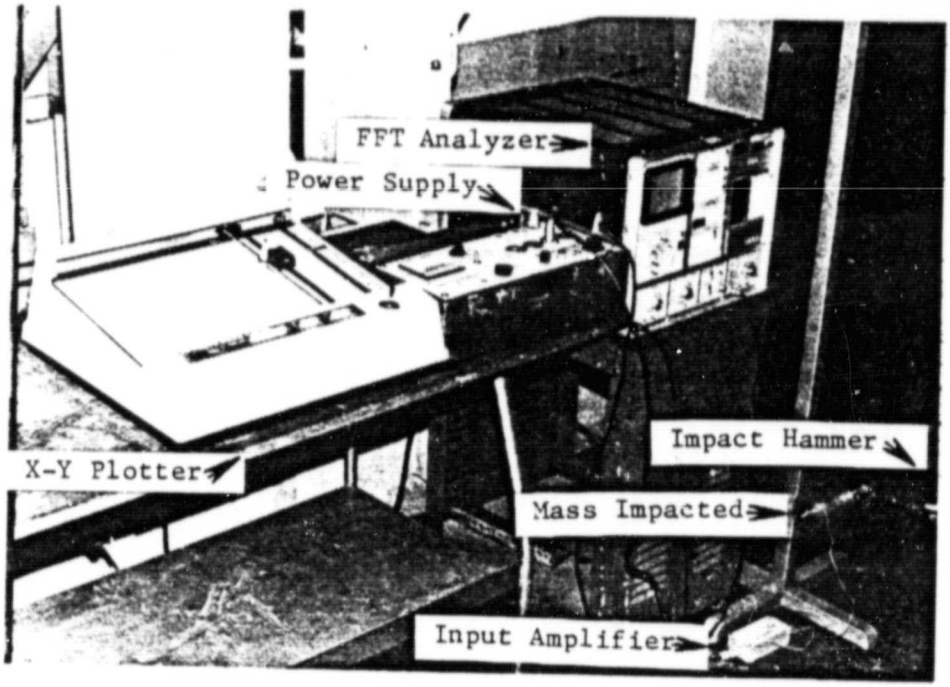

Figure 7.3. Test setup for calibration of the impact hammer.

(aluminum), but having different cross-sectional areas.

As a very important concept, damping for the same family of models could be much more easily handled if we could get it in a scaled form with respect to the chord and the thickness. These blade models are shown in Fig. 7.4. Geometrical and material properties of these models are given in Table 7.1. The sixth model was an aluminum curved blade, as shown in Fig. 7.5. The objective of this test was just to measure natural frequencies. A different setup was used for testing of the sixth model.

7.5. The Modal-Testing Procedure

The modal testing was performed on the five blade models described earlier by the Nicolet 660A Dual-Channel FFT Analyzer using impulsive excitation. The accelerometer was bonded beneath the tip of the blade (using adhesive). The "target" points were bonded to the upper surface of the blade, along the elastic line (a locus of shear centers). Only four points equally spaced counting from the tip were used as impacting points. Since the data were analyzed over a 2 KHz range, all frequencies should be excited in that range. To accomplish this, extreme care was taken to locate the target points properly. The nodal points for the first five modes were defined and good arrangement of the impact points was done to avoid their location at any of the nodal points. Figure 7.6 shows the arrangement of the nodal points of the blades for the first five modes. For this type of model, the first 5-6 natural frequencies are within the chosen frequency range of 2 KHz.

ORIGINAL PAGE IS
OF POOR QUALITY

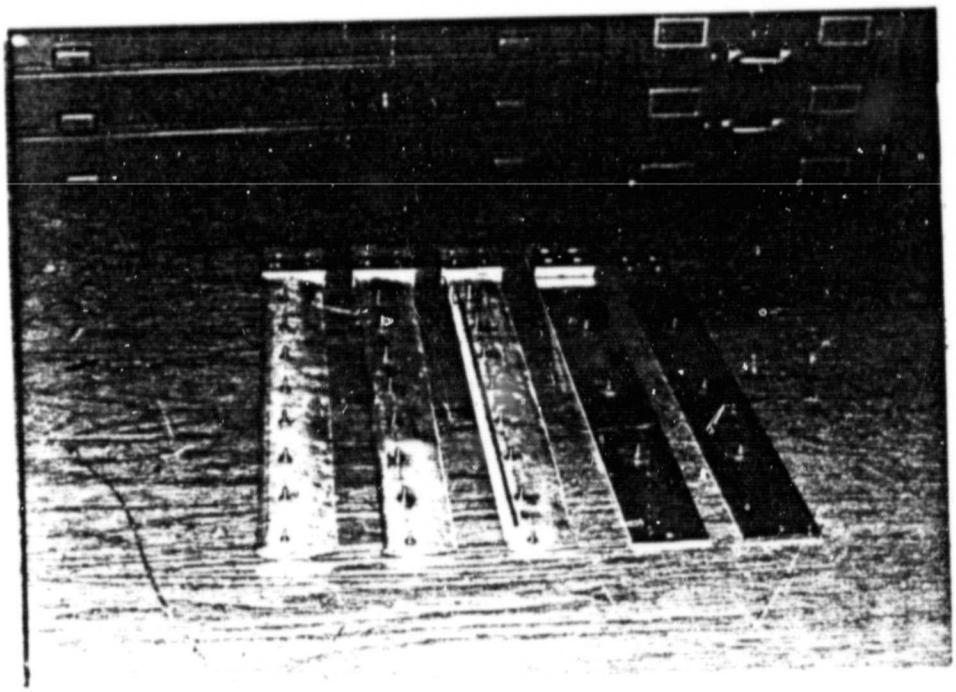

Figure 7.4. The blade models used for modal testing.

Table 7.1. Geometrical and material properties of blade models used for modal testing.

Cross-section	Shape	Dimen. of cross section	Length	Material	Modulus of elasticity	Weight of the model	Mass of the model	Area moment of inertia	Cross-sectional area
		a [in] b [in]	L [in]		E [lb/in^2]	W [lb]	m [$\frac{lbsec^2}{in}$]	I_x [in^4]	A [in^2]
NACA 0021	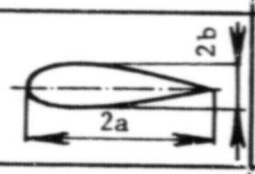	a = 1.0 b = 0.21	15.0	Aluminum	10.5×10^6	0.812	0.210×10^{-2}	0.0058	0.5695
NACA 0015	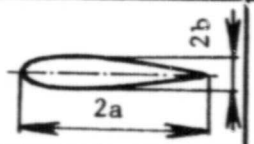	a = 1.0 b = 0.15	15.0	Aluminum	10.5×10^6	0.562	0.1454×10^{-2}	0.0015	0.3370
NACA 0009	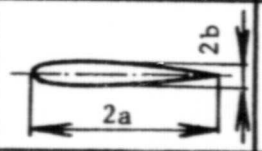	a = 1.0 b = 0.09	15.0	Aluminum	10.5×10^6	0.375	0.9704×10^{-3}	0.0003	0.2022
Rectangle	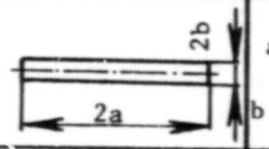	a = 0.1 b = 0.0625	15.0	Aluminum	10.5×10^6	0.4688	0.1213×10^{-2}	0.0003	0.25
Rectangle	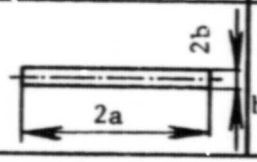	a = 1.0 b = 0.0625	15.0	Aluminum	30.0×10^6	1.1581	0.2997×10^{-2}	0.0003	0.25

ORIGINAL PAGE IS
OF POOR QUALITY

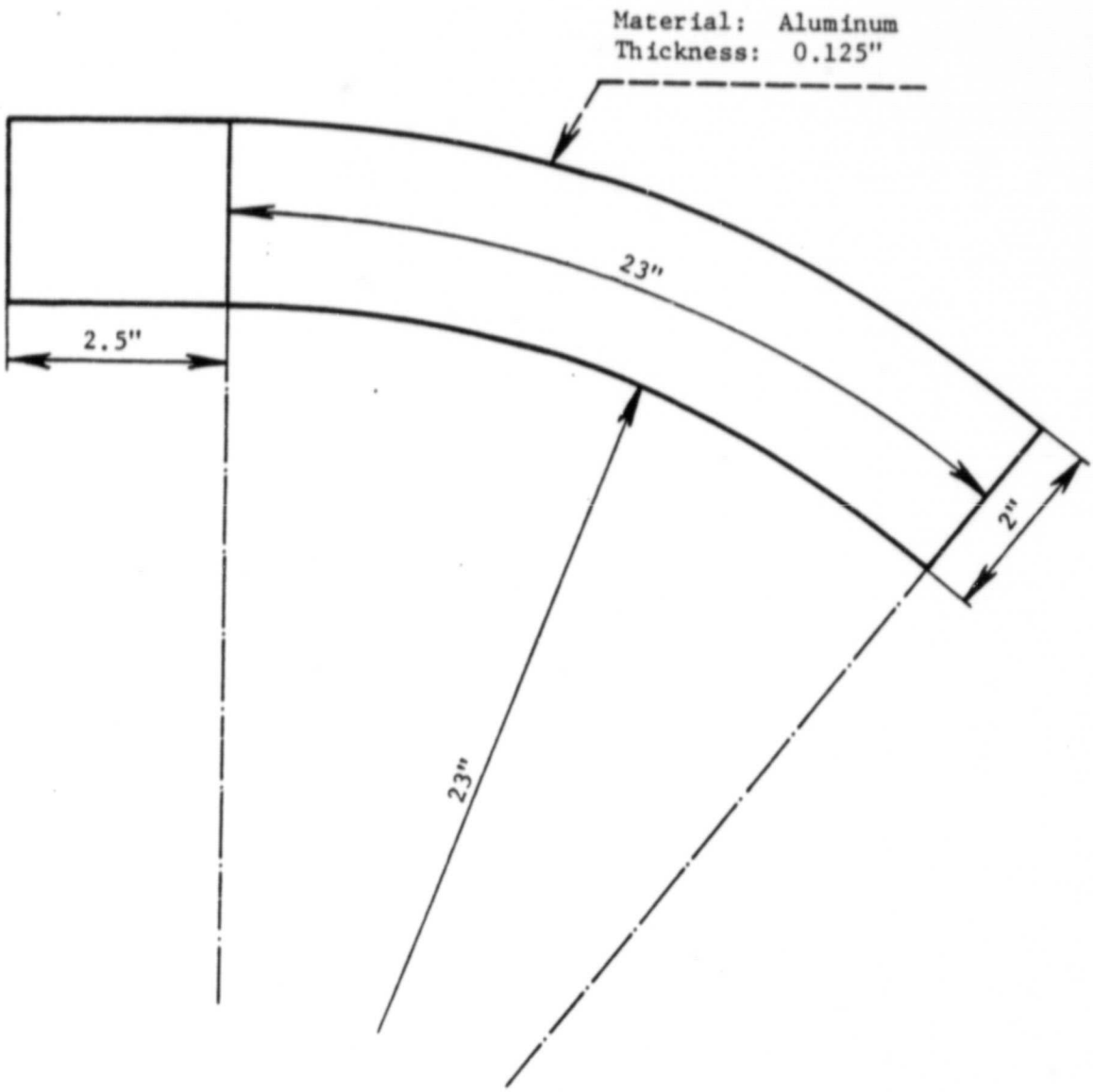

Figure 7.5. Top view of a curved beam model.

ORIGINAL PAGE IS
OF POOR QUALITY

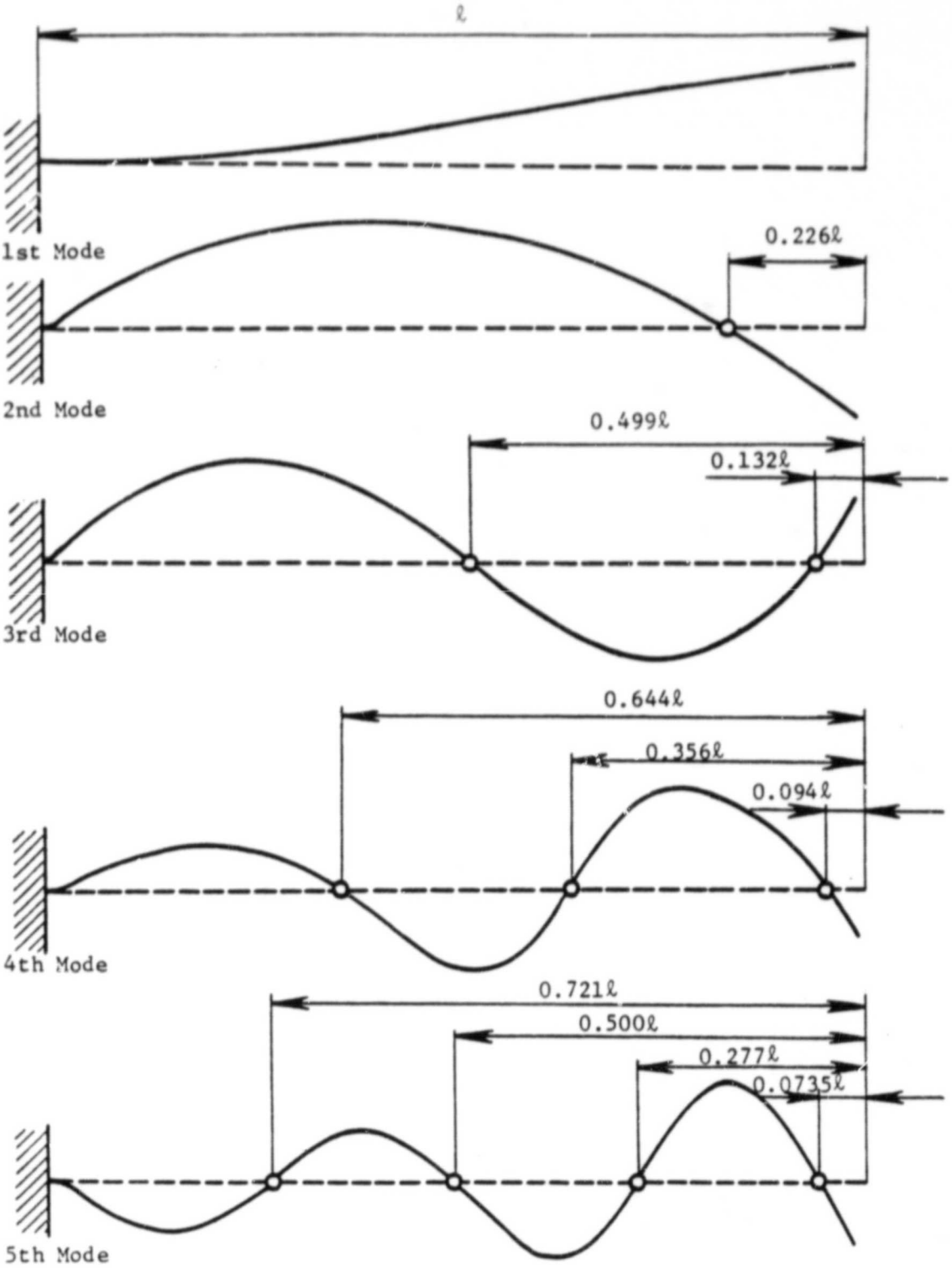

Figure 7.6. The nodal points of the first five modes. (The modal shapes are greatly exaggerated.)

The accelerometer's signal was conditioned by an Endevco Input Amplifier, Model 2616B, with a voltage gain of 10. During the calibration procedure, we defined the total sensitivity as $S_a = 0.686 \times 10^{-5}\left[\frac{V}{in/sec^2}\right]$. The blade models were excited by impacting the targets with an impact hammer, shown in Fig. 7.1(b). A force transducer, Kistler Instrument Quartz, Model 901A-903, was mounted to the machined face of the hammer with a threaded stud. A plastic tip (Teflon) was mounted to the force transducer to serve as the striking surface. The reason for its mounting was discussed in the previous chapter. During the calibration procedure, we defined the total sensitivity of the force transducer and impact hammer system as $S_f = 0.363 \times 10^{-2}\left[\frac{V}{lb}\right]$.

We discussed earlier the importance of ensemble-averaging both signals in the time domain. When the signals recovered from noise, they were Fourier-transformed and the transfer function was calculated. To obtain above both transient signals in the time domain, they were captured and stored. The best way to do this is by automatic capturing of the signals. Working with this analyzer, we set the trigger on channel A (force signal) to activate the system (capturing and storing) of both signals at the $\frac{1}{16}$ of the maximum amplitude. Also, the type of averaging was chosen so that besides the automatic triggering, capturing and storing the averaging was done automatically. The blade was struck a number of times until the satisfactory coherence function was observed on the screen of the FFT analyzer. The stable data were considered when the coherence function exceeded a value of 0.9 around each resonance. This was an indication of

valid data free from nonlinear effects and noise contamination. Since the trigger was very sensitive on the level of the force signal, enough time was allowed between two impacts for the transient vibration of the model to die out completely. By our observation, this period was usually to two minutes. The whole process of averaging and the capturing of signals was observed on the screen. When good coherence was reached, the transfer function was calculated and displayed on the screen. Also, this function could be described in all three modes: Bode plot, Nyquist plot, and real and imaginary part vs. frequency. Then, the picture from the screen was reproduced on the paper by the plotter attached to the FFT analyzer. The same procedure was repeated for all target points of the blade. The setup for modal testing used is shown in Fig. 7.7. Figure 7.8 shows all components of the setup ready for testing. This test was performed in the structural area of the Department of Aerospace Engineering of The Pennsylvania State University during February and March, 1982.

7.6. The Results Obtained by Modal Testing

The objective of this test was to analyze the natural frequencies and modal damping of the blade models. Ths mode shapes were not analyzed, since a very good conditioning of both signals was required. The accuracy in measurement of mode shapes directly depends on the accuracy of the determined relationship between electrical and engineering units. For accurate measurement of frequencies and damping, we do not need such an accurate conditioning of the signals.

Frequencies and damping were calculated from the point transfer-function of the blade. The point transfer-function is calculated

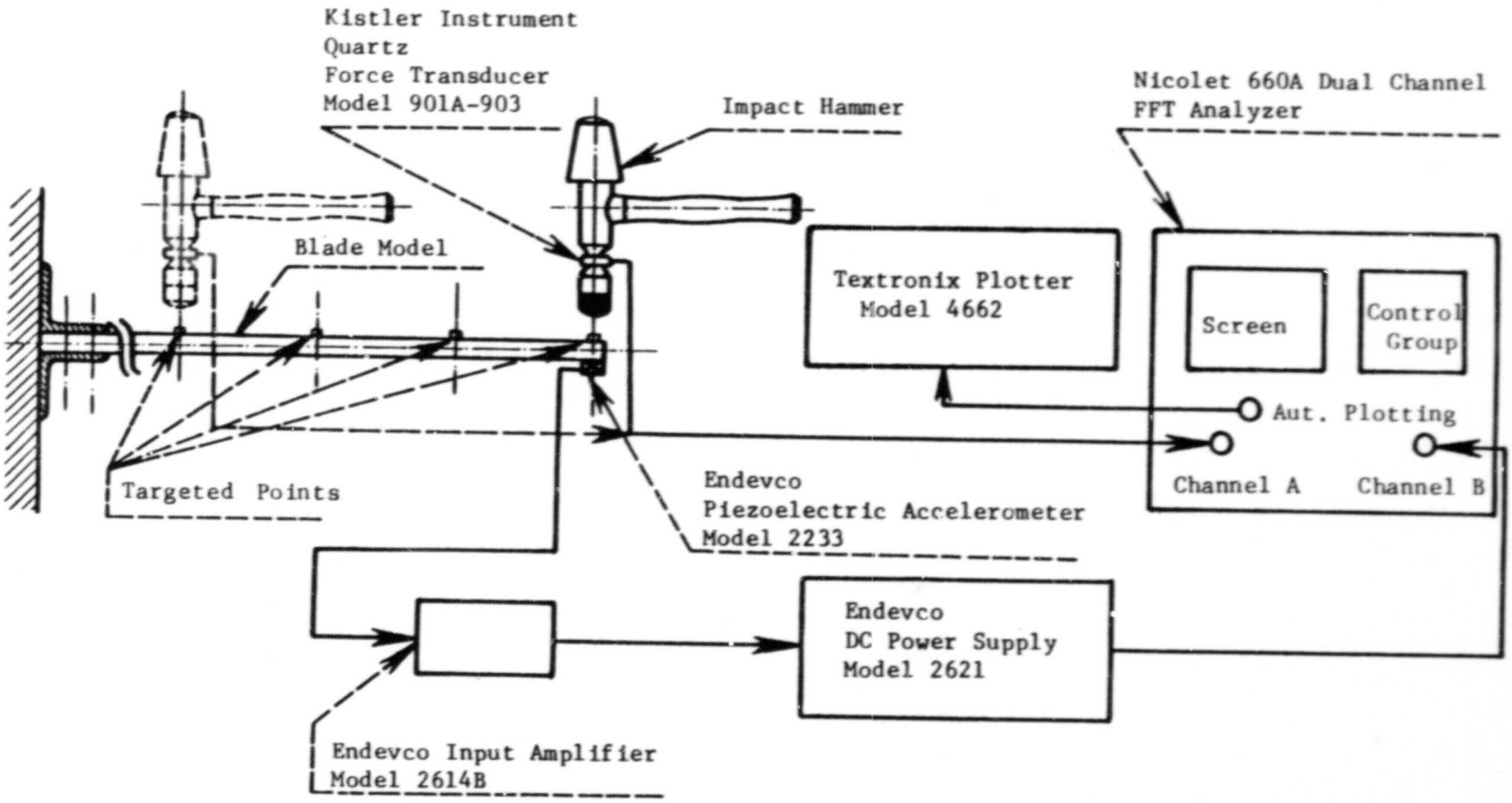

Figure 7.7. Schematic of the setup for modal testing using the Nicolet 660A Dual Channel FFT Analyzer.

ORIGINAL PAGE IS
OF POOR QUALITY

ORIGINAL PAGE IS
OF POOR QUALITY

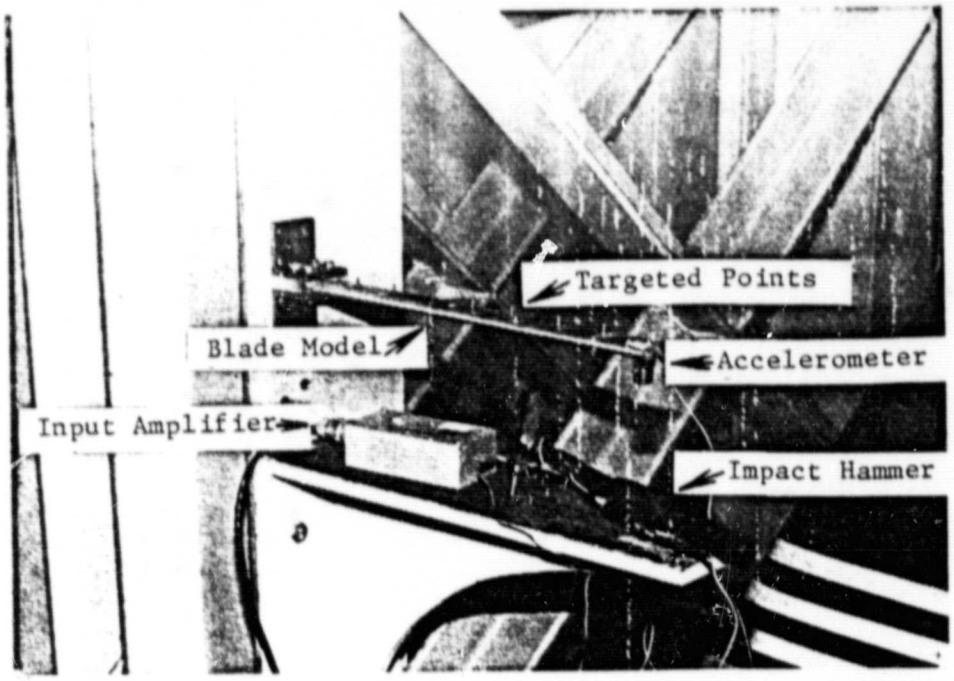

(a)

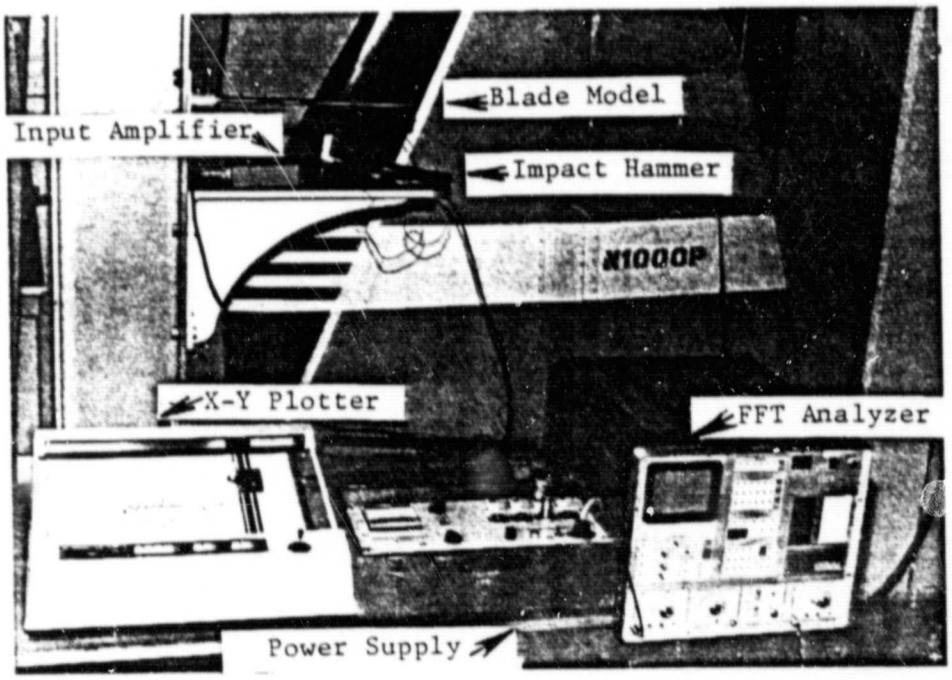

(b)

Figure 7.8. The setup for modal testing; (a) the blade model of the test stand, (b) the components of the setup.

for the station where the input and output signals are taken from the same point on the blade. In our case, this point was the first target point at the tip (the target and accelerometer were aligned at the same axis). Since the natural frequencies and damping are the global property of the linear structure, any arrangement of the impact point and accelerometer should give the same natural frequencies and damping. The measurements and plots were made for four different locations of impact points, and good agreement was observed.

When good coherence was reached, the transfer function was displayed on the screen of the FFT analyzer, and the frequencies were read accurately, but using the cursor line, as digital numbers. Figure 7.9 shows the moments of impacting with the blade. Figure 7.9(a) shows impacting with target No. 1, and Fig. 7.9(b) shows impacting with target No. 4. Figure 7.10 presents the test setup for modal testing of a steel blade. Since we do not have enough space to show all graphs reproduced from the analyzer screen, only those graphs typical of all blade models will be shown including an aluminum blade model having NACA 0015 as its cross section, and a steel blade model having a rectangular cross section.

The complete results for all five models are given in Table 7.2. They will be used in the following chapter in the numerical model of the dynamic response of the blades. At this point, we cannot make any conclusion concerning the data measured. A preliminary check shows that at least we have good agreement regarding natural frequencies compared with the natural frequencies of continuous beam models. Also, we observe that the damping is concentrated in the first three or four modes.

ORIGINAL PAGE
BLACK AND WHITE PHOTOGRAPH

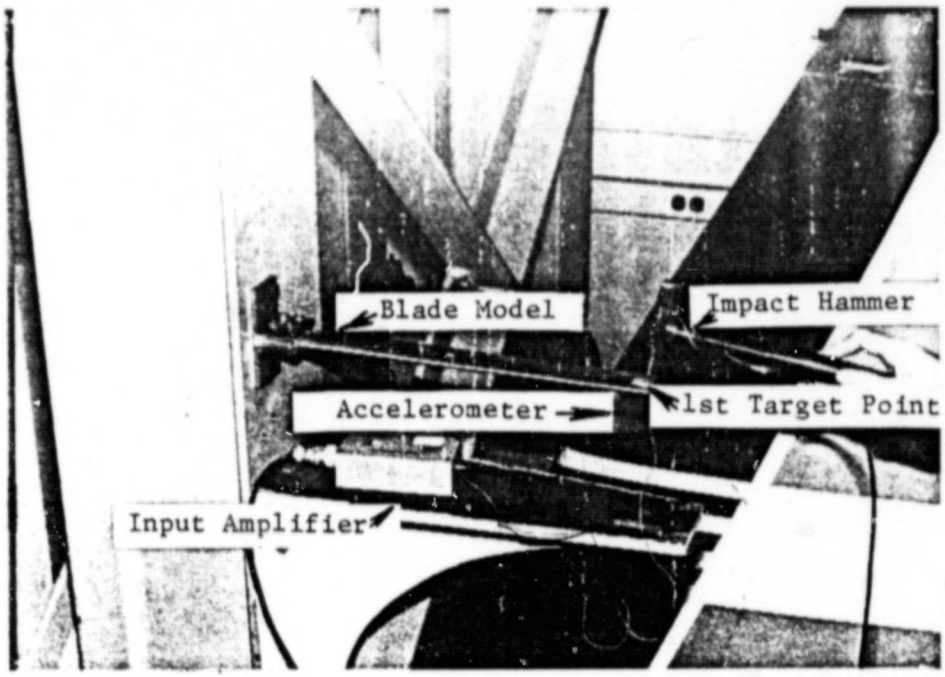

(a)

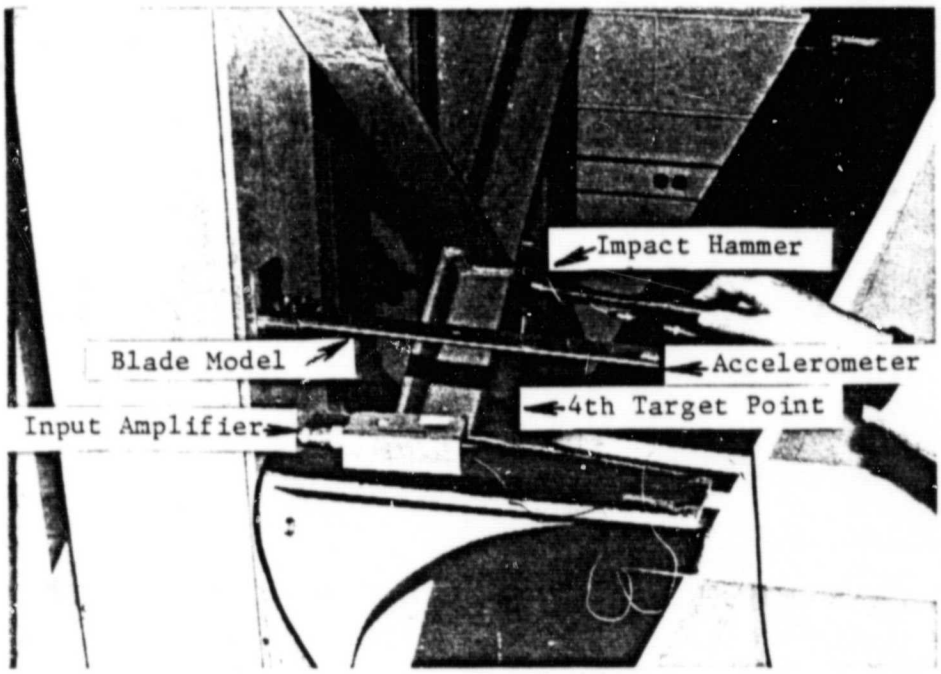

(b)

Figure 7.9. Blade model at the stand; (a) giving the impulse to the point 1 and taking the output from point 1, (b) giving the impulse to the point 4 and taking the output from point 1.

ORIGINAL PAGE
BLACK AND WHITE PHOTOGRAPH

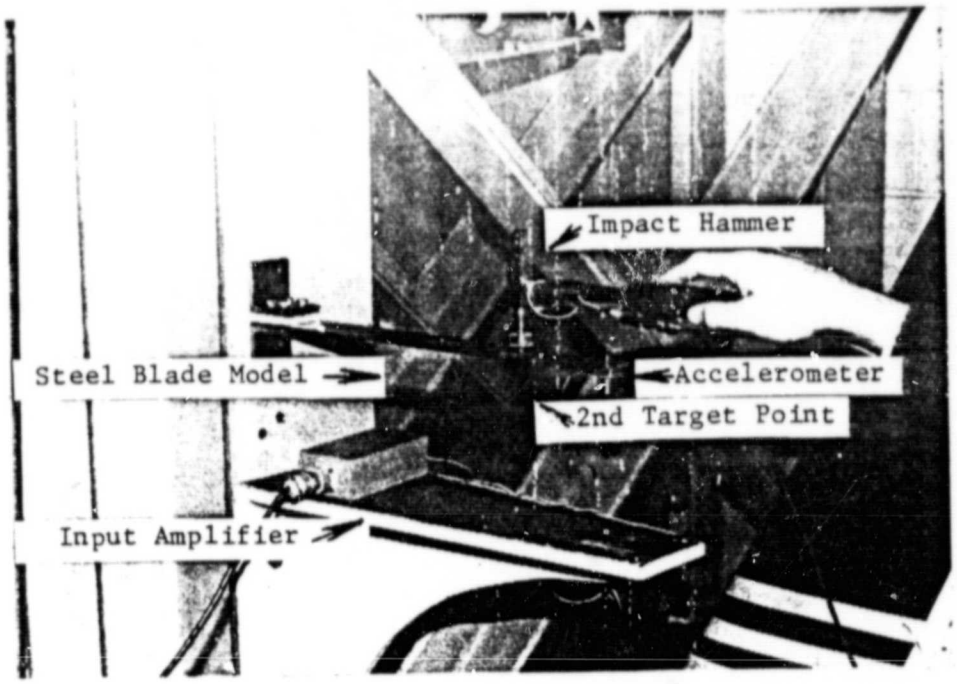

(a)

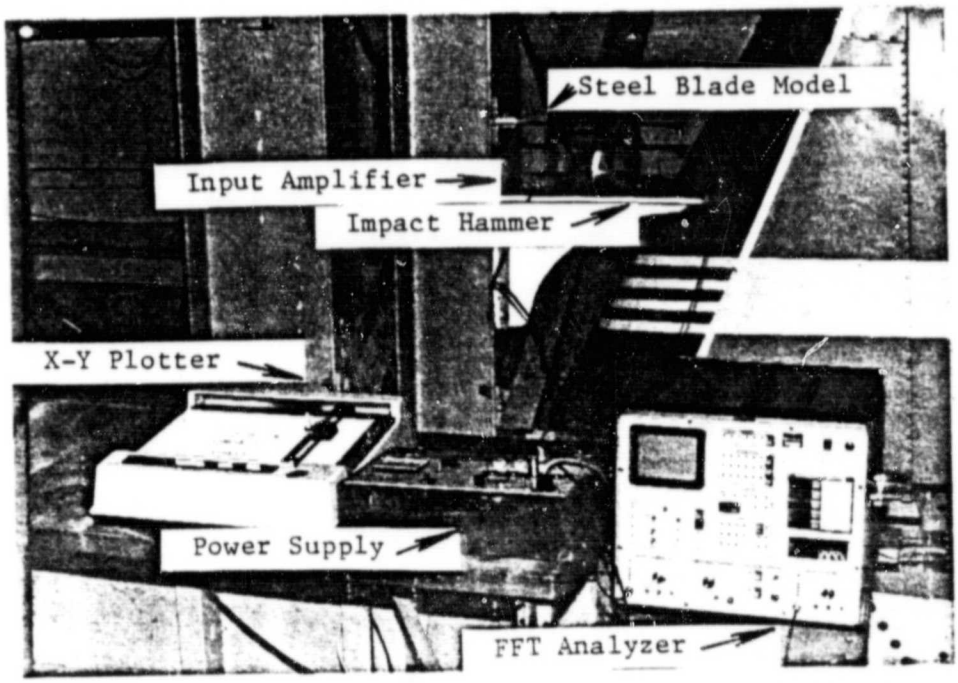

(b)

Figure 7.10. (a) The steel blade at the test stand, (b) the setup for modal testing of the steel blade.

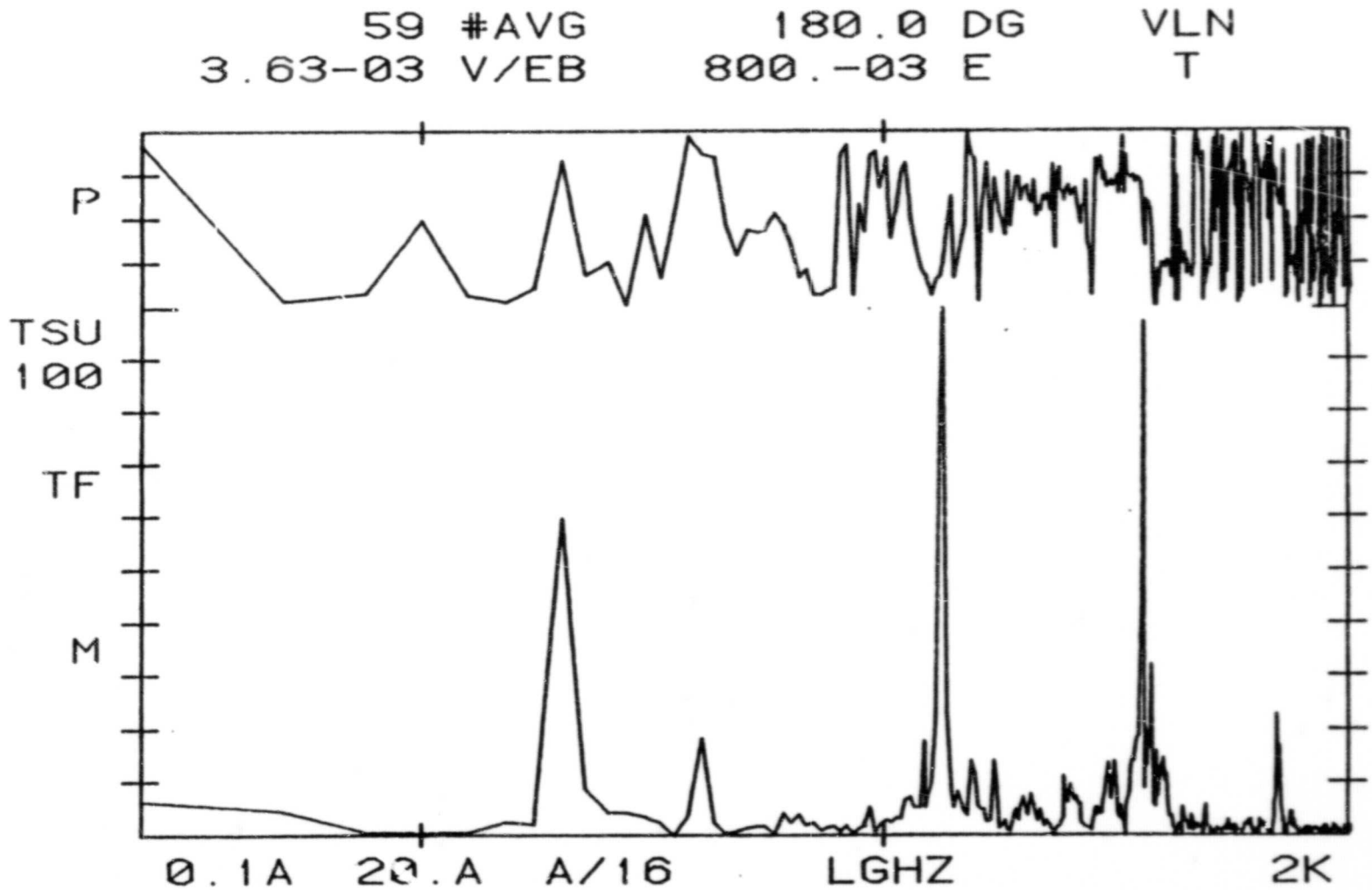

Figure 7.11. The magnitude and phase of the point transfer function of a model having an NACA 0021 cross section (peaks of the magnitude correspond to the model's natural frequencies).

ORIGINAL PAGE IS
OF POOR QUALITY

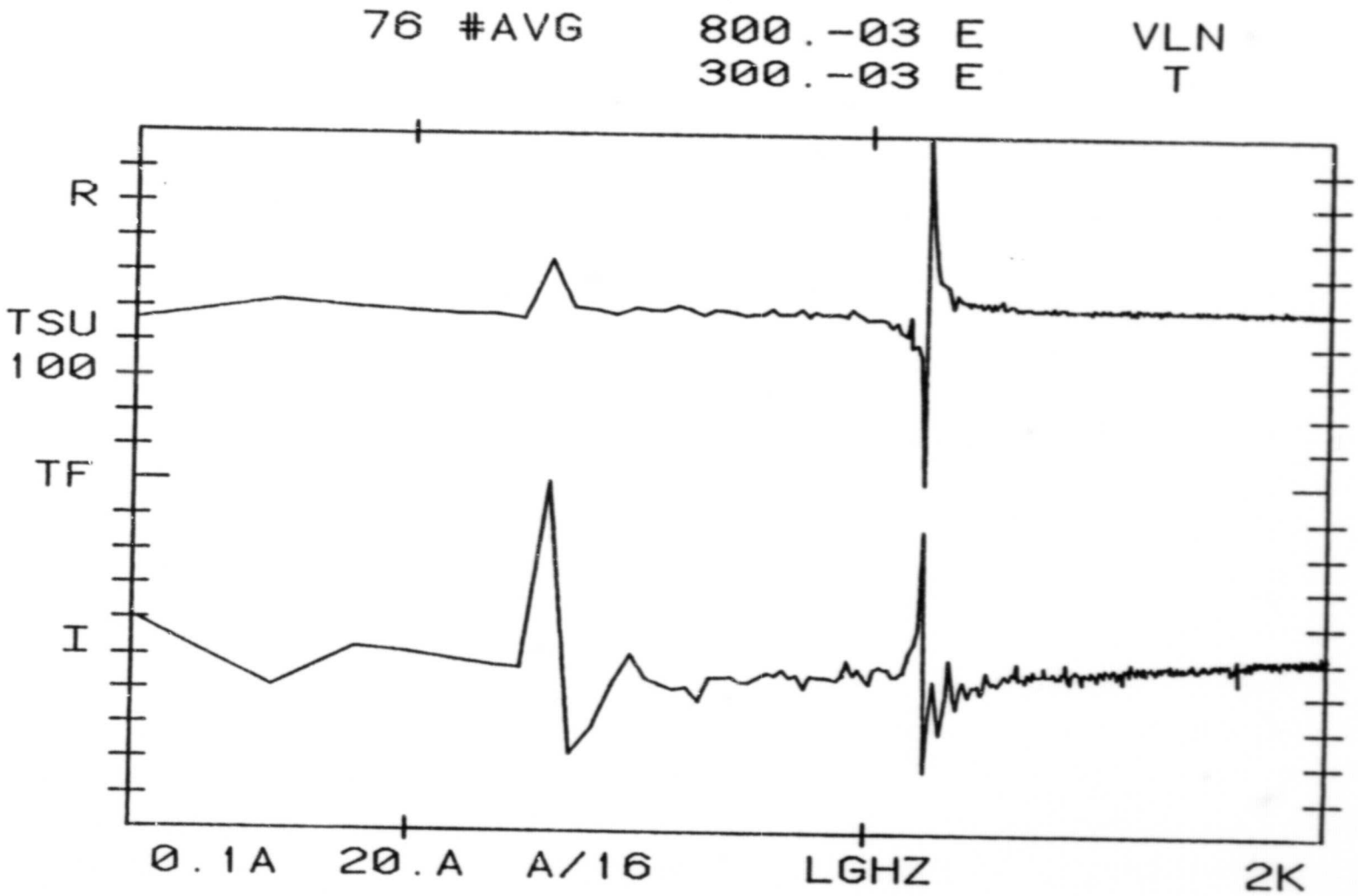

Figure 7.12. The real and imaginary parts of the point transfer function of a model having an NACA 0021 airfoil cross section.

ORIGINAL PAGE IS
OF POOR QUALITY

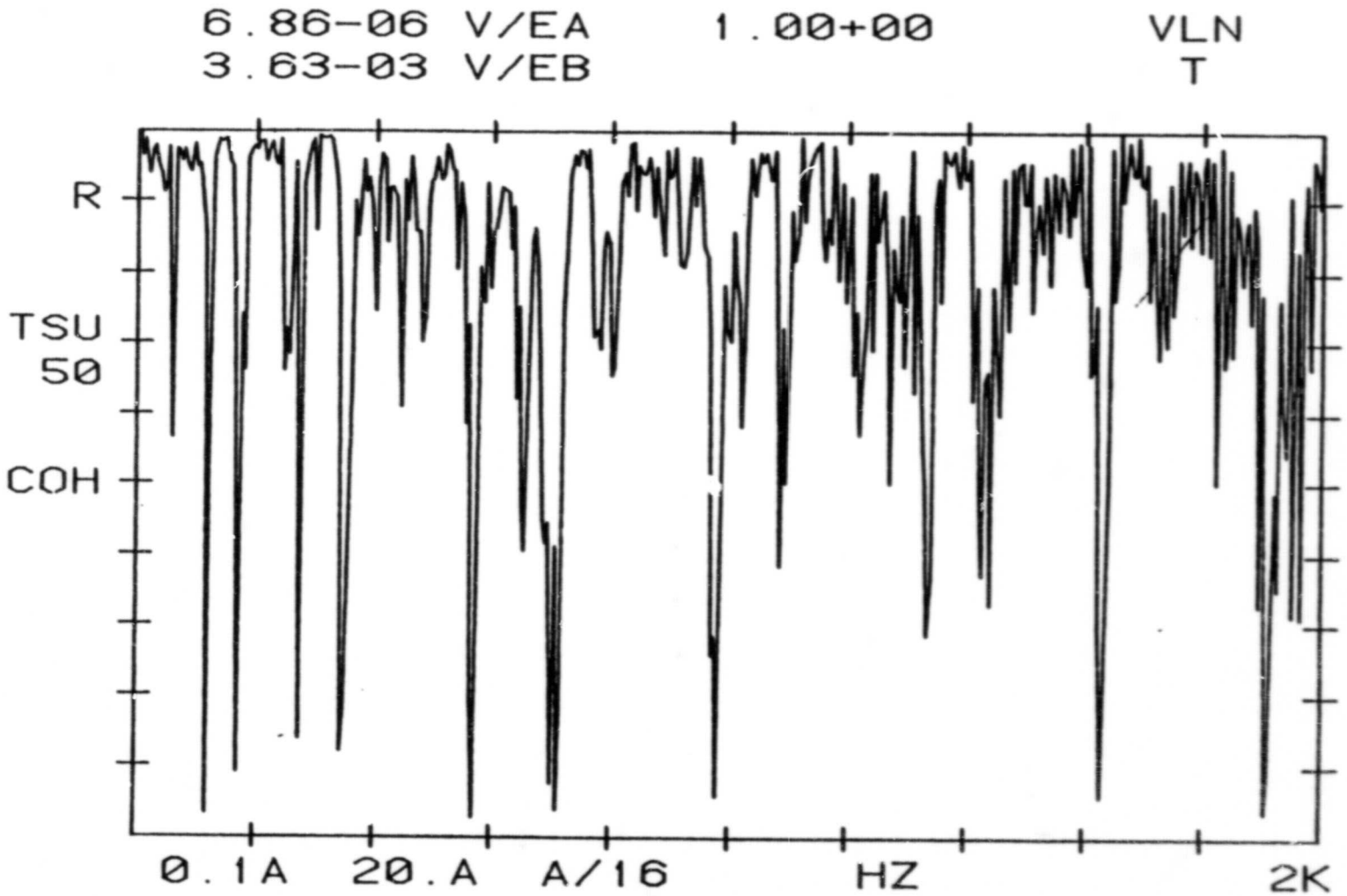

Figure 7.13. The coherence function related to input/output used for determining the point transfer function of a model having an NACA 0015 airfoil cross section.

ORIGINAL PAGE IS
OF POOR QUALITY

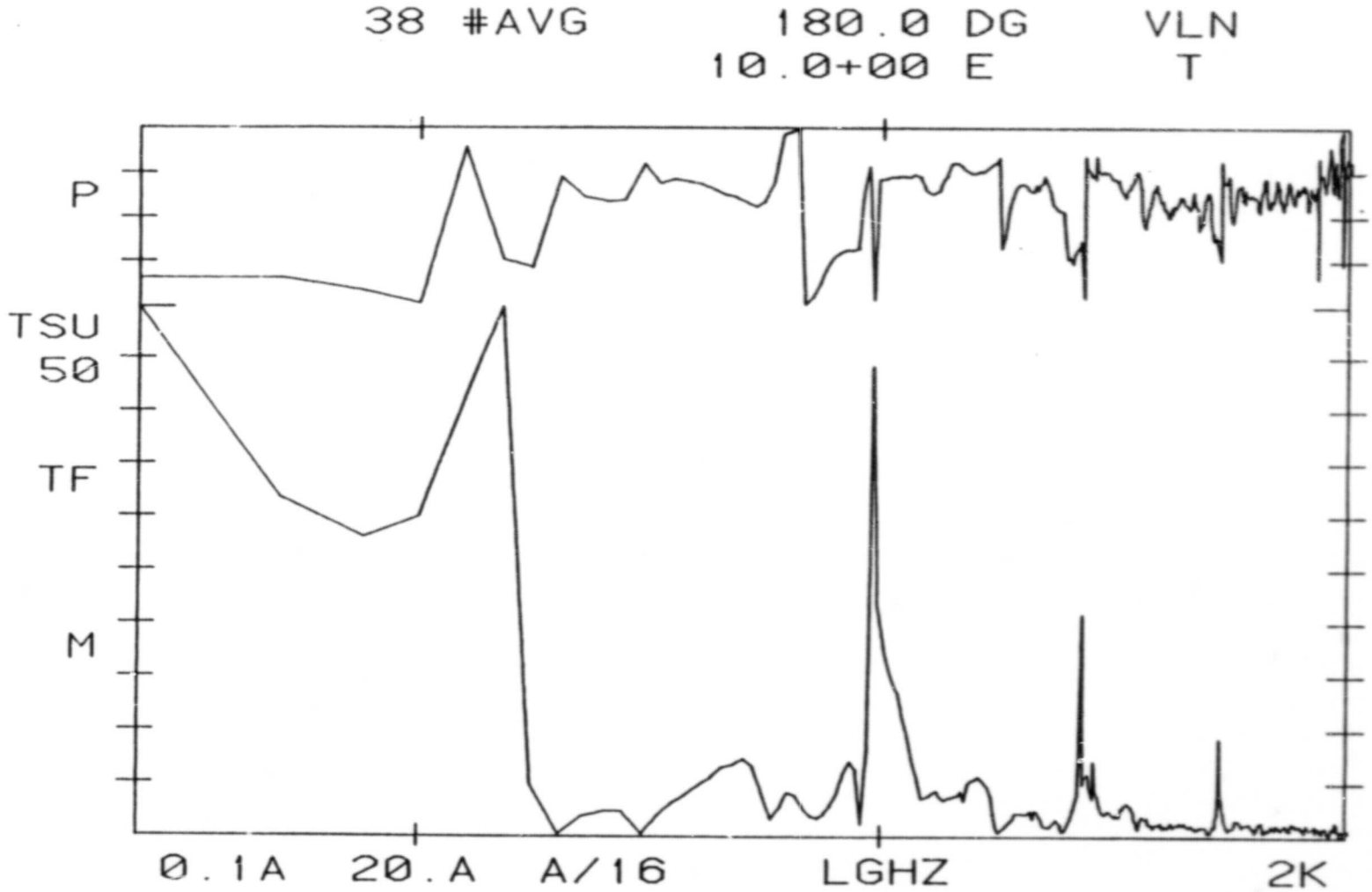

Figure 7.14. The magnitude and phase of the point transfer function of a model having an NACA 0015 cross section (peaks of the magnitude correspond to the model's natural frequencies).

ORIGINAL PAGE IS
OF POOR QUALITY

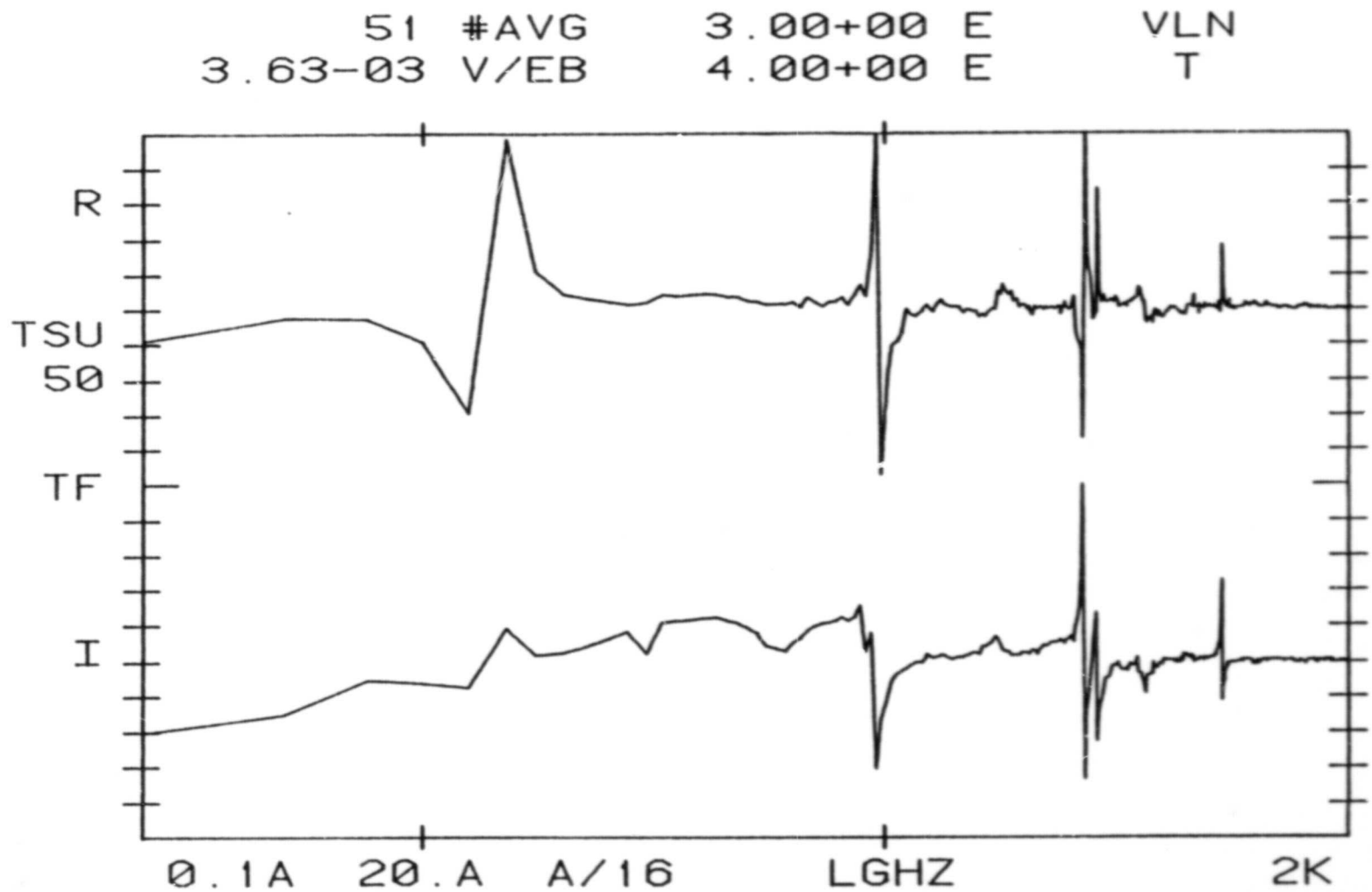

Figure 7.15. The real and imaginary parts of the point transfer function of a model having an NACA 0015 airfoil cross section.

ORIGINAL PAGE IS
OF POOR QUALITY

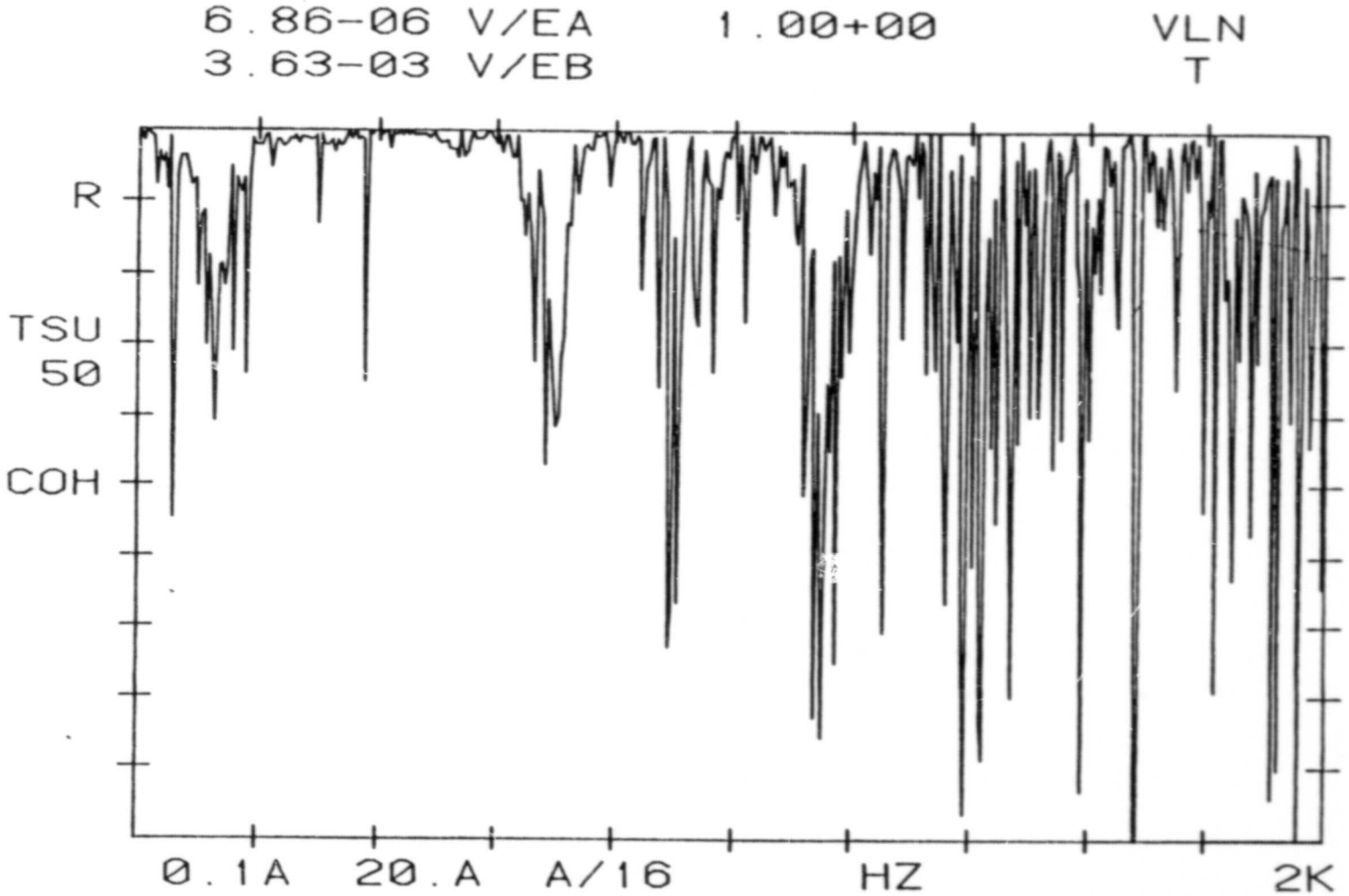

Figure 7.16. The coherence function related to the input/output used for determining the point transfer function of a model having an NACA 0015 airfoil cross section.

ORIGINAL PAGE IS
OF POOR QUALITY

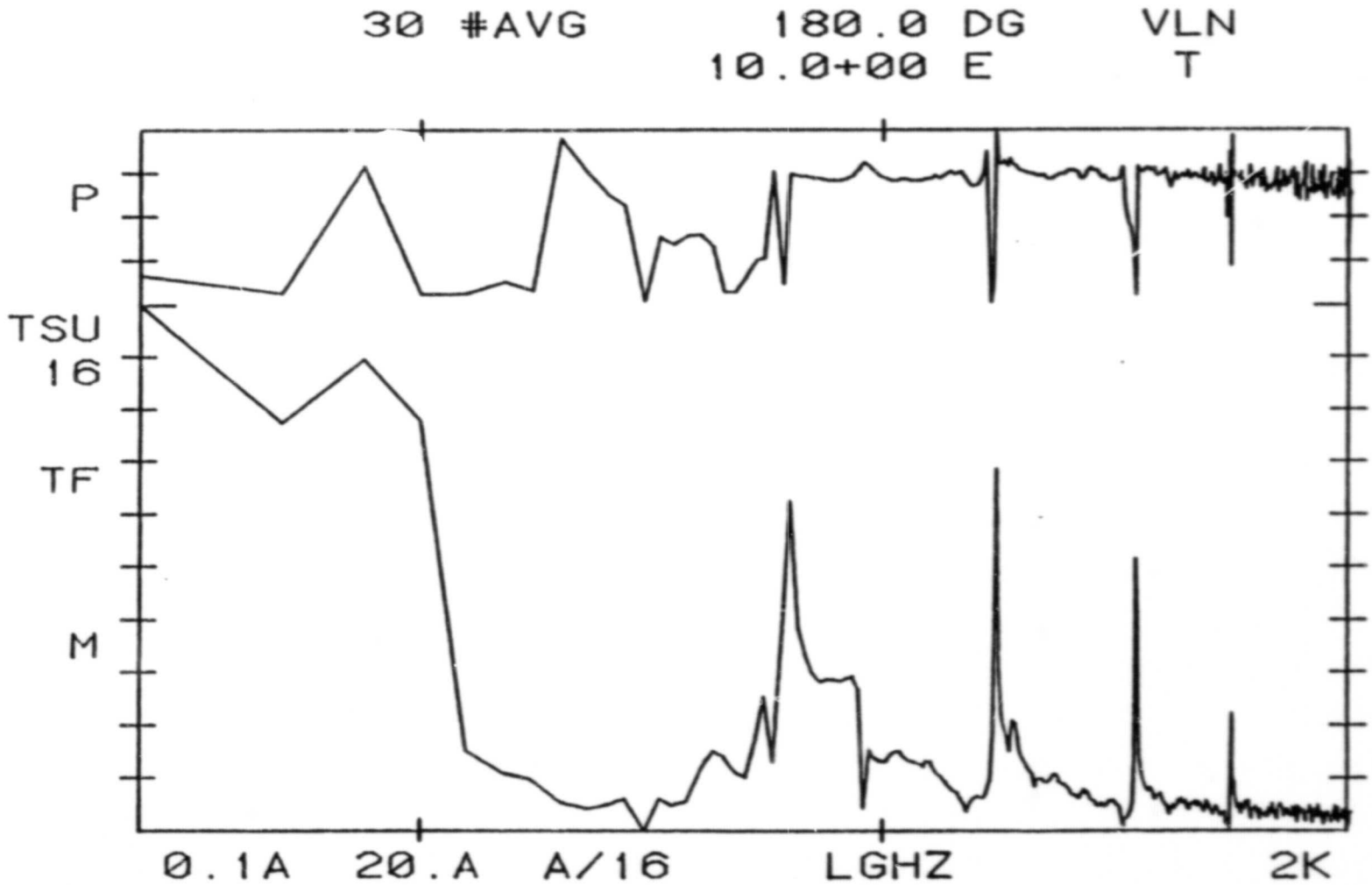

Figure 7.17. The magnitude and phase of the point transfer function of a model having an NACA 0009 airfoil cross section (peaks of the magnitude correspond to the model's natural frequencies).

ORIGINAL PAGE IS
OF POOR QUALITY

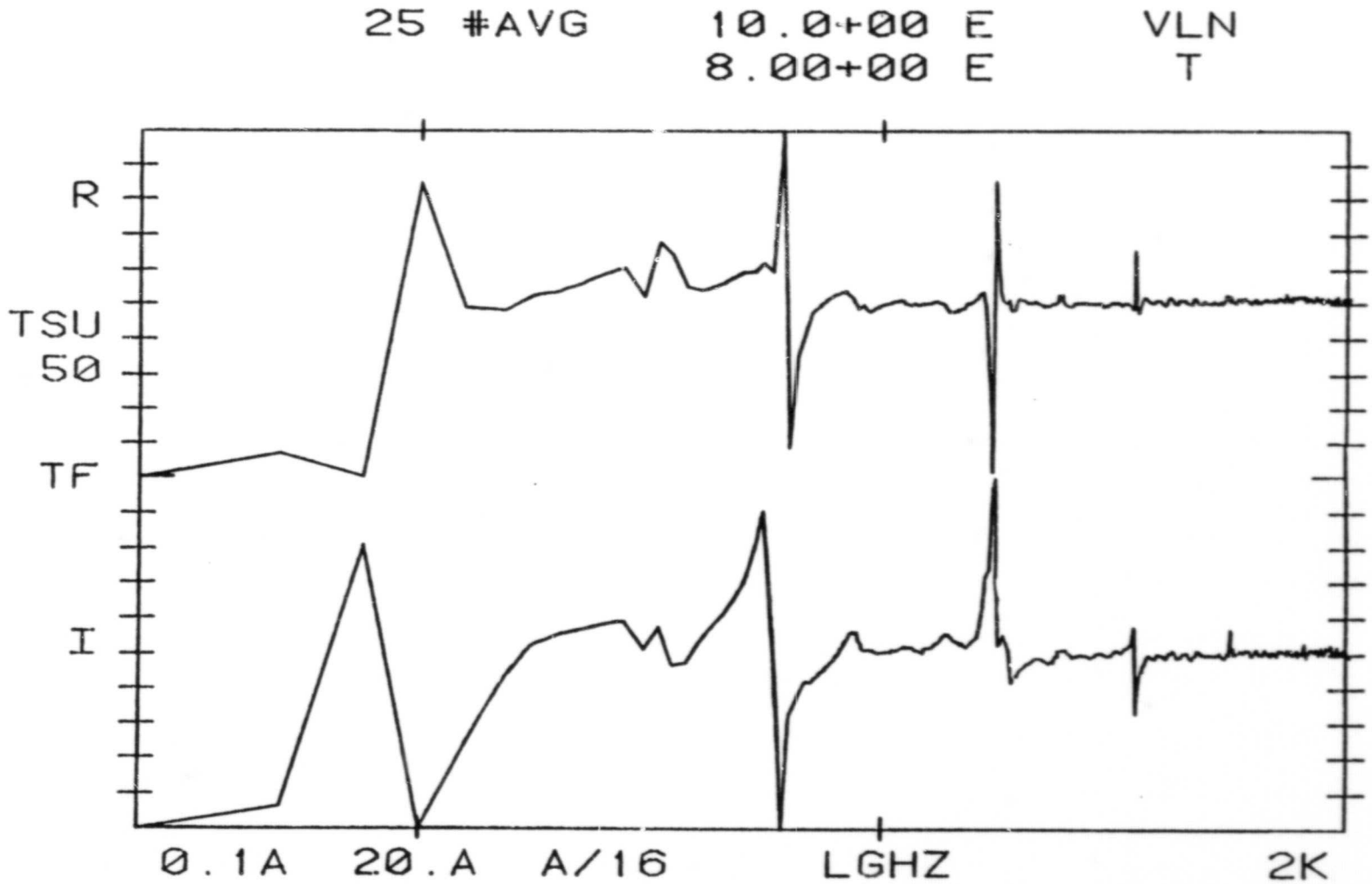

Figure 7.18. The real and imaginary parts of the point transfer function of a model having an NACA 0009 airfoil cross section.

ORIGINAL PAGE IS
OF POOR QUALITY

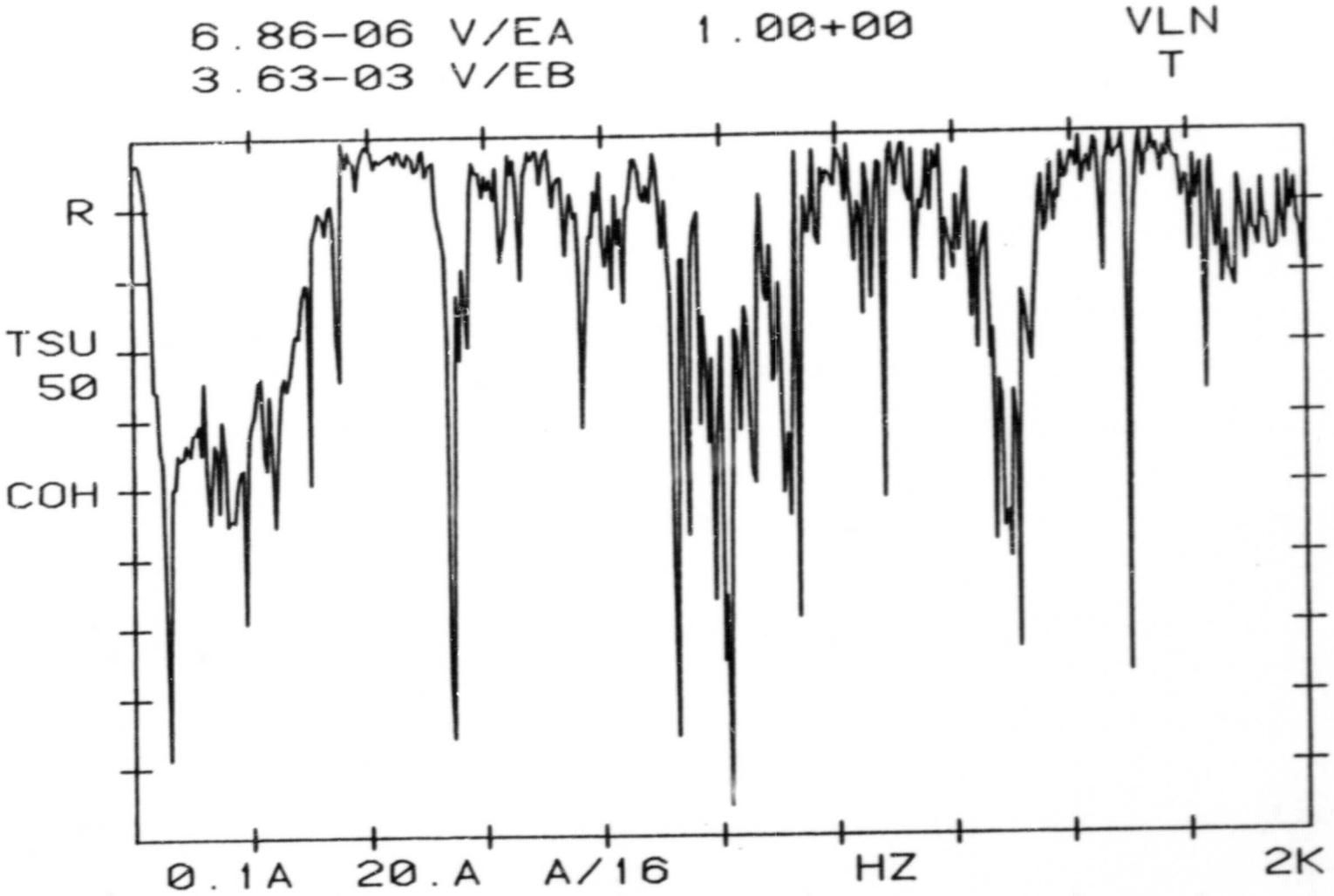

Figure 7.19. The coherence function related to the input/output used for determining the point transfer function of a model having an NACA 0009 airfoil cross section.

ORIGINAL PAGE IS
OF POOR QUALITY

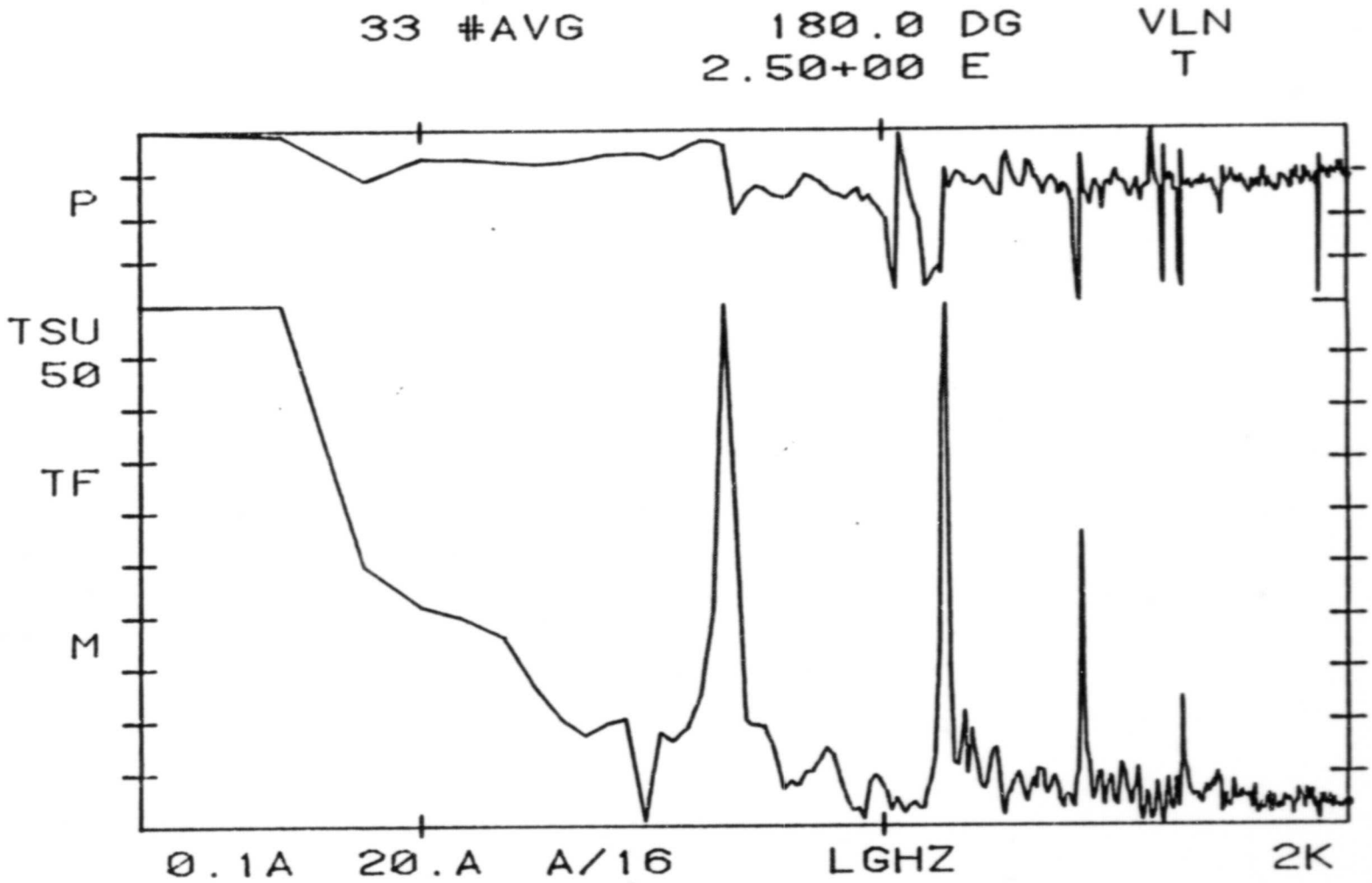

Figure 7.20. The magnitude and phase of the point transfer function of an aluminum model having a rectangular cross section (peaks of the magnitude correspond to the model's natural frequencies).

ORIGINAL PAGE IS
OF POOR QUALITY

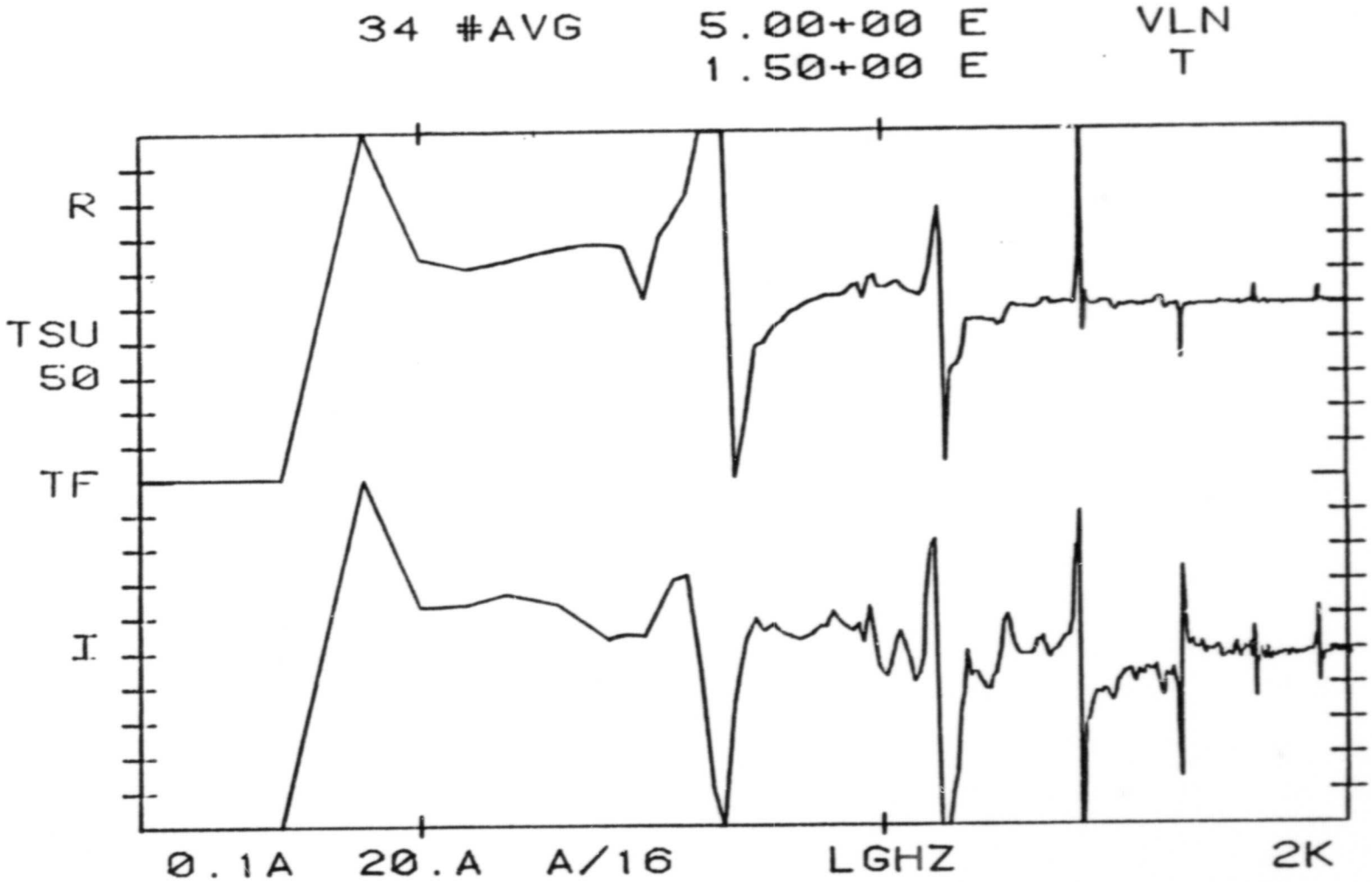

Figure 7.21. The real and imaginary parts of the point transfer function of an aluminum model having a rectangular cross section.

ORIGINAL PAGE IS
OF POOR QUALITY

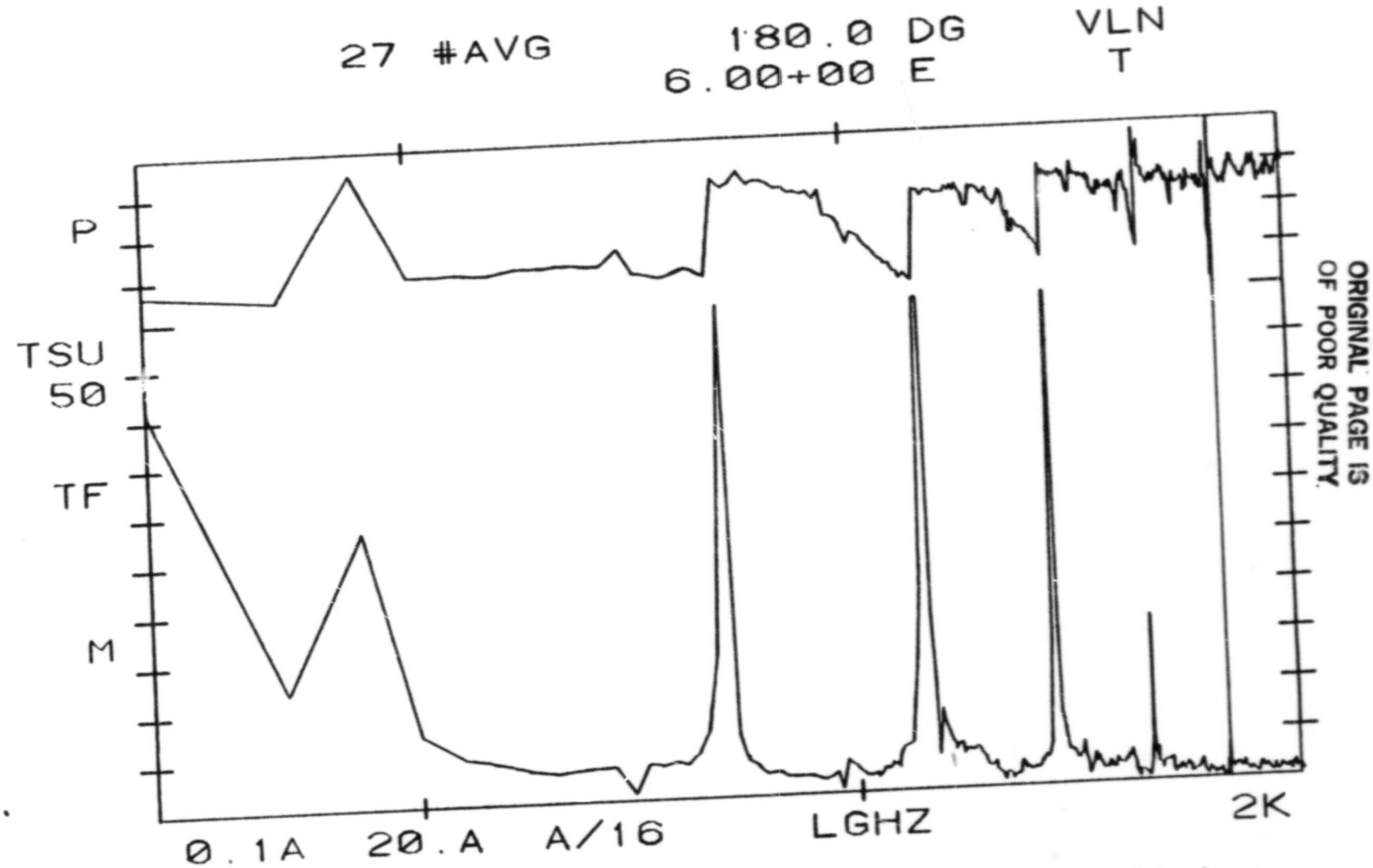

ORIGINAL PAGE IS
OF POOR QUALITY

Figure 7.22. The magnitude and phase of the point transfer function of a steel model having a rectangular cross section (peaks of the magnitude correspond to the model's natural frequencies).

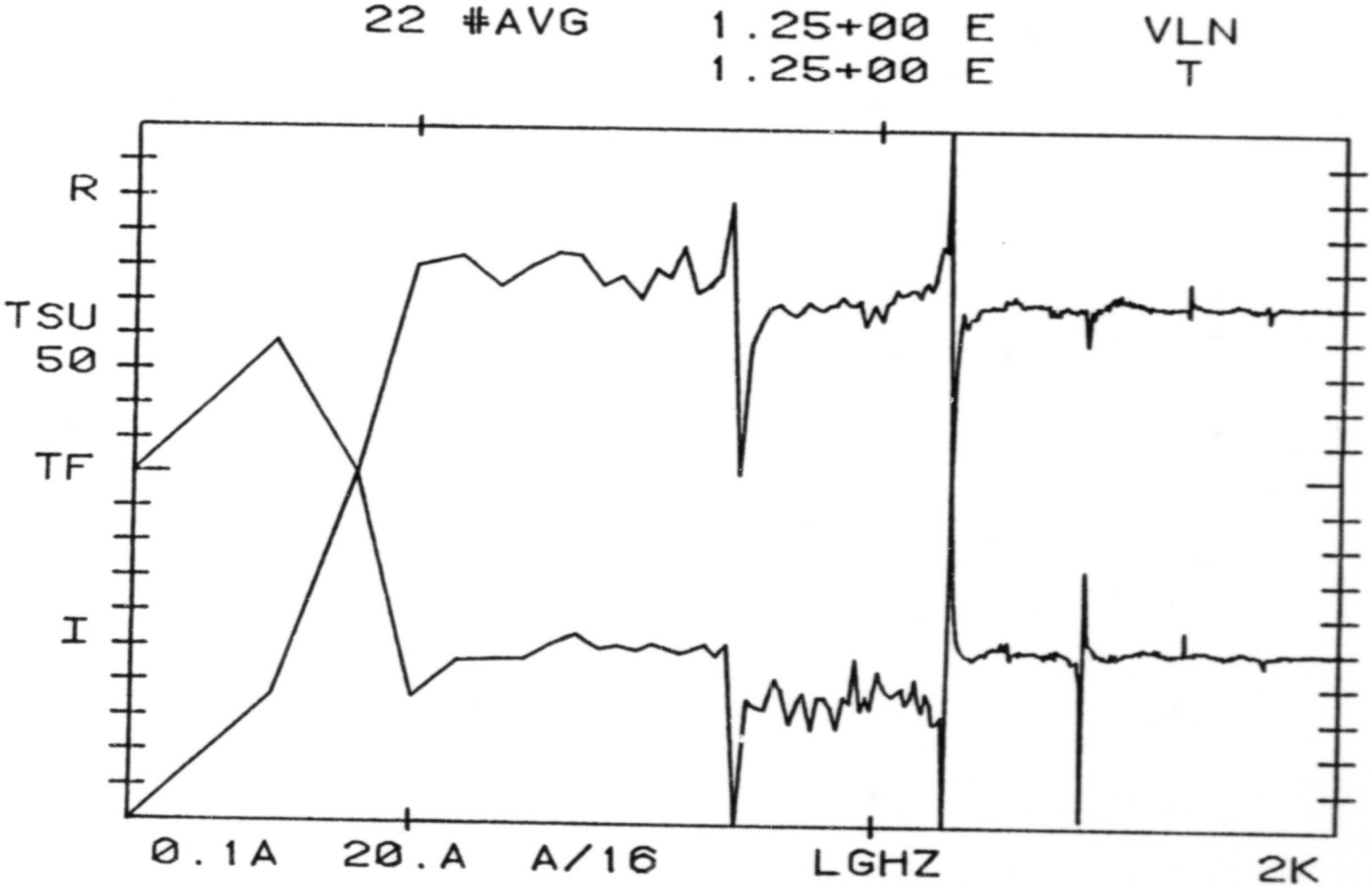

Figure 7.23. The real and imaginary parts of the point transfer function of a steel model having a rectangular cross section.

ORIGINAL PAGE IS
OF POOR QUALITY

Table 7.2. Natural frequencies and modal damping ratios obtained by modal testing.

	Dimensions	Length	Mode	Frequency	Frequency	Frequency lower peak	Frequency upper peak	Quality Factor	Damping Ratio
	[in]	[in]	No.	ω[rad/sec]	f [Hz]	fa [Hz]	fb [Hz]	Q [unitless]	ζ [unitless]
NACA 0021 (Al) 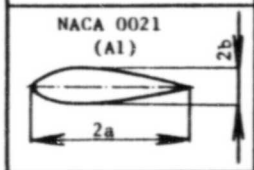	a = 1.0 b = 0.21	15.	1	0.2513×10^{3}	0.4000×10^{2}	0.4500×10^{2}	0.4000×10^{2}	0.8529×10	0.5860×10^{-1}
			2	0.1665×10^{4}	0.2650×10^{3}	0.2600×10^{3}	0.2400×10^{3}	0.1252×10^{2}	0.3993×10^{-1}
			3	0.4523×10^{4}	0.7200×10^{3}	0.7250×10^{3}	0.7200×10^{3}	0.1445×10^{3}	0.3460×10^{-2}
			4	0.8859×10^{4}	0.1410×10^{4}	0.1425×10^{4}	0.1410×10^{4}	0.9450×10^{2}	0.5290×10^{-2}
			5	--	--	--	--	--	--
NACA 0015 (Al) 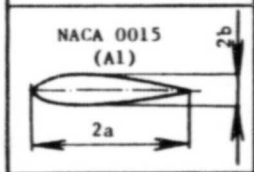	a = 1.0 b = 0.15	15.	1	0.1885×10^{3}	0.3000×10^{2}	0.3000×10^{2}	0.2000×10^{2}	0.2600×10	0.1923
			2	0.1194×10^{4}	0.1900×10^{3}	0.1900×10^{3}	0.1750×10^{3}	0.1218×10^{2}	0.4102×10^{-1}
			3	0.3361×10^{4}	0.5350×10^{3}	0.5350×10^{3}	0.5300×10^{3}	0.1065×10^{3}	0.4694×10^{-2}
			4	0.6660×10^{4}	0.1060×10^{4}	0.1060×10^{4}	0.1050×10^{4}	0.1055×10^{3}	0.4739×10^{-2}
			5	0.1256×10^{5}	0.2000×10^{4}	0.2020×10^{4}	0.1995×10^{4}	0.5690×10^{2}	0.8786×10^{-2}
NACA 0009 (Al) 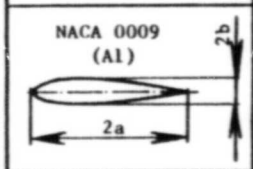	a = 1.0 b = 0.09	15.	1	0.9424×10^{2}	0.1500×10^{2}	0.2000×10^{2}	0.1500×10^{2}	0.3571×10	0.1400
			2	0.7539×10^{3}	0.1200×10^{3}	0.1200×10^{3}	0.1150×10^{3}	0.2351×10^{2}	0.2126×10^{-1}
			3	0.2167×10^{4}	0.3450×10^{3}	0.3450×10^{3}	0.3150×10^{3}	0.1102×10^{2}	0.4536×10^{-1}
			4	0.4398×10^{4}	0.7000×10^{3}	0.7000×10^{3}	0.6850×10^{3}	0.4617×10^{2}	0.8290×10^{-2}
			5	0.7005×10^{4}	0.1115×10^{4}	0.1115×10^{4}	0.1105×10^{4}	0.1110×10^{3}	0.4504×10^{-2}
Rectangular (Al) 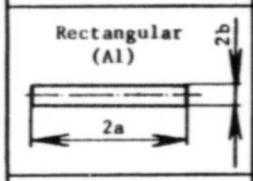	a = 1.0 b = 0.062	15.	1	0.6283×10^{2}	0.1000×10^{2}	0.2000×10^{2}	0.1500×10^{2}	0.3571×10^{2}	0.1400
			2	0.5654×10^{3}	0.9000×10^{2}	0.9000×10^{2}	0.8000×10^{2}	0.2351×10^{2}	0.2126×10^{-1}
			3	0.1696×10^{4}	0.2700×10^{3}	0.2700×10^{3}	0.2500×10^{3}	0.1102×10^{2}	0.4536×10^{-1}
			4	0.3330×10^{4}	0.5300×10^{3}	0.5300×10^{3}	0.5150×10^{3}	0.4617×10^{2}	0.1082×10^{-1}
			5	0.5497×10^{4}	0.8750×10^{3}	0.8750×10^{3}	0.8600×10^{3}	0.1110×10^{3}	0.4504×10^{-2}
Rectangular (steel) 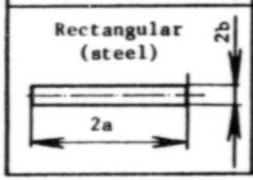	a = 1.0 b = 0.062	15.	1	0.9424×10^{2}	0.1500×10^{2}	0.1500×10^{2}	0.1000×10^{2}	0.2600×10	0.1923
			2	0.6283×10^{3}	0.1000×10^{3}	0.1000×10^{3}	0.8500×10^{2}	0.6207×10^{2}	0.8055×10^{-1}
			3	0.1790×10^{4}	0.2850×10^{3}	0.2850×10^{3}	0.2550×10^{3}	0.1800×10^{2}	0.2777×10^{-1}
			4	0.3487×10^{4}	0.5550×10^{3}	0.5600×10^{3}	0.5500×10^{3}	0.1110×10^{3}	0.4504×10^{-2}
			5	0.5780×10^{4}	0.9200×10^{3}	0.9200×10^{3}	0.9100×10^{3}	0.1830×10^{3}	0.2732×10^{-2}

ORIGINAL PAGE IS
OF POOR QUALITY

ORIGINAL PAGE IS
OF POOR QUALITY

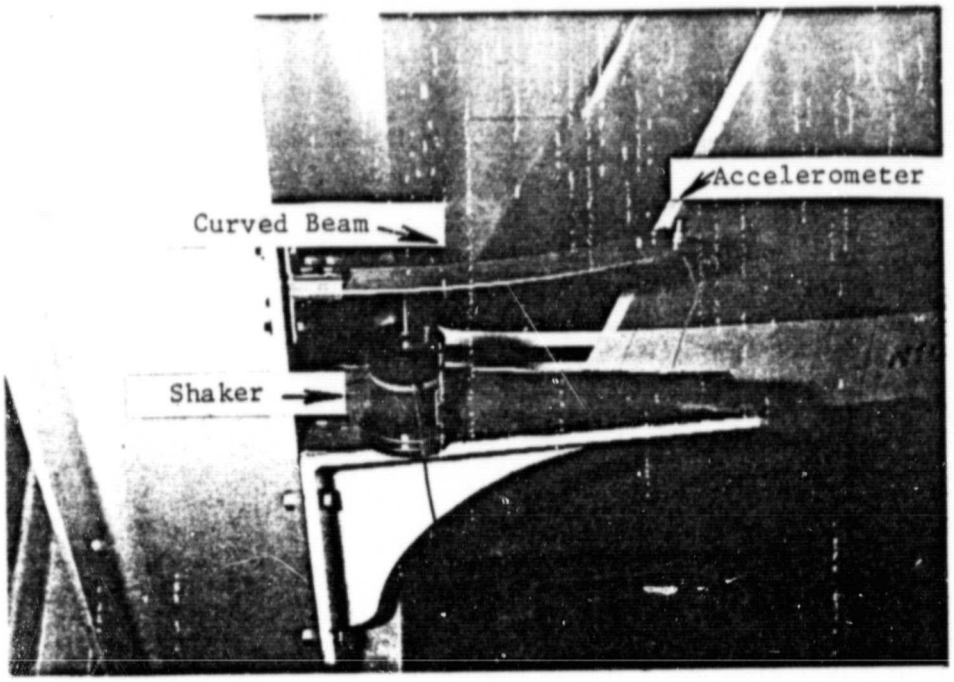

(a)

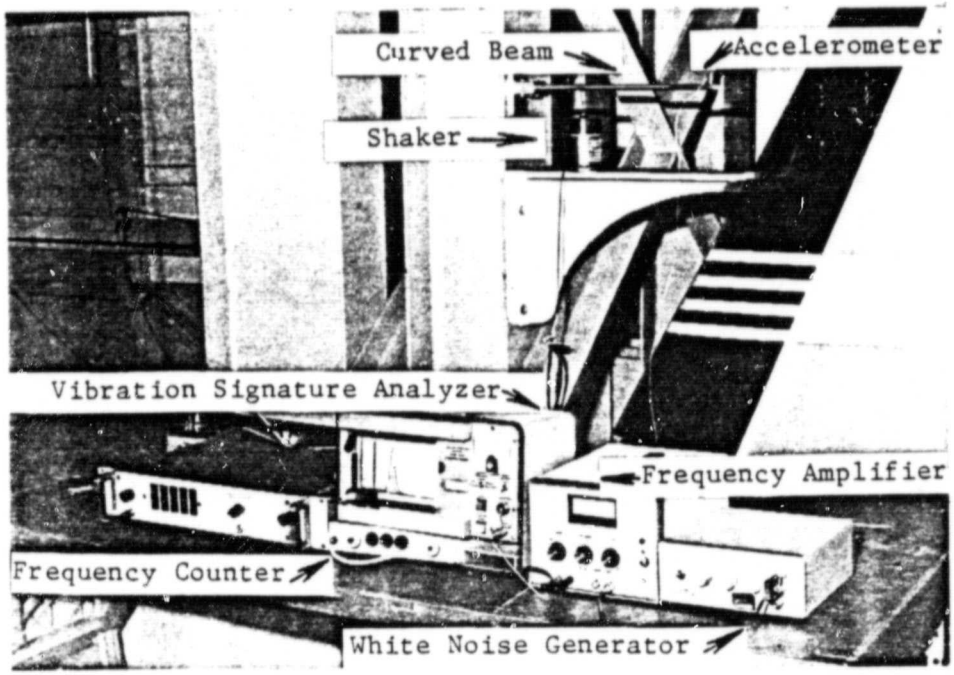

(b)

Figure 7.24. (a) A curved blade model at the test stand, (b) the test setup for measuring frequencies of a curved blade.

ORIGINAL PAGE IS
OF POOR QUALITY

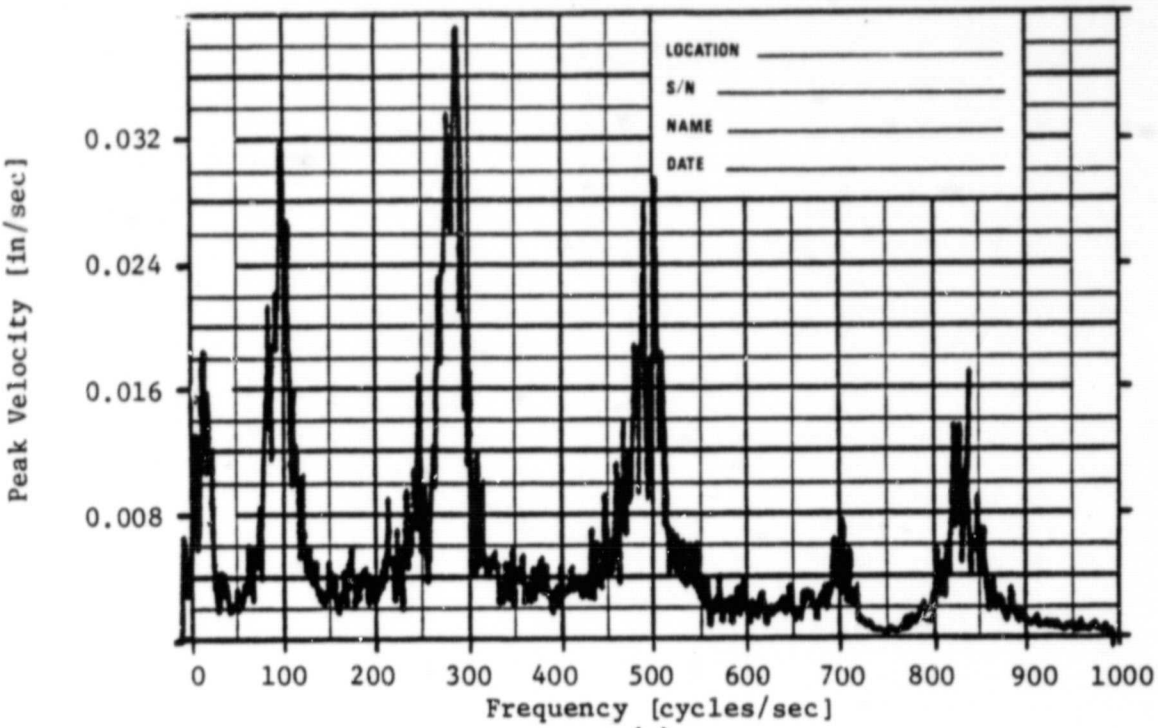

(a)

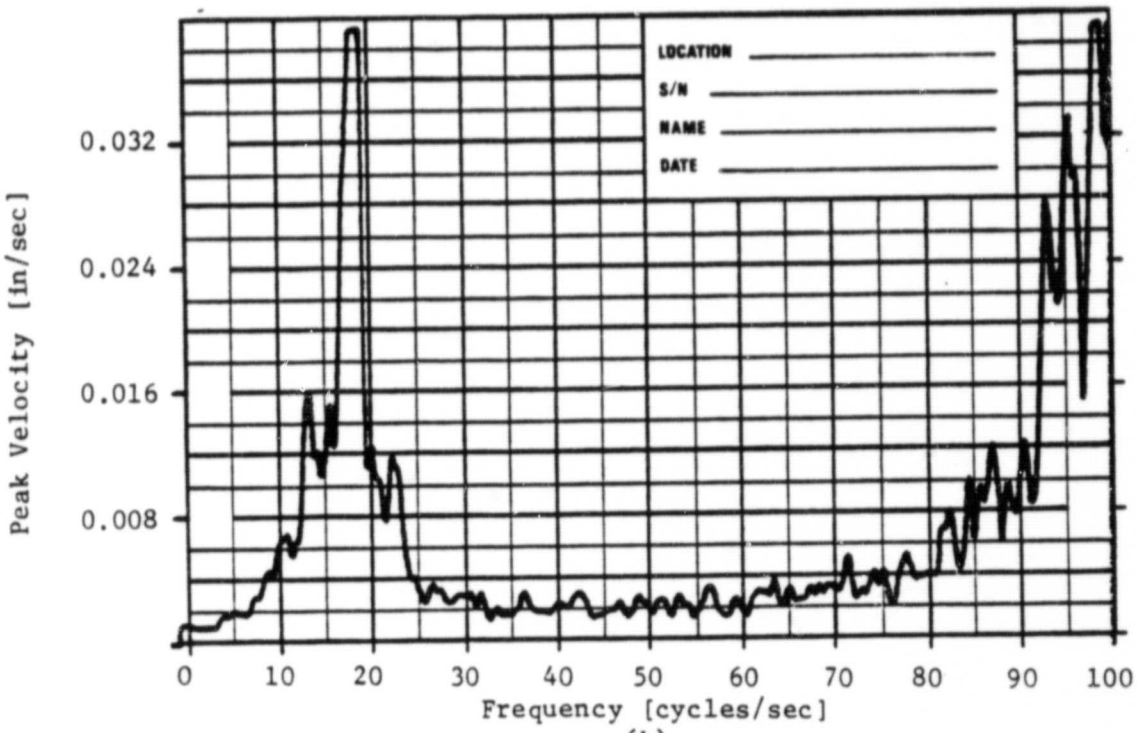

(b)

Figure 7.25. (a) Natural frequencies of a curved blade swept by a vibration analyzer over a bandwidth of 0-1000 [Hz], (b) natural frequencies swept over a bandwidth of 0-100 [Hz].

ORIGINAL PAGE IS
OF POOR QUALITY

Chapter 8

NUMERICAL MODELING AND RESULTS OF THE DYNAMIC FLEXURAL RESPONSE OF UNIFORM PROPELLER BLADES

8.1. Introduction

This chapter is a summary and discussion of the results and findings of this study. A small computer code was developed to perform a complete modal analysis of all five blade models, including the dynamic response of the models as undamped and damped multi-degree-of-freedom systems. The data obtained experimentally by using the FFT analyzer, which were analyzed in Chapter 7, will be used for a damped case. Some important results of numerical modal analysis will be shown and discussed. A very brief description of the computer program will be given in the last section. A flowchart of the computer program is given in Appendix C.

8.2. Formulation of the Equation of Motion

Since we are going to model the blades as undamped multi-degree-of-freedom free-vibration cases, the formulations of the [m] and [k] matrices are necessary. In section 5.4, we gave a detailed description of methods for deriving the mass matrix [m]. We found it convenient to assemble this matrix as a diagonal matrix having only diagonal terms and lumped masses. A schematic representation of this model is given in Fig. 8.1.

The formulation of the stiffness matrix [k] is done in the following manner. First, the matrix of flexibility influence coefficients is found; then, by inversion of this matrix, [k] is

ORIGINAL PAGE IS
OF POOR QUALITY

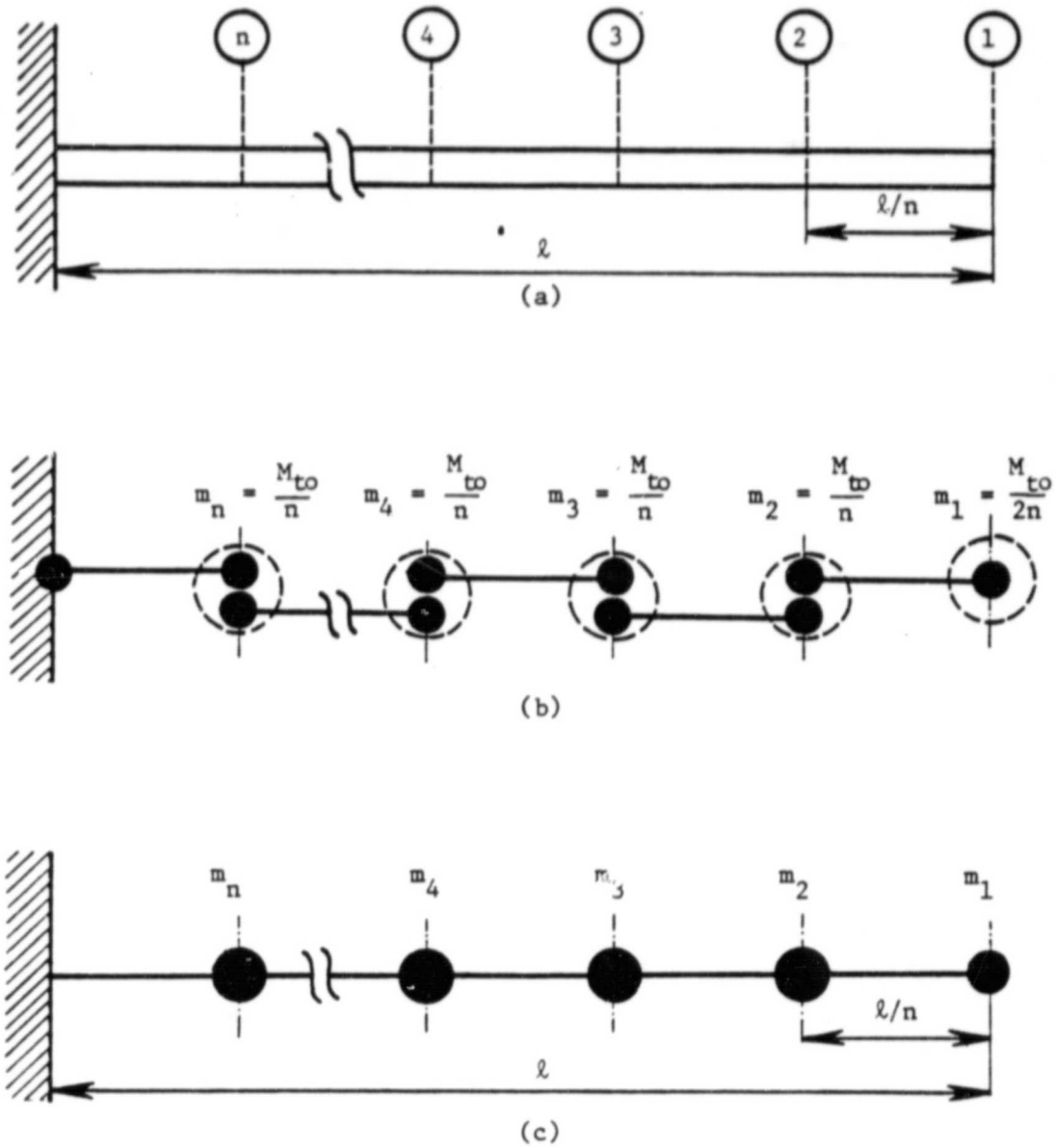

Figure 8.1. (a) Schematic of the blade model, (b) masses lumped at each node of the model segment, (c) final arrangement of the lumped masses of the blade model.

computed. Both of them have to be symmetric matrices. The matrix [k] can also be calculated by using the direct stiffness method. The computer program is capable of handling the equation system when we have a full-mass matrix [m]. The program is run for two cases: when the order of these matrices is 8x8, and when it is 10x10. The program is capable of handling larger arrays.

8.3. Eigenvalues, Natural Frequencies, and Eigenvectors

Since the accurate calculation of these parameters is very important for the dynamic analysis of the models, extreme care and rigorousness was taken in the process of setting up the algorithm of computer program. The governing equations of motion can be written as

$$[m]\{\ddot{x}(t)\} + [k]\{x(t)\} = \{0\}. \tag{8.1}$$

The Jacobi method is used to calculate all eigenvalues and corresponding eigenvectors of the generalized eigenproblem

$$[k][\phi] = \omega^2 [m][\phi]. \tag{8.2}$$

The program basically transforms the initial system of equation (8.1) into a new system having only the diagonal elements in both matrices. This is a so-called modal system of equations, using the modal mass matrix $[M]$ and modal stiffness matrix $[K]$ instead of matrices [m] and [k]. In Chapter 5, we showed that the following relationship exists:

$$[\phi][m][\phi] = [M], \tag{8.3}$$

and

$$[\phi][k][\phi] = [K] \tag{8.4}$$

where the matrix $[\phi]$ is called the modal matrix or array of eigenvectors of the system. Also, in Chapter 5 we showed that we could scale the eigenvector matrix in a certain manner to get the identity matrix $[I]$ instead of the matrix $[M]$. We established the following relations:

$$[\Phi][m][\Phi] = [I], \tag{8.5}$$

and

$$[\Phi][k][\Phi] = [\omega^2], \tag{8.6}$$

where $[\Phi]$ is the matrix of scaled eigenvectors. We showed also that it is much more convenient to work with unit masses, where we could avoid some computational expenses during the dynamic analysis of the system, especially for imposing the initial conditions of the system. We will be working with the scaled system of equations throughout the rest of the program. In order to visualize the deformation pattern, it is convenient to scale eigenvectors in a similar manner as to how unit vectors are defined. Then they have values only between zero and one, and it is easy to see the relative motion of certain points of the system in different modes. The natural frequencies are also calculated when the blades are modelled as continuous beams (Bernoulli-Euler Model). In Table 8.1, the frequencies are given for all five models for the first eight modes. Comparison is usually satisfactory among the three approaches used up to the fifth mode. A continuous system and lumped parameter system are used as numerical approaches to identify the first eight

Table 8.1. Predicted and measured natural frequencies for five blade models.

Cross Section	Results Obtained	1st-Mode	2nd-Mode	3rd-Mode	4th-Mode	5th-Mode	6th-Mode	7th-Mode	8th-Mode
		[Hz]	[Hz]	[Hz]	[Hz]	[Hz]	[Hz]	[Hz]	[Hz]
NACA 0021 (Al) 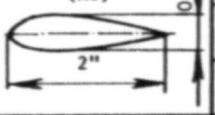	Continuous System	0.5184×10^{2}	0.3229×10^{3}	0.9091×10^{3}	0.1781×10^{4}	0.2945×10^{4}	0.4400×10^{4}	0.6146×10^{4}	0.8182×10^{4}
	Lumped Par. System	0.5145×10^{2}	0.3169×10^{3}	0.8737×10^{3}	0.1684×10^{4}	0.2732×10^{4}	0.3962×10^{4}	0.5216×10^{4}	0.6179×10^{4}
	Measured	0.4000×10^{2}	0.2650×10^{3}	0.7200×10^{3}	0.1410×10^{4}	--	--	--	--
NACA 0015 (Al) 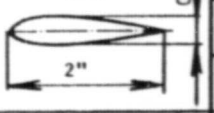	Continuous System	0.3224×10^{2}	0.2008×10^{3}	0.5654×10^{3}	0.1108×10^{4}	0.1832×10^{4}	0.2736×10^{4}	0.3822×10^{4}	0.5089×10^{4}
	Lumped Par. System	0.3208×10^{2}	0.1988×10^{3}	0.5511×10^{3}	0.1068×10^{4}	0.1747×10^{4}	0.2574×10^{4}	0.3524×10^{4}	0.4528×10^{4}
	Measured	0.3000×10^{2}	0.1900×10^{3}	0.5350×10^{3}	0.1060×10^{4}	0.1410×10^{4}	--	--	--
NACA 0009 (Al) 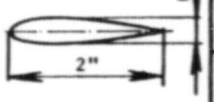	Continuous System	0.1831×10^{2}	0.1140×10^{3}	0.3211×10^{3}	0.6294×10^{3}	0.1040×10^{4}	0.1554×10^{4}	0.2171×10^{4}	0.2890×10^{4}
	Lumped Par. System	0.1817×10^{2}	0.1119×10^{3}	0.3086×10^{3}	0.5950×10^{3}	0.9652×10^{4}	0.1399×10^{4}	0.1842×10^{4}	0.2182×10^{4}
	Measured	0.1500×10^{2}	0.1200×10^{3}	0.3450×10^{3}	0.7000×10^{3}	0.1115×10^{4}	--	--	--
Rectangular (Al) 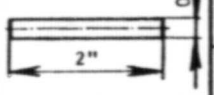	Continuous System	0.1617×10^{2}	0.1007×10^{3}	0.2836×10^{3}	0.5559×10^{3}	0.9190×10^{3}	0.1372×10^{4}	0.1917×10^{4}	0.2562×10^{4}
	Lumped Par. System	$0.160[illegible] \times 10^{2}$	0.9886×10^{3}	0.2725×10^{3}	0.5255×10^{3}	0.8524×10^{3}	0.1236×10^{4}	0.1627×10^{4}	0.1927×10^{4}
	Measured	0.1500×10^{2}	0.9027×10^{2}	0.2700×10^{3}	0.5300×10^{3}	0.8750×10^{3}	--	--	--
Rectangular (steel) 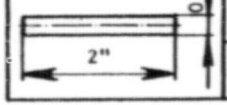	Continuous System	0.1739×10^{2}	0.1083×10^{3}	0.3050×10^{3}	0.5978×10^{3}	0.9883×10^{3}	0.1476×10^{4}	0.2062×10^{4}	0.2745×10^{4}
	Lumped Par. System	0.1726×10^{2}	0.1063×10^{3}	0.2931×10^{3}	0.5652×10^{3}	0.9168×10^{3}	0.1329×10^{4}	0.1750×10^{4}	0.2073×10^{4}
	Measured	0.1500×10^{2}	0.1000×10^{3}	0.2850×10^{3}	0.5600×10^{3}	0.9200×10^{3}	--	--	--

ORIGINAL PAGE IS
OF POOR QUALITY

frequencies. Only the first five frequencies are measured by the FFT analyzer (since the frequency range chosen was 0-2 KHz).

In Fig. 8.2, the deformation pattern is given for the first five modes (greatly exaggerated). Also, pictorial representation of every element of the modal matrix is given. This is given only for five modes, although the pattern is the same for any number of modes. In Table 8.2, the normalized mode shapes are given for blades having NACA 0015 airfoil cross sections. The system of notation corresponds exactly to the pattern given in Fig. 8.2.

8.4. Identification of Modal Parameters Including Damping

In a previous section, we showed the natural frequencies and modal shapes for some of the blade models we studied. In this section, we are going to introduce the damping measured and analyzed in Chapter 7, then perform a complete modal analysis of blade models modeled as damped multi-degree-of-freedom systems. We assume that the natural frequencies and modal shapes are not seriously affected by introducing the damping, which is valid for systems having light damping. As we described earlier, the damping ratios are measured in the first five modes. Measured data cannot be used directly in an analytical model without modification.

In Chapter 6, it was shown that we have to impose some conditions under which the modal matrix decouples the equation of motion for the damped multi-degree-of-freedom system. The damping forces could be decoupled only if the damping matrix is a linear combination of the mass matrix [m] and stiffness matrix [k]. The damping ratios are measured only in the first five modes. In the

ORIGINAL PAGE IS
OF POOR QUALITY

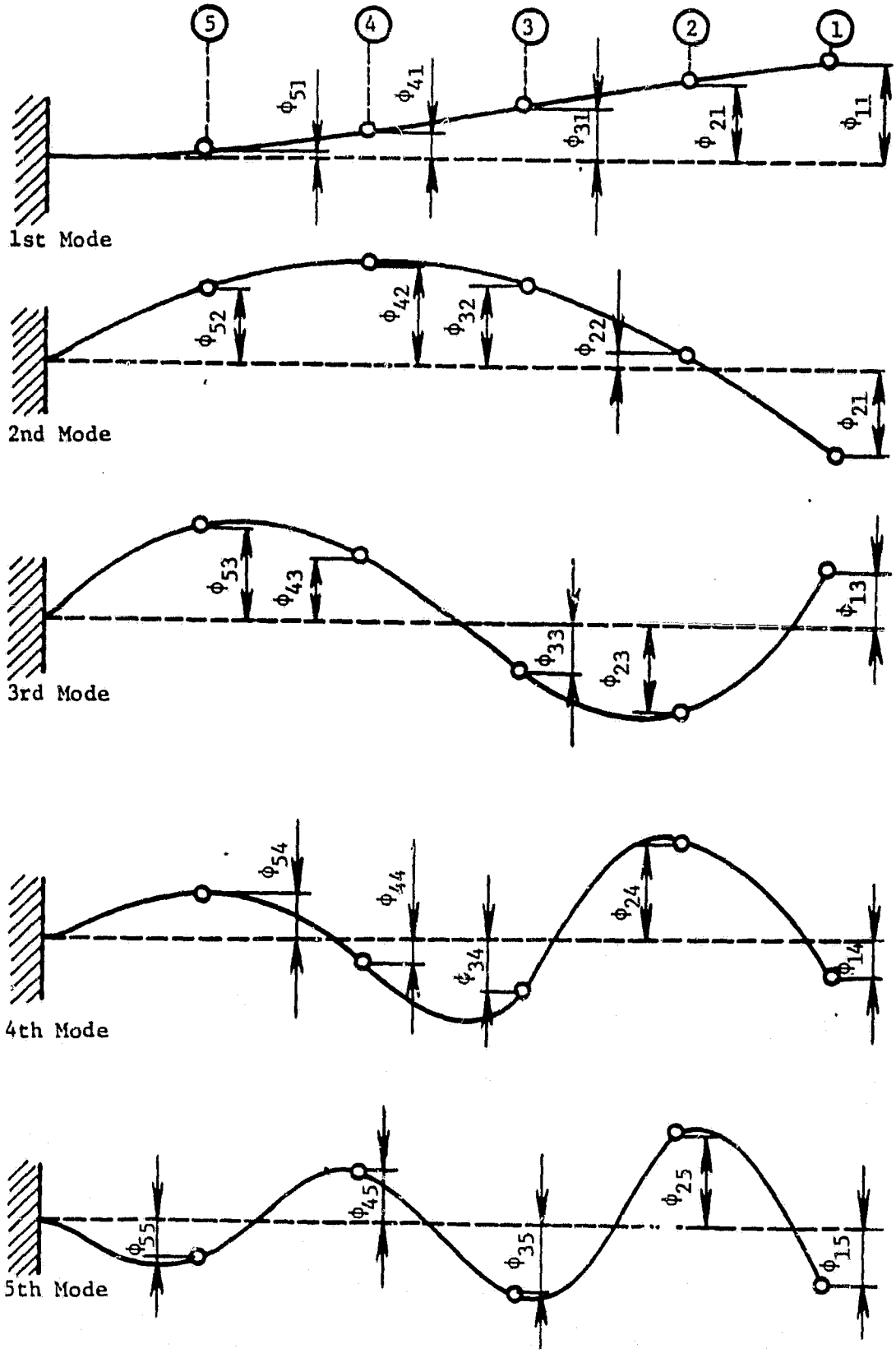

Figure 8.2. Pictorial representation of the first five modes of the blade model.

Table 8.2. The frequencies and normalized mode shapes for a blade having an NACA 0015 airfoil cross section.

Mode	1	2	3	4	5	6	7	8
Spat. location \ Freq. [Hz]	0.31946×10^{2}	0.19676×10^{3}	0.54246×10^{3}	0.10459×10^{4}	0.16965×10^{4}	0.24600×10^{4}	0.32384×10^{4}	0.38368×10^{4}
1	0.62939	-0.61039	0.57473	0.51316	0.42365	-0.31356	-0.19828	0.92111×10^{-1}
2	0.52078	-0.23483	-0.26339×10^{-1}	-0.26037	-0.40604	0.42698	0.33218	-0.17192
3	0.41338	0.10186	-0.38464	-0.35402	-0.26121×10^{-1}	-0.34314	-0.47585	0.31083
4	0.30959	0.34508	-0.32747	0.17033	0.46502	-0.12124	0.38540	-0.40867
5	0.21310	0.44992	0.47290×10^{-1}	0.45021	-0.94646×10^{-1}	-0.45814	-0.11928	0.46094
6	0.12849	0.40788	0.40624	0.36438×10^{-1}	-0.43463	-0.32749	-0.20206	-0.46135
7	0.60998×10^{-1}	0.25842	0.45428	-0.45306	0.22855	-0.13129	0.42762	0.40858
8	0.16228×10^{-1}	0.85052×10^{-1}	0.20036	-0.32439	0.43429	0.50251	-0.48727	-0.32568

ORIGINAL PAGE IS
OF POOR QUALITY

analytical model, the damping ratios in the rest of the modes are taken to be zero, and the least-squares approximation straight line fits through these points, starting at the origin. The damping ratios modeled in this manner satisfy eq. (6.13), which is rewritten here as

$$\{\Phi_i\}[c]\{\Phi_j\} = [2\omega_i\zeta_i]\delta_{ij}, \tag{8.7}$$

where ζ_i is the modal damping ratio and δ_{ij} is the Kronecker delta ($\delta_{ij} = 1$, for $i = j$, $\delta_{ij} = 0$, for $i \neq j$). Using the transformation matrix of scaled eigenvectors $[\Phi]$ and eqs. (8.5) and (8.6), the governing equation of free vibration of an undamped multi-degree-of-freedom system becomes

$$[I]\{\ddot{q}(t)\} + [2\omega\zeta]\{\dot{q}(t)] + [\omega^2]\{q(t)\} = \{0\}, \tag{(8.8)}$$

where the relation between original and modal displacements is given by

$$\{x(t)\} = [\Phi]\{q(t)\}. \tag{8.9}$$

We have defined the necessary parameters for uncoupling the equations of motion. Since we have imposed some conditions on the damping ratios obtained by measurement in order to decouple the damping forces, the related parameters such as the amplification factor, critical damping, damping in a mode, and damped natural frequencies have new values. These parameters are given for all five models in the first 8 modes in Table 8.3. Since we do not have much interest in a free vibration, most of these parameters will be used in the following section, where we are going to

Table 8.3. The modal parameters identified for the blades modeled as damped MDOF systems.

Shape	Param.	Units	Mode 1st	2nd	3rd	4th	5th	6th	7th	8th
NACA 0021 (Al) 0.42" 2"	Damp. Rat.	unitless	0.190×10^{-3}	0.117×10^{-2}	0.324×10^{-2}	0.624×10^{-2}	0.101×10^{-1}	0.146×10^{-1}	0.193×10^{-1}	0.229×10^{-1}
	Crit. Damp.	lbxsec/in	0.828	0.157	0.149	0.146	0.141	0.130	0.998	0.408
	Damp at Mode	lbxsec/in	0.158×10^{-3}	0.185×10^{-2}	0.483×10^{-2}	0.915×10^{-2}	0.143×10^{-1}	0.194×10^{-1}	0.193×10^{-1}	0.936×10^{-1}
	Ampl. Fact.	unitless	0.261×10^{4}	0.425×10^{3}	0.154×10^{3}	0.800×10^{2}	0.493×10^{2}	0.340×10^{2}	0.258×10^{2}	0.218×10^{2}
	Damp. Freq.	rad/sec	0.323×10^{3}	0.199×10^{4}	0.548×10^{4}	0.105×10^{5}	0.176×10^{5}	0.248×10^{5}	0.327×10^{5}	0.388×10^{5}
NACA 0015 (Al) 0.30" 2"	Damp. Rat.	unitless	0.312×10^{-3}	0.193×10^{-2}	0.537×10^{-2}	0.104×10^{-1}	0.170×10^{-1}	0.251×10^{-1}	0.343×10^{-1}	0.441×10^{-1}
	Crit. Damp.	lbxsec/in	0.358	0.685	0.651	0.644	0.634	0.618	0.585	0.510
	Damp at Mode	lbxsec/in	0.219×10^{-3}	0.257×10^{-2}	0.670×10^{-2}	0.126×10^{-1}	0.199×10^{-1}	0.265×10^{-1}	0.267×10^{-1}	0.129×10^{-1}
	Ampl. Fact.	unitless	0.811×10^{3}	0.131×10^{3}	0.478×10^{2}	0.247×10^{2}	0.152×10^{2}	0.105×10^{2}	0.800×10	0.675×10
	Damp. Freq.	rad/sec	0.200×10^{3}	0.123×10^{4}	0.340×10^{4}	0.657×10^{4}	0.106×10^{5}	0.154×10^{5}	0.203×10^{5}	0.240×10^{5}
NACA 0009 (Al) 0.18" 2"	Damp. Rat.	unitless	0.615×10^{-3}	0.379×10^{-2}	0.104×10^{-1}	0.201×10^{-1}	0.327×10^{-1}	0.474×10^{-1}	0.624×10^{-1}	0.739×10^{-1}
	Crit. Damp.	lbxsec/in	0.135	0.257	0.243	0.239	0.231	0.212	0.162	0.686×10^{-1}
	Damp at Mode	lbxsec/in	0.831×10^{-4}	0.977×10^{-3}	0.254×10^{-2}	0.481×10^{-2}	0.756×10^{-2}	0.100×10^{-1}	0.101×10^{-1}	0.493×10^{-2}
	Ampl. Fact.	unitless	0.812×10^{3}	0.131×10^{3}	0.478×10^{2}	0.247×10^{2}	0.152×10^{2}	0.105×10^{2}	0.800×10	0.675×10
	Damp. Freq.	rad/sec	0.114×10^{3}	0.703×10^{3}	0.193×10^{4}	0.373×10^{4}	0.606×10^{4}	0.878×10^{4}	0.115×10^{5}	0.136×10^{5}
Rectangular (Al) 0.125" 2"	Damp. Rat.	unitless	0.543×10^{-3}	0.334×10^{-2}	0.922×10^{-2}	0.177×10^{-1}	0.288×10^{-1}	0.418×10^{-1}	0.550×10^{-1}	0.652×10^{-1}
	Crit. Damp.	lbxsec/in	0.149	0.284	0.268	0.263	0.255	0.234	0.179	0.735
	Damp at Mode	lbxsec/in	0.810×10^{-4}	0.951×10^{-3}	0.247×10^{-2}	0.469×10^{-2}	0.736×10^{-2}	0.981×10^{-2}	0.990×10^{-2}	0.480×10^{-2}
	Ampl. Fact.	unitless	0.920×10^{3}	0.149×10^{3}	0.543×10^{2}	0.281×10^{2}	0.173×10^{2}	0.119×10^{2}	0.907×10	0.766×10
	Damp. Freq.	rad/sec	0.100×10^{3}	0.621×10^{3}	0.171×10^{4}	0.330×10^{4}	0.535×10^{4}	0.776×10^{4}	0.102×10^{5}	0.120×10^{5}
Rectangular (steel) 0.125" 2"	Damp. Rat.	unitless	0.815×10^{-3}	0.502×10^{-2}	0.138×10^{-1}	0.266×10^{-1}	0.433×10^{-1}	0.627×10^{-1}	0.826×10^{-1}	0.979×10^{-1}
	Crit. Damp.	lbxsec/in	0.396	0.755	0.713	0.701	0.678	0.623	0.477	0.195
	Damp at Mode	lbxsec/in	0.323×10^{-3}	0.379×10^{-2}	0.988×10^{-2}	0.187×10^{-1}	0.290×10^{-1}	0.391×10^{-1}	0.394×10^{-1}	0.191×10^{-1}
	Ampl. Fact.	unitless	0.613×10^{3}	0.995×10^{2}	0.361×10^{2}	0.187×10^{2}	0.115×10^{2}	0.796×10	0.604×10	0.510×10
	Damp. Nt. Fr.	rad/sec	0.108×10^{3}	0.668×10^{3}	0.184×10^{4}	0.354×10^{4}	0.575×10^{4}	0.833×10^{4}	0.109×10^{5}	0.129×10^{5}

ORIGINAL PAGE IS
OF POOR QUALITY

consider the dynamic response of the blade models modeled as damped and undamped multi-degree-of-freedom systems.

8.5. The Dynamic Response of Blade Models Modeled by Modal Analysis as Undamped and Damped Multi-Degree-of-Freedom Systems

In Chapter 6, we defined analytically the dynamic response of blade models modeled as multi-degree-of-freedom systems. The excitation force was assumed to be one harmonic of the Fourier series. The equation of motion for an n-degree-of-freedom system was given as

$$[m]\{\ddot{x}(t)\} + [c]\{\dot{x}(t)\} + [k]\{x(t)\} = \{F(t)\} = \frac{1}{2}\{F_0\} + \\ + \{F_{0r}\}e^{j(\omega_f t+\psi_i)}, \quad i = 1,2,3,\ldots,n. \tag{8.10}$$

Quantities $\{F_{0r}\}$ and ψ_i are defined by

$$\{F_{0r}\} = \sqrt{\{F_{os}\}^2 + \{F_{0c}\}^2}, \tag{*.11}$$

and

$$\psi_i = \arctan\left[\frac{(F_{0c})_i}{(F_{oc})_i}\right], \quad i = 1,2,3,\ldots,n. \tag{8.12}$$

The equations above are written assuming that the vector of the excitation forces can be written as

$$\{F(t)\} = \frac{1}{2}\{F_0\} + \{F_{0s}\}\sin\omega_f t + \{F_{0c}\}\cos\omega_f t. \tag{8.13}$$

Premultiplying eq. (8.10) by $[\Phi]^T$ and using linear transformation $\{x(t)\} = [\Phi]\{q(t)\}$, eq. (8.10) becomes

$$[I]\{\ddot{q}(t)\} + [2\zeta\omega]\{\dot{q}(t)\} + [\omega^2]\{q(t)\} = \frac{1}{2}[\Phi]^T\{F_0\} +$$

$$+ [\Phi]^T\{F_{0r}\}e^{j(\omega_f t+\psi_i)}, \quad i = 1,2,3,\ldots,n. \qquad (8.14)$$

This is a so-called modal equation which decouples the system of equations into n independent equations. Then we showed how to obtain the homogenous and particular solution of eq. (8.14). Finally, the displacement of the system was transformed into the original coordinate system by transformation $\{x(t)\} = [\Phi]\{q(t)\}$.

The computer code has been developed for a simpler mode (regarding the excitation forces) than the analytical model developed in Chapter 6. For the test program, it is assumed that the excitation force is of the type $F = \sin\omega_f t$, and that it acts at the tip of the blade. Also, the dynamic response (steady-state) is defined when the blades are modeled as a continuous system. The main idea in this study was to compare the response obtained by two approaches. Also, the initial conditions are assumed to be zero. The procedure of imposing initial conditions was given in Chapter 6. This could be done easily by carrying out the calculation in a matrix notation. The procedure for calculating the dynamic response is implemented in a computer code for cases when the blade models are modeled either as undamped or damped multi-degree-of-freedom systems. For an undamped case with a given excitation force and initial conditions equal zero, eq. (8.14) is reduced to

$$[I]\{\ddot{q}(t)\} + [\omega^2]\{q(t)\} = [\Phi]^T\{F_{0s}\}\sin(\omega_f t), \qquad (8.15)$$

where the term on the right-hand side represents the scaled modal force or the excitation force in a new transformed system. The steady-state response of the system given by the equation above for the r-th mode is given as

$$q_r(t) = \frac{\{\Phi_r\}^T\{F_{0s}\}}{\omega_r^2-\omega_f^2}\sin(\omega_f t),\ r = 1,2,3,\ldots,n. \tag{8.16}$$

The final displacements of masses are obtained by superposition of the response in each mode:

$$\{x(t)\} = [\Phi]\{q(t)\}. \tag{8.17}$$

For the damped case with a given excitation force and initial conditions equal zero, eq. (8.14) reduced to

$$[I]\{\ddot{q}(t)\} + [2\zeta\omega]\{\dot{q}(t)\} + [\omega^2]\{q(t)\} = [\Phi]^T\{F_{0s}\}\sin(\omega_f t). \tag{8.18}$$

The steady-state response of the system given by eq. (8.18) for the r-th mode is as follows:

$$q_r(t) = \mathrm{Im}\ \frac{\{\Phi_r\}^T\{F_{0s}\}e^{j\omega_f t}}{\omega_r^2-\omega_f^2+j2\zeta_r\omega_r\omega_f}, \tag{8.19}$$

or

$$q_r(t) = \mathrm{Im}\ \frac{\{\Phi_r\}^T\{F_{0s}\}e^{j(\omega_f t-\delta_r)}}{\sqrt{(\omega_r^2-\omega_f^2)^2+(2\zeta_r\omega_r\omega_f)^2}} \tag{8.20}$$

where

$$\delta_r = \arctan\left(\frac{2\zeta_r\omega_r\omega_f}{\omega_r^2-\omega_f^2}\right). \tag{8.21}$$

ORIGINAL PAGE IS
OF POOR QUALITY

Equation (8.20) can be written as

$$q_r(t) = \frac{\{\Phi_r\}^T\{F_{0s}\}\sin(\omega_f t-\delta_r)}{\sqrt{(\omega_r^2-\omega_f^2)^2+(2\zeta_r\omega_r\omega_f)^2}} \cdot \tag{8.22}$$

The same procedure can be applied for any of n decoupled equations of motion. The final displacement of lumped masses is as:

$$\{x(t)\} = [\Phi]\{q(t)\}. \tag{8.23}$$

8.6. Predicted Results for the Dynamic Response of Blades

In section 8.5, we gave the outline of the model used in a computer program. We decoupled the equation of motion, getting the scaled modal equation of motion. The coefficients and excitation forces of eq. (8.18) are given for all eight modes in Table 8.4. As we have already stated, the frequency of the excitation force lies between the first and second natural frequencies of the blade models.

The steady-state response is predicted by two approaches: when the system is modeled as a continuous or as a lumped parameter system. The response of the tip point along the first half of the time period of the excitation force (at 10 instants of time) is given in Table 8.5. A good agreement is obtained by the two different approaches over the entire interval of time considered.

To obtain an insight on the participation of damping in a dynamic response and relate it to the dynamic response of an undamped system, responses in both approaches are calculated along the two time periods of the excitation force. In Table 8.6, the responses are given by the two approaches when the excitation force reaches

Table 8.4. The coefficients of the decoupled equation of motion of the blade models.

Cross Section	Parameter	Units	Mode							
			1st	2nd	3rd	4th	5th	6th	7th	8th
NACA 0021 (Al) 0.42" 2"	Sc.Mod.Ms.	$lbxsec^2/in$	$0.100x10$	$0.100x10$	$0.100x10$	$0.100x10$	$0.100x10$	$0.100x10$	$0.100x10$	$0.100x10$
	Sc.Mod.Dp.	lbxsec/in	0.123	$0.468x10$	$0.178x10^4$	$0.132x10^3$	$0.126x10^4$	$0.355x10^2$	$0.348x10^3$	$0.731x10^3$
	Sc.Mod.St.	lb/in	$0.104x10^6$	$0.396x10^7$	$0.150x10^{10}$	$0.112x10^9$	$0.107x10^{10}$	$0.301x10^8$	$0.294x10^9$	$0.619x10^9$
	Sc.Mod.Fc.	lb	$0.433x10^2$	$-0.417x10^2$	$0.569x10$	$0.339x10^2$	$-0.123x10^2$	$0.388x10^2$	$0.273x10^2$	$-0.198x10^2$
	Eff. Mass	$lbxsec^2/in$	$0.128x10^{-2}$	$0.396x10^{-3}$	$0.526x10^{-5}$	$0.692x10^{-4}$	$0.152x10^{-4}$	$0.135x10^{-4}$	$0.412x10^{-4}$	$0.261x10^{-4}$
NACA 0015 (Al) 0.30" 2"	Sc.Mod.Ms.	$lbxsec^2/in$	$0.100x10$	$0.100x10$	$0.100x10$	$0.100x10$	$0.100x10$	$0.100x10$	$0.100x10$	$0.100x10$
	Sc.Mod.Dp.	lbxsec/in	0.247	$0.937x10$	$0.356x10^4$	$0.265x10^3$	$0.254x10^4$	$0.712x10^2$	$0.697x10^3$	$0.146x10^4$
	Sc.Mod.St.	lb/in	$0.402x10^5$	$0.152x10^7$	$0.581x10^9$	$0.431x10^8$	$0.418x10^9$	$0.116x10^8$	$0.113x10^9$	$0.238x10^9$
	Sc.Mod.Fc.	lb	$0.521x10^2$	$-0.501x10^2$	$0.684x10$	$0.408x10^2$	$-0.148x10^2$	$0.466x10^2$	$0.329x10^2$	$-0.238x10^2$
	Eff. Mass	$lbxsec^2/in$	$0.886x10^{-3}$	$0.274x10^{-3}$	$0.364x10^{-5}$	$0.478x10^{-4}$	$0.105x10^{-4}$	$0.940x10^{-4}$	$0.285x10^{-4}$	$0.181x10^{-4}$
NACA 0009 (Al) 0.18" 2"	Sc.Mod.Ms.	$lbxsec^2/in$	$0.100x10$	$0.100x10$	$0.100x10$	$0.100x10$	$0.100x10$	$0.100x10$	$0.100x10$	$0.100x10$
	Sc.Mod.Dp.	lbxsec/in	0.140	$0.533x10$	$0.202x10^4$	$0.150x10^3$	$0.144x10^4$	$0.405x10^2$	$0.366x10^3$	$0.834x10^3$
	Sc.Mod.St.	lb/in	$0.130x10^5$	$0.494x10^6$	$0.188x10^9$	$0.139x10^8$	$0.134x10^9$	$0.376x10^7$	$0.367x10^8$	$0.773x10^8$
	Sc.Mod.Fc. (sine Fc.)	lb	$0.638x10^2$	$-0.614x10^2$	$0.838x10^2$	$0.499x10^2$	$-0.181x10^2$	$0.571x10^2$	$0.403x10^2$	$-0.291x10^2$
	Eff. Mass	$lbxsec^2/in$	$0.591x10^{-3}$	$0.183x10^{-3}$	$0.243x10^{-5}$	$0.319x10^{-4}$	$0.703x10^{-5}$	$0.627x10^{-4}$	$0.190x10^{-4}$	$0.120x10^{-4}$
Rectangular (Al) 0.125" 2"	Sc.Mod.Ms.	$lbxsec^2/in$	$0.100x10$	$0.100x10$	$0.100x10$	$0.100x10$	$0.100x10$	$0.100x10$	$0.100x10$	$0.100x10$
	Sc.Mod.Dp.	lbxsec/in	0.109	$0.415x10$	$0.158x10^4$	$0.117x10^3$	$0.112x10^4$	$0.316x10^2$	$0.309x10^3$	$0.650x10^3$
	Sc.Mod.St.	lb/in	$0.101x10^5$	$0.385x10^6$	$0.146x10^9$	$0.109x10^8$	$0.104x10^9$	$0.293x10^7$	$0.286x10^8$	$0.603x10^8$
	Sc.Mod.Fc. (sine Fc.)	lb	$0.570x10^2$	$-0.549x10^2$	$0.749x10$	$0.447x10^2$	$-0.162x10^2$	$0.510x10^2$	$0.360x10^2$	$-0.261x10^2$
	Eff. Mass	$lbxsec^2/in$	$0.739x10^{-3}$	$0.228x10^{-3}$	$0.303x10^{-5}$	$0.399x10^{-4}$	$0.879x10^{-5}$	$0.784x10^{-4}$	$0.238x10^{-4}$	$0.150x10^{-4}$
Rectangular (Steel) 0.125" 2"	Sc.Mod.Ms.	$lbxsec^2/in$	$0.100x10$	$0.100x10$	$0.100x10$	$0.100x10$	$0.100x10$	$0.100x10$	$0.100x10$	$0.100x10$
	Sc.Mod.Dp.	lbxsec/in	0.117	$0.447x10$	$0.170x10^4$	$0.126x10^3$	$0.121x10^4$	$0.339x10^2$	$0.332x10^3$	$0.699x10^3$
	Sc.Mod.St.	lb/in	$0.117x10^5$	0.446	$0.169x10^9$	$0.126x10^8$	$0.120x10^9$	$0.339x10^7$	$0.331x10^8$	$0.697x10^8$
	Sc.Mod.Fc. (sine Fc.)	lb	$0.363x10^2$	$-0.349x10^2$	$0.476x10$	$0.284x10^2$	$-0.103x10^2$	$0.324x10^2$	$0.229x10^2$	$-0.166x10^2$
	Eff. Mass	$lbxsec^2/in$	$0.182x10^{-2}$	$0.565x10^{-3}$	$0.750x10^{-5}$	$0.987x10^{-4}$	$0.217x10^{-4}$	$0.193x10^{-3}$	$0.588x10^{-4}$	$0.372x10^{-4}$

ORIGINAL PAGE IS
OF POOR QUALITY

Table 8.5. The dynamic responses of the tips of the blades subjected to a harmonic force of $F = \sin\omega_f t$ at the tip, $\omega_f = 400$ [rad/sec](continuous and lumped parameter modeling, half-cycle of the forcing function).

		Response of the tip of the blade during the first half-period of the forcing function [in]									
	No. of Time Int.	1	2	3	4	5	6	7	8	9	10
	Time [sec]	0.800×10^{-3}	0.160×10^{-2}	0.240×10^{-2}	0.310×10^{-2}	0.390×10^{-2}	0.470×10^{-2}	0.550×10^{-2}	0.630×10^{-2}	0.710×10^{-2}	0.790×10^{-2}
NACA 0021 (Al)	Continuous System	-0.107×10^{-1}	-0.203×10^{-1}	-0.280×10^{-1}	-0.330×10^{-1}	-0.347×10^{-1}	-0.330×10^{-1}	-0.280×10^{-1}	-0.203×10^{-1}	-0.107×10^{-1}	-0.879×10^{-7}
	Lumped Par. Sys.	-0.103×10^{-1}	-0.196×10^{-1}	-0.269×10^{-1}	-0.317×10^{-1}	-0.333×10^{-1}	-0.317×10^{-1}	-0.269×10^{-1}	-0.196×10^{-1}	-0.103×10^{-1}	-0.846×10^{-7}
NACA 0015 (Al)	Continuous System	-0.644×10^{-2}	-0.122×10^{-1}	-0.168×10^{-1}	-0.198×10^{-1}	-0.208×10^{-1}	-0.198×10^{-1}	-0.168×10^{-1}	-0.122×10^{-1}	-0.644×10^{-2}	-0.528×10^{-7}
	Lumped Par. Sys.	-0.637×10^{-2}	-0.121×10^{-1}	-0.166×10^{-1}	-0.196×10^{-1}	-0.206×10^{-1}	-0.196×10^{-1}	-0.166×10^{-1}	-0.121×10^{-1}	-0.637×10^{-1}	-0.522×10^{-7}
NACA 0009 (Al)	Continuous System	-0.466×10^{-2}	-0.887×10^{-2}	-0.122×10^{-1}	-0.1430×10^{-1}	-0.151×10^{-1}	-0.143×10^{-1}	-0.122×10^{-1}	-0.887×10^{-1}	-0.466×10^{-2}	-0.382×10^{-7}
	Lumped Par. Sys.	-0.472×10^{-2}	-0.898×10^{-2}	-0.123×10^{-1}	-0.145×10^{-1}	-0.152×10^{-1}	-0.145×10^{-1}	-0.123×10^{-1}	-0.898×10^{-2}	-0.472×10^{-2}	-0.387×10^{-7}
Rect. (Al)	Continuous System	-0.216×10^{-2}	-0.412×10^{-2}	-0.567×10^{-2}	-0.667×10^{-2}	-0.701×10^{-2}	-0.667×10^{-2}	-0.567×10^{-2}	-0.412×10^{-2}	-0.216×10^{-2}	-0.177×10^{-2}
	Lumped Par. Syst.	-0.222×10^{-2}	-0.422×10^{-2}	-0.581×10^{-2}	-0.683×10^{-2}	-0.719×10^{-2}	-0.683×10^{-2}	-0.581×10^{-2}	-0.422×10^{-2}	-0.222×10^{-2}	-0.182×10^{-7}
Rect. (Steel)	Continuous System	-0.128×10^{-2}	-0.243×10^{-2}	-0.335×10^{-2}	-0.394×10^{-2}	-0.414×10^{-2}	-0.394×10^{-2}	-0.335×10^{-2}	-0.243×10^{-2}	-0.128×10^{-2}	-0.105×10^{-7}
	Lumped System	-0.130×10^{-2}	-0.247×10^{-2}	-0.340×10^{-2}	-0.400×10^{-2}	-0.421×10^{-2}	-0.400×10^{-2}	-0.340×10^{-2}	-0.247×10^{-2}	-0.130×10^{-2}	-0.106×10^{-7}

ORIGINAL PAGE IS OF POOR QUALITY

its peak. The displacements are given at eight stations along the blade. Also, the ratios of undamped and damped responses at all stations are given. This is one of the most important findings we have obtained so far, for it shows how much less the response of the damped system is as compared to that of the undamped system. For our models, at the excitation frequency of 400 [rad/sec], this ratio is about 1:20. We cannot take this information as the definite parameter of our system, it is only true when the system is driven at a frequency of 400 [rad/sec]. At different frequencies, this ratio will be different, and generally it will tend to increase if we are driving the system closer to the natural frequency. For our models, this ratio is fairly high. Knowing that the low natural frequencies are closely spaced, when we are driving the system between the first and second natural frequencies we are fairly close to the resonance where damping becomes a very important parameter of the system. Also, for the thickest blade, we get a very uniform ratio between the undamped and damped responses at the stations along the blade. When thinner blades are used, this ratio is not so well (uniformly) distributed. Taking into account the geometrical and material characteristics of the blade, and the condition of the dynamic load (the amplitude of the excitation force is 1 lb.), we might be very close to the borderline of the elastic range of the blades.

Also, another very important observation is that when the blades are driven (numerically) at a frequency less than the first natural frequency, the response of the blades at stations along the length is

very close to the static displacement of the load at that instant of time. In other words, the response of the system at the frequencies below the first natural frequency is directly dependent on the stiffness of the system. At frequencies higher than the first but not close to the second natural frequency, the response depends on the mass of the system. This is very well documented in Table 8.6 for all blade models.

From the results above, we can make a very important statement about the resonant motion of mechanical vibratory systems with widely-spaced modes. Basically, each resonance is characterized by three zones of activity. At frequencies below the resonance, the activity of the structural system is controlled by stiffness terms, which are proportional to the displacement and contain phases. At the resonant frequency, all restoring forces come from the damping terms, which are proportional to the velocity of the driving point. At frequencies above the resonance, the restoring force is dominated by the inertial mass terms, which are proportional to the acceleration at the driving point.

Table 8.6. Ratios between undamped and damped response when the forcing function reaches a peak. The blade was forced by the $F = \sin\omega_f t$ at the tip, $\omega = 400$ [rad/sec].

			Station							
	Parameter	Units	1st	2nd	3rd	4th	5th	6th	7th	8th
NACA 0021 (Al) 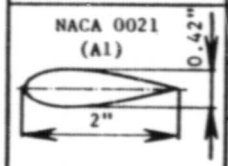	Undamped Response	in	-0.333×10^{-1}	-0.278×10^{-1}	-0.223×10^{-1}	-0.169×10^{-1}	-0.118×10^{-1}	-0.719×10^{-2}	0.344×10^{-2}	-0.924×10^{-3}
	Damped Response	in	-0.176×10^{-2}	-0.145×10^{-2}	0.115×10^{-2}	-0.864×10^{-3}	-0.594×10^{-3}	-0.358×10^{-3}	0.169×10^{-3}	-0.451×10^{-4}
	Undamped / Damped	unitless	0.189×10^{2}	0.191×10^{2}	0.193×10^{2}	$0.19\ \times10^{2}$	0.198×10^{2}	0.200×10^{2}	0.202×10^{2}	$0.2\ 4\times10^{2}$
NACA 0015 (Al) 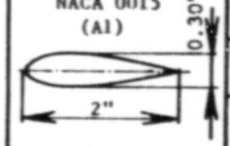	Undamped Response	in	-0.206×10^{-1}	-0.181×10^{-1}	-0.153×10^{-1}	-0.122×10^{-1}	-0.899×10^{-2}	-0.573×10^{-2}	-0.285×10^{-2}	-0.792×10^{-3}
	Damped Response	in	-0.115×10^{-2}	-0.931×10^{-3}	-0.717×10^{-3}	-0.516×10^{-3}	-0.340×10^{-3}	-0.195×10^{-3}	-0.886×10^{-4}	-0.225×10^{-4}
	Undamped / Damped	unitless	0.178×10^{2}	0.194×10^{2}	0.214×10^{2}	0.237×10^{2}	0.264×10^{2}	0.292×10^{2}	0.322×10^{2}	0.352×10^{2}
NACA 0009 (Al) 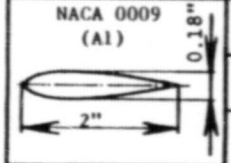	Undamped Response	in	-0.152×10^{-1}	-0.187×10^{-1}	-0.207×10^{-1}	-0.204×10^{-1}	-0.174×10^{-1}	-0.125×10^{-1}	-0.687×10^{-2}	-0.205×10^{-2}
	Damped Response	in	-0.128×10^{-2}	-0.768×10^{-3}	-0.297×10^{-3}	-0.609×10^{-4}	-0.260×10^{-3}	-0.294×10^{-3}	-0.203×10^{-3}	0.700×10^{-6}
	Undamped / Damped	unitless	0.118×10^{2}	0.244×10^{2}	0.698×10^{2}	0.334×10^{2}	0.671×10^{2}	0.427×10^{2}	0.337×10^{2}	0.293×10^{2}
Rectangular (Al) 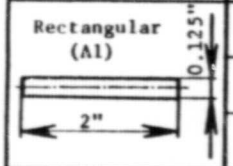	Undamped Response	in	-0.718×10^{-2}	-0.130×10^{-1}	-0.172×10^{-1}	-0.186×10^{-1}	-0.169×10^{-1}	-0.127×10^{-1}	-0.716×10^{-2}	-0.217×10^{-2}
	Damped Response	in	-0.142×10^{-2}	-0.727×10^{-3}	-0.104×10^{-3}	-0.354×10^{-3}	-0.579×10^{-3}	-0.560×10^{-3}	-0.365×10^{-3}	0.121×10^{-3}
	Undamped / Damped	unitless	0.505×10^{2}	0.207×10^{2}	0.193×10^{2}	0.604×10^{2}	0.338×10^{2}	0.262×10^{2}	0.226×10^{2}	0.206×10^{2}
Rectangular (Steel) 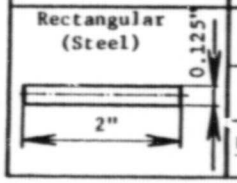	Undamped Response	in	-0.421×10^{-2}	-0.578×10^{-2}	-0.681×10^{-2}	-0.693×10^{-2}	-0.608×10^{-2}	-0.444×10^{-2}	-0.245×10^{-2}	-0.703×10^{-3}
	Damped Response	in	-0.600×10^{-3}	-0.337×10^{-3}	-0.100×10^{-3}	-0.779×10^{-4}	-0.171×10^{-3}	-0.177×10^{-3}	0.118×10^{-3}	0.402×10^{-4}
	Undamped / Damped	unitless	0.667×10	0.169×10^{2}	0.647×10^{2}	0.845×10^{2}	0.337×10^{2}	0.238×10^{2}	0.196×10^{2}	0.174×10^{2}

ORIGINAL PAGE IS OF POOR QUALITY

Chapter 9

CONCLUSIONS

An analytical model and the experimental results have been obtained for prediction of the torsional stiffness of five blade models having NACA four-digit symmetrical airfoil cross sections. These five models, three with the airfoil cross sections and two with rectangular cross sections (aluminum and steel), were modeled by modal analysis as either undamped or damped multi-degree-of-freedom systems. The complete identification of modal parameters for both cases was carried out.

The dynamic response of undamped and damped blades was calculated. The excitation force $F(t) = \sin(\omega_f t)$ was acting at the tip of the beam. The natural frequencies and damping at particular modes were obtained by testing with a Nicolet 660A Dual-Channel Vibration Analyzer. Based on the measured data, the analytical model was used to model damping in such a manner as to get a decoupled equation of motion. A small code was developed to identify all modal parameters and to predict the dynamic response of undamped and damped blade models which were modeled as multi-degree-of-freedom systems.

From the analytical, experimental, and numerical phases of this study, the following conclusions can be made:

1. Fairly accurate results were obtained for the torsional stiffness of blade models having NACA four-digit symmetrical airfoil cross sections.

2. The results for torsional stiffness have been scaled in non-dimensional form, such that for any model of an arbitrary length having a NACA four-digit cross section, the torsional constant can be calculated as product of the torsional stiffness, the scaling factor, and the reciprocal value of the length.

3. Predicted values of natural frequencies were in good agreement with experimental results obtained by the FFT analyzer.

4. The modal parameters were identified when either undamped or damped blade models were considered. They were essential for dynamic analysis of multi-degree-of-freedom systems.

5. A good agreement was obtained between the continuous and lumped parameter models for the dynamic response of the blade when the tip of the blade was subjected to a harmonic force of $F(t) = \sin(\omega_f t)$.

6. The dynamic response of the five blade models was predicted using the same excitation force. The damping obtained in the experimental phase was modeled analytically and included in the calculation of dynamic response.

7. A comparison of undamped and damped responses of the blades was made for the same load conditions. The ratio was determined, and was very much dependent on the forcing frequency and the amount of damping in the system.

8. A much better insight into the damping of aluminum blades and its influence on the dynamic response of blades was obtained. This is of special interest when considering a system driven on high frequencies which are fairly close to resonance.

Several recommendations for future work can be made from this study, as follows:

1. Since the torsional vibration mode has to be considered in propeller, rotor, and turbomachinery blade dynamics, accurate calculation of torsional stiffness is of special interest. This study could be used as a basis for the development of a small finite-element code using Galerkin's method. Experience has shown that this method is more accurate and universal than other approximate methods in boundary-value problems. References such as Richards (62), Vemuri and Karplus (88), Segerlind (73), and Rao (61) give a very elaborate treatment of boundary-value problems by employing the finite-element approach and Galerkin's approach.

2. With the information on the amount of damping in the system provided in this study, this model can be related to another model which may be more convenient in application. The best way to relate the two models is to equate the dissipation of energy per cycle for both models. Knowing the damped dynamic response, the damping constants of dashpots located at the nodal points could be calculated.

3. For the experimental phase, it is recommended that a modern FFT analyzer be adapted for modal analysis in structural dynamics, with an option in the methods for identification of modal parameters. Using these analyzers, one would be able to visualize the system and to observe the deformation pattern during different load conditions (transient and steady state).

4. The concepts of this study for the analytical and experimental phases can be used for identification of modal

parameters in the torsional mode of vibration. With a slight modification, the computer program is capable of handling the torsional vibration on a full scale.

5. The most difficult task one faces is to develop gradually the analytical and computational procedure for dynamic response of real blades. In order to accomplish that, one must consider the complicated geometry of blades, the strong coupling between flexural and torsional nodes of vibration, centrifugal stiffening, the effect of the Coriolis force for thin and long blades, and unsteady excitation forces varying along the length and azimuth of blades.

BIBLIOGRAPHY

1. Asher, G. W., "Dynamics and Aeroelasticity," Proc. Nat. Specialists Meeting (Inst. Aeronautical Science), Ft. Worth, Texas, 1958.

2. Ayre, R. S. and Morosow, G., "Modal Test and Analysis," The Shock and Vibration Bulletin, Vol. 44, August 1974.

3. Bathe, K. J., Numerical Methods in Finite Element Analysis, Prentice-Hall, Inc., Englewood Cliffs, N.J., 1976.

4. Bisplinghoff, R. L., Ashley, H., and Halfman, R. L., Aeroelasticity, Addison-Wesley Publishing Co., 1965.

5. Brown, D. L. and Halvorsen, W. G., "Impulse Technique for Structural Frequency Response Testing," Sound and Vibration, November 1977.

6. Caughey, T. L., "Classical Normal Modes in Damped Linear Dynamic Systems," Journal of Applied Mechanics, Vol. 27, 1960.

7. Chou, P. C. and Pagano, N., Elasticity, D. Van Nostrand Co., New York, 1967.

8. Clough, R. W. and Penzien, J., Dynamics of Structures, McGraw-Hill Inc., New York, 1975.

9. Cook, R. D., Concepts and Applications of Finite Element Analysis, John Wiley & Sons, New York, 1981.

10. Craig, R. R., Structural Dynamics: An Introduction To Computer Methods, John Wiley & Sons, New York, 1981.

11. Crandal, S. H., Engineering Analysis, McGraw-Hill, Inc., New York, 1956.

12. Dowell, E. H. and Klein, L. R., "Analysis of Modal Damping by Component Modes Using Langrange Multipliers," Journal of Applied Mechanics, June 1974.

13. Duncan, W. J., "Application of the Galerkin Method to the Torsion and Flexure of Cylinders and Prisms," Philosophical Magazine, Ser. 7, Vol. 25, 1938.

14. Dym, C. L. and Shames, I. H., Solid Mechanics (A Variational Approach), McGraw-Hill, Inc., New York, 1973.

15. Finlayson, B. A. and Scriven, L. E., "The Method of Weighted Residuals--A Review," Applied Mechanics Review, Vol. 19, No. 9, 1966.

16. Halvorsen, W. G. and Bendat, J. S., "Noise Source Identification Using Coherent Output Power Spectra," Sound and Vibration, August 1975.

17. Harris, F. J., "On the Use of Windows for Harmonic Analysis with the Discrete Fourier Transform," Proceedings of the IEEE, Vol. 66, No. 1, January 1978.

18. Harris, F. J.. "Trigonometric Transforms: A Unique Introduction to the FFT," Structural Dynamics Co., Technical Publication DSP-005, October 1977.

19. Hartog, J. P. D., Advanced Strength of Materials, McGraw-Hill Inc., New York, 1952.

20. Hewlett-Packard Co., "Digital Auto Power Spectrum Measurement," Application Note 140-4, September 1974.

21. Hewlett-Packard Co., "The Fundamentals of Signal Analysis," Application Note 243, November 1981.

22. Hewlett-Packard Co., "Improving the Accuracy of Structural Response Measurements," Application Note 240-2, May 1980.

23. Hieber, G., "The Fundamentals of Vibration Testing," Institute of Environmental Sciences Tutorial Lecture, Series-Dynamics, RCA Astro-Electronics Division, Princeton, N.J., 1971.

24. Hou, S. N., "Review of a Modal Synthesis Technique, A New Approach," Shock and Vibration Bulletin, No. 40, Part 4, 1969.

25. Huebner, K. H., The Finite Element Method for Engineers," John Wiley and Sons, Inc., New York, 1975.

26. Hutton, S. G., and Anderson, D. L., "Finite Element Method: A Galerkin Approach," Journal of the Engineering Mechanics Division, Proceedings of ASCE, Vol. 97, No. EM5, 1971.

27. Karman, V. T., and Biot, M., Mathematical Methods in Engineering, McGraw-Hill, Inc., New York, 1940.

28. Keller, A. C., "Considerations in the Analysis of Arbitrary Waveforms," Spectral Dynamics Co., Technical Publication No. PS-2, April 1967.

29. Keller, A. C., "Fundamentals for Mechanical Impedance Analysis," Spectral Dynamics Co., Technical Publication No. M-2, July 1967.

30. Keller, A. C., "Vector Component Technique: A Modern Way to Measure Modes," Reprinted from Sound and Vibration by Spectral Dynamics Co., n.d.

31. Kenedy, C. C. and Pancy, C. D. P., "Use of Vectors in Vibration Measurement and Analysis," Journal of Aeronautical Sciences, Vol. 14, No. 11, 1947.

32. Klosterman, A. L., "A Combined Experimental and Analytical Procedure for Improving Automotive System Dynamics," SAE 720093, January 1972.

33. Klosterman, A. L., "Dynamic Analysis and Simulation of Complex Structures," Structural Dynamics Research Co., Cincinnati, Ohio, 1972.

34. Klosterman, A. L., "On the Experimental Determination and Use of Modal Representation of Dynamic Characteristics," Ph.D. Thesis, University of Cincinnati, 1971.

35. Klosterman, A. L. and Peterson, E. L., "Obtaining Good Results from an Experimental Modal Survey," Technical Paper Presented at the 1977 Symposium of the Society of Environmental Engineers, London, England.

36. Klosterman, A. L. and Zimmerman, R., "Modal Survey Activity Via Frequency Response Functions," National Aerospace Engineering Meeting, Culver City, Los Angeles, November 1975.

37. Lally, R. W., "Gravimetric Calibration of Accelerometers," PCB Co. Application Note, n.d.

38. Lally, R. W., "Hammer Calibration," PCB Co. Technical Note 291481, February 1980.

39. Lang, G. F., "Shake, Rattle or Rap," Nicolet Scientific Co., Application Note 10, 1978.

40. Lang, G. F., "Understanding Vibration Measurements," Nicolet Scientific Co., Application Note 9, 1978.

41. Lang, G. F. and Flannelly, W. G., "Modal Analysis for Managers," Sound and Vibration, 1979.

42. Lewis and Wrisley, "A System for the Excitation of Pure Natural Modes of Complex Structures," Journal of the Aeronautical Sciences, Volume 17, November 1950.

43. Lorentz, R. D., "Applied Vibration Engineering," Union College Short Course, February 15-17, 1982.

44. Marguerre, K. and Wolfel, K., Mechanics of Vibration, Sijthoff & Noordhoff International Publishers, Rockville, MD, 1979.

45. Martinovic, Z. N., "A Study of the Dynamic Behavior of Propeller Blades," M.S. Thesis, Department of Aerospace Engineering, The Pennsylvania State University, March 1979.

46. McKinley, J. W., Fundamentals of Stress Analysis, Matrix Publishers, Inc., 1979.

47. McNitt, R. P., Notes on Variational and Energy Methods in Mechanics, Department of Engineering Mechanics, The Pennsylvania State University, 1982.

48. Meirowitch, L., Analytical Methods in Vibration, The MacMillan Co., New York, 1967.

49. Meirowitch, L., Computational Methods in Structural Dynamics, Sijthoff & Noordhoff, Rockville, MD, 1980.

50. Mitchell, L. D. and Lynch, G. A., "Origins of Noise," Machine Design, May 1, 1969.

51. Nicolet Scientific Co., "Instruction Manual for the Structural Analysis System, Model 6602."

52. Nicolet Scientific Co., "Instruction Manual for the Structural Modification Program."

53. Nicolet Scientific Co., "Making Sense of Vibration Measurement: A Practical Discussion of Vibration Transducers and Calibration," Application Note 17, July 1981.

54. Nicolet Scientifc Co., "Signal Processing and Dual Channel Guide," n.d.

55. Oden, J. T. and Ripperger, E. A., Mechanics of Elastic Structures, 2nd Edition, McGraw-Hill, Inc., 1982.

56. Paz, M., Structural Dynamics (Theory and Computation), Van Nostrand Reinhold Co., New York, 1980.

57. Pestel, C. E. and Leckie, F. A., Matrix Methods in Elastomechanics, McGraw-Hill, Inc., New York, 1963.

58. Potter, R., "Application of Digital Signal Analysis Techniques," Hewlett-Packard Co. Application Note, 1975.

59. Potter, R., "A General Theory of Modal Analysis for Linear Systems," The Shock and Vibration Digest, November 1975.

60. Ramsey, K. A., "Effective Measurements for Structural Dynamics Testing," Parts I and II, Sound and Vibration, Vol. 10, April 1976.

61. Rao, S. S., The Finite Element Method in Engineering, Pergamon Press Ltd., Headington Hill Hall, Oxford OX3 OBW, England, 1982.

62. Richards, T. H., Energy Methods in Stress Analysis, Ellis Harwood Limited Co., London, 1977.

63. Richardson, M. H., "Fundamentals of the Discrete Fourier Transform," Journal of Sound and Vibration, March 1978.

64. Richardson, M. H., "Modal Analysis Using Digital Test Systems," Seminar on Understanding Digital Control and Analysis in Vibration Test Systems, Shock and Vibration Information Center Publication, Naval Research Lab., Washington, D.C., May 1975.

65. Richardson, M. H. and Kniskern, J., "Identifying Modes of Large Structures from Multiple Input and Response Measurement," SAE Aerospace Engineering and Manufacturing Meeting Proceedings, San Diego, 1976.

66. Richardson, M. H. and Potter, R., "Identification of the Modal Properties of an Elastic Structure from Measured Transfer Function Data," Presented at the 20th International Instrumentation Symposium, Albuquerque, New Mexico, May 1974.

67. Richardson, M. H. and Ramsey, K. A., "Integration of Dynamic Testing into the Product Design Cycle," Journal of Sound and Vibration, November 1981.

68. Richardson, M. H. and Potter, R., "Mass, Stiffness, and Damping Matrices from Measured Modal Parameters," International Instrumentation-Automation Conference Exhibit, New York City, October 1974.

69. Rieger, N. F., Practical Vibration Analysis, Stress Technology Incorporated, Rochester, N.Y., 1982.

70. Rizai, M. H., "The Impact of Modal Analysis on the Engineering Curriculum," M.S. Thesis, Department of Mechanical Engineering, Michigan State University, 1980.

71. Rockland System Co., "Analog-to-Digital Conversion, Anti-Aliasing, and Windowing," March 1974.

72. Russell, R. H. and Deel, J. C., "Modal Analysis: Trouble-Shooting to Product Design," Sound and Vibration, November 1977.

73. Segerlind, L. J., Applied Finite Element Analysis, John Wiley and Sons, Inc., New York, 1976.

74. Seshadri, T. V., "Shock and Vibration Analysis Using Finite Element Technique," The Shock and Vibration Digest, Vol. 10, No. 12, December 1978.

75. Shmitberg, R. A., "Solving Vibration Problems Using Modal Analysis," Nicolet Scientific Co. Application Note 14, 1981.

76. Smith, C. C., Thornhill, R. J. and Richardson, M. H., Modal Vibration Analysis, The American Society of Mechanical Engineers, Chicago, November 1980.

77. Spectral Dynamics Co., "Application for Coherent Output Power Measurements," Application Manual DSP-009, July 1976.

78. Spectral Dynamics Co., "Detecting, Enhancing or Eliminating Signals in Noise," Application Manual DSP-015, November 1976.

79. Spectral Dynamics Co., "Dynamic Analysis Workshop," San Diego, 1972.

80. Spectral Dynamics Co., "Measuring Frequency Response Functions on Operating Systems," Application Manual DSP-035, May 1980.

81. Spectral Dynamics Co., "Measuring Structural Transfer Functions in Real Time," Application Manual DSP-015, November 1976.

82. Spectral Dynamics Co., "Signal Analysis Using Digital Techniques," Application Manual DSP-004, August 1978.

83. Spectral Dynamics Co., "Solution for Mechanical Impedance Measurement Problems," Technical Publication No. M-11, September 1966.

84. Spectral Dynamics Co., "Solution to Signal Processing and Data Analysis Problems," Application Manual DSP-034, February 1980.

85. Thomson, W. T., Theory of Vibration with Applications, 2nd Edition, Prentice Hall, Englewood Cliffs, N. J., 1981.

86. Timoshenko, S. P. and Goodier, J. N., Theory of Elasticity, McGraw-Hill, Inc., New York, 1970.

87. Trail and Nash, "On the Excitation of Pure Natural Modes in Aircraft Resonance Testing," Journal of Aerospace Sciences, Vol. 25, December 1958.

88. Vemuri, V. and Karplus, W. J., Digital Computer Treatment of Partial Differential Equations, Prentice Hall, Inc., Englewood Cliffs, N.J., 1981.

89. Vierk, R. K., Vibration Analysis, Harper and Row, New York, 1979.

90. Walgrave, S. C. and Ehlbeck, J. M., "Understanding Modal Analysis," SAE, West Coast Meeting, San Diego, August 1978.

91. Wavetek Rockland Co., "Spectrum Analysis-Theory Implementation and Applications," 1977.

92. Wavetek Rockland Co., "The Application of Filters to Analog and Digital Signal Processing," 1979.

93. Zienkiewicz, O. C., The Finite Element Method, McGraw-Hill, Inc., New York, 1977.

Appendix A

MODAL PARAMETERS IDENTIFICATION

A.1. Introduction

Before we start considering the techniques for modal parameters identification, it is instructive to describe the distribution of the magnitudes of the transfer functions along the frequency range in real structural systems.

When a structure is excited by a broad-band input force, many of its modes of vibration (degrees-of-freedom) are excited simultaneously. Since the structure is assumed to behave in a linear manner, its transfer functions are really the sums of the resonance curves for each of its modes of vibration, as shown in Figure A.1. In other words, at any given frequency, the transfer function represents the sum of all the modes of motion which have been excited. However, near the natural frequency of a particular mode, its contribution to the overall motion is generally the greatest. The degree of mode overlap, i.e., the contribution of the tails of adjacent modal resonant curves to the transfer-function magnitude at a mode's natural frequency, is governed by the amount of damping of the modes and their frequency separation. Figure A.1 illustrates light and heavy modal overlap. Figure A.1(b) shows modes with light damping and sufficient separation so that there is a little modal overlap. Figure A.1(c) shows modes with heavy damping such that there is plenty of modal overlap.

In cases where modal overlap is light, the transfer function data can be considered in the vicinity of each modal resonance as if

ORIGINAL PAGE IS
OF POOR QUALITY

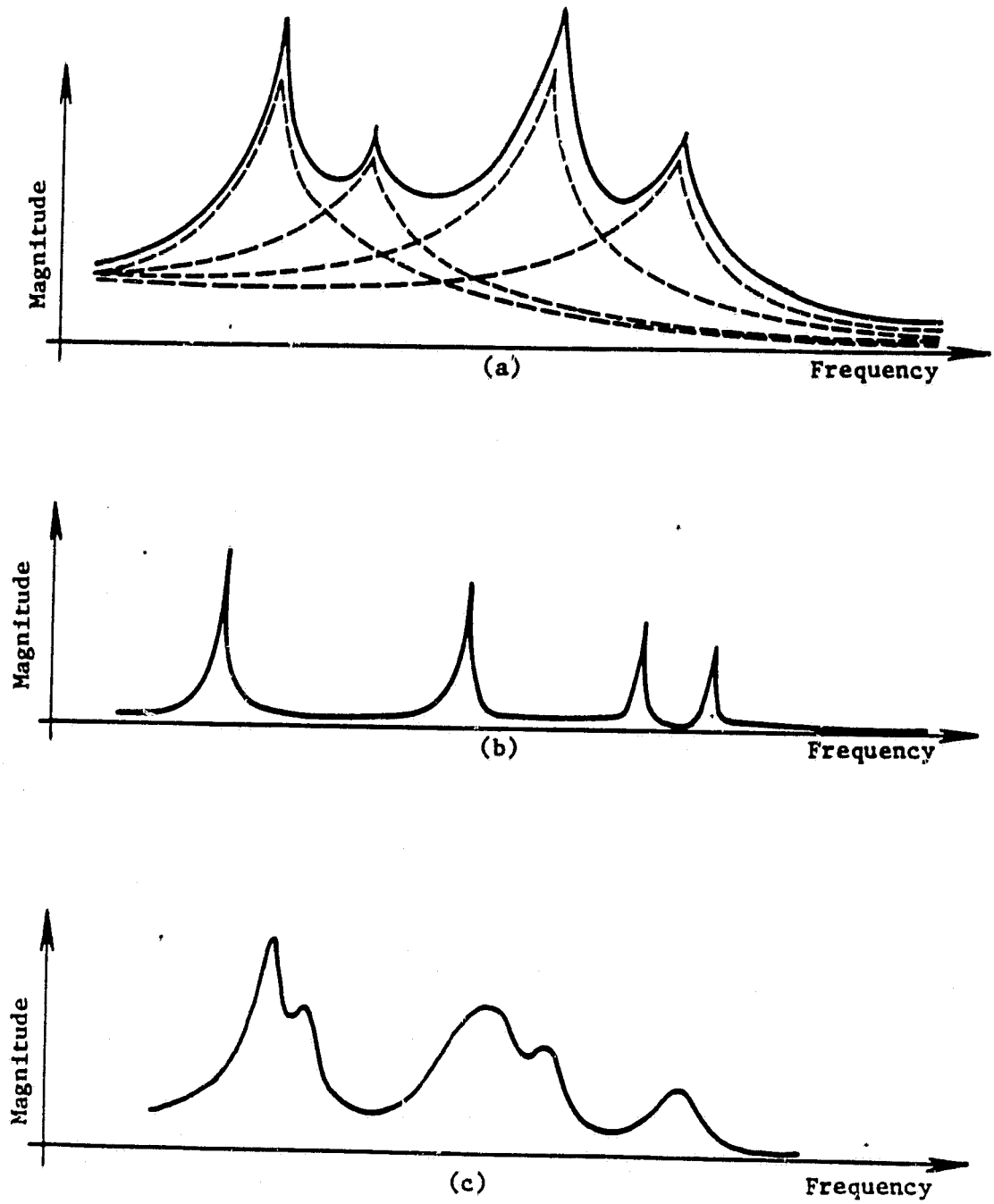

Figure A.1 (a) Magnitude of a multi-degree-of-freedom system transfer function, (b) light modal overlap, (c) heavy modal overlap.

it were a single-degree-of-freedom system. In other words, it is assumed that contribution of the tails of adjacent modes near each modal resonance is negligibly small. On the contrary, when modal overlap is heavy, a single-degree-of-freedom for modal parameter identification will not work; the parameters of all the modes must be identified simultaneously.

Usually, four residue-extraction techniques are used and named by the method:

1. Quadrature response
2. Peak picking
3. Circle fitting
4. Least squares.

In the following sections, a detailed treatment and application is given for all four modal parameter identification techniques.

A.2. Mode Identification by the Frequency Response

The accuracy of the residue estimate obtained by this method is a function of how well each mode of the system is represented by a single-degree-of-freedom model. The magnitude of the complex frequency function for the r-th mode $|h(\omega_r)|$ is determined from

$$|h(j\omega_r)| = \sqrt{h(\omega_r)\cdot h^*(\omega_r)} \tag{A.1}$$

where $h^*(j\omega_r)$ is the complex conjugate of the frequency response function

$$h^*(j\omega_r) = \frac{R_r}{1 - (\frac{\omega}{\Omega_r})^2 - j2\zeta_r(\frac{\omega}{\Omega_r})}, \tag{A.2}$$

ORIGINAL PAGE IS
OF POOR QUALITY

Thus,

$$|h^{*}(j\omega)|^2 = \frac{R_r^{\ 2}}{(1-(\frac{\omega}{\Omega_r}))^2 + (2\zeta_r(\frac{\omega}{\Omega_r}))^2} \tag{A.3}$$

where R_r is the modal residue and ζ_r and Ω_r are defined by the control theory approach. The plot of $|h(\omega_r)|$ is shown in Figure A.2. The peak amplitude of the frequency-response function is obtained by differentiating eq. (A.3) with respect to ω and letting the result equal zero. The peak occurs when

$$\omega_r = \Omega_r\sqrt{1-2\zeta_r^{\ 2}}\ . \tag{A.4}$$

Thus, the peak of the magnitude of the frequency response function occurs at a frequency less than both ω_r and Ω_r. For very lightly damped systems, the peak occurs at approximately the undamped natural frequency Ω_r.

The maximum value of $|h(\omega_r)|$ for a single-degree-of-freedom system in the r-th mode is referred to as the "Q_r" of the system. When a system has a light damping,

$$|h(\Omega_r)| \simeq Q_r \simeq \frac{1}{q\zeta_r}. \tag{A.5}$$

An approximate value of damping for a single-degree-of-freedom system can be computed by using the frequency difference between the system's half-power points. The half-power points are defined as the amplitude

$$\frac{|h(\omega_r)|^2_{max}}{2} \tag{A.6}$$

ORIGINAL PAGE IS
OF POOR QUALITY

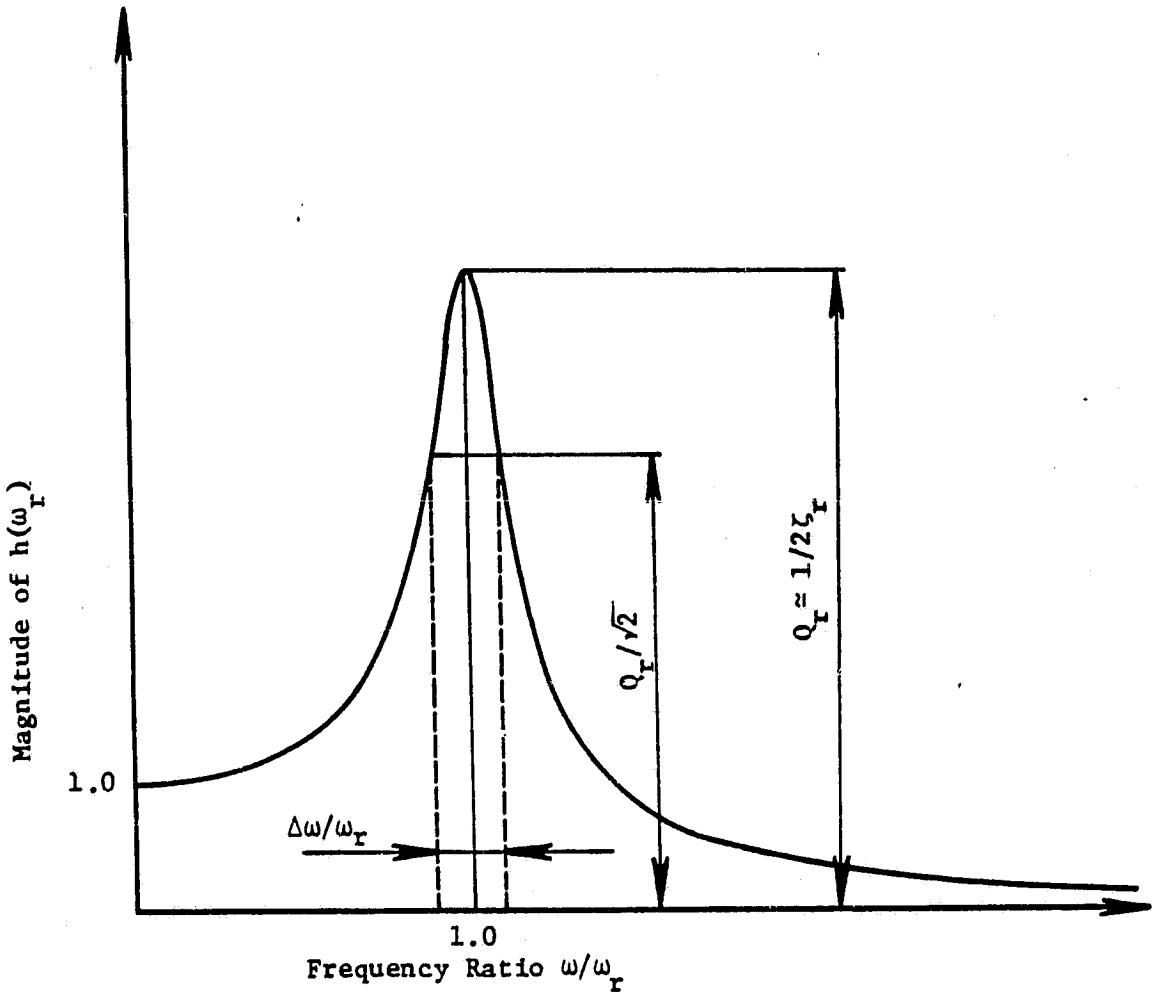

Figure A.2. Magnitude of a frequency-response function for a single-degree-of-freedom system (in the r-th mode).

C-3

ORIGINAL PAGE IS
OF POOR QUALITY

or in terms of the magnitude $|h(\omega)|$, when it is equal to "Q_r". The half-power points occur when

$$\left(\frac{Q_r}{\sqrt{2}}\right)^2 = \frac{1}{2}\left(\frac{1}{2\zeta_r}\right)^2 = \frac{1}{\left(1 - \left(\frac{\omega}{\Omega_r}\right)^2\right)^2 + \left(2\zeta_r \frac{\omega}{\Omega_r}\right)^2} . \tag{A.7}$$

Assuming light damping in the r-th mode, $\zeta_r << 1$, eq. (A.7) becomes

$$\left(\frac{\omega}{\Omega_r}\right)^2 = 1 \pm 2\zeta_r . \tag{A.8}$$

Now, let the roots of eq. (A.8) be equal to the frequencies ω_1 and ω_2. Then the difference of these two frequencies is referred to as the bandwidth of the resonance

$$\omega_2 - \omega_1 = \Delta\omega_r = \text{bandwidth.}$$

For lightly-damped structures,

$$\Delta\omega_r = 2\zeta_r\Omega_r . \tag{A.9}$$

The approximate damping ratio of the system can be obtained from the magnitude of the frequency-response function by

$$\zeta_r = \frac{\Delta\omega_r}{2\Omega_r} . \tag{A.10}$$

The identical procedure can be repeated for the other modes. We derived the formulas above under the condition of light modal overlap (the modes are well spaced along the frequency range).

ORIGINAL PAGE IS
OF POOR QUALITY

A.3. Mode Identification by the Peak Picking Method

The peak picking method is essentially a single-degree-of-freedom system technique. Again, as in the previous case, the accuracy of the residue estimate is a function of how well each mode of the system is presented by a single-degree-of-freedom system model. From system dynamics it is known that the properties of the transfer function for a single-degree-of-freedom system in the r-th mode could be determined from measurements of the frequency response function, expressed in terms of its poles and residues as:

$$h(\omega_r) = \frac{R_r}{2j(j\omega_r - P_r)} - \frac{R_r^*}{2j(j\omega_r - P_r^*)}. \tag{A.11}$$

For the single-degree-of-freedom system, the residue is seen to be real value, given by

$$R_r = \frac{1/m}{\omega_r\sqrt{1-\zeta_r}} = \frac{1}{m\omega_{dr}}. \tag{A.12}$$

In general, the residue may be considered complex and may be expressed as

$$R_r = |R_r|e^{j\alpha_r} = |R_r|(a_r + jb_r), \tag{A.13}$$

where $|R_r|$ is the magnitude of the residue

$$|R_r| = \sqrt{Re^2(R_r)\ Im^2(R_r)} \tag{A.14}$$

and α_r is the phase angle of the residue in the r-th mode

$$\alpha_r = \arctan\frac{Im(R_r)}{Re(R_r)}. \tag{A.15}$$

The constants a and b are expressed as

$$a_r = \cos\alpha_r$$

$$b_r = \sin\alpha_r . \tag{A.16}$$

Substituting the expressions above for R_r in eq. (A.11), we have

$$h(\omega_r) = \frac{|R_r|}{2}\left[\frac{a_r(\omega_{dr}-\omega)+b_r\zeta_r\omega_r}{(\omega_{dr}-\omega)^2+(\zeta_r\omega)^2}\right] + j\,\frac{|R_r|}{2}\left[\frac{b_r(\omega_{dr}-\omega)-a_r\zeta_r\omega_r}{(\omega_{dr}-\omega)^2+(\zeta_r\omega)^2}\right] +$$

$$+\frac{|R_r|}{2}\left[\frac{a_r(\omega_{dr}+\omega)+b_r\zeta_r\omega_r}{(\omega_{dr}+\omega)^2+(\zeta_r\omega)^2}\right] - j\,\frac{|R_r|}{2}\left[\frac{b_r(\omega_{dr}+\omega)-a_r\zeta_r\omega_r}{(\omega_{dr}+\omega)^2+(\zeta_r\omega)^2}\right] . \tag{A.17}$$

In eq. (A.17), the real and imaginary parts of the frequency-response function are explicitly revealed. Again, the first two terms represent the contribution of the positive pole, while the last two terms represent the contribution of the negative pole.

For the purpose of graphic interpretation, it is useful to rewrite equation (A.17) in a dimensionless form. To accomplish this, we divide eq. (A.17) by the static frequency-response function:

$$h_r(0) = |R_r|\,\frac{a_r\sqrt{1-\zeta_r^2} + b_r\zeta_r}{\omega_r} = |R_r|\,\frac{A}{\omega_r} . \tag{A.18}$$

For a single-degree-of-freedom system, the static frequency-response function is simply the inverse of the spring constant. The following dimensionless frequencies are also defined as:

ORIGINAL PAGE IS
OF POOR QUALITY

$$\gamma = \frac{\omega}{\omega_r}, \text{ and}$$

$$\beta = \frac{\omega_{dr}}{\omega_r} = \sqrt{1-\zeta_r^2}\,. \tag{A.19}$$

Equation (A.17) may be rewritten as

$$\frac{h(\omega_r)}{h_r(0)} = \frac{1}{2A}\left[\frac{q_r(\beta-\gamma)+b_r\zeta_r}{(\beta-\gamma)^2+\zeta_r^2}\right] + \frac{j}{2A}\left[\frac{b_r(\beta-\gamma)-a_r\zeta_r}{(\beta-\gamma)^2+\zeta_r^2}\right] +$$

$$+\frac{1}{2A}\left[\frac{a_r(\beta+\gamma)+b_r\zeta_r}{(\beta+\gamma)^2+\zeta_r^2}\right] - \frac{j}{2A}\left[\frac{b_r(\beta+\gamma)+a_r\zeta_r}{(\beta+\gamma)^2+\zeta_r^2}\right]. \tag{A.20}$$

Equation (A.20) is shown graphically for various values of the damping ratio in Fig. A.3. For all curves in this figure, the residue is taken as real ($a = 1$, $b = 0$). Thus, Fig. A.3 represents the frequency-response function for a single-degree-of-freedom system. Figure A.3(a) shows the real part of eq. (A.20), while Fig. A.3(b) shows the imaginary part. It should be noted that the real part is symmetric in frequency, while the imaginary part is anti-symmetric. This property is called conjugate evenness, and is characteristic of structures with real residues. Since, for structural systems, we have interest only in a positive frequency range, eq. (A.20) is plotted in Fig. A.4 for positive frequencies only. In this figure, the residue is real and the damping ratio of 0.05 is selected. The parameters of interest in this figure are the frequencies at which the real and imaginary parts of the frequency response function have extremes.

ORIGINAL PAGE IS
OF POOR QUALITY

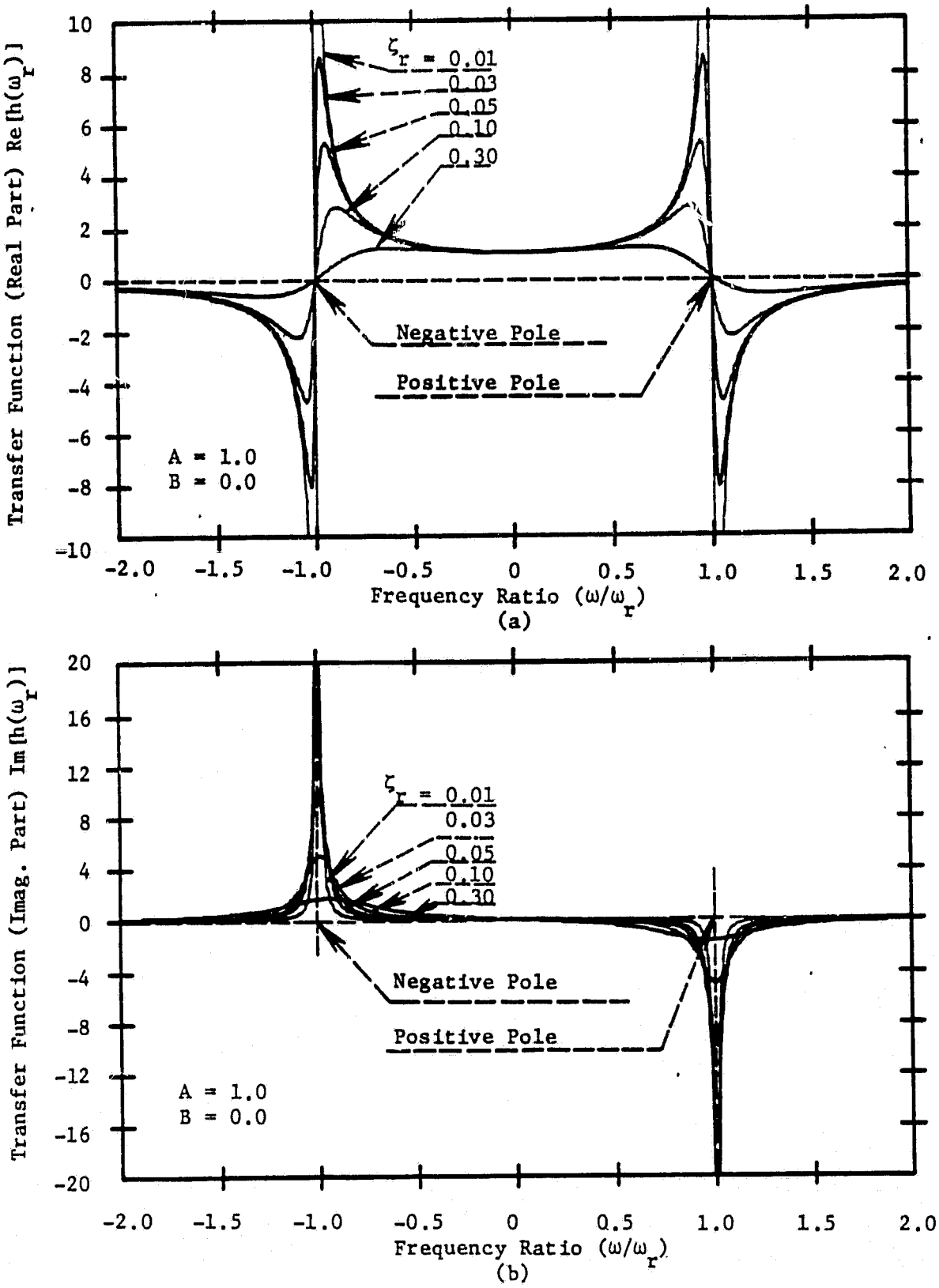

Figure A.3. Single-degree-of-freedom system transfer function (real modes); (a) real part, (b) imaginary part.

ORIGINAL PAGE IS
OF POOR QUALITY

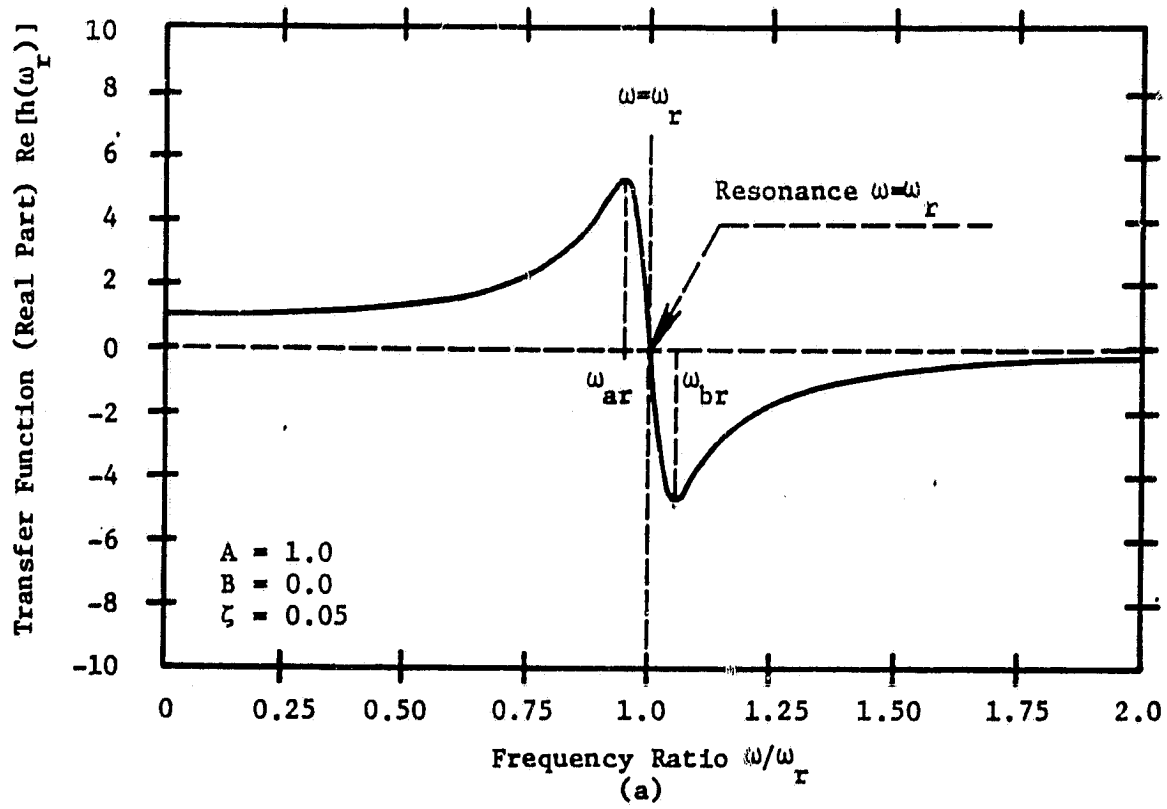

(a)

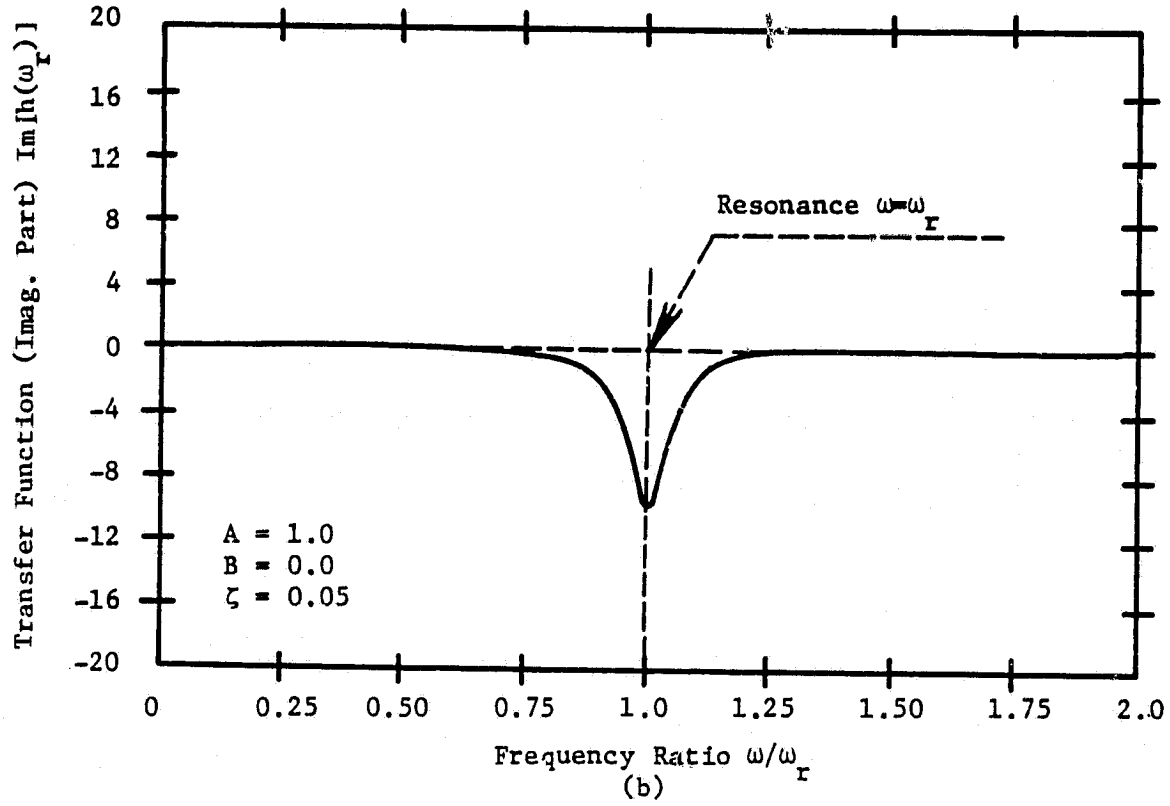

(b)

Figure A.4. Single-degree-of-freedom system transfer function; (a) real part, (b) imaginary part.

The frequency corresponding to the negative peak in Fig. A.4(b) (imaginary part) is found by equating the frequency derivative of the imaginary part of eq. (A.17) to zero. For a real residue, the imaginary part of eq. (A.17) is

$$I_m[h(\omega_r)] = \frac{R_r}{2}\left[\frac{-\zeta_r\omega_r}{(\omega_{dr}-\omega)^2+(\zeta_r\omega_r)^2}\right] - \frac{R_r}{2}\left[\frac{-\zeta_r\omega_r}{(\omega_{dr}+\omega)^2+(\zeta_r\omega_r)^2}\right]. \quad (A.21)$$

Equating the derivative to zero gives

$$\frac{d}{d\omega} I_m[h(\omega_r)] = 0 = -|R_r|\frac{\zeta_r\omega_r(\omega_r-\omega)}{\left[(\omega_{dr}-\omega_r)^2\right]^2} - |R_r|\zeta_r\omega_r\varepsilon_r(\omega). \quad (A.22)$$

In eq. (A.22), the term $\varepsilon_r(\omega)$ represents the contribution of the negative pole. For frequencies near the natural frequency of the system, this term is negligible

$$\varepsilon_r(\omega\approx\omega_r) \simeq \frac{1}{8\omega_r^3}. \quad (A.23)$$

Neglecting this term, equation (A.22) indicates that the peak in the imaginary display of Fig. A.4(b) occurs at

$$\omega = \omega_{dr}. \quad (A.24)$$

That is, the peak in the imaginary part of the frequency response function is at the damped natural frequency of the system. If we consider the real part of the frequency response shown in Fig. A.3(a), near the damped natural frequency this function has two extreme values, one positive and one negative. The frequency at which these extremes occur is found by equating the frequency derivative

ORIGINAL PAGE IS
OF POOR QUALITY

of the real part of eq. (A.17) to zero. For a real residue, the real part of eq. (A.17) is

$$R_e[h(\omega_r)] = \frac{R_r}{2}\left[\frac{(\omega_{dr}-\omega)}{(\omega_{dr}-\omega)^2+(\zeta_r\omega_r)^2}\right] + \frac{R_r}{2}\left[\frac{(\omega_{dr}+\omega)}{(\omega_{dr}+\omega)^2+(\zeta_r\omega_r)^2}\right]. \quad (A.25)$$

Equating the derivative of this expression to zero gives

$$\frac{d}{d\omega} R_e[h(\omega_r)] = 0 = \frac{R_r}{2} \cdot \left[\frac{(\omega_{dr}-\omega)}{\left[(\omega_{dr}-\omega^2)+(\zeta_r\omega_r)^2\right]^2}\right] - \frac{R_r}{2}\,\varepsilon_r(\omega). \quad (A.26)$$

In the expression above, the term $\varepsilon_r(\omega)$ again represents the contribution of the negative pole. For frequencies near the natural frequency of the system, this term is negligible:

$$\varepsilon_r(\omega\approx\omega_r) \simeq \frac{1}{4\omega^2}. \quad (A.27)$$

Neglecting this term, eq. (A.26) indicates that the extremes in the real display of Fig. A.4(a) occur at

$$\omega = \omega_{dr} \pm \zeta_r\omega. \quad (A.28)$$

The difference between these two frequencies is

$$\Delta\omega = \zeta_r\omega_r.$$

The damping is then estimated from

$$\zeta_r = \frac{\Delta\omega}{\omega_r}. \quad (A.29)$$

The damping properties at resonance in the r-th mode can be described by an amplification factor Q_r. The amplification factor Q_r is related to the viscous damping factor, ζ, by the relationship

$$Q_r = \frac{1}{2\zeta_r} \tag{A.30}$$

where ζ_r is the damping ratio of actual and critical damping of the system in the r-th mode. This method is the most precise in practical implementation, particularly when dealing with high Q modes. It has the distinct advantage of being directly applicable to the real part of the transfer function. From Fig. A.4(a), we have

$$Q_r = \frac{(\omega_{ar}/\omega_{br})^2 + 1}{(\omega_{ar}/\omega_{br})^2 - 1} \tag{A.31}$$

where

ω_{ar} = frequency above resonance in the r-th mode, where the real part of the frequency transfer function reaches the peak.

ω_{br} = frequency below resonance in the r-th mode, where the real part of frequency transfer function reaches the peak of the opposite sign.

To summarize, the essence of the peak-picking identification method is, therefore, the determination of the three frequencies associated with the extreme in the real and imaginary representation of the frequency response function. This method is effective under the following conditions:

1. The frequency response function has real, or very nearly real, residues.

2. The frequency response function can be approximated by the sum of the frequency response functions of several single-degree-of-freedom systems whose natural frequencies are distinct and "well separated."

3. The influence of the negative poles on the measured (positive frequency) frequency response function is negligible, for moderate and high damping may not be consistent with the accurate determination of the modal damping ratios.

Whether or not adequate separation of poles exists in a given frequency response function is a matter of judgment and experience. In general, a minimum of five half-power bandwidths ($\Delta\omega$) should separate modes for adequate measurement purposes. Two extreme examples are shown in Figs. A.5 and A.6.

Figure A.5 shows two "well-separated" modes. Between resonances, both the real and imaginary parts of this frequency response function are relatively flat. Figure A.6 shows two "poorly separated" modes. The effect of one mode on the other is quite apparent, especially in the real part of the frequency response function. Similar phenomena can be observed if the magnitude of the frequency response function is plotted.

ORIGINAL PAGE IS
OF POOR QUALITY

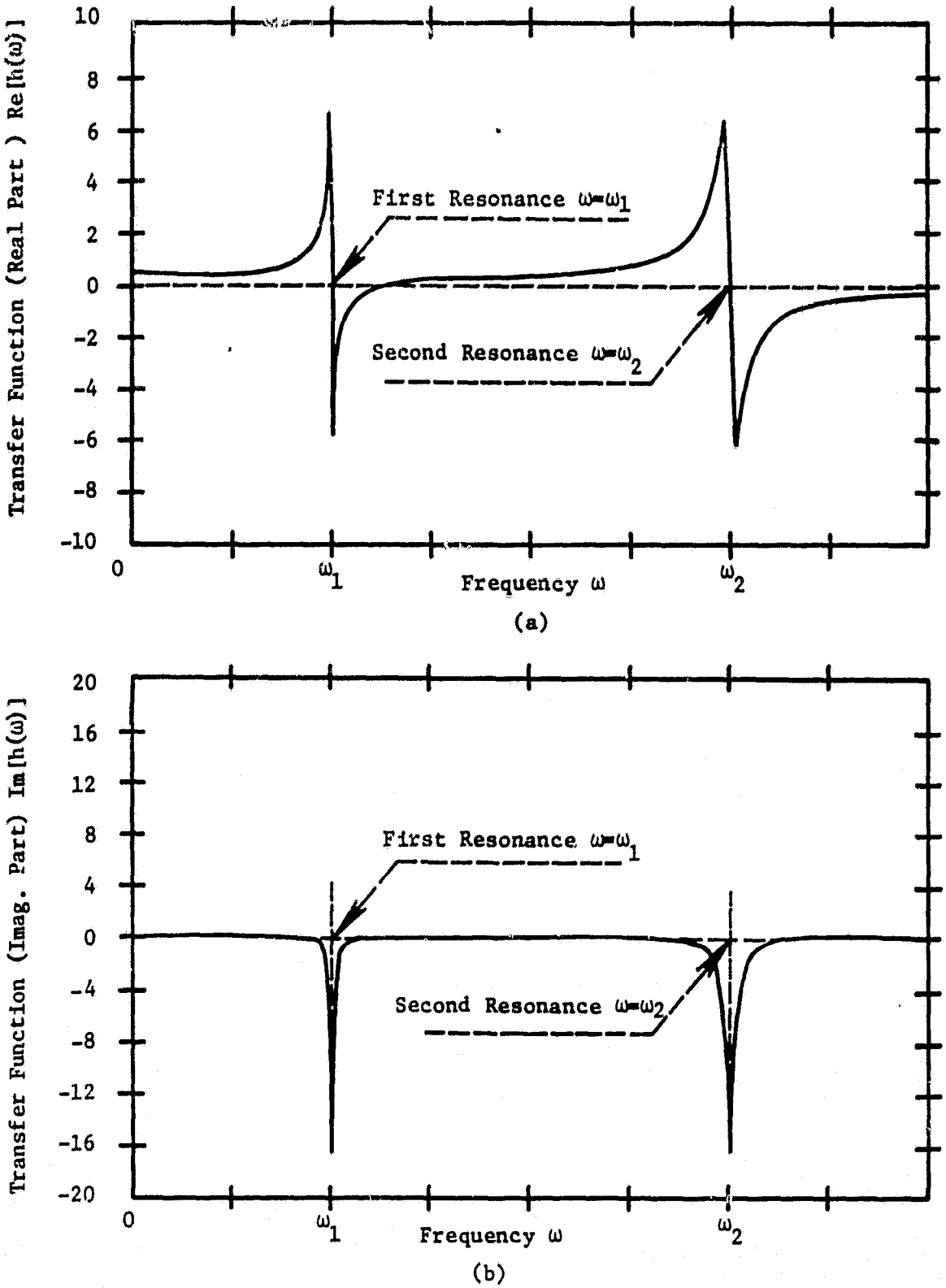

Figure A.5. Two-degree-of-freedom system transfer functions with two distantly coupled modes; (a) real part, (b) imaginary part.

ORIGINAL PAGE IS
OF POOR QUALITY

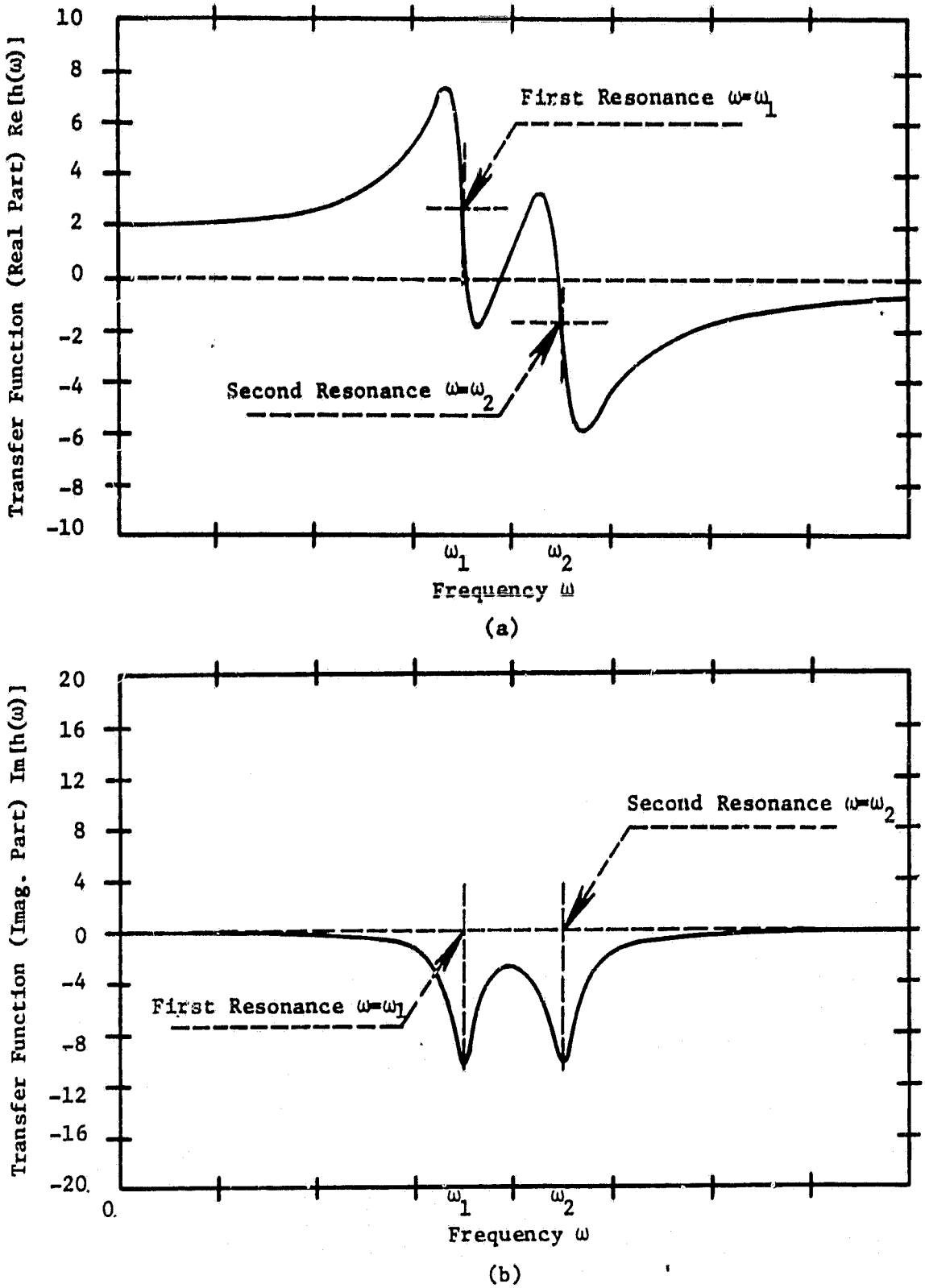

Figure A.6. Two-degree-of-freedom system transfer functions with two closely coupled modes; (a) real part, (b) imaginary part.

Appendix B

SYSTEM EXCITATION AND EXPERIMENTAL TECHNIQUE

B.1. Introduction

The transfer characteristics may be measured by isolating the structure from its normal environmental loading and subjecting it to an excitation of a simpler nature. In practice, the structure is subjected to a force introduced at a single point with a fixed orientation, and the resultant motions are measured at one or more fixed points. This permits measurement of a series of transfer functions, thus characterizing the structure.

Each transfer function provides two pieces of cause/effect information:

1. The ratio of force/motion (as a function of frequency) relating the force input point and the motional response point.
2. The degree of phase lag (as a function of frequency) between the force and motion introduced by the structural path.

As we stated previously, the transfer functions identify the resonant frequencies, damping characteristics, mode shapes, stiffness, and inertia of the structure.

Six transfer-function types are frequently measured. These are:

1. Compliance = Displacement/Force
2. Mobility = Velocity/Force
3. Inertance = Acceleration/Force

4. Apparent Stiffness = Force/Displacement

5. Impedance = Force/Velocity

6. Apparent Mass = Force/Acceleration

All six of the descriptive transfer functions are interrelated by simple algebraic operations. Having knowledge of one of the six frequency response forms is equivalent to having knowledge of all six. The nature of available instrumentation, local conventions and history, and problem specifics normally dictate the selection of one of the six functions for measurement.

B.2. System Excitation

The transfer functions can be measured using three broadly different test procedures. These techniques are called swept sine, random, and impulsive excitation. There is no "right" technique for all problems. Modern FFT analyzers are fully capable of performing analyses for all three types of testing. The following is a summary of all three techniques.

Swept-sine testing is the oldest of the three techniques. In this procedure, the structure is subjected to sinusoidal excitation, and the frequency of the sinusoid is slowly swept through a range of frequencies. If the sweep rate is sufficiently slow (as determined both by the structure and the measurement equipment), the transfer functions computed from this technique are identical to the results obtained by "resting" at a sequence of frequencies.

In random excitation, testing for the source of excitation is provided by a broad-band noise generator which produces an output signal with a "white" spectrum (a spectrum flat to at least the

bandwidth of the analysis). Probability distribution of the broad-band excitation is Gaussian. This source of excitation is fed through a mass-compensation network, if required, for the examination of the light structures with high "Q" modes, then through a power amplifier to the drive coil of the shaker. Both the excitation force and the response variable are measured simultaneously using a dual-channel FFT analyzer.

The methodology for impact testing involves striking the structure with an impactor, usually a hand-held hammer, which has a load cell attached to measure the force input. The input and output, usually accelerations, are simultaneously measured. The two signals are Fourier-transformed, and the frequency response ratio is formed. It is assumed that the impulse is of sufficiently short duration to have the necessary frequency content to excite all frequencies in the band of interest simultaneously. Since this technique is very much of interest in this area of study, it is going to be treated in detail in the following sections.

To summarize, sinusoidal testing is the slowest but most precise procedure for performing frequency response measurements. Impulsive force-input techniques are the fastest but least precise.

Sinusoidal techniques have retained their popularity throughout history. Transient techniques have come into recent vogue as a means of performing rapid analysis on complex problems. The quick "look-see" capability offered by impulsive techniques is often sufficient to solve a problem. Frequently, initial studies are conducted using impulsive techniques, and higher-resolution information is gathered (where required) using either the random or swept-sine

techniques.

FFT processing analyzers have gained enormous popularity because they are capable of performing transfer-function measurements using any of the three types of excitation.

B.3. Impulsive Testing

This procedure utilizes short-duration inputs (with corresponding broad-band spectra) to excite all frequencies in the structure simultaneously. Impulsive testing is normally conducted using some form of an instrumented hammer such as that shown in Fig. B.1. A force transducer is mounted either on the head of the hammer or on that portion of the structure to be impacted.

An accelerometer is used to measure the response of the structure. By far the most popular technique for impulsive excitation is to mount an accelerometer at a fixed location and to excite the structure at a multiplicity of locations using a hammer with a force transducer on its face to impact the system at many points. The data is analyzed with a dual-channel FFT analyzer. Each time the structure is impacted with the hammer, both the impulse and the response acceleration are captured by the FFT analyzer, using the impulse force as a transient-capture trigger condition. These two transient histories are Fourier-transformed to yield the input and output spectra. The resultant ratio of the output and input spectra is the desired transfer function.

Usually, the results of several transient excitations are averaged. In this situation, the most desirable procedure is to compute the cross-spectrum between the input and response, and the

ORIGINAL PAGE IS
OF POOR QUALITY

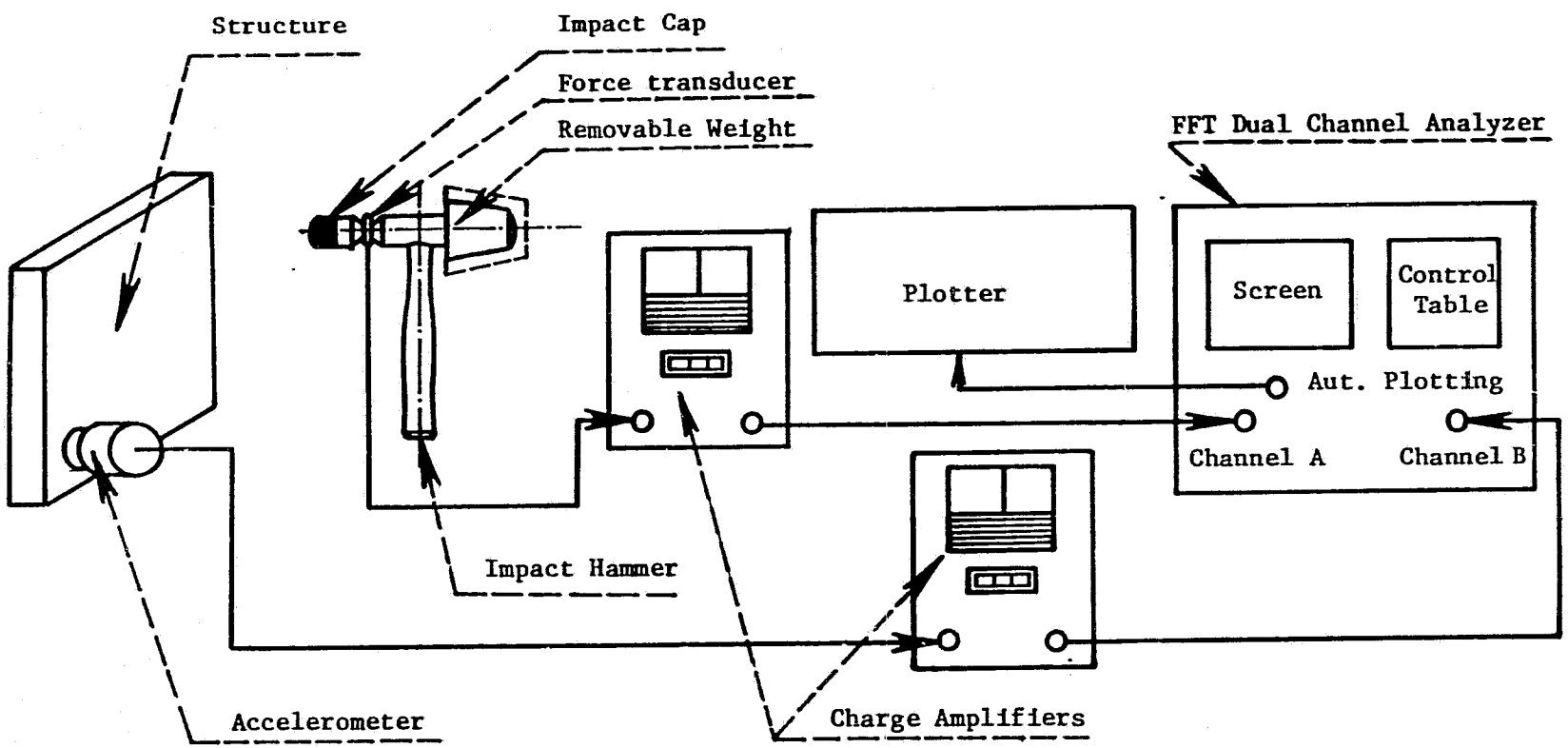

Figure B.1. The setup for impulsive testing.

power spectrum of the input. The resultant averaged transfer characteristic is derived by dividing the cross-spectrum by the input power spectrum.

There are several advantages to impulsive testing. It is, by far, the most rapid technique that can be applied to the study of a complex structure. Its fundamental advantage is that no shaker system needs to be mounted to the test object. The testing time required for each spacial position on the structure is determined by the number of times the tester wishes to impact the structure with a hammer. Because the response transducer is mounted at a fixed location, no time is required to move the response transducer from point to point and, of course, a hammer may be easily moved from one point on the structure to another.

Some disadvantages of impulsive testing, however, also exist, as follows:

1. Impulsive techniques impose stringent requirements on the analysis instrumentation. Specifically, the FFT analyzer must have considerable more dynamic range than is required for sinusoidal or random testing.

2. Precision of the results is strongly affected by the care with which data is initially acquired. If the signal-conditioning amplifier or analog-to-digital converters of the FFT analyzer are allowed to momentarily overload during the acquisition of a transient, the results are grossly affected.

3. It is important to match the duration of the impulsive force input to the band of frequencies to be analyzed. This requires

selecting the mass and geometry of the hammer as well as the nature of the material and the hammer/structure interface to "shape" the input pulse.

4. The mass of the striking "tip" between the force transducer (mounted on the face of the hammer) and the structure can introduce errors when exciting light structures. Unfortunately, there is no currently-available technique for performing on-line mass cancellation. The results of impulsive testing have lower signal-to-noise ratios than those from any other form of excitation.

B.4. Impactor Selection

The impactor is usually a hand-held hammer instrumented with a force transducer. The force transducer has an impact cap attached to it, and the hammer may have an extension attached to it. The hammer could be very small, weighing only a few ounces, or as large as a sledge hammer.

The frequency content of a force pulse is determined by its shape. Often it is desirable to shape the pulse to ensure that the impact excites the structure in a particular desired frequency range. The three parameters which characterize the pulse are:

1. Pulse height. This is largely controlled by the impact velocity. A higher impact velocity would require a larger force to decelerate a given mass, resulting in an increase in pulse height.

2. Rise time. This can be controlled by the choise of impact caps. If the impact cap is thought of as a spring, it seems reasonable that an impact with a soft spring (soft impact cap, such as rubber or plastic) would have a longer rise time than an impact

with a hard spring (hard impact cap).

3. Pulse width. To a certain extent, the pulse width can be controlled by the use of extenders to change the hammer mass. For example, a larger mass (hammer with extender) moving at the same velocity will have a larger amount of kinetic energy and require a longer time to be stopped by a given spring (the impact cap). This produces a wider pulse.

It is necessary to point out that methods of shaping the pulse are all interactive. For example, installing a softer impact cap will increase the pulse width as well as increase the rise time. It is best to try various configurations of impact caps, extenders, and impact velocities and Fourier-transform the time signals to ensure that the desired frequencies are being excited.

B.5. Hammer Calibration

In order to calibrate the frequency response plots generated by impact testing, it is necessary to dynamically calibrate the load cell which is part of the hammer structure. In Fig. B.2, a typical calibration setup for an impact hammer and accelerometer is shown.

On impact, the structure experiences the force which is necessary to stop the entire hammer assembly. The load cell's crystal element experiences only the force necessary to stop the mass of the hammer head and extender. It does not sense the force component necessary to stop the mass of the impact cap and the load cell's seismic mass. Because of this, the sensitivity of the load cell appears to change as the mass of the impact cap and the

ORIGINAL PAGE IS
OF POOR QUALITY

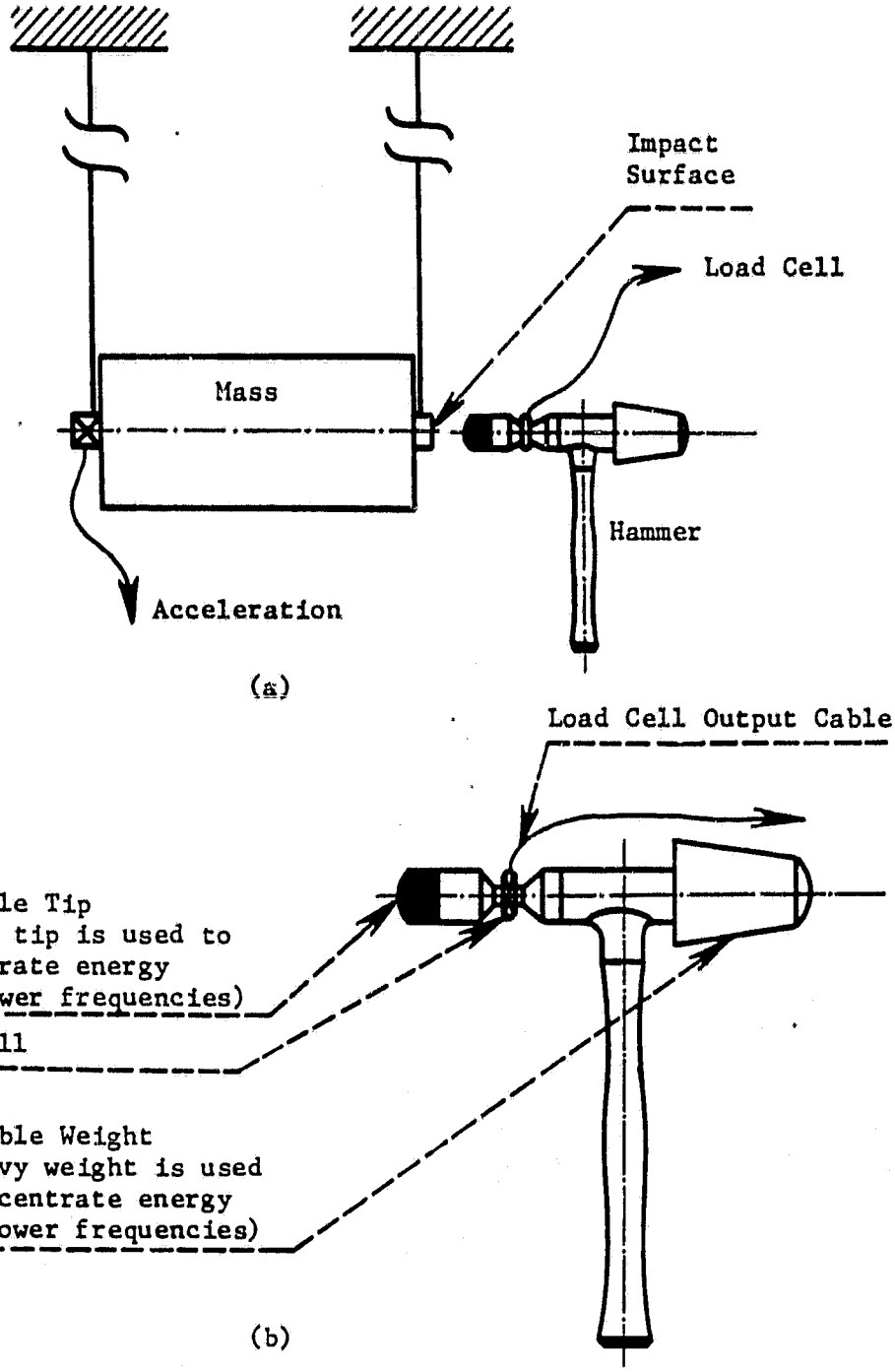

Figure B.2(a). Typical calibration setup for an impact hammer and accelerometer set, (b) typical impact hammer with a load cell.

mass of the hammer are changed. Increasing the ratio of the hammer head plus extender to the total mass of the hammer structure decreases the apparent sensitivity change, but as the total mass increases, it can introduce problems of multiple impacts and penetration. The mathematical model of hammer calibration is given in the following text.

The hammer calibration involves testing of the functional transfer behavior of a test object, with a known mass acting as a rigid body employed as the test object. For scaling a test object measurement, only the ratio of the accelerometer sensitivity to the hammer sensitivity (S_a/S_f) is needed. However, the actual sensitivity of the hammer "S_f" can be determined from equation (b) in Fig. B.3 when a precision quartz accelerometer with a known sensitivity "S_a" is employed as a reference. The "sensitivity" of a load cell or hammer structure is just another way of expressing its functional transfer behavior. Calibration (scaling) factors can be calculated from the peaks of the time-varying signals from the ratio of their frequency components.

The sensitivity of a hammer differs from the static sensitivity of its force-sensor component because of the normal behavior of the hammer structure. The force experienced by the crystal sensing elements sandwiched within the hammer structure is not the same as the force applied on the test object. For this reason, the hammer assembly ought to be calibrated as it is used. To test small hammers, a several-pound cylindrical mass with the accelerometer attached and suspended with a long leads should be used. For a given

ORIGINAL PAGE IS
OF POOR QUALITY

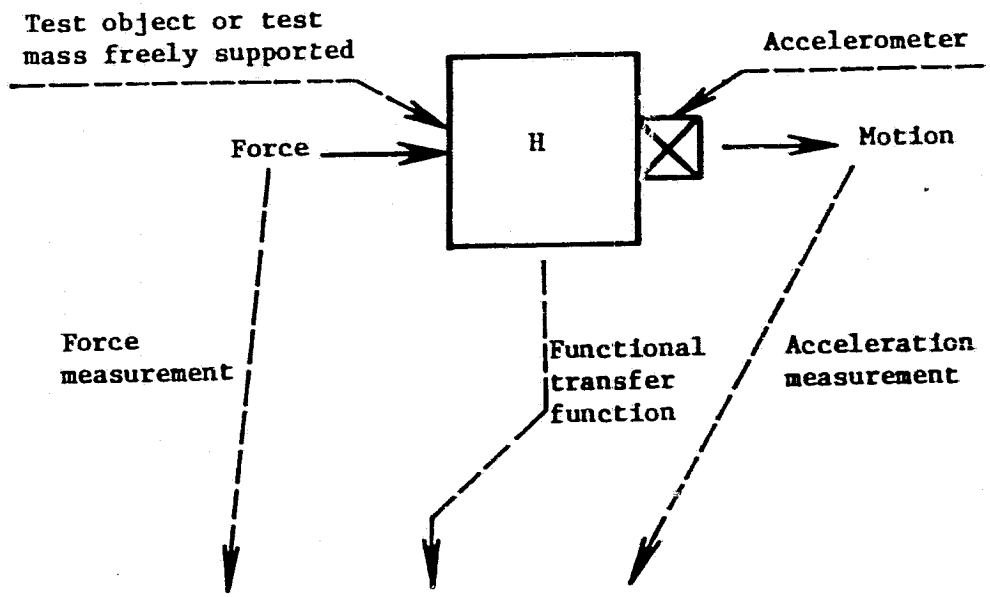

A. Test object $\frac{E_f'}{S_f} \cdot H = \frac{E_a'}{S_a}$ or $H = \frac{E_a'/E_f'}{(S_a/S_f)}$

B. Calibration sensors $\frac{E_f}{S_f} \cdot \frac{1}{m_c} = \frac{E_a}{S_a}$ or $(S_a/S_f) = m_c E_a/E_f$

Figure B.3. The mathematical model of hammer calibration, where: E_a'/E_f' and E_a/E_f are acceleration signal ratios (processed by an FFT analyzer). (S_a/S_f) is a scaling factor (the ratio of accelerometer sensitivities and hammer sensitivities). The test mass and the accelerometer assembly are of a known magnitude m_c. All variables are a function of time and frequency.

hammer structure, the sensitivity of the moving hammer differs from its static sensitivity by a constant percentage proportional to the ratio of the mass of the tip and cap in front of the crystals to the total mass of the hammer assembly.

Three methods of scaling a frequency response measurement are:

1. Inserting the average sensitivities supplied by the manufacturer.
2. Measuring and using the "ratio" of sensitivities as outlined above.
3. Calibrating the hammer sensitivity, using an accelerometer as a reference.

With methods 2 and 3, an average scaling factor can be estimated or a scaling factor at each discrete frequency in the spectrum of interest can be measured and used, thus compensating for any anomalies in the hammer or motion-sensor behavior.

Behavior objectives for hammer and sensor structures are straight lines relating input and output and their ratio (sensitivity) with frequency. In other words, ideal sensors treat amplitudes proportionally and frequencies the same, and do not delay the signal. The results for one typical impact hammer are given in Fig. B.4.

ORIGINAL PAGE IS
OF POOR QUALITY

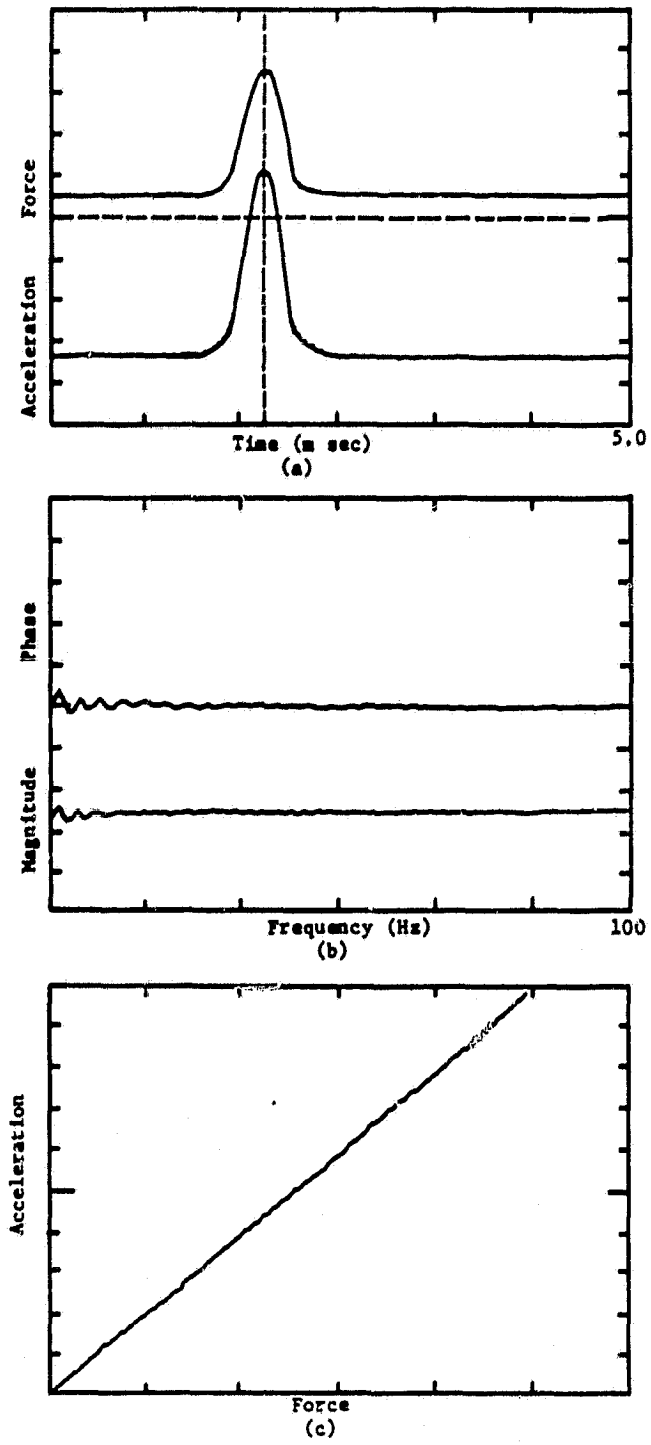

Figure B.4. Typical results from calibration of an impact hammer and accelerometer; (a) time record, (b) frequency response, (c) amplitude linearity.

Appendix C

FLOW CHART FOR THE COMPUTER PROGRAM FOR PREDICTION OF DYNAMIC FLEXURAL RESPONSES OF PROPELLER BLADES

Start

Main program

Call subroutine INPUT

Subroutine INPUT

1. Read and print material and geometrical properties of model.
2. Read and print the amplitudes, frequency, and time increment of the forcing function.
3. Read and print the initial displacements and initial velocities at nodal points.
4. Calculate the cross-sectional area and cross-sectional moment of inertia for an N.A.C.A. four-digit symmetrical airfoil sectional area.

Main Program

1. Calculate and print lumped masses at all nodal points.
2. Calculate and print flexibility influence coefficients.
3. Call function SIMUL.
4. Calculate and print the stiffness influence coefficients matrix by inversion of the flexibility influence coefficients matrix.

Call function SIMUL

Function SIMUL

1. When INDIC is negative, SIMUL computes the inverse of the N by N matrix in place.
2. When INDIC is zero, SIMUL computes the N solutions X1(1)..X(N) corresponding to the set of linear equations.
3. When INDIC is positive, the set of equations is solved, but the inverse is not computed in place.

1

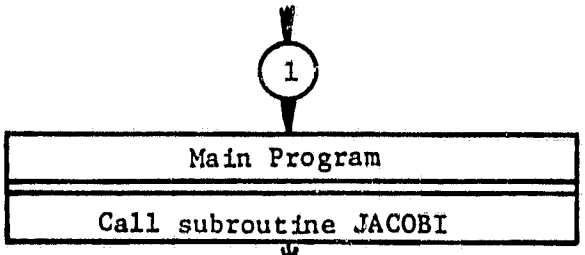

Subroutine JACOBI

This subroutine solves the generalized eigenproblem using the generalized Jacobi iteration.

Input variables

A(N,N)	= Stiffness matrix (assumed positive-definite)
B(N,N)	= Mass matrix (assumed positive-definite)
X(N,N)	= Matrix storing eigenvalues on solution exit
EIGV(N)	= Vector storing eigenvalues on solution exit
D(N)	= Working vector
N	= Order of matrices A and B
RTOL	= Convergence tolerance (usually set to 10**-12)
NSMAX	= Maximum number of sweeps allowed (set to 15)
IFPR	= Flag for printing during iteration
EQ=0	No printing
EQ=1	Intermediate results are printed
IOUT	= Output device number

Output variables

All eigenvectors are stored columnwise

A(N,N)	= Diagonalized stiffness matrix
B(N,N)	= Diagonalized mass matrix
X(N,N)	= Eigenvectors
XS(N,N)	= Scaled eigenvectors XS(I,J)TR*M1(I,J)*XS(I,J)=(I)
XL(N,N)	= Orthonormalized eigenvectors
EIGV(N)	= Eigenvectors

The eigenvalues and corresponding eigenvectors are not calculated in an ascending or descending order.

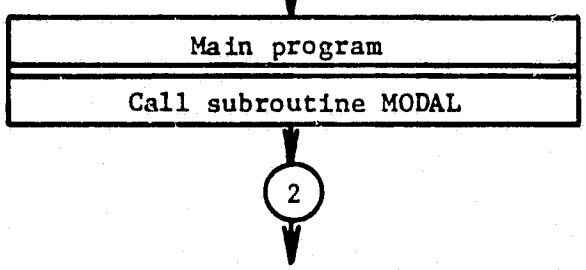

2

Subroutine MODAL

This subroutine defines and prints out the following parameters:

1. The coefficients of the modal equation.
2. The orthogonality relations of eigenvectors.
3. Modal mass and modal stiffness.
4. Effective mass in a mode.
5. The percentage of total mass taken into consideration by modal analysis.
6. The participation factor (modal force).
7. Natural frequencies sorted in an ascending order.
8. Critical damping, amplification factor, damping ratio, and damping coefficients in a particular mode.

Main program

Call subroutine SORT

Subroutine SORT

This subroutine defines and prints out the following parameters:

1. The eigenvalues and corresponding eigenvectors sorted in an ascending order.
2. Natural frequencies obtained from a continuous beam model.
3. First five natural frequencies measured by FFT analyzer.

Scaled eigenvectors sorted in an ascending order columnwise represent the modal shapes in a particular mode.

Main program

Call subroutine EXACT

3

3

Subroutine EXACT

This subroutine calculates and prints out the dynamic response of the blade modeled as a continuous cantilever beam, subjected to a harmonic force of F = FO*SIN (OMEGAF*T) at the tip. The Bernoulli-Euler equation for a continuous beam is used and appropriate boundary conditions are applied. This program gives the steady-state response of the system and does not take into account the transient solution. Damping is neglected. The displacements are calculated at all N nodal points (along the length) at each time-step interval through two time periods of forcing frequency.

Main program

Call subroutine RESP

Subroutine RESP

Subroutine RESP calculates the dynamic response of the uniform continuous blade (cantilever beam) modeled by modal analysis with the damping neglected. A decoupled system of equations is used. For the complete response, the solution of all N equations, I = 1,2,...,N, is calculated, and then the nodal-point displacements are obtained by superposition of the response in each mode. Initial conditions are taken into account for the transient is added to the steady-state response.

The test program calculates and prints out only a steady-state response of the blade subjected to a harmonic force of F = FO*SIN (OMEGAF*T) at the tip. Initial conditions are assumed to be zero (the system is driven from the rest). The displacements are calculated at all N nodal points (along the length) at each time-step interval during two time periods of forcing frequency.

Main program

Call subroutine LEAST

4

4

Subroutine LEAST

Subroutine LEAST does a linear least-square approximation of measured data (damping ratios vs. natural frequencies). The idea is to decouple the damping forces in equations of motion in a manner similar to that in which the elastic and inertial forces are uncoupled. This information is going to be used later on for calculation of the damping modal matrix and the full-damping matrix.

Main program

Call subroutine DAMP

Subroutine DAMP

Subroutine DAMP defines the conditions under which the damping forces are uncoupled. The uncoupling of the equations of motion is possible only by imposing some restrictions or conditions on the functional expression for the damping coefficients. The damping normally present in structure does not affect the calculation of natural frequencies and modal shapes of the system.

This subroutine defines a system-damping matrix by employing a particular form of proportional damping called Rayleigh damping, composed of a linear combination of the mass and stiffness matrices CDMP(I,J) = ALPHA*M1(I,J) + BETA*STF(I,J). Coefficients alpha and beta are defined using the straight line XI(I) vs. OMEGA(I) obtained by subroutine LEAST and assuming that the form of proportional damping is:

XS(I,J)TR*(ALPHA*M1(I,J) + BETA*STF(I,J))*XS(I,J) = 2*OMEGA(I)*XI(I). Values of the scaled damping matrix and full-damping matrix are calculated and printed. Damped and undamped natural frequencies are printed for the number of modes chosen by the program.

5

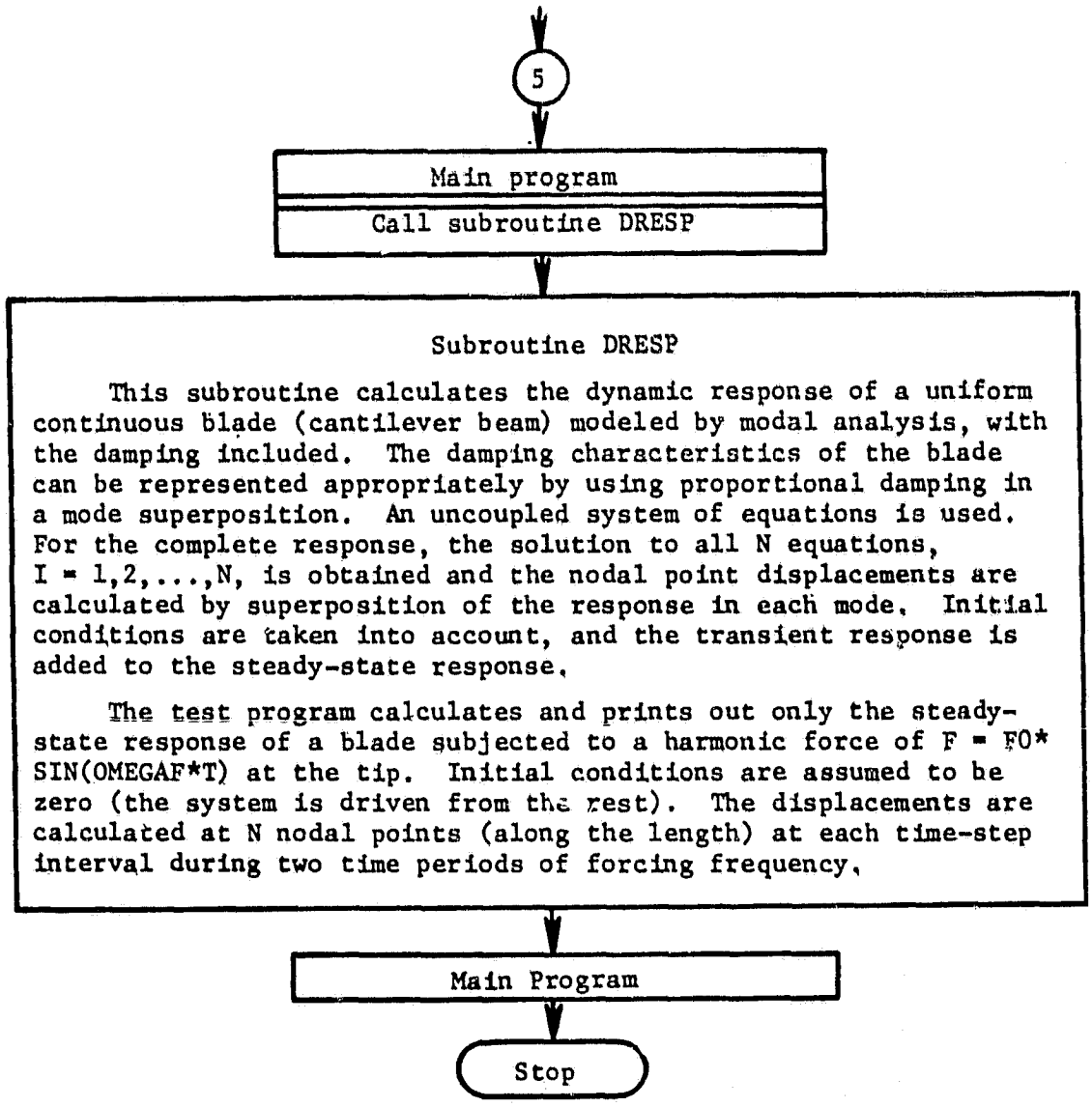
5
Main program
Call subroutine DRESP
Subroutine DRESP
This subroutine calculates the dynamic response of a uniform continuous blade (cantilever beam) modeled by modal analysis, with the damping included. The damping characteristics of the blade can be represented appropriately by using proportional damping in a mode superposition. An uncoupled system of equations is used. For the complete response, the solution to all N equations, I = 1,2,...,N, is obtained and the nodal point displacements are calculated by superposition of the response in each mode. Initial conditions are taken into account, and the transient response is added to the steady-state response.
The test program calculates and prints out only the steady-state response of a blade subjected to a harmonic force of F = F0* SIN(OMEGAF*T) at the tip. Initial conditions are assumed to be zero (the system is driven from the rest). The displacements are calculated at N nodal points (along the length) at each time-step interval during two time periods of forcing frequency.
Main Program
Stop